

AD-A100 017

GEORGIA INST OF TECH ATLANTA  
PARAMETRIC INVESTIGATION OF RADOME ANALYSIS METHODS. VOLUME IV--ETC(U)  
FEB 81 H L BASSETT, J M NEWTON, W ADAMS AFOSR-77-3469

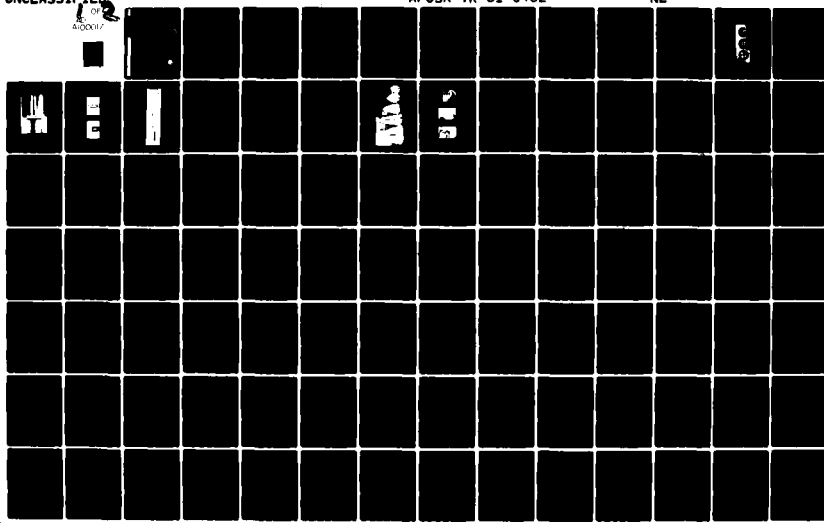
AFOSR-TR-81-0462

F/6 17/9

NL

UNCLASSIFIED

OF  
AFOSR



PARAMETRIC INVESTIGATION  
OF  
RADOME ANALYSIS METHODS:

LEVEL  
12

EXPERIMENTAL RESULTS

ADA100017

By

H. L. Bassett, J. M. Newton, W. Adams, J. S. Ussailis,  
M. J. Hadsell, & G. K. Huddleston



C

Prepared for

AIR FORCE OFFICE OF SCIENTIFIC RESEARCH (AFSC)  
BOLLING AIR FORCE BASE, D. C. 20332

FINAL TECHNICAL REPORT, VOLUME IV OF IV  
GRANT AFOSR-77-3469

30 September 1977 – 31 December 1980

February 1981

**GEORGIA INSTITUTE OF TECHNOLOGY**  
Engineering Experiment Station &  
SCHOOL OF ELECTRICAL ENGINEERING  
ATLANTA, GEORGIA 30332

1981



FILE COPY

81 6 10 027

Approved for public release;  
distribution unlimited.

DMIC

The views and conclusions contained in this document are those of the authors and  
should not be interpreted as necessarily representing the official policies or endorsements  
of the Air Force Office of Scientific Research or the U. S. Government.

UNCLASSIFIED

SECURITY CLASSIFICATION OF THIS PAGE (When Data Entered)

REPORT DOCUMENTATION PAGE		READ INSTRUCTIONS BEFORE COMPLETING FORM
1. REPORT NUMBER <b>AFOSR-TR-81-0462</b>	2. GOVT ACCESSION NO. <b>AD-A10017</b>	3. RECIPIENT'S CATALOG NUMBER
4. TITLE (and Subtitle) PARAMETRIC INVESTIGATION OF RADOME ANALYSIS METHODS; EXPERIMENTAL RESULTS,		5. TYPE OF REPORT & PERIOD COVERED Final Technical Report, Vol. 4 of 4/September 1977-Dec. 1980
		6. PERFORMING ORG. REPORT NUMBER
7. AUTHOR(s) H. L. Bassett, J. M. Newton, W. Adams, J. S. Ussailis, M. J. Hadsell, and G. K. Huddleston		8. CONTRACT OR GRANT NUMBER(S) <b>AFOSR-77-3469</b>
9. PERFORMING ORGANIZATION NAME AND ADDRESS Georgia Institute of Technology Engineering Experiment Station & School of EE Atlanta, Georgia 30332		10. PROGRAM ELEMENT, PROJECT, TASK AREA & WORK UNIT NUMBERS <b>61102F 2301/A6</b>
11. CONTROLLING OFFICE NAME AND ADDRESS Air Force Office of Scientific Research (AFSC) <b>/NP</b> Physics Directorate Bolling AFB, D.C. 20332		12. REPORT DATE <b>February-1981</b>
14. MONITORING AGENCY NAME & ADDRESS (if different from Controlling Office)		13. NUMBER OF PAGES <b>189</b>
		15. SECURITY CLASS. (of this report) <b>UNCLASSIFIED</b>
		15a. DECLASSIFICATION/DOWNGRADING SCHEDULE
16. DISTRIBUTION STATEMENT (of this Report)  Approved for public release; distribution unlimited.		
17. DISTRIBUTION STATEMENT (of the abstract entered in Block 20, if different from Report)		
18. SUPPLEMENTARY NOTES		
19. KEY WORDS (Continue on reverse side if necessary and identify by block number) Radome Measurements Antenna Measurements Millimeter Wave Radome Radome Analysis		
20. ABSTRACT (Continue on reverse side if necessary and identify by block number)  This Volume 4 of four volumes presents 140 measured far-field patterns and boresight error data for eight combinations of three monopulse antennas and five tangent ogive Rexolite radomes at 35 GHz. The antennas and radomes, all of different sizes, were selected to provide a range of parameters as found in the applications. The measured data serve as true data in the parametric investigation of radome analysis methods to determine the accuracies and ranges of validity of selected methods of analysis.		

PARAMETRIC INVESTIGATION OF RADOME ANALYSIS METHODS:

EXPERIMENTAL RESULTS

by

H. L. Bassett, J. M. Newton\*, W. Adams\*,  
J. S. Ussaillis, & M. J. Hadsell  
Engineering Experiment Station  
Electromagnetics Laboratory\* and  
Radar and Instrumentation Laboratory  
Georgia Institute of Technology

&

G. K. Huddleston  
School of Electrical Engineering  
Georgia Institute of Technology  
Atlanta, Georgia 30332

Final Technical Report, Volume IV of IV

for

Air Force Office of Scientific Research (AFSC)  
Physics Directorate (Code NP-77-148)  
Bolling Air Force Base, D. C. 20332

under

Grant AFOSR-77-3469  
30 September 1977 - 31 December 1980

February 1981

AIR FORCE OFFICE OF SCIENTIFIC RESEARCH (AFSC)  
NOTICE OF TRANSMITTAL TO DDC  
This technical report has been reviewed and is  
approved for public release IAW AFR 190-12 (7b).  
Distribution is unlimited.

A. D. BLOSE  
Technical Information Officer

TABLE OF CONTENTS

	<u>Page</u>
<u>CHAPTER I</u>	
Introduction. . . . .	1
<u>CHAPTER II</u>	
Antennas. . . . .	2
<u>CHAPTER III</u>	
Radomes and Mounting Hardware . . . . .	6
<u>CHAPTER IV</u>	
Pattern Measurements. . . . .	12
<u>CHAPTER V</u>	
Boresight Error Measurements. . . . .	18

Accession For	
NTIS GRA&I	<input checked="" type="checkbox"/>
DNIC TAB	<input type="checkbox"/>
Unannounced	<input type="checkbox"/>
Justification	
By _____	
Distribution/ _____	
Availability Codes	
Avail and/or	
Dist : Special	
A	

LIST OF ILLUSTRATIONS

<u>FIGURE</u>		<u>Page</u>
1	Schematic Drawing of Four-Horn Monopulse Antenna Array. . .	4
2	Photograph of Front View of Large, Medium and Small Antennas. . . . .	5
3	Photograph of Medium Antenna Showing Tuning Screws in Waveguide Feeds . . . . .	7
4	Photograph of Input and Output Ports of Monopulse Comparator. . . . .	8
5	Photograph of Complete Antenna Assembly Using Small Array. 9	
6	Illustration of Dimensions of Tangent Ogive Radomes . . .	10
7	Photograph of the Five Radomes, Three Baseplates, Three Adapter Inserts, and Two Extension Rings Used in the Experimental Work . . . . .	13
8	Radome Positioning Procedure: Large Array and Large F=1 Radome Shown. . . . .	14
9	Coordinate System Used for Antenna Pattern Measurements	

LIST OF TABLES

<u>TABLE</u>		<u>Page</u>
1	Ratios of Radome Inside Diameter to Antenna Aperture Diameter for Antenna/Radome Combinations Measured. . . . .	3
2	Monopulse Array Dimensions . . . . .	3
3	Radome Dimensions in Inches. . . . .	11
4	Measured Loss in Gain (decibels) For Eight Antenna/Radome Combinations . . . . .	22

PARAMETRIC INVESTIGATION OF RADOME ANALYSIS METHODS:

EXPERIMENTAL RESULTS

I. Introduction

This technical report documents the pattern and boresight error measurements made on eight combinations of three monopulse antennas and five tangent ogive radomes at 35 GHz in support of the parametric investigation of radome analysis methods carried out under grant AFOSR-77-3469. The measurements program was carried out by personnel in the Electromagnetics Laboratory and the Radar and Instrumentation Laboratory of the Engineering Experiment Station at Georgia Institute of Technology during the period October 1977 through December 1980.

This report is Volume IV of four volumes which comprise the final technical report for this research grant. Volume I presents an overview of this research and salient results. Volume II documents the analytical method and Fortran computer code used to analyze the various antenna/radome combinations using a fast receiving formulation based on Lorentz reciprocity and geometrical optics. Volume III documents the analytical method and additional Fortran software required for radome analysis based on the Huygens-Fresnel principle (surface integration).

The overall objective of this research is to develop a general theory of radome analysis and to determine the accuracies of three computer-aided radome analysis methods under controlled conditions of antenna size and placement, wavelength and radome size and shape. The measured data presented here is used as true data in the assessments of the accuracies of those methods. It is expected that this measured data will be

used in the future by other investigators for the same purposes. It is for this reason, and the fact that no similar data base currently exists, that these measured data are so tediously documented.

Three antennas, representing small, medium, and large in terms of radiating aperture size, were combined with five tangent ogive radomes to provide a range of antenna/radome parameters that is likely to be encountered in the applications and for which the accuracies of likely computer codes are to be determined. The parameters of the radomes include both size (small, medium, large) and fineness ratio; i.e., ratio of radome length to diameter. The tangent ogive shape was chosen because of its ease of fabrication, analytical tractability, and widespread use in the applications. The eight combinations of antennas and radomes measured are summarized by the entries in Table 1.

The physical characteristics of the antennas and radomes used are presented below: The measurement procedures and coordinate systems are also described. The measured pattern data and boresight error data are presented in Appendices A through K. Principal plane patterns and diagonal plane patterns of the sum, elevation difference, and azimuth difference channels of the three antennas alone are presented in Appendices A, B, and C. Measured principal plane patterns of the antennas with radomes are presented in Appendices D through K for the eight combinations used. Each of these eight appendices is concluded with measured boresight error data.

## II. Antennas

The antennas are four-element monopulse arrays as shown in Figures 1 and 2. Their dimensions in wavelengths ( $\lambda$ ) at 35 GHz and in inches are given in Table 2. Each element is a conical horn with a circular to

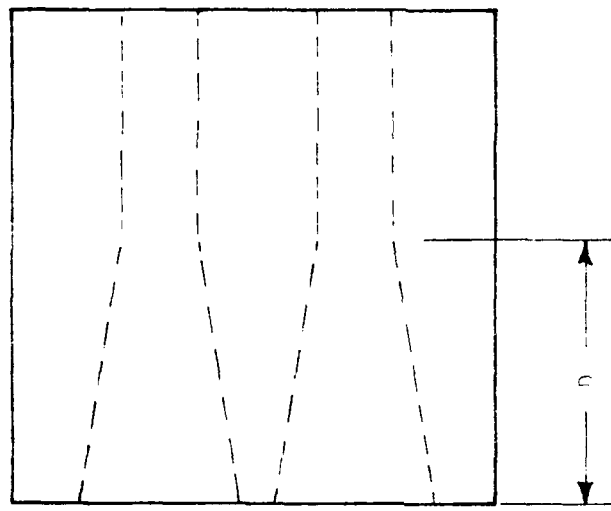
Table 1. Ratios of Radome Inside Diameter to Antenna Aperture Diameter for Antenna/Radome Combinations Measured.

<u>Radome</u>	<u>Antenna</u>		
	<u>Small</u>	<u>Medium</u>	<u>Large</u>
Small (F=1.0)	2.33	--	--
Medium (F=1.0)	3.98	2.33	--
Medium (F=1.5)	--	2.33	--
Medium (F=2.0)	--	2.33	--
Large (F=1.0)	7.28	4.27	2.33

Table 2. Monopulse Array Dimensions.

Dimension (See Figure 1)	Small Array		Medium Array		Large Array	
	$\lambda$	inches	$\lambda$	inches	$\lambda$	inches
A	0.919	0.310	1.839	0.620	3.633	1.225
B	2.589	0.875	4.567	1.540	9.015	3.040
C	2.108	.160	1.054	.320	2.604	0.878
D	1.275	0.430	5.456	1.840	6.153	2.075

FRONT VIEW



END VIEW

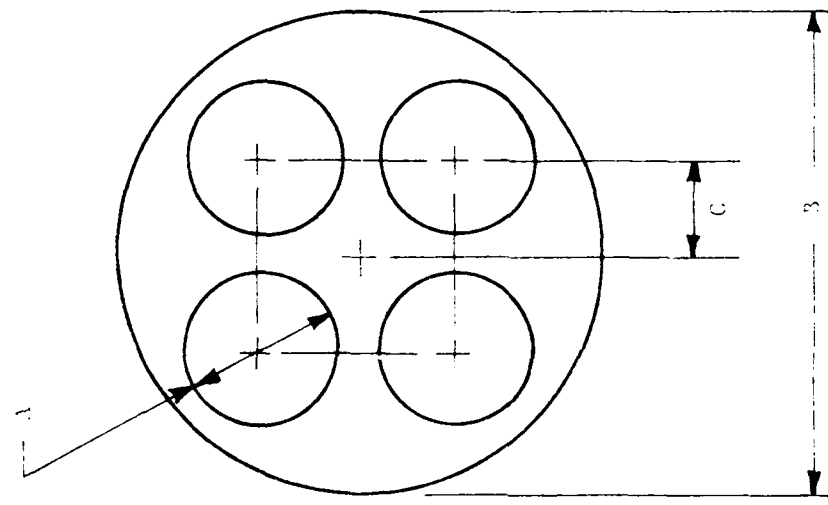


Figure 1. Schematic Drawing of Four-horn Monopulse Antenna Array

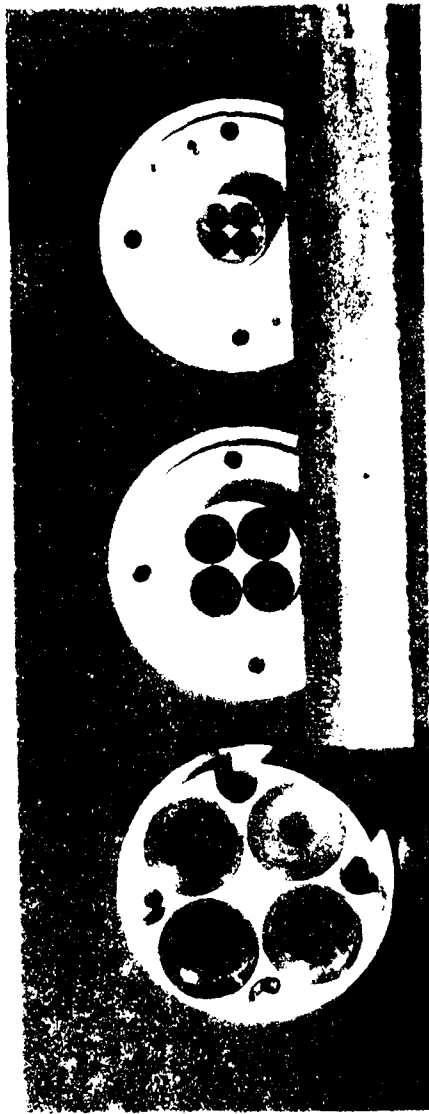


Figure 1. Photograph of Front View of Large, Medium and Small Antennas

rectangular waveguide transition at the throat. All four elements are machined into a single piece of aluminum for stability and to facilitate pattern measurements with and without the various radomes. The three arrays produce measured sum pattern beam widths of  $28^\circ$  (small array),  $15^\circ$  (medium), and  $8^\circ$  (large) as shown in Appendices A through C.

Signals received by the horn elements are fed into a monopulse comparator via four rectangular waveguide sections. The signal paths to this point are not of exactly equal length; hence, low-loss dielectric screws were introduced into the waveguide sections to adjust the phase delay in each signal path to a single constant. That constant was determined by the relative phase of the longest signal path at the comparator input port. An example of a waveguide section tuned in this way is shown in Figure 3.

The monopulse comparator is a single unit of several waveguide couplers. Signals received at the four input ports are combined to produce a sum, azimuth difference, and elevation difference channels. Input and output port views of the comparator are shown in Figure 4.

The complete antenna assembly for the small horn is presented in Figure 5. The elevation difference channel is shown connected to a harmonic mixer. The remaining channels are terminated in matching impedances.

### III. Radomes and Mounting Hardware

Five radomes of tangent ogive shape were fabricated for use with the three antennas. Three radomes have fineness ratios of 1:1 and three different base diameters designated as small, medium and large. The remaining two radomes have medium base diameters with fineness ratios of 1.5:1 and 2.0:1. Figure 6 and Table 3 present the radome dimensions in freespace wavelengths ( $\lambda$ ) and in inches (").

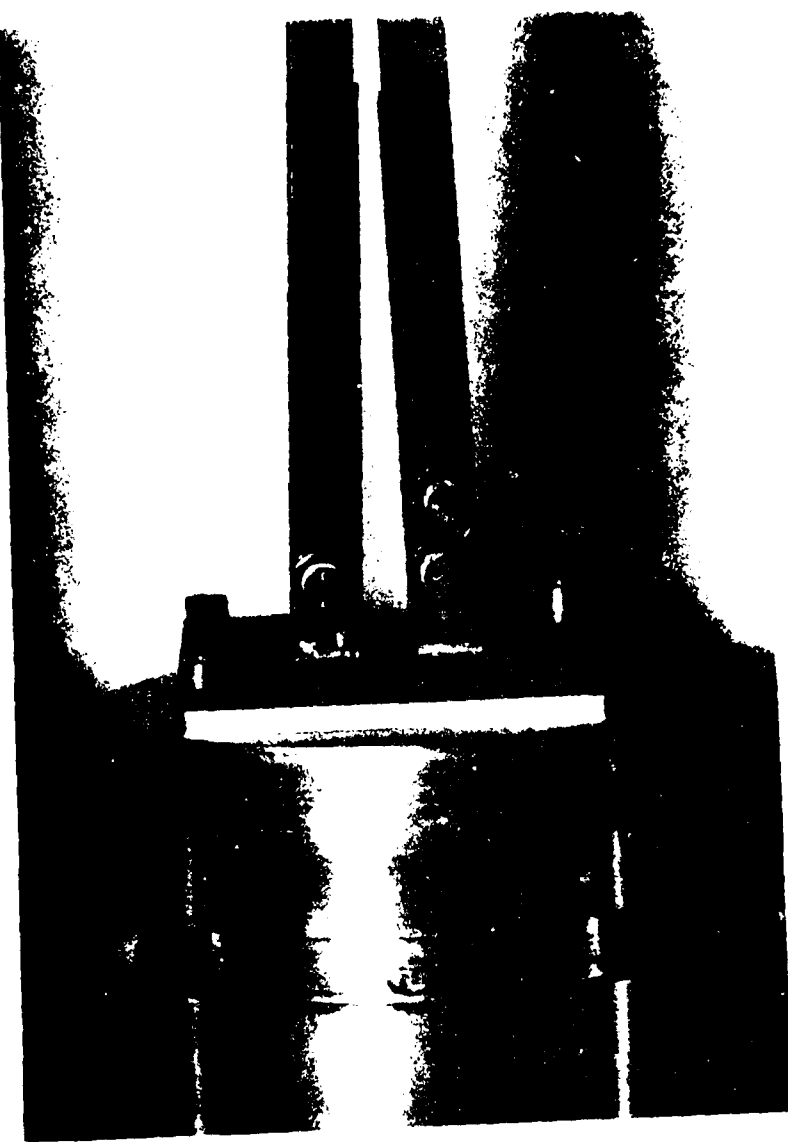
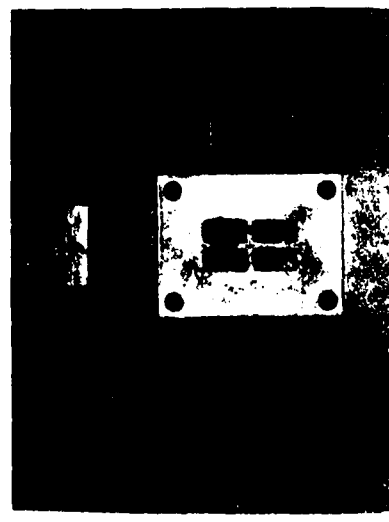
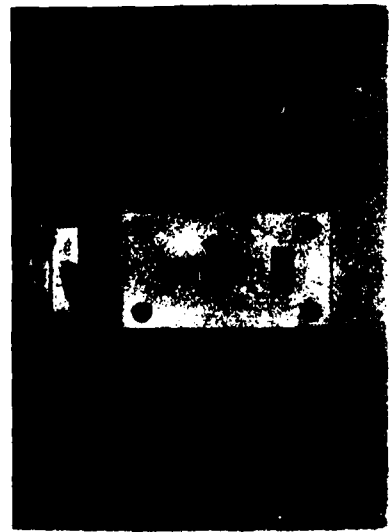


**Figure 3.** Photograph of Medium Antenna with Adjusting Screws in Waveguide Feeds.



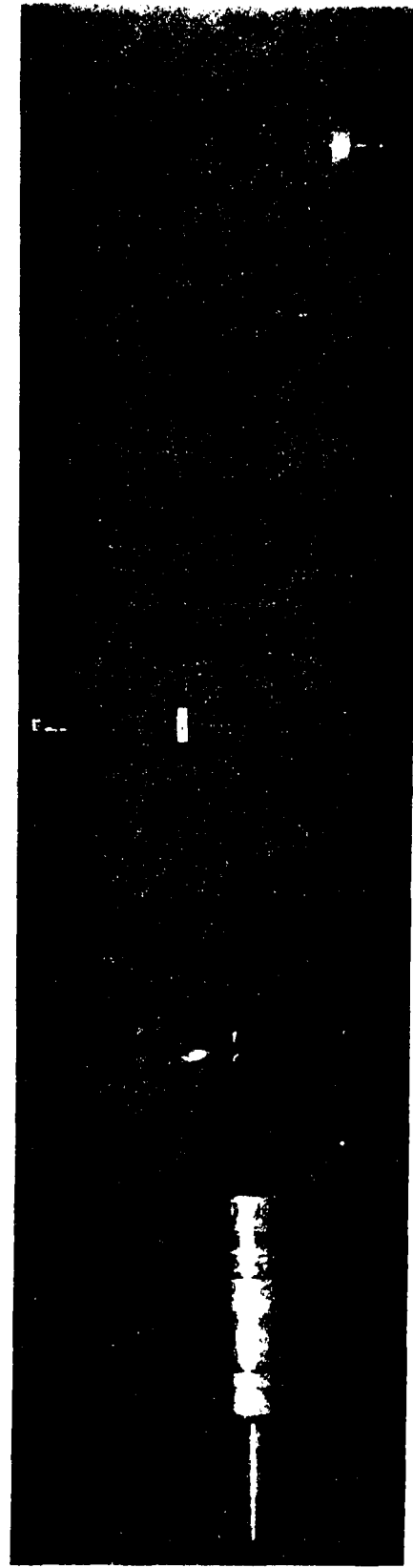
Input Port



Output Port

Figure 4. Photograph of Input and output ports of micropulse comparator.

Figure 5. Photograph of Complete Antenna Assembly Using Small Arms



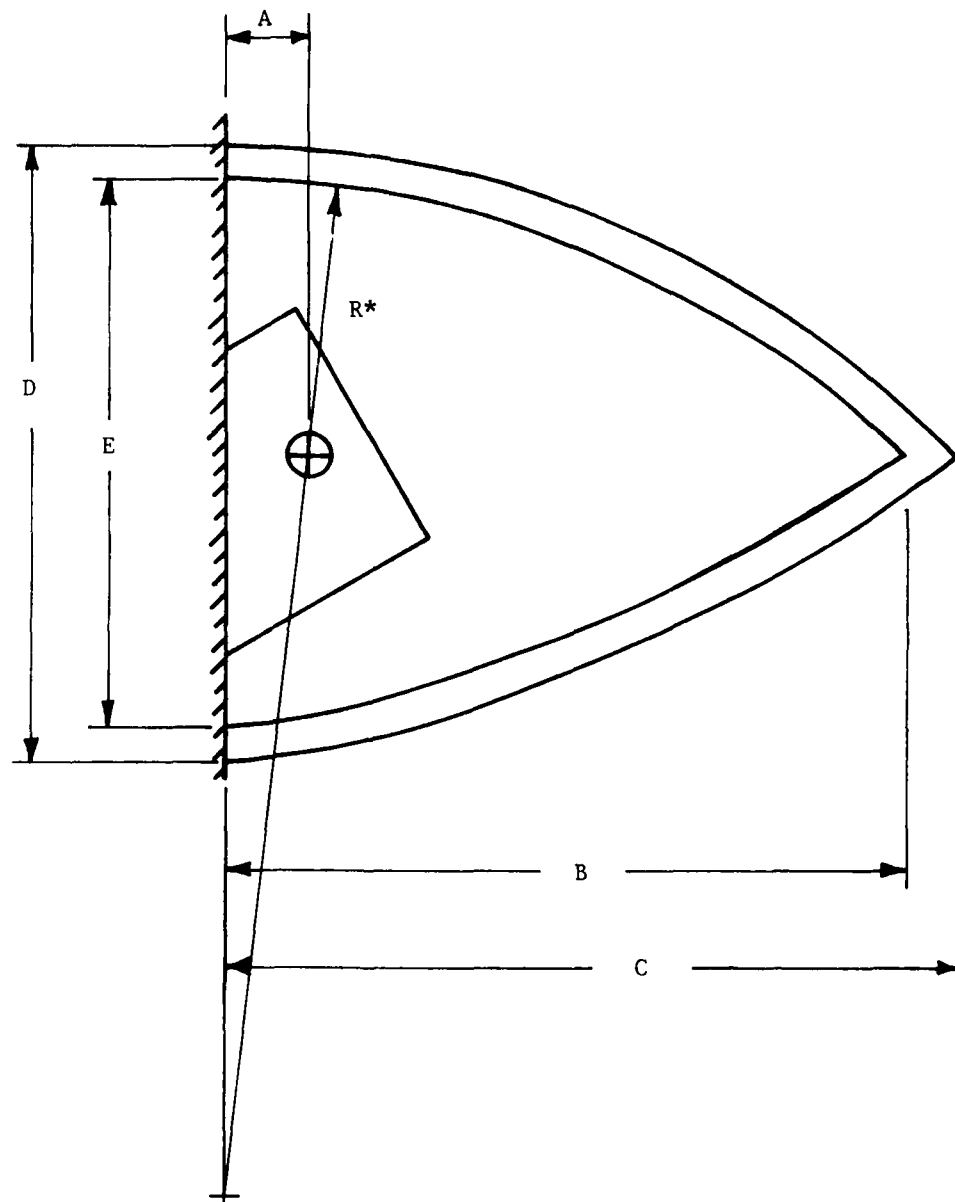


Figure 6. Illustration of Dimensions of Tangent Ogive Radomes

Table 3. Radome Dimensions in Inches.

	Small <u>F=1.0</u>	Medium <u>F=1.0</u>	Medium <u>F=1.5</u>	Medium <u>F=2.0</u>	Large <u>F=1.0</u>
A	0.1875	0.250	0.250	0.250	0.375
B	2.110	3.440	5.250	6.940	6.318
C	2.370	3.825	5.663	7.540	6.875
D	2.550	4.015	3.993	4.000	6.910
E	2.050	3.510	3.497	3.500	6.410

The radomes were machined from cylinders of Rexolite<sup>®</sup> ( $\epsilon_r = 2.54$ ).

The wall thickness for all radomes was chosen to be on the order of one wavelength in Rexolite at 35 GHz. This thickness provided adequate strength and rigidity in the larger radomes and consistent effects for all sizes.

The radomes were mounted to specially machined baseplates as shown in Figure 7. The baseplates were then affixed to selected extension tubes for mounting the radome over the selected antenna. A cylindrical hole was machined in each extension tube to fix the angle between the radome axis and the antenna axis to precisely 15°, and to accurately position the antenna inside the radome.

Additional mounting hardware was fabricated to allow the radome with base plate assembly to be rotated about the axis of the antenna as shown in Figure 8. This hardware allowed for accurate positioning of the tip of the radome with respect to the principal planes of the antenna to facilitate boresight error measurements. Provision was also made to rotate the antenna/radome combination by any specified angle so that great circle pattern cuts could be made using a single azimuth positioner rotating about a vertical axis.

#### IV. Pattern Measurements

The far field range facilitates the measurement of microwave antennas with far field regions forty feet or less distant. For this program, a mounting pedestal was built to allow orientation of the antenna under test. The receiving (test) pedestal is supported by a Scientific Atlanta horizontal positioner unit, which can be positioned down range by rolling on four wheels along a level horizontal track. The transmitter pedestal allows adjustment of the height and polarization of the

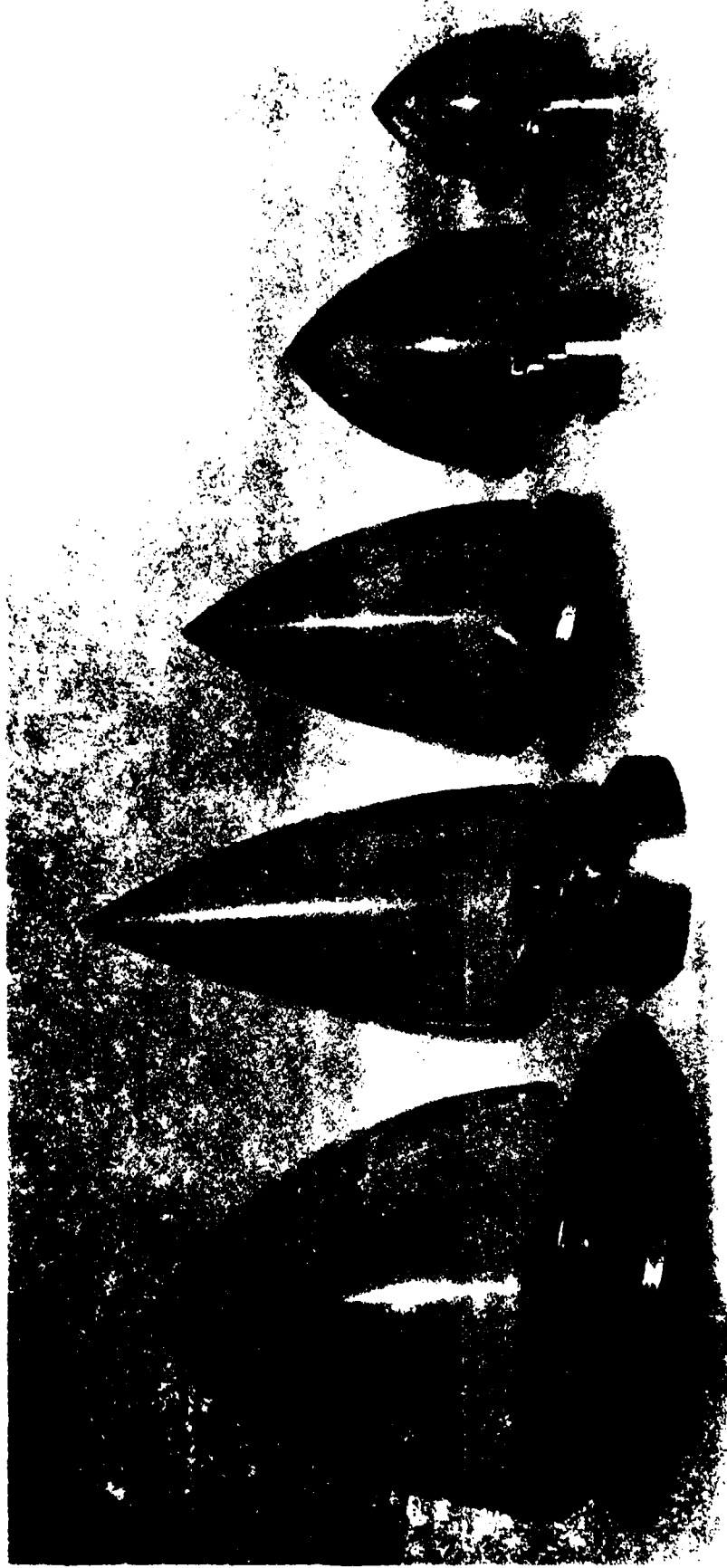
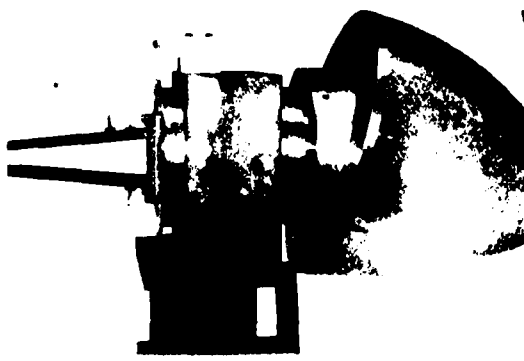


FIGURE 7. Preparation of the five fragments, three pre-lutes, three Aduat, 3, 1, 1, 1, 1, and two Extinction Rings used in the Experimental Work.



Radome Locked in Vertical Position



Rotation of Antenna with Radome Locked in Vertical Position

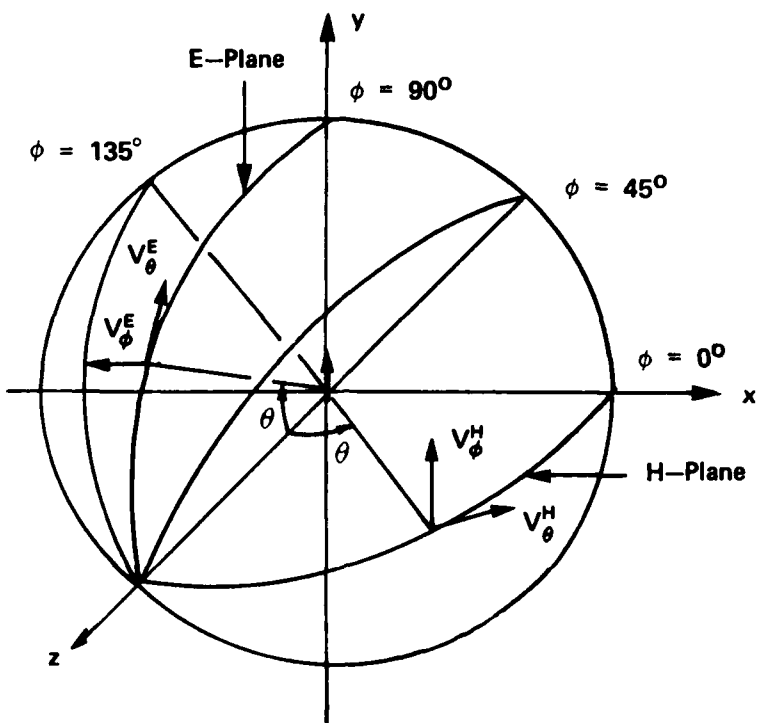


Rotation of Radome/Antenna Assembly to Desired Polarization

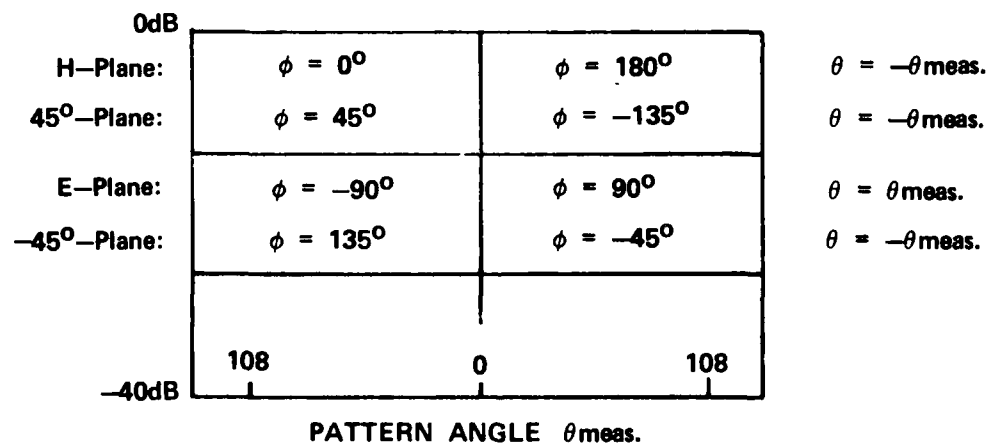
Figure 8. Radome Positioning Procedure: Large Array and Large F=1 Radome Shown

transmitting antenna (in this case, a 35 GHz horn). Signals received by the antenna under test are heterodyned by the phase/amplitude receiver (SA 1753) as the antenna under test (AUT) is rotated about the vertical axis. From the received signal amplitudes, a 1 kHz AM signal is produced as the input to the pattern recorder (SA 1522-40). The recorder produces a 10" x 20" rectangular plot of relative power one way versus the angular position of the antenna. The angular movement of the recorder is directly linked to the test antenna positioner through a synchro-transmitter-receiver feedback loop. No phase measurements were attempted because of instabilities in the Klystron source and because of the mechanical stability difficulties inherent at 35 GHz on an outdoor range.

To understand the pattern measurement procedure, consider the initial position of the four-horn array (AUT) on the receiving pedestal to be such that it is vertically polarized with respect to the horizontal surface of the earth. The horizontal plane containing the axis of symmetry of the antenna (z-axis) is the H-plane and corresponds to the  $\phi=0^\circ$  and  $\phi=180^\circ$  planes of the spherical coordinate system shown in Figure 9(a). H-plane measurements were made by rotating the azimuth positioner in the clockwise direction (Observer #1 looking down on it), starting from a position such that the antenna would be to the left of Observer #2 standing upright behind the receiving pedestal and looking toward the transmitting antenna at the other end of the range. When the transmitting antenna is aligned rotationally about its axis to be vertically polarized, the so called parallel polarization component  $V_\phi^H$  in Figure 9(a) is recorded. By rotating only the transmitting antenna by  $90^\circ$  clockwise (Observer #2) to yield horizontal polarization, the cross polarization component  $V_\phi^H$  in Figure 9(a) was measured.



(a) Antenna Coordinate System



(b) Relationships to Recorded Pattern Measurements.

FIGURE 9. Coordinate System Used for Antenna Pattern Measurements.

The recorded pattern angle  $\theta_{\text{meas}}$  for the H-plane patterns measured during this program is exactly the negative of the polar angle  $\theta$  defined in Figure 9(a). This statement is true for all pattern measurements, except the E-plane patterns, and the relationships between the patterns presented in Appendices A through K and the antenna coordinate system are summarized in Figure 9(b). These relationships are of critical importance to ensure that accurate comparisons to computed patterns are made, especially when the radome is present.

The E-plane of the AUT is the vertical plane which contains the antenna axis of symmetry; i.e., the  $yz$ -plane of the antenna coordinate system shown in Figure 9(a). Pattern measurements in the E-plane were made by first rotating both the AUT and transmitting antenna  $90^\circ$  clockwise (Observer #2 behind AUT). Pattern recordings of the parallel component  $V_\theta^E$  of Figure 9(a) were then made as described above for the H-plane. By rotating the transmitting antenna  $90^\circ$  (Observer #2), the cross component  $V_\phi^E$  of Figure 9(a) was measured. The relationships between the recorded patterns and the antenna coordinate system are summarized in Figure 9(b).

Diagonal plane pattern measurements were made on the antennas alone for modeling purposes. The planes are defined by  $\phi=45^\circ$  and  $\phi=-45^\circ$  in the antenna coordinate system of Figure 9(a). The relationships to the recorded patterns are shown in Figure 9(b).

The receiver used had only a single channel, and pattern measurements on each channel ( $\Sigma$ ,  $\Delta_{\text{EL}}$ ,  $\Delta_{\text{AZ}}$ ) of each antenna were done one channel at a time. The harmonic mixer was installed on the desired port of the monopulse comparator. The other ports were terminated in matched waveguide loads. The mixer and loads were interchanged until all the channels were measured.

All pattern measurements with the radomes in place were done in the same manner as with the antennas alone. The radome under test was always mounted so that its axis of symmetry made an angle of  $15^\circ$  with the axis of symmetry of the antenna; furthermore, the radome was rotated by angle  $\alpha$  so that the tip was located in the  $\phi = -45^\circ$  plane of the antenna coordinate system of Figure 9(a). This position was selected to produce measurable boresight errors and pattern asymmetries in both principal planes. Boresight error measurements were later made as a function of this angle  $\alpha$  as explained in the next section.

Measured pattern data for the antennas alone are presented in Appendices A, B, and C. Patterns with the radomes are presented in Appendices D through K. Note that for these latter patterns, the pattern of the antenna alone is shown as a dashed line for reference purposes. Although some effort was made to show the relative gain and boresight data correctly on these patterns, the boresight error graphs presented at the end of each appendix and the measured relative gain data presented below should be consulted as the final, correct data.

#### V. Boresight Error Measurements

When a radome is placed over the monopulse antenna, an error in the boresight of the antenna on the order of a few tens of milliradians may result. Electrical boresight is indicated when the antenna is positioned in the central nulls of the two orthogonal monopulse channels ( $\Delta_{EL}$ ,  $\Delta_{AZ}$ ). This position of the antenna without radome is the true boresight of the antenna.

Boresight error caused by the radome is defined here as being the actual angular position of the target (transmitting antenna) in the coordinate system of Figure 9(a) when electrical boresight is indicated in

the difference channels. For example, a positive boresight error in azimuth (elevation) would place the target in the  $\phi=0$  plane ( $\phi=90^\circ$  plane) of Figure 9(a). Equal, positive boresight errors in both azimuth and elevation should place the target in the  $\phi=45^\circ$  plane. Negative boresight errors may also occur.

Boresight error measurements were made during this investigation using a precision milling machine rotary table as a turntable mount for the receiving monopulse antenna and radome. Error measurements were made in the elevation and azimuth channels separately. Boresight errors in azimuth were measured by first positioning the monopulse array and transmitting antenna on the far-field range to yield vertical polarization. The turntable was carefully rotated until electrical boresight in the  $\Delta_{AZ}$  channel was indicated. The radome was then placed over the antenna and positioned in the angle  $\alpha$ . The turntable was carefully adjusted to indicated electrical boresight in the  $\Delta_{AZ}$  channel. The boresight error was then read directly from the vernier scale of the turntable. Boresight errors in the elevation channel ( $\Delta_{EL}$ ) were done similarly by rotating both antennas  $90^\circ$  clockwise (Observer #1) about their common axis of symmetry and repeating the above procedure.

The indication of electrical boresight was obtained using a Hewlett-Packard 415 VSWR meter, crystal detector, and 1-kHz amplitude modulation on the 35 GHz signal being transmitted. The detector was installed on the difference channel port of interest and connected to the VSWR meter. The difference channel null position was determined by measuring equal amplitudes on either side of the null as the turntable was rotated about the null position, and then taking the average of the two angular readings on the turntable vernier scale. This method was adopted

After it was discovered that such measurements using the azimuth positioner, heterodyne receiver, and pattern recorder yielded erratic results due to positioner inaccuracies.

As mentioned above, the radome mounting hardware was machined so that the radome axis of symmetry ( $z_R$ -axis) made an angle of  $15^\circ$  with the monopulse array axis of symmetry ( $z$ -axis). Also, the radome with baseplate could be rotated about the  $z$ -axis of the antenna such that the radome tip could be positioned to lie in any  $\phi=\alpha$  plane of Figure 5(b).

Boresight error measurements were made as a function of this angle  $\alpha$ . For example, when  $\alpha=0$ , the radome tip lies in the  $\phi=0$  plane of the antenna, causing boresight error in azimuth but none in elevation due to symmetry. When  $\alpha=90^\circ$ , no boresight error in the  $A_{AZ}$  channel would be expected (due to symmetry), but errors in  $A_{EL}$  would be expected. For any other value of  $\alpha$ , errors would be expected in both channels.

The measured boresight errors for the eight antenna/radome combinations shown in Table I are presented as the last figure of each of Appendices D through K. Each figure presents four error graphs in azimuth and in elevation. For each graph the abscissa is the angle  $\alpha$ , and the ordinate is boresight error in degrees. Measurements were made in  $15^\circ$  increments in  $\alpha$  over the complete range of zero to  $360^\circ$ . Ideally, the boresight errors are antisymmetric in  $\alpha$  with a "period" of  $180^\circ$  degrees; hence, the measured data over two periods provide an indication of repeatability and consistency.

A radome also causes a loss in on-axis gain of the sum channel of the monopulse antenna. The gain loss was measured simply by monitoring the sum channel signal before and after the radome was installed. The monopulse antenna and transmitting antenna were aligned for maximum

received signal in the sum channel. Gain loss was measured at the four angular positions  $\alpha$  of the radome as presented in Table 4.

Table 4. Measured Loss in Gain (decibels) For Eight Antenna/Radome Combinations

Antenna	Radome	Gain Loss (dB)		
		$\alpha = 0^\circ$	$\alpha = 45^\circ$	$\alpha = 90^\circ$
Small	Small ( $F=1.0$ )	0.4	0.7	0.6
"	Medium ( $F=1.0$ )	1.3	1.7	1.5
"	Large ( $F=1.0$ )	1.4	1.6	1.4
Medium	Medium ( $F=1.0$ )	1.4	1.4	0.8
"	Medium ( $F=1.5$ )	1.0	1.0	1.0
"	Medium ( $F=2.0$ )	0.2	0.5	0.6
"	Large ( $F=1.0$ )	1.8	1.4	1.4
Large	Large ( $F=1.0$ )	1.7	1.6	1.3

APPENDIX A

Antenna Patterns of Small Array Without Radome

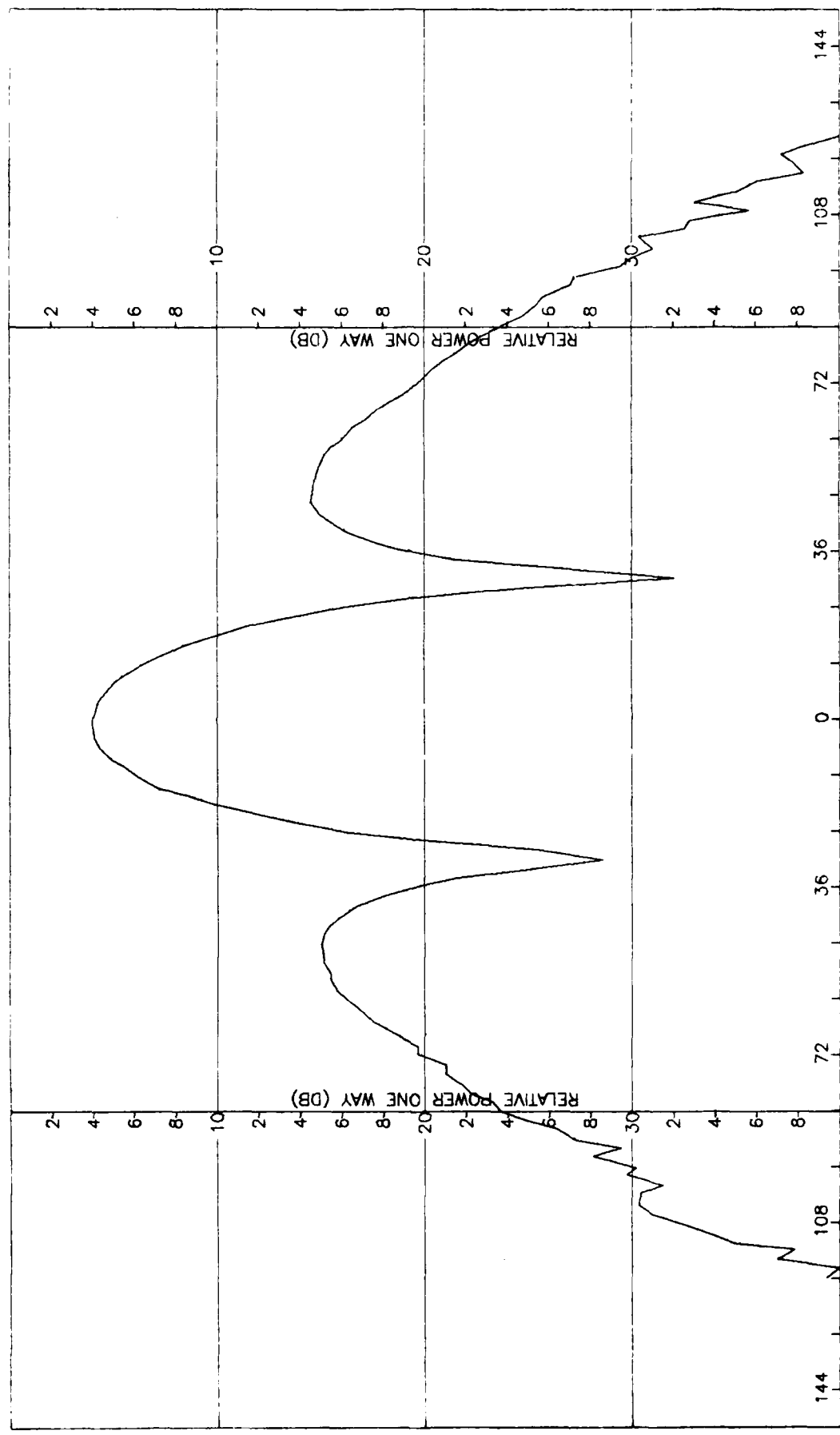


Figure A-1. Pattern of Small Array: H-Plane, Sum,  $\phi$ -Component, No Radome.

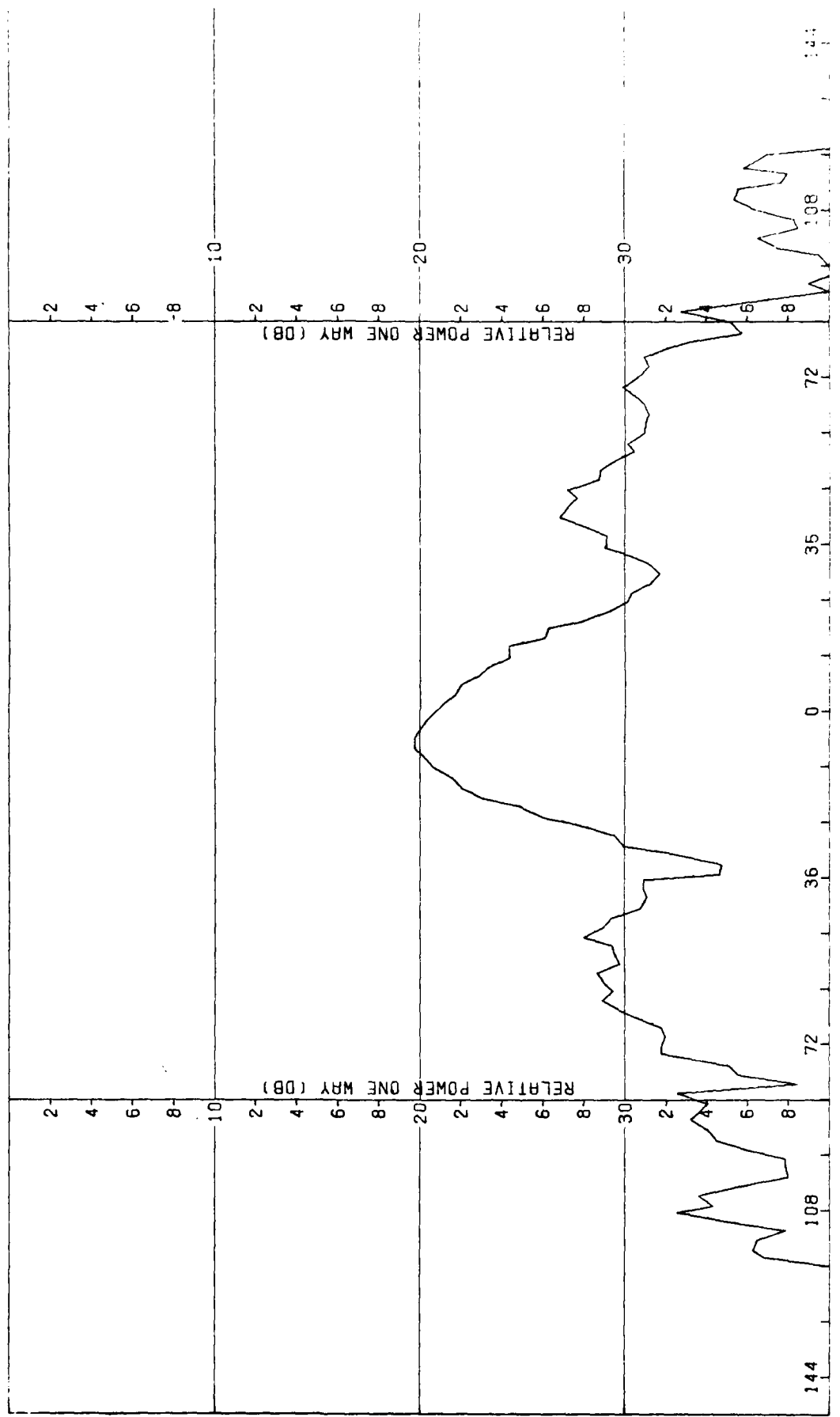


Figure A-2. Pattern of Small Array: H-plane, sum,  $\theta$ -component, No R-idome.

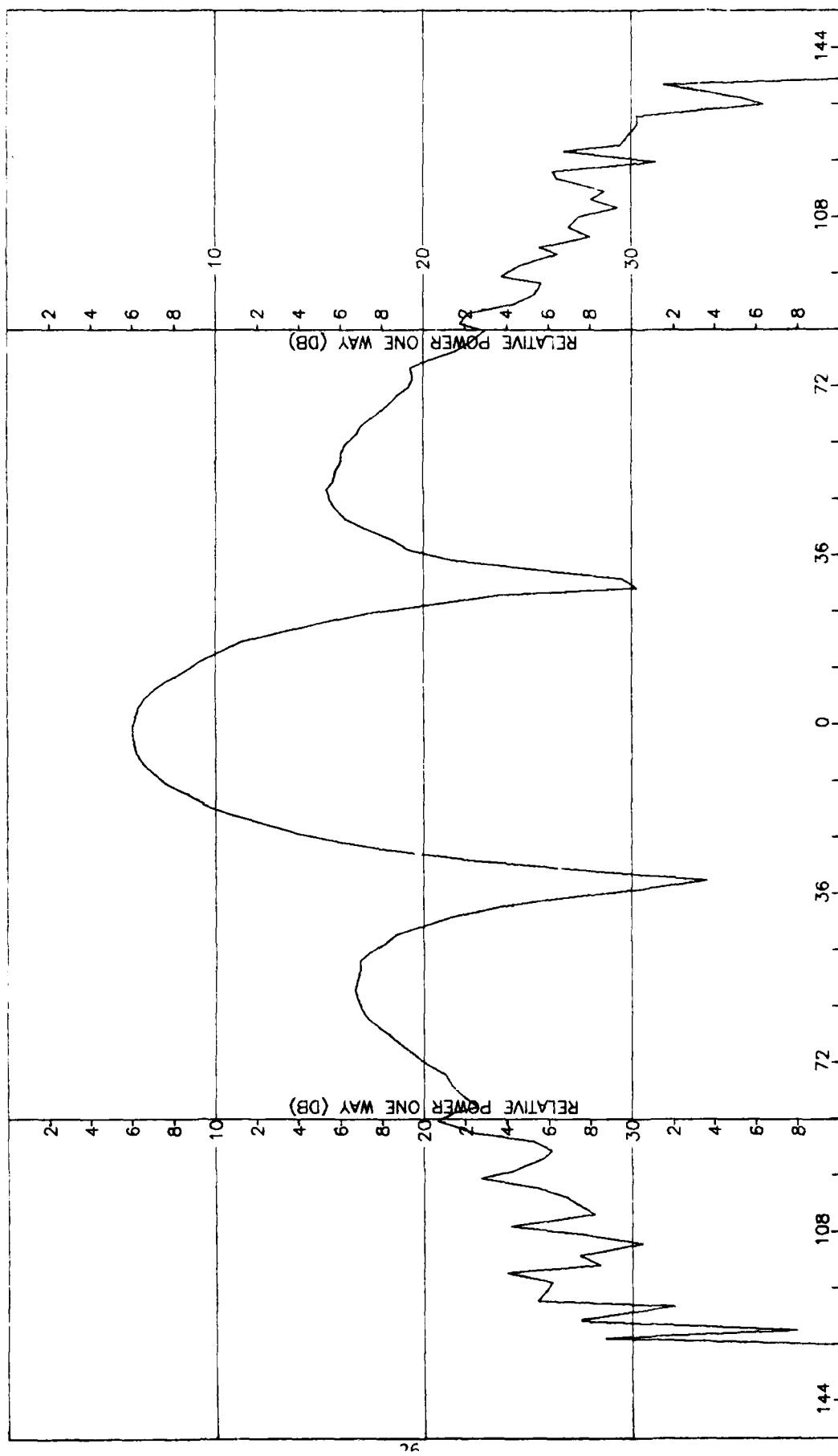


Figure A-3. Pattern of Small Array: E-Plane, Sum,  $\psi$ -Component, No Radome.

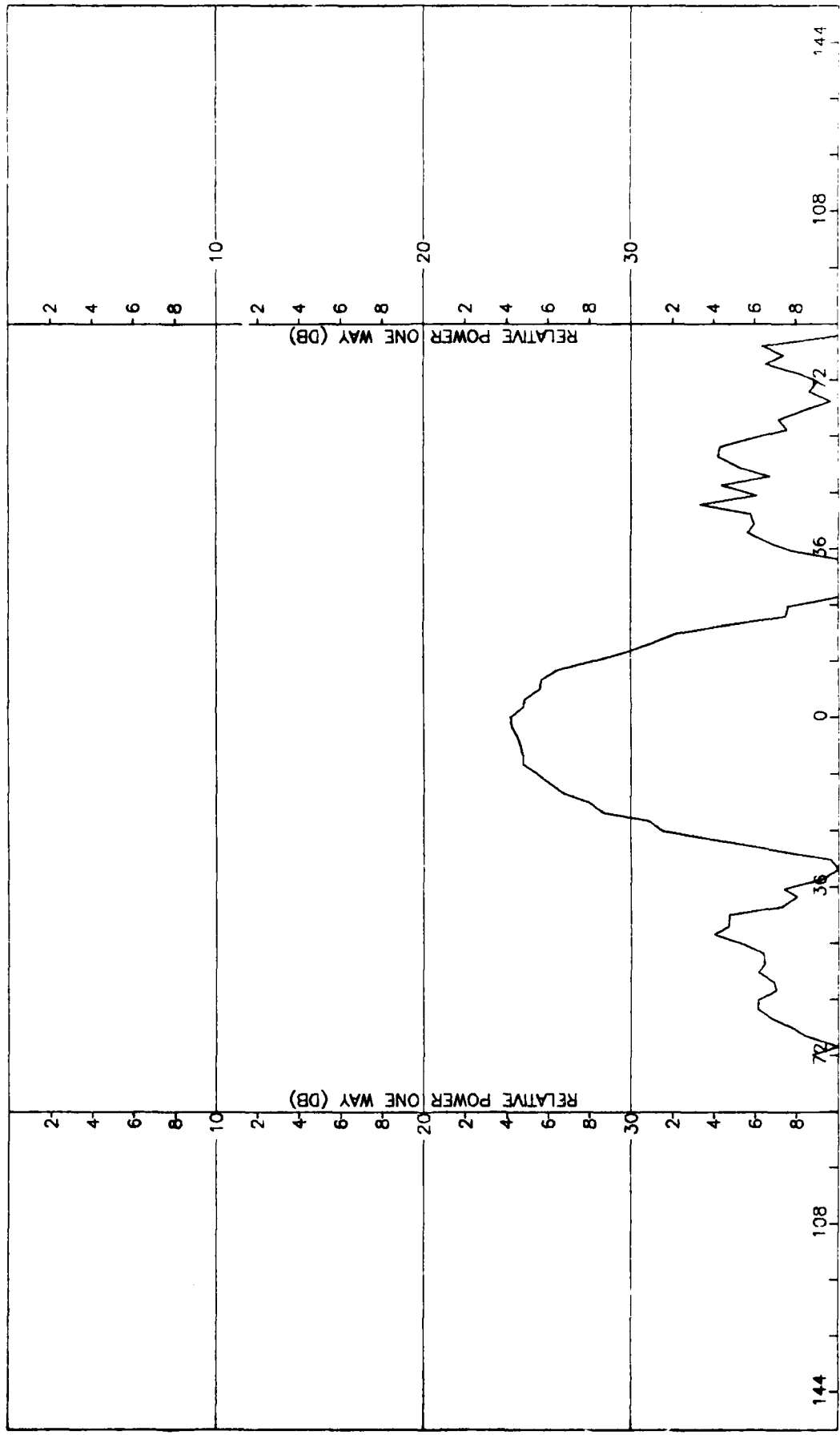


Figure A-4. Pattern of Small Array: E-Plane, Sum,  $\phi$ -component, No Radome.

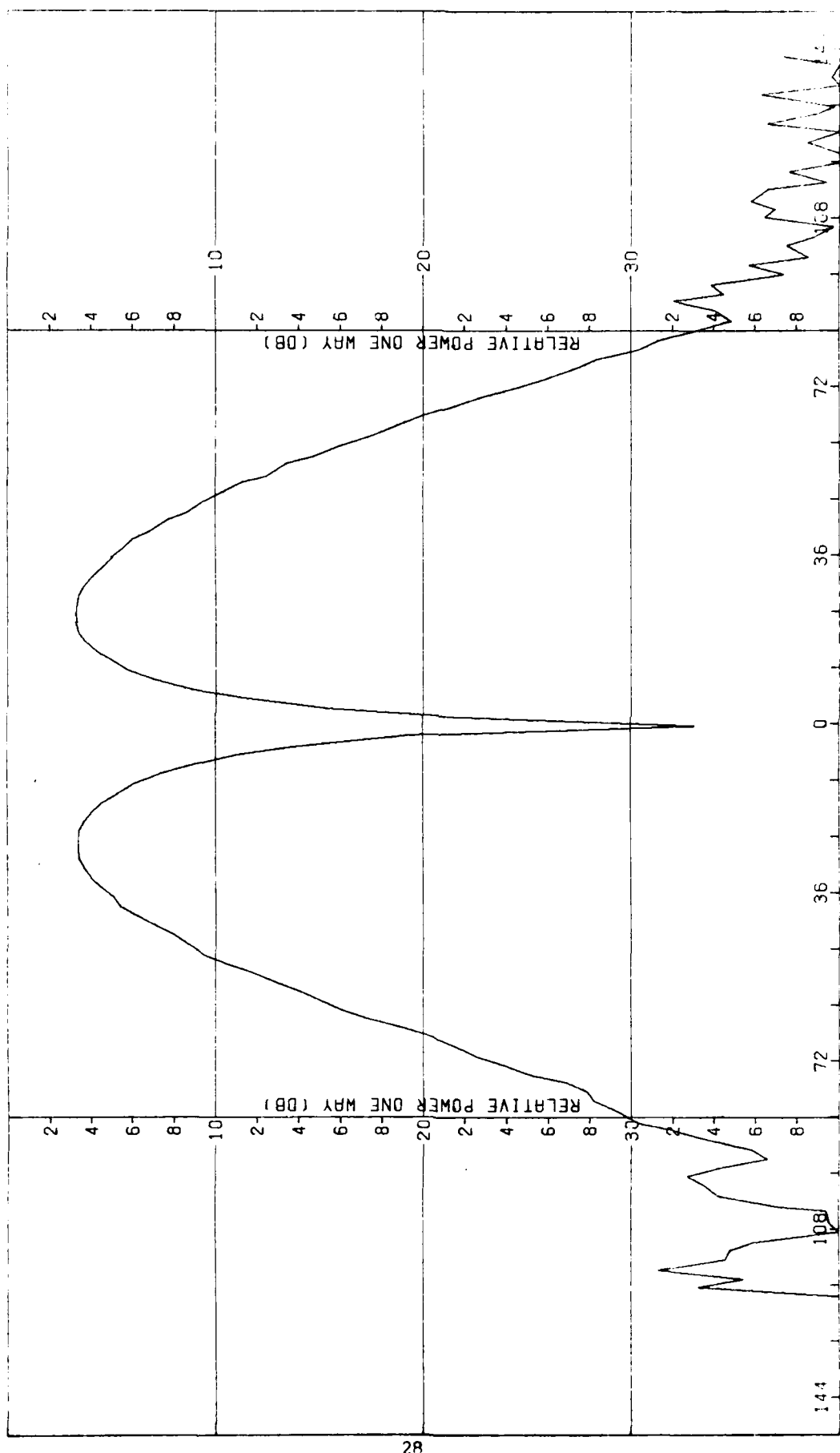


Figure A-5. Pattern of Small Array: H-Plane, Azimuth Difference,  $\phi$ -Component, No Radome.

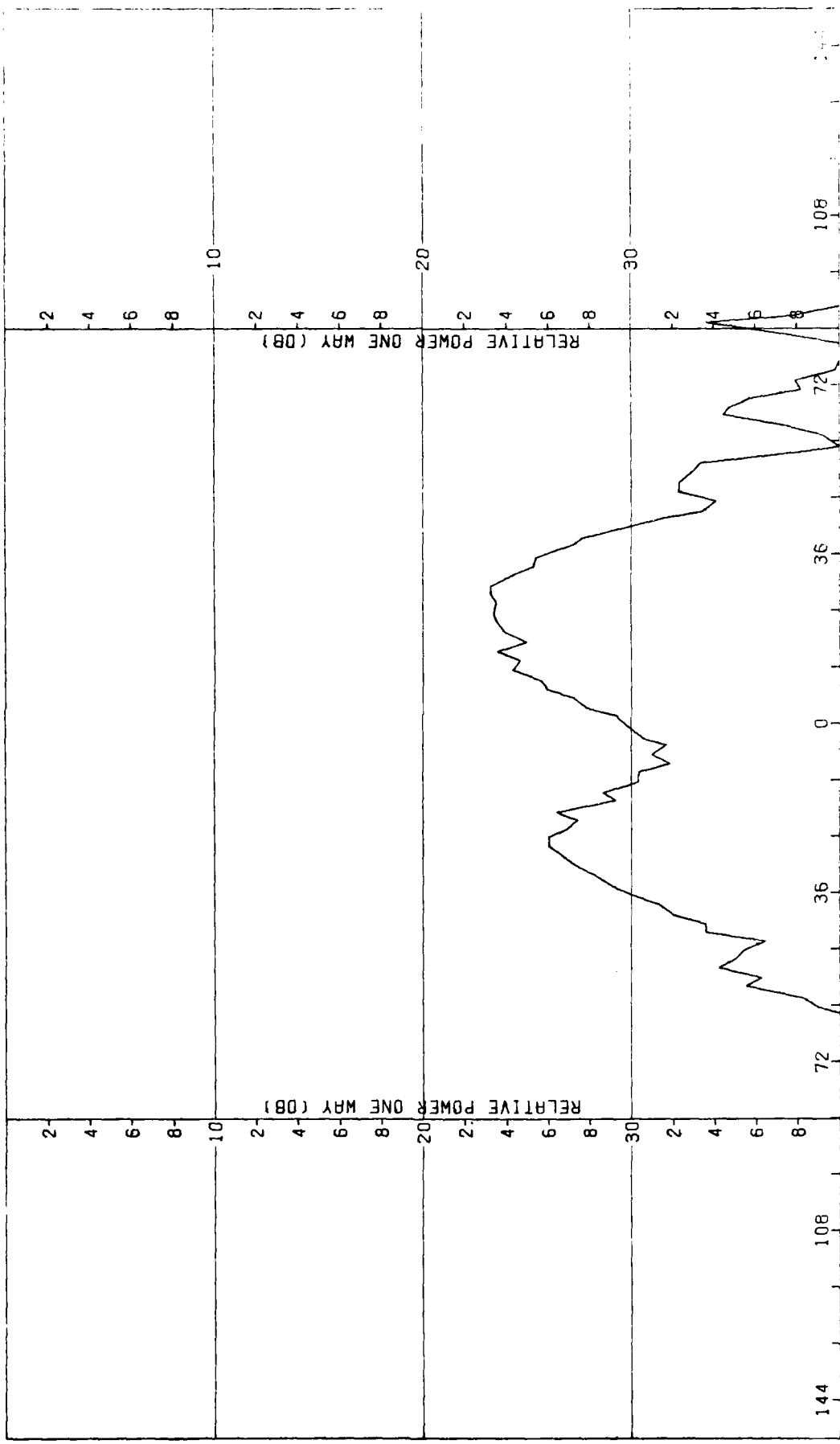


Figure A-6. Pattern of Small Array: H-Plane, Azimuth Difference,  $\theta$ -Component, No Radome.

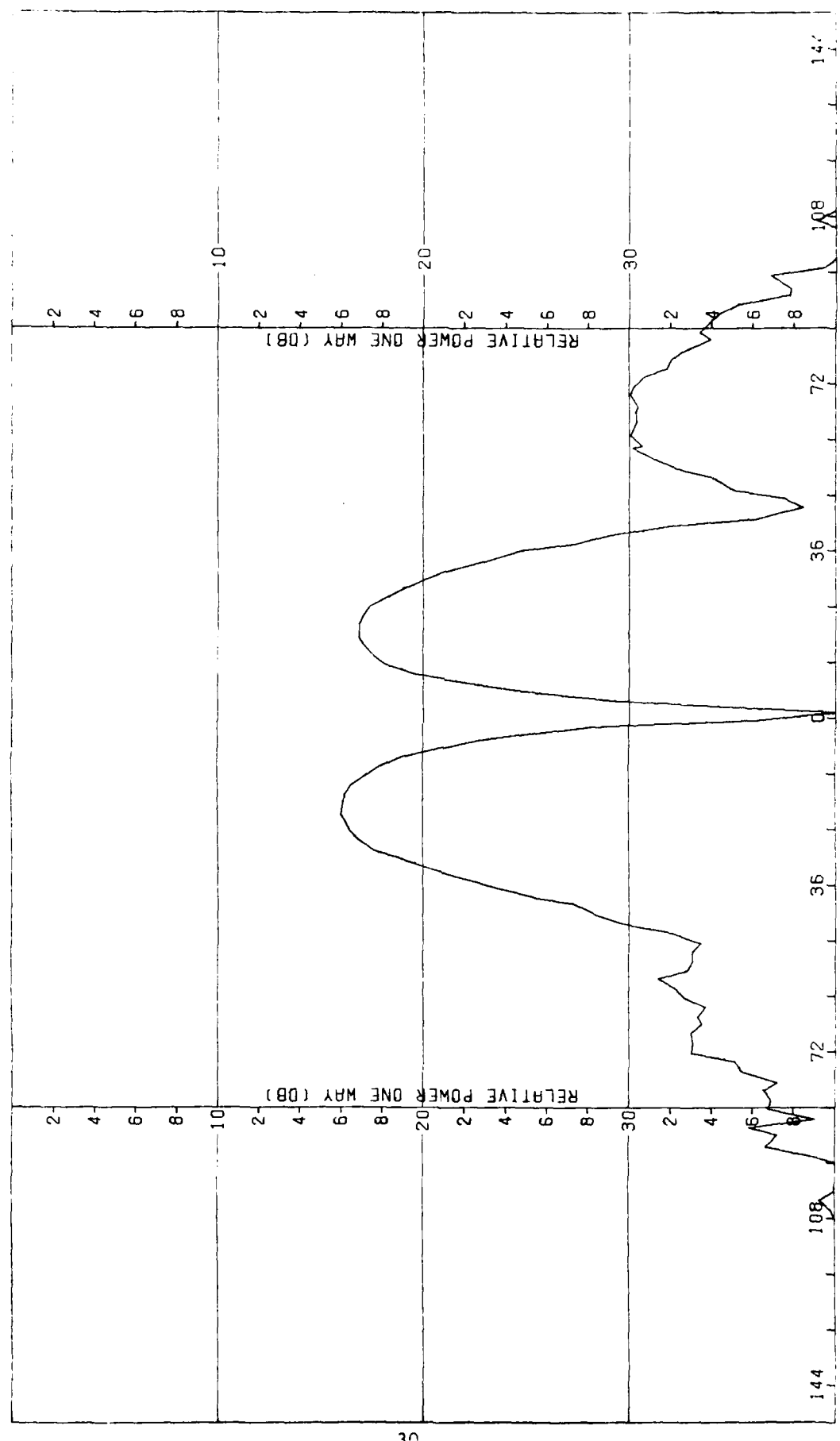


Figure A-7. Pattern of Small Array: E-Plane, Azimuth Difference,  $\theta$ -Component, No Radome.

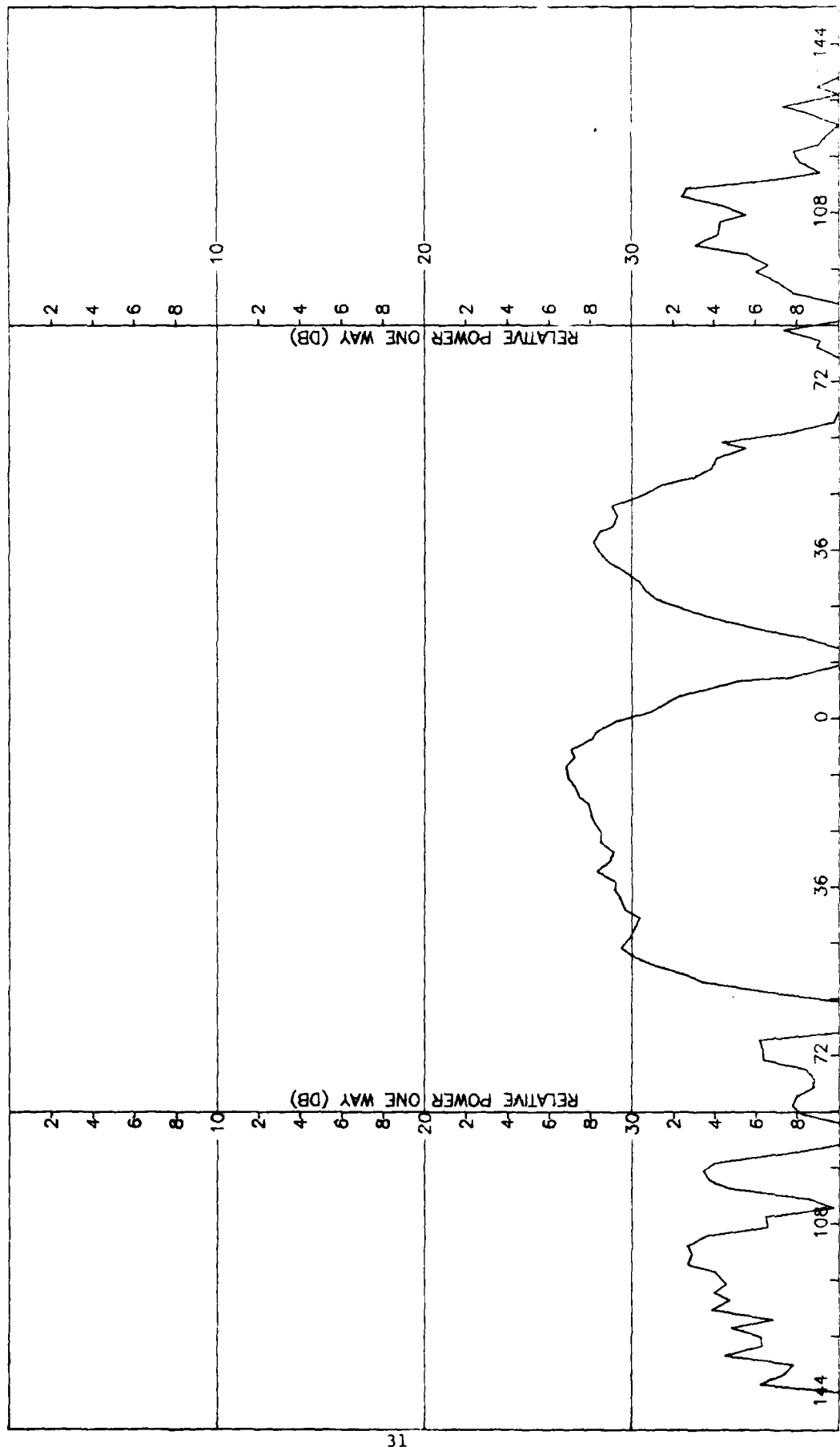


Figure A-8. Pattern of Small Array; E-Plane, Azimuth Difference,  $\phi$ -Component, No Radome.

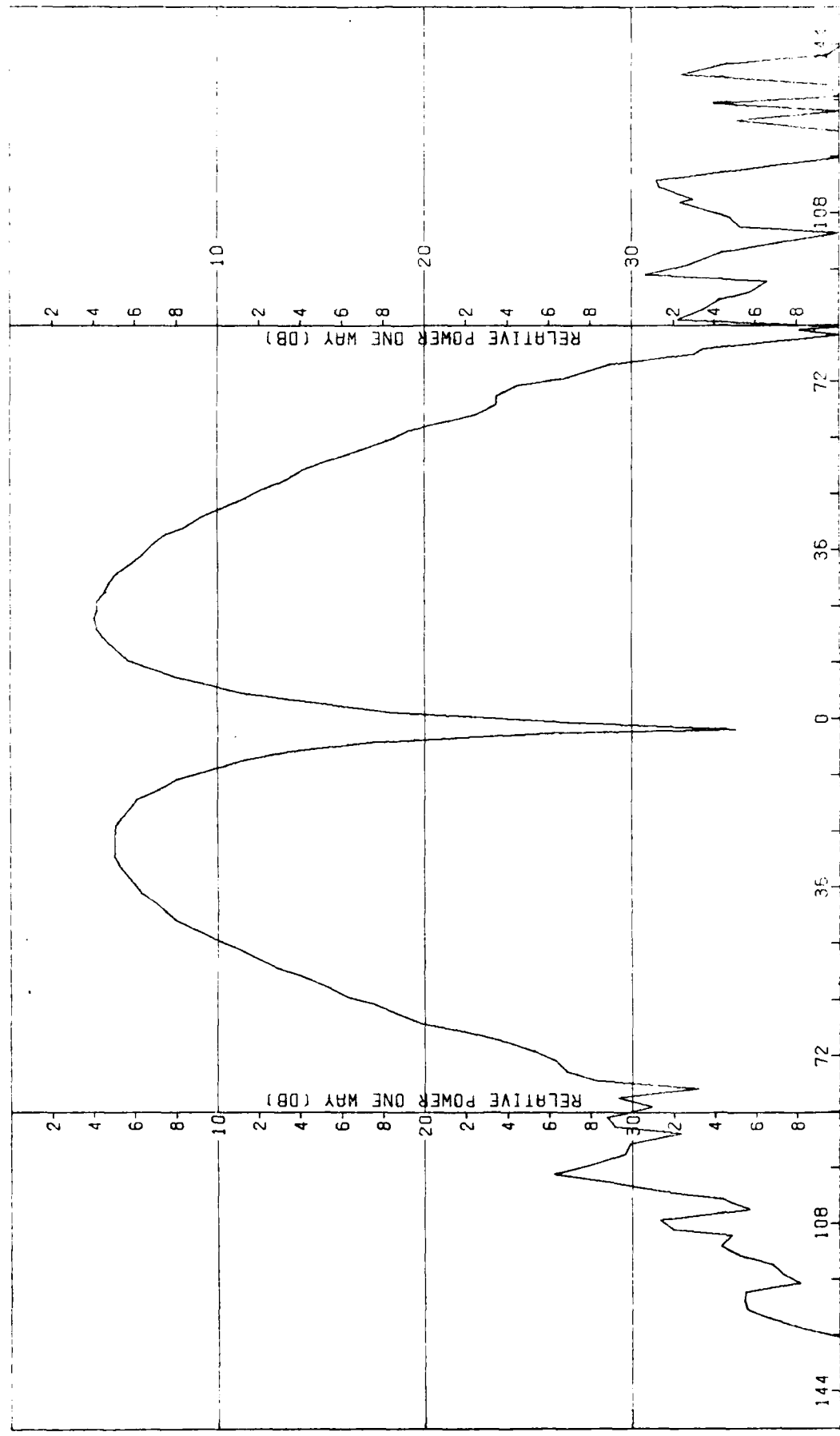


Figure A-9. Pattern of Small Array: E-Plane, Elevation Difference,  $\theta$ -Component, No Radome.

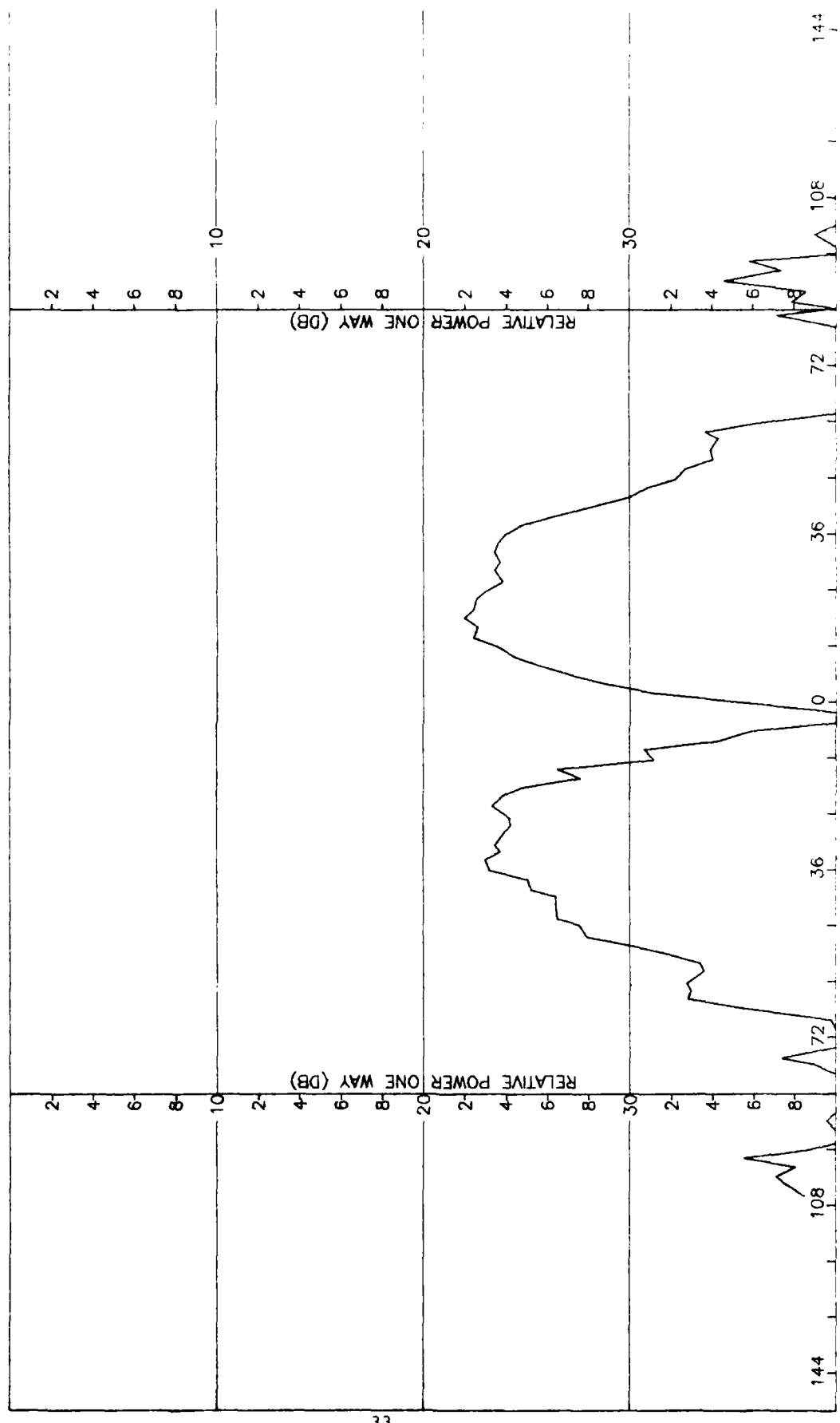


Figure A-10. Pattern of Small Array: E-Plane, Elevation Difference,  $\phi$ -Component, No Radome.

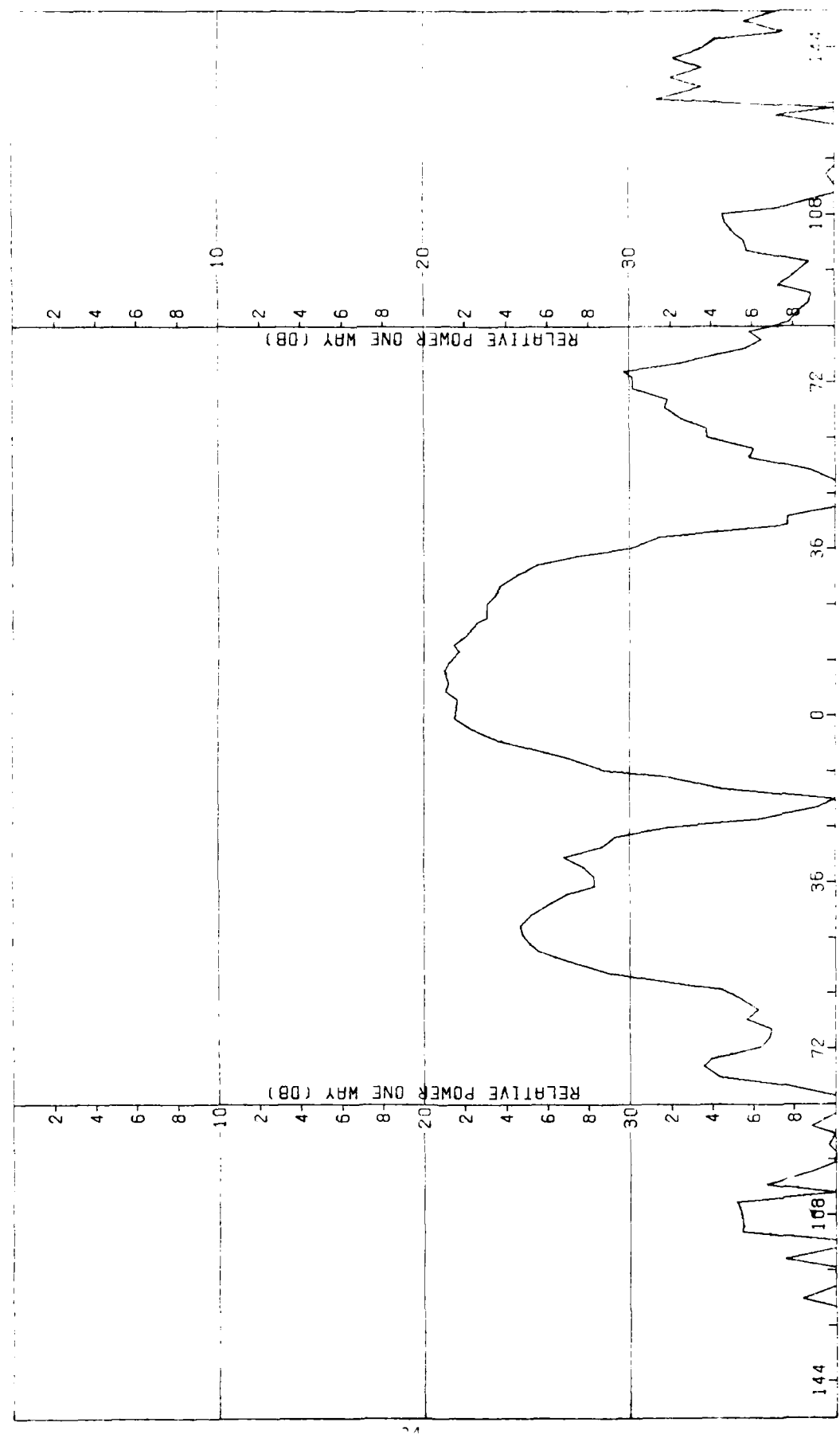


Figure A-11. Pattern of Small Array: R-Plane, Elevation Difference,  $\phi$ -Component, No Radome.

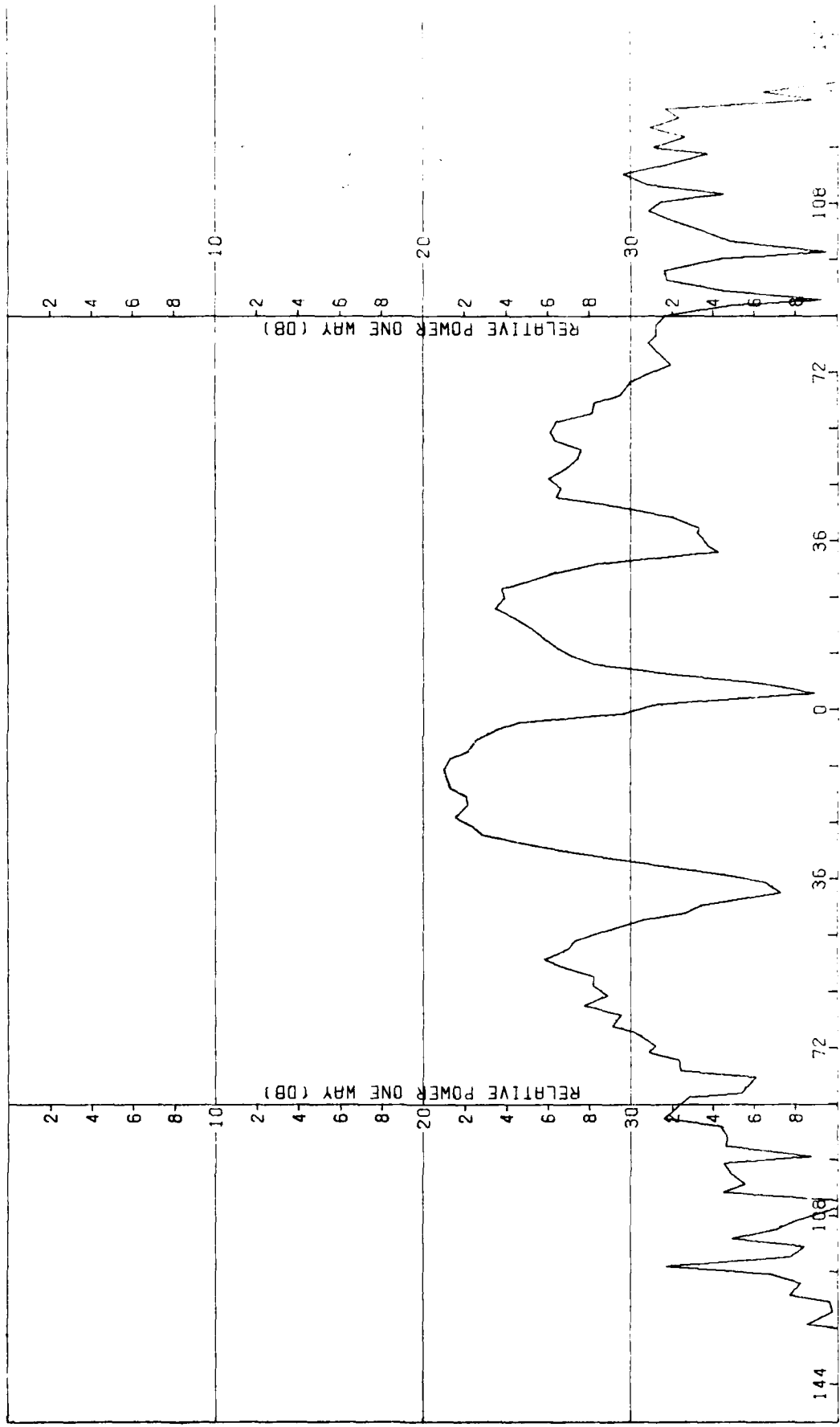


Figure A-12. Pattern of Small Array, H-Plane, Elevation Difference,  $q$ -Component, No Radome.

APPENDIX B

Antenna Patterns of Medium Array Without Radome

PRECEDING PAGE BLANK-NOT FILMED

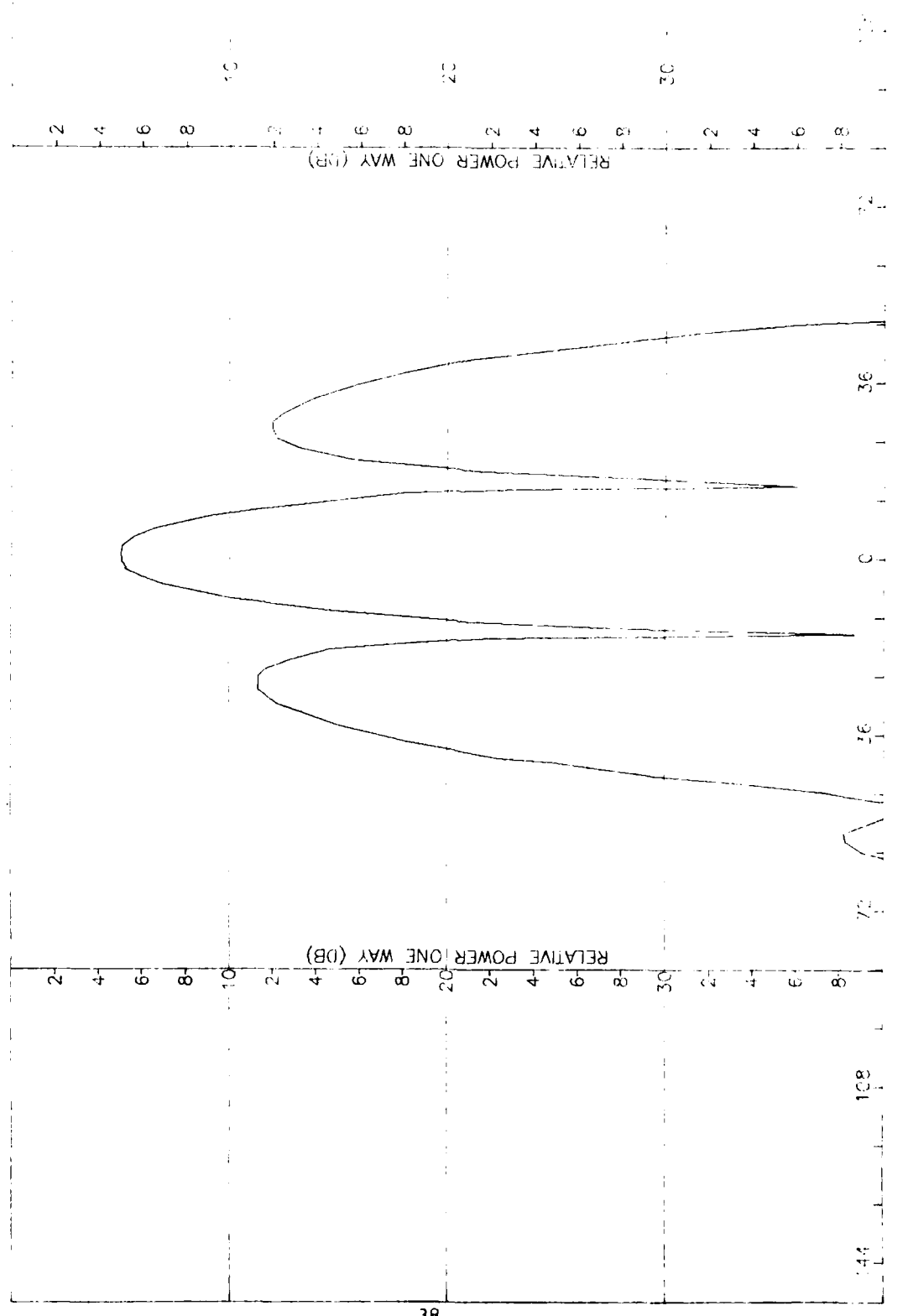


Figure B-1. Pattern of Medium Array: H-Plane Sum,  $\phi$ -Component, No Radome

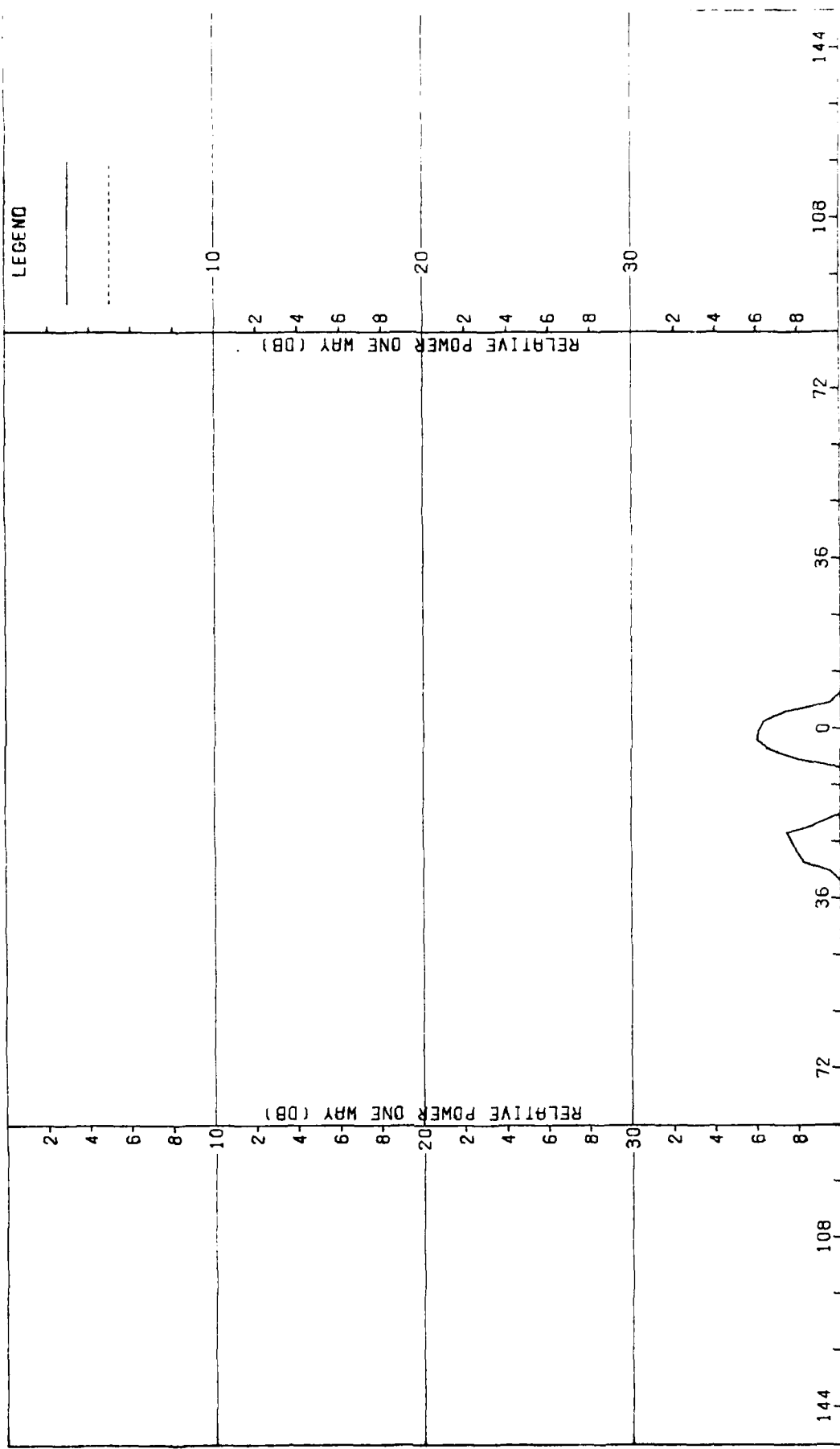


Figure B-2. Pattern of Medium Array: H-Plane, Sum, a-Component, No Radome

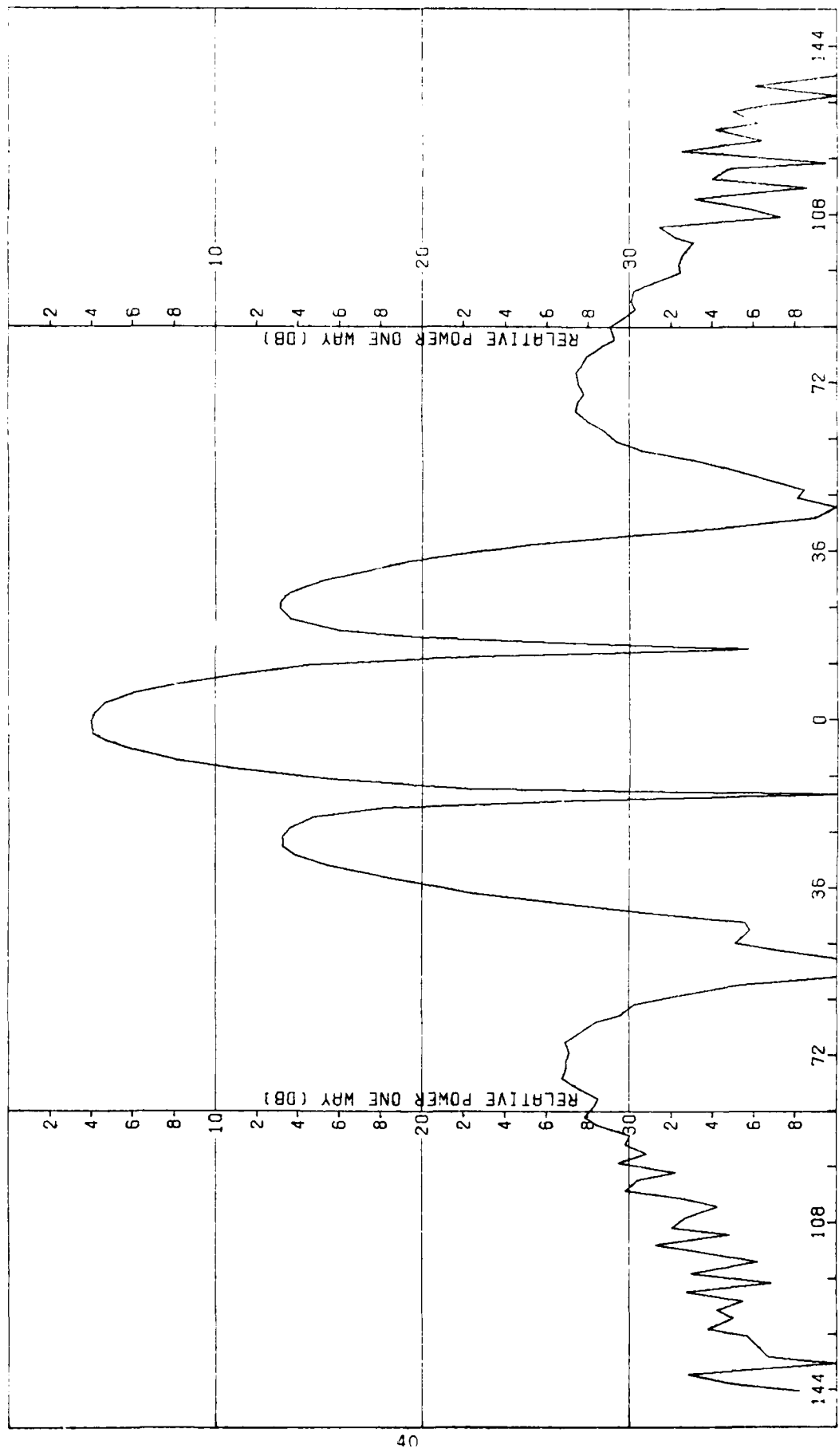


Figure B-3. Pattern of Medium Array: E-Plane Sum,  $\alpha$ -Component, No Radome

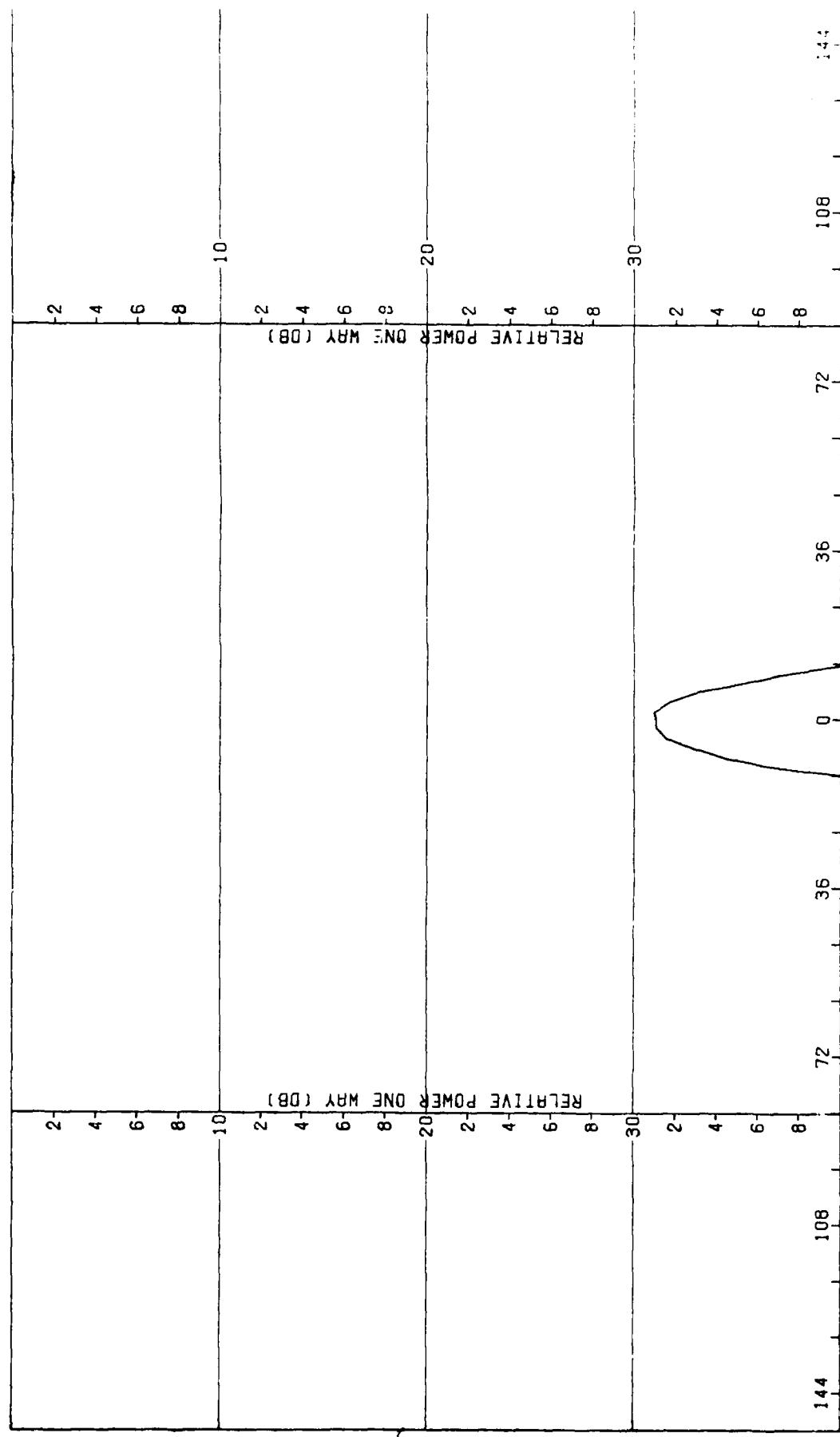


Figure B-4. Pattern of Medium Array: E-Plane Sum,  $\phi$ -Component, No Radome

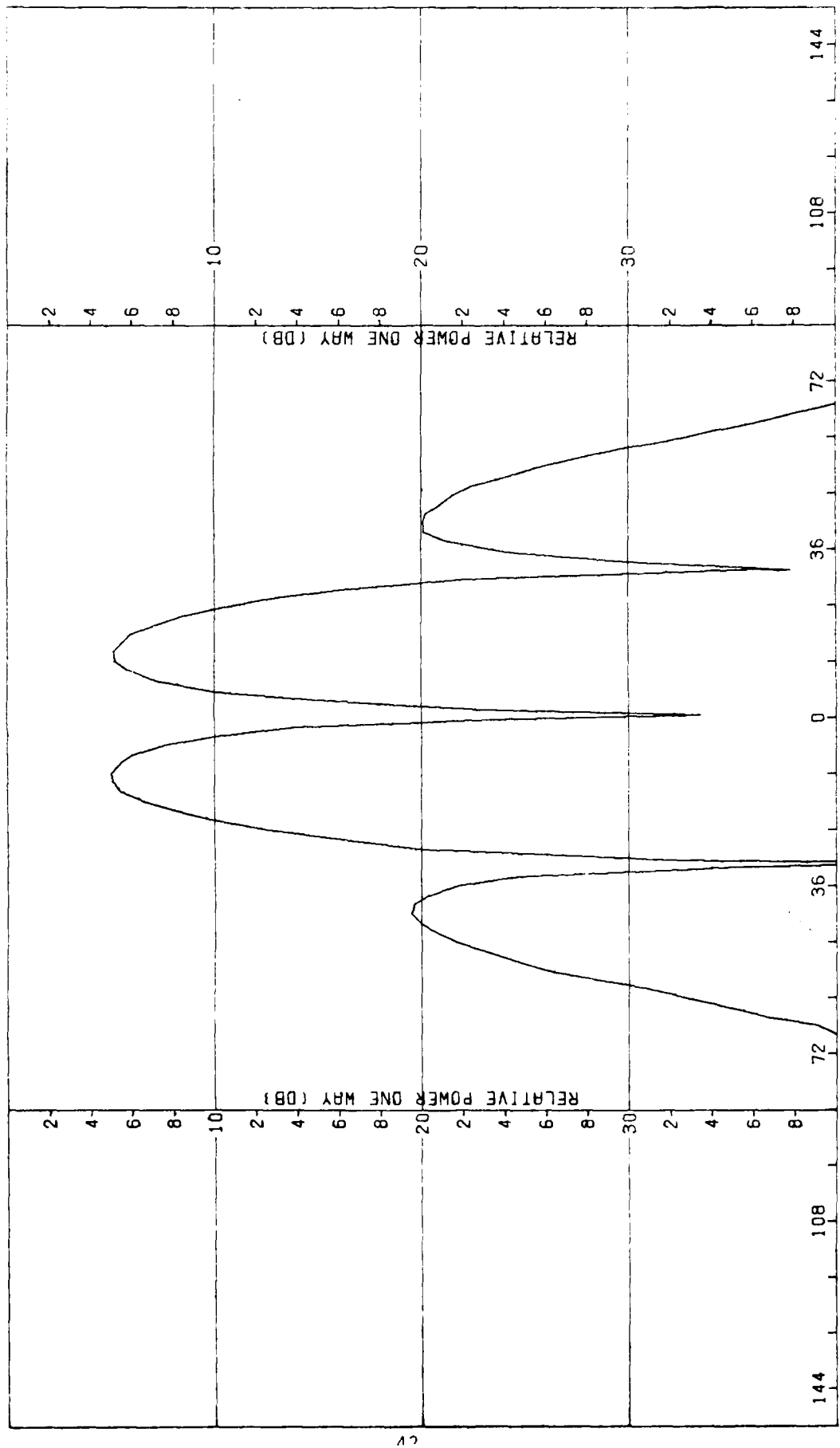


Figure B-5. Pattern of Medium Array: H-Plane, Azimuth difference,  $\frac{1}{2}$ -Component, No Radome

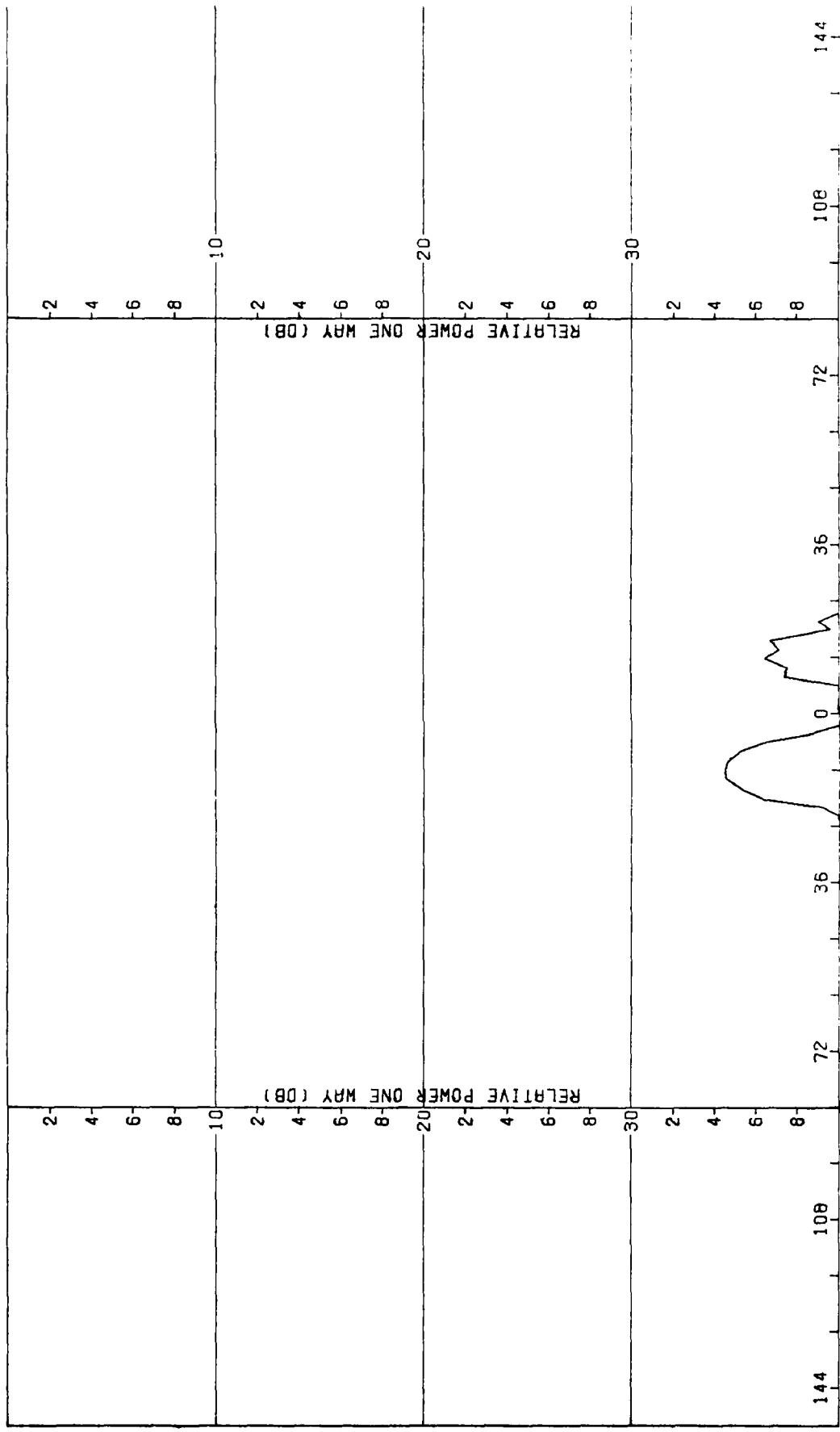


Figure B-6. Pattern of Medium Array: H-Plane, Azimuth Difference,  $\pm$ -Component, No Radome

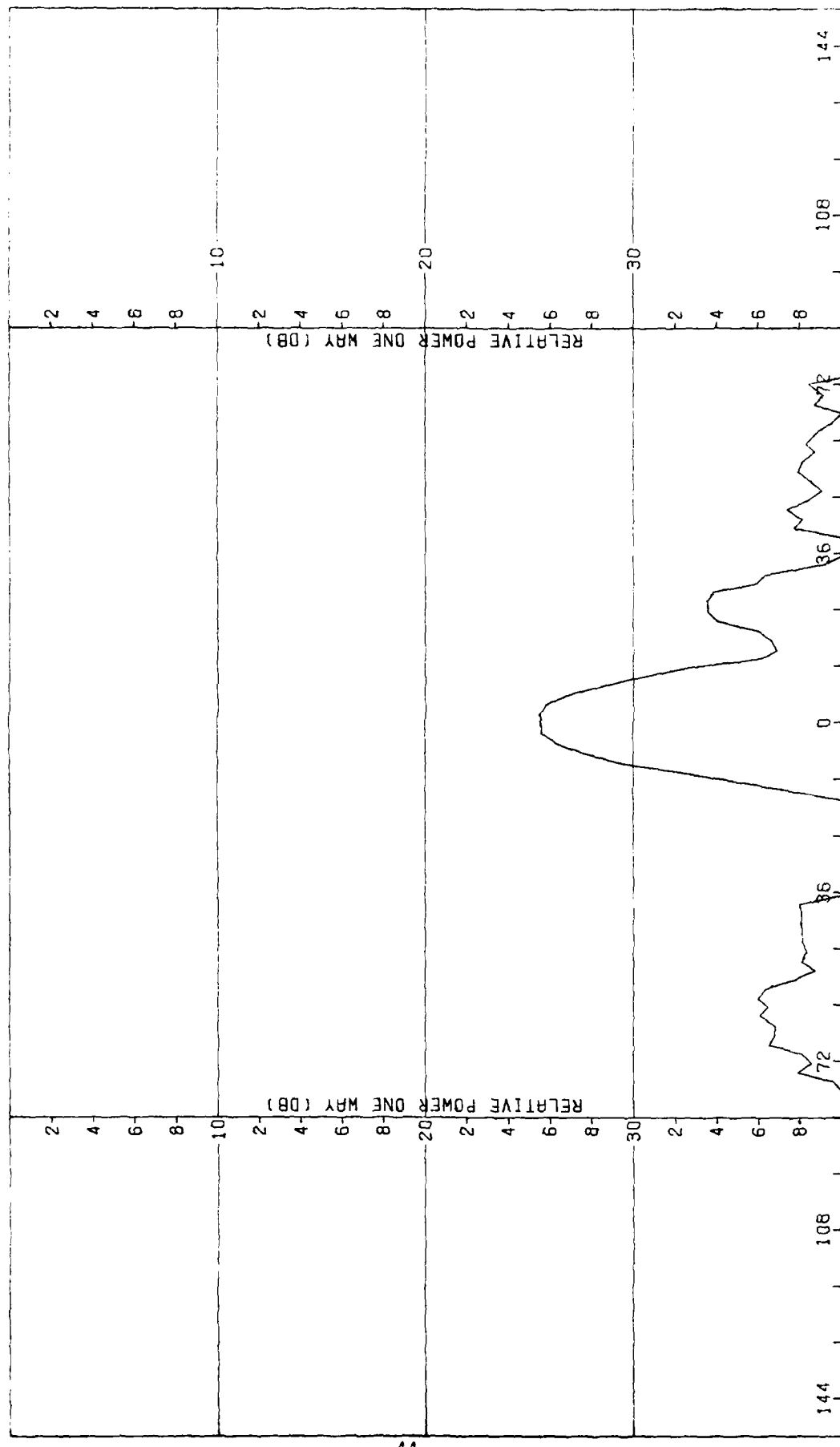


Figure B-7. Pattern of Medium Array: E-Plane, Azimuth Difference, (—)Component, No Radome

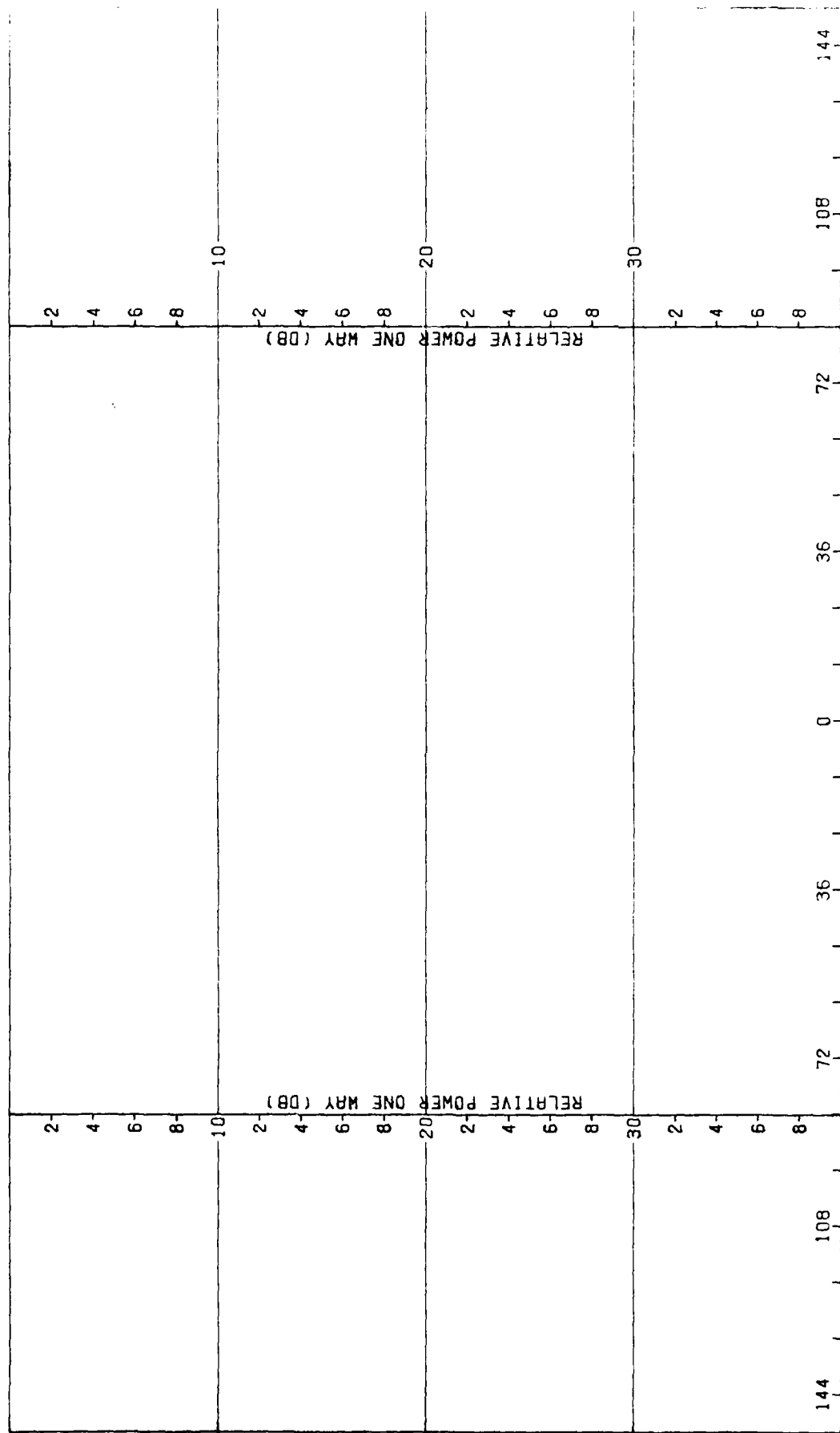


Figure B-8. Pattern of Medium Array: E-Plane, Azimuth Difference,  $\phi$ -Component, No Radome

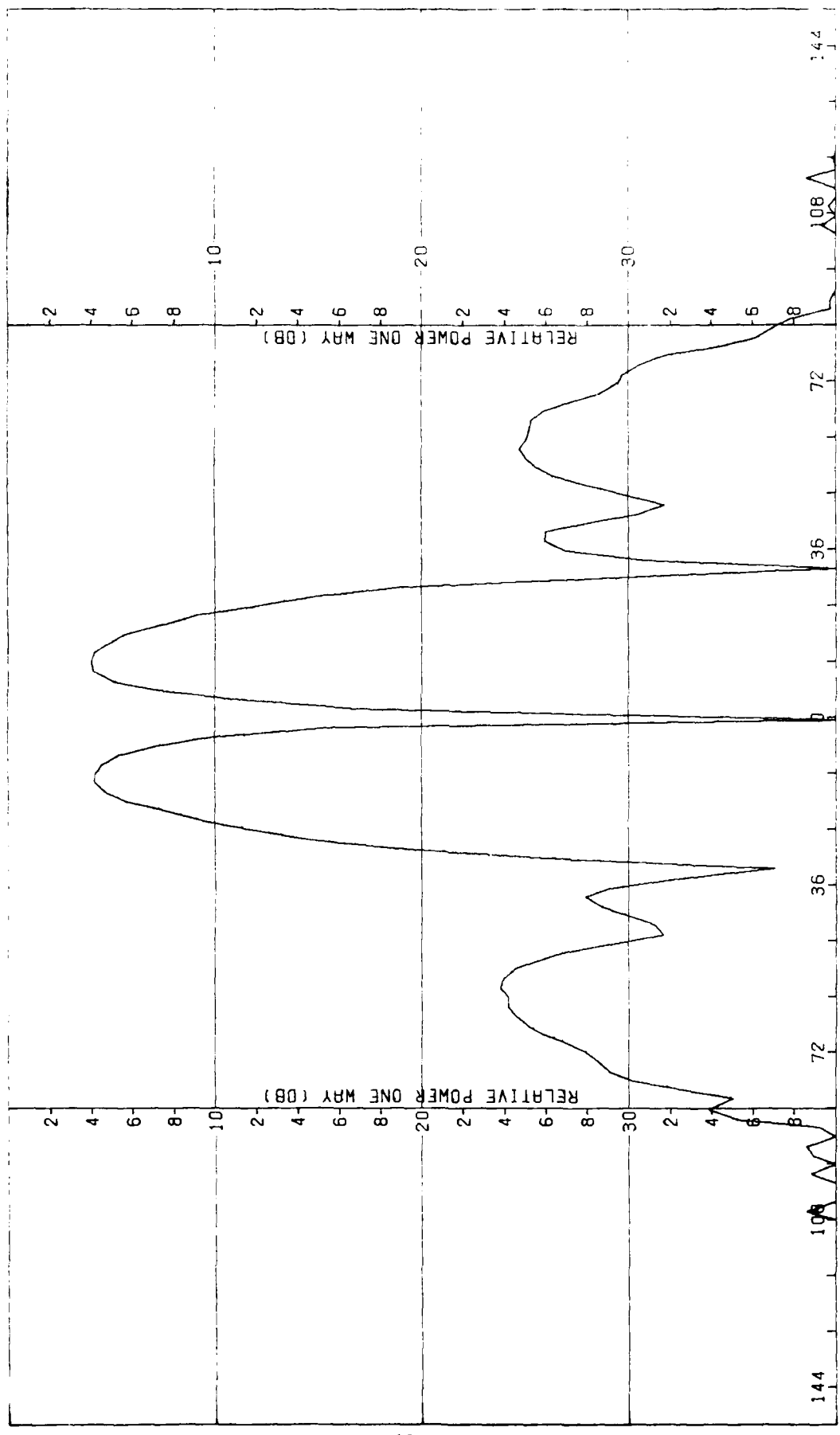


Figure B-9. Pattern of Small Array: E-Plane, H-Plane, Elevation difference, E-component, "o Radome

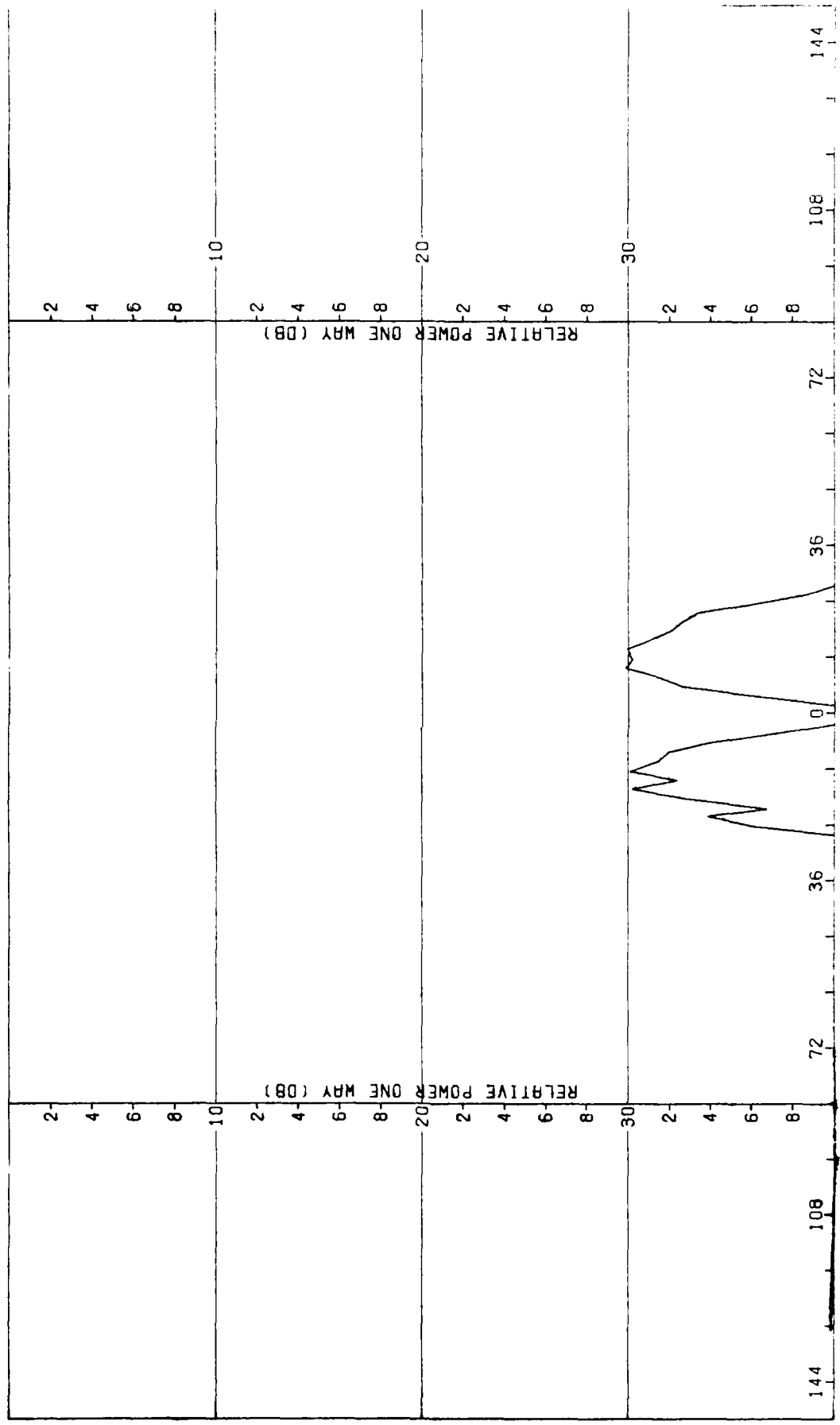


Figure B-10. Pattern of Medium Array: Elevation Difference,  $\phi$ -Component, No Radome

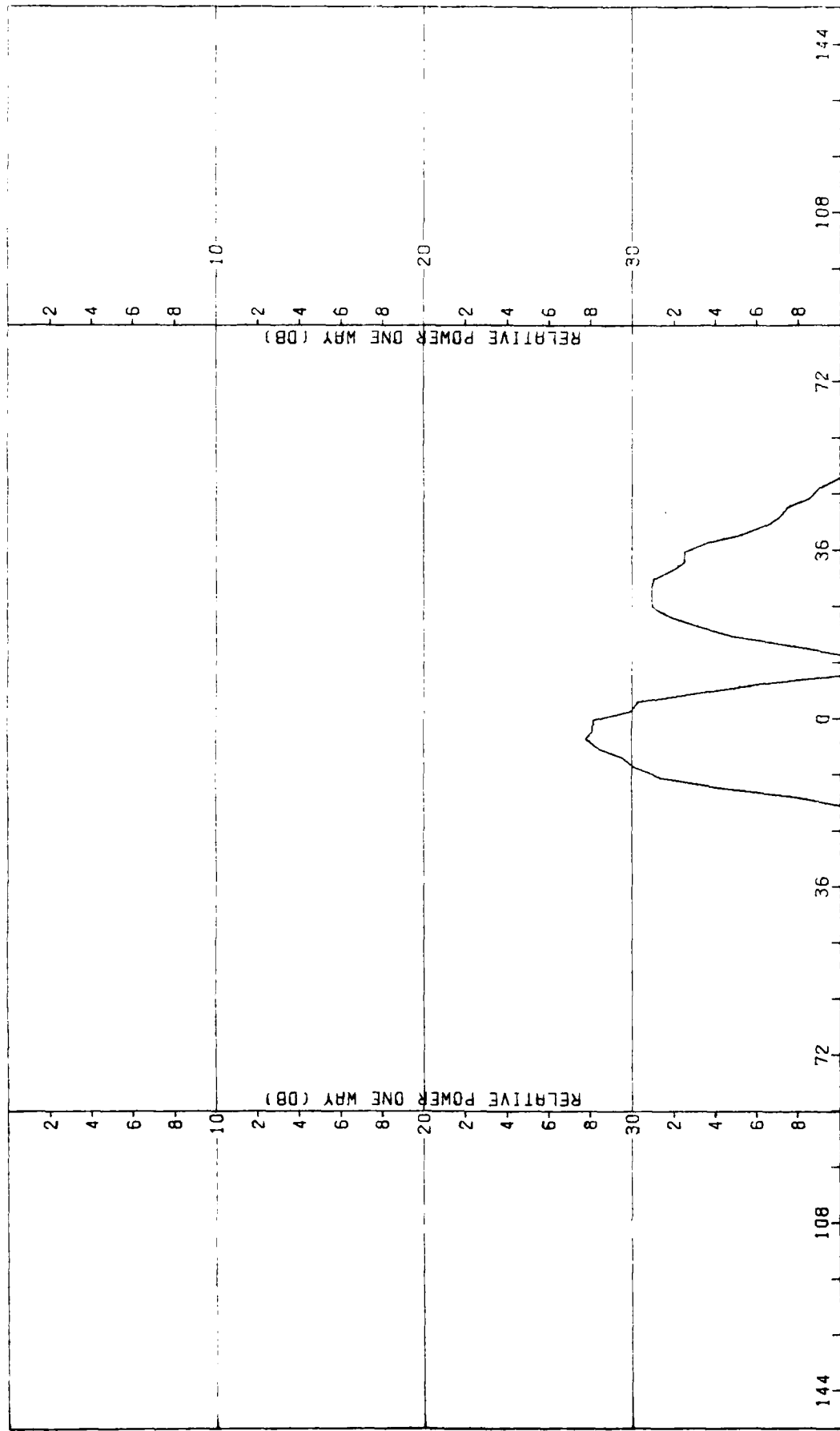


Figure B-11. Pattern of Medium Array: H-Plane, Elevation Difference,  $\phi$ -Component, No Radome

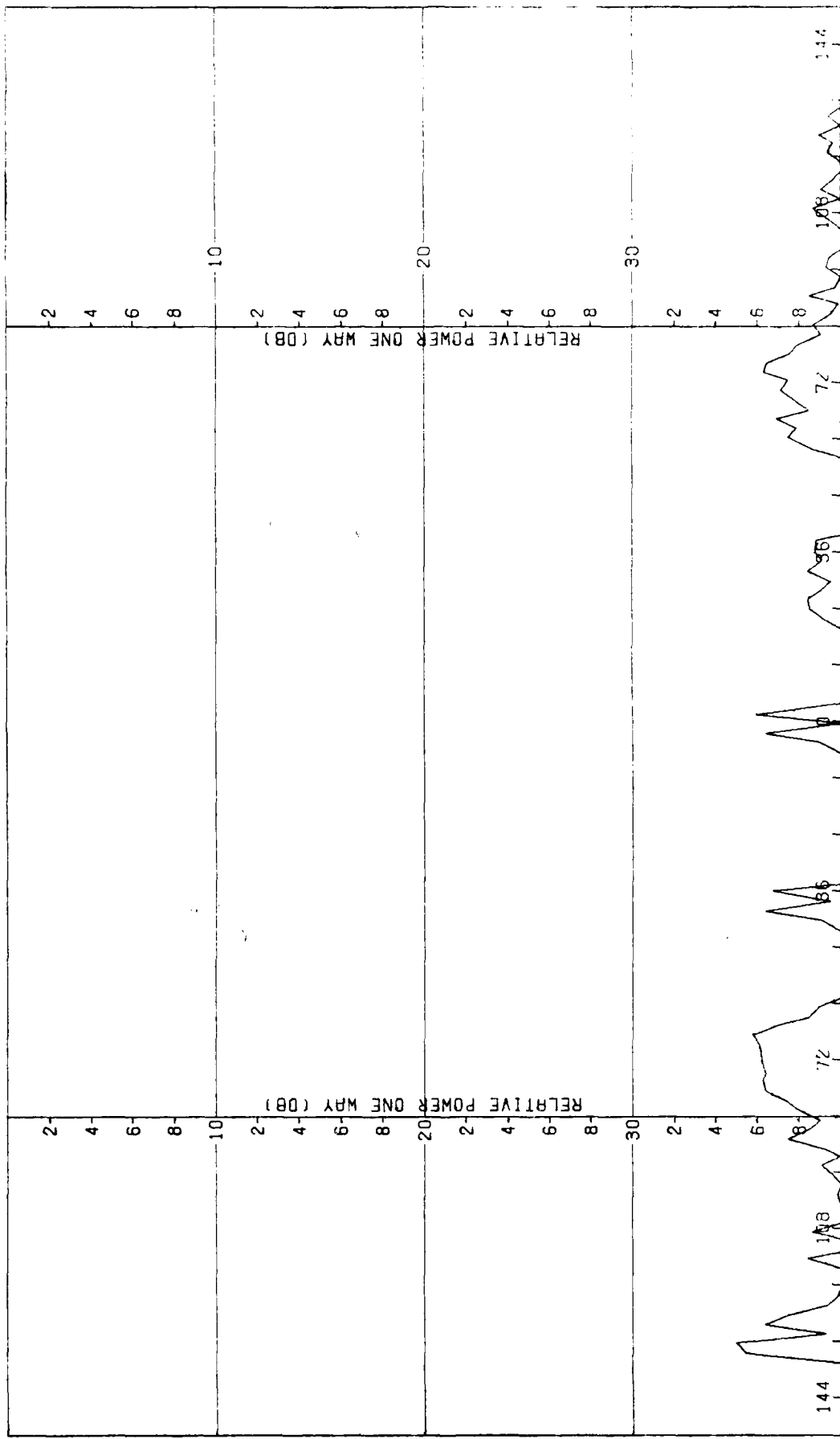


Figure B-12. Pattern of Medium Array: H-Plane, Elevation Difference,  $\pm$ -Component, No. Radom.

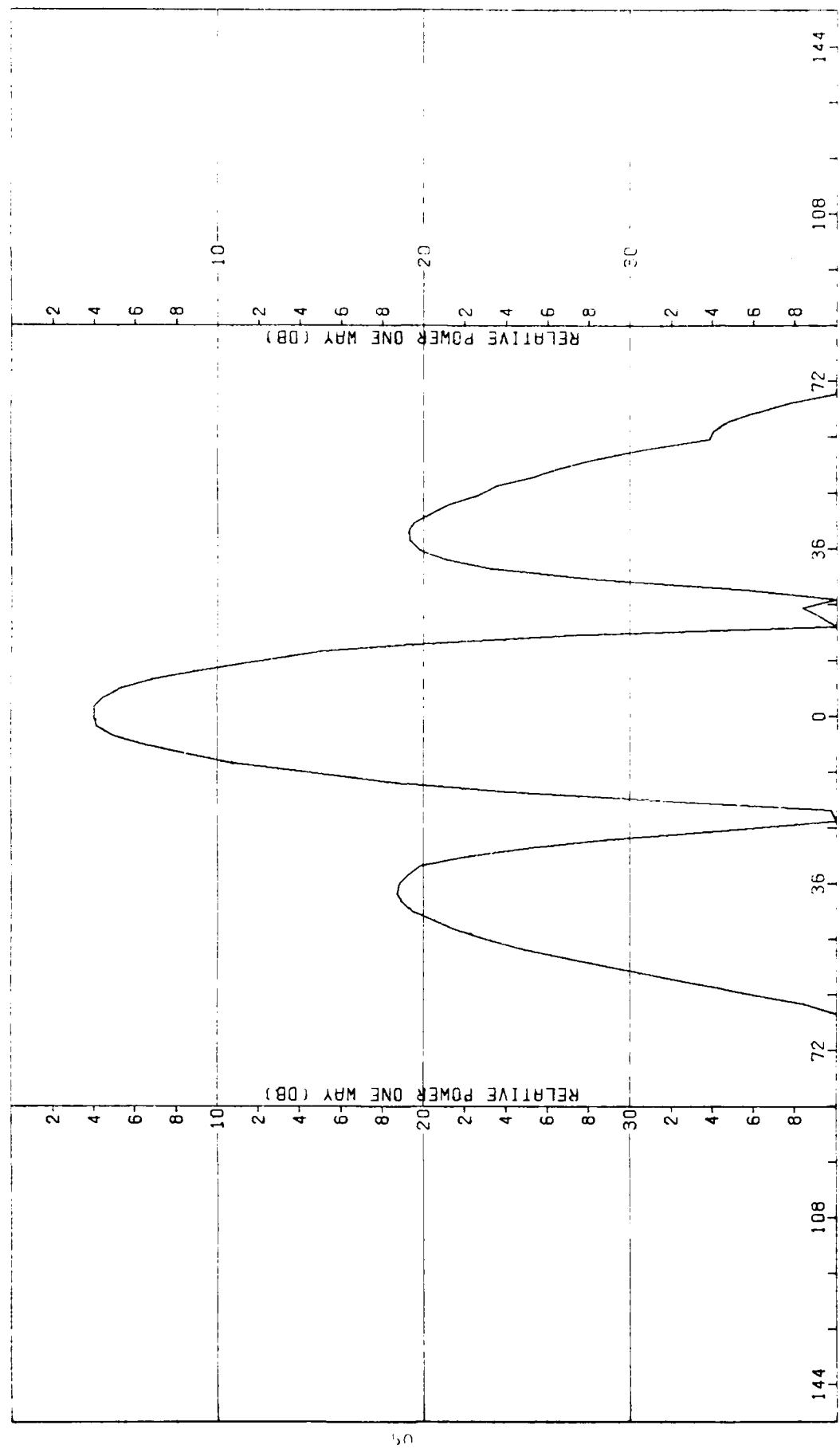


Figure B-13. Pattern of Medium Array:  $\theta=45^\circ$  Plane, Sum,  $\theta$ -component, No Radiome

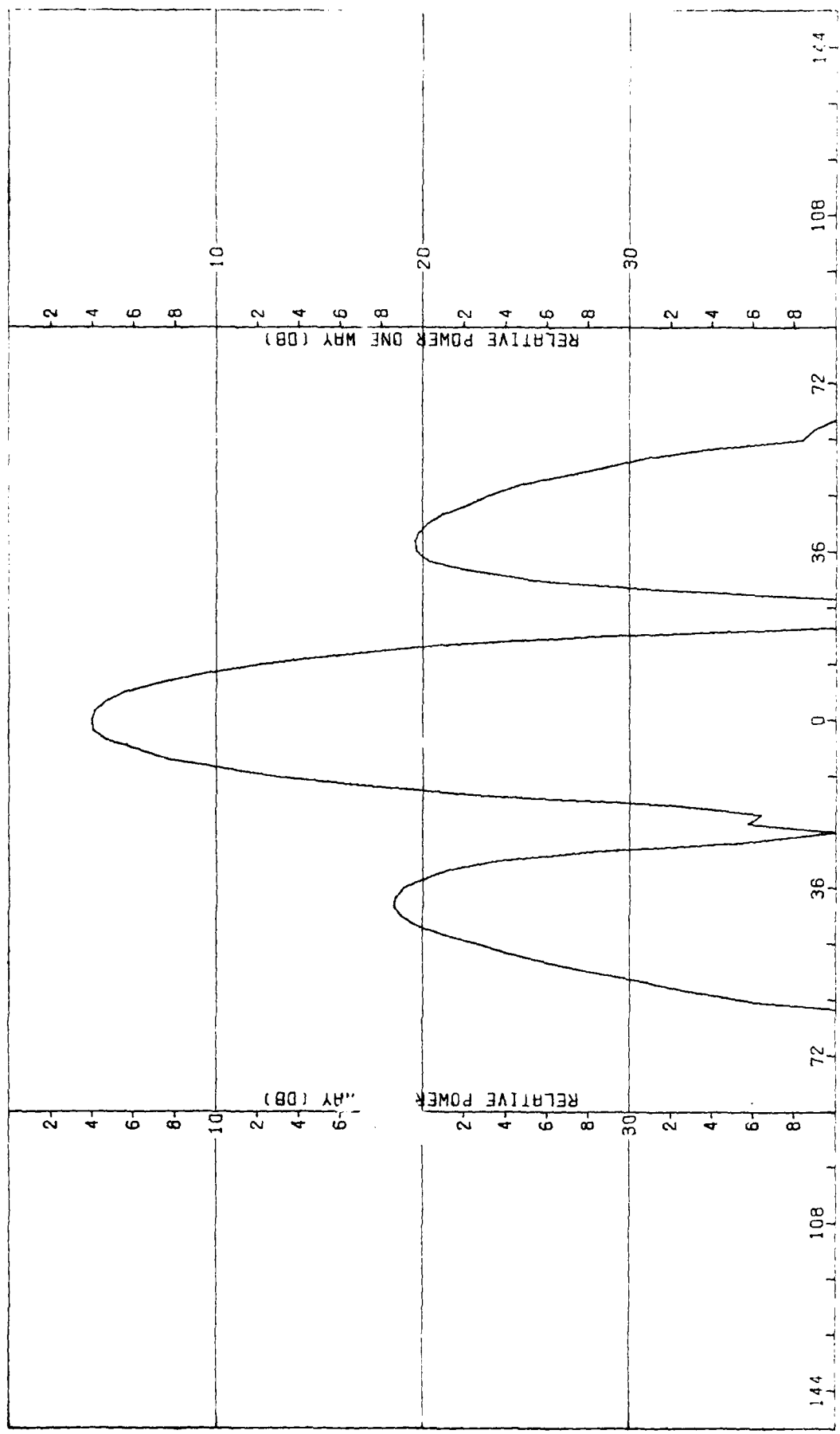


Figure B-14. Pattern of Medium Array:  $\phi=45^\circ$  Plane, Sum,  $\phi$ -Component, No Radome

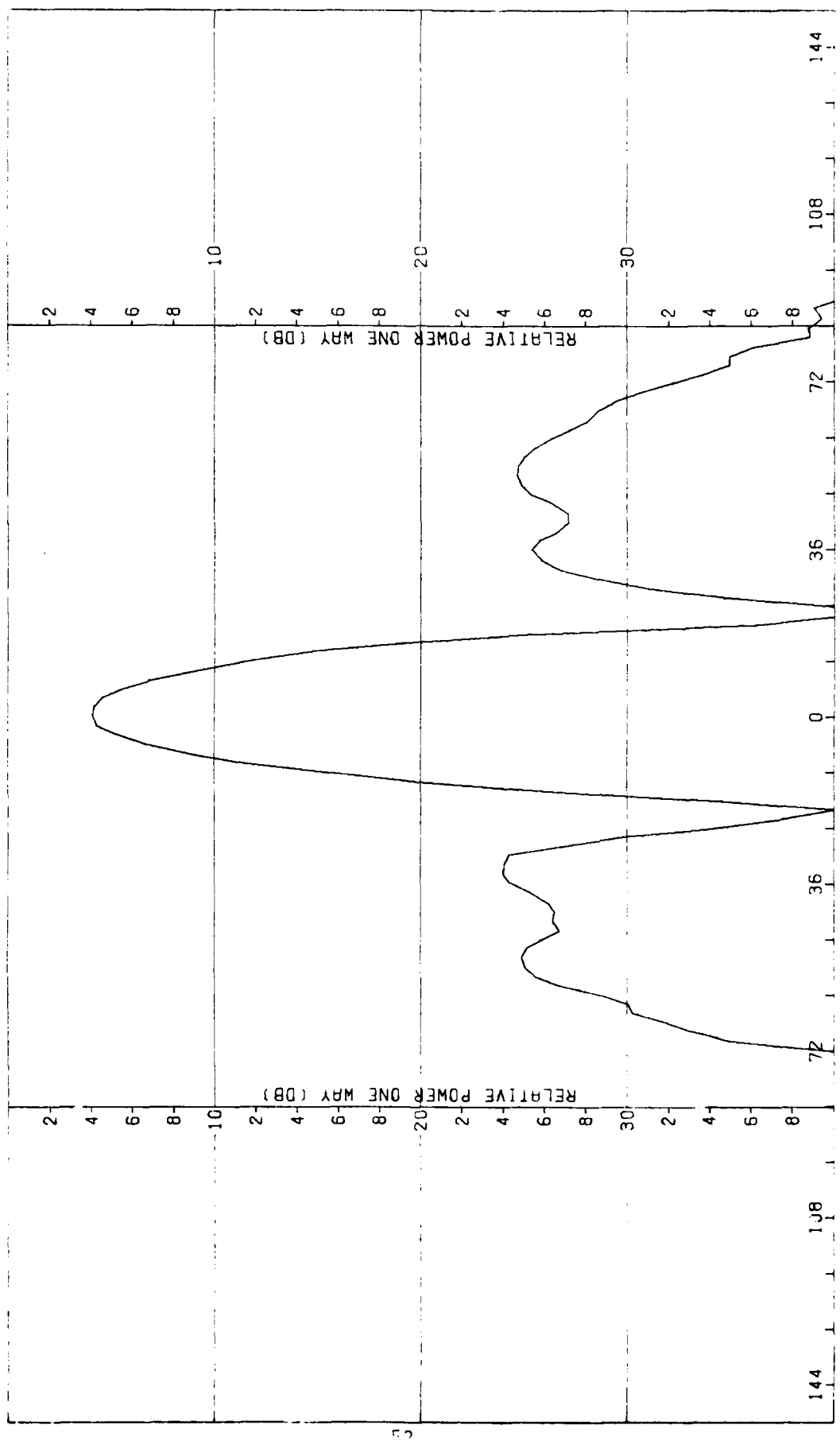


Figure B-15. Pattern of Medium Array:  $\phi = -45^\circ$  Plane, Sum,  $\theta$ -Component, No Radome

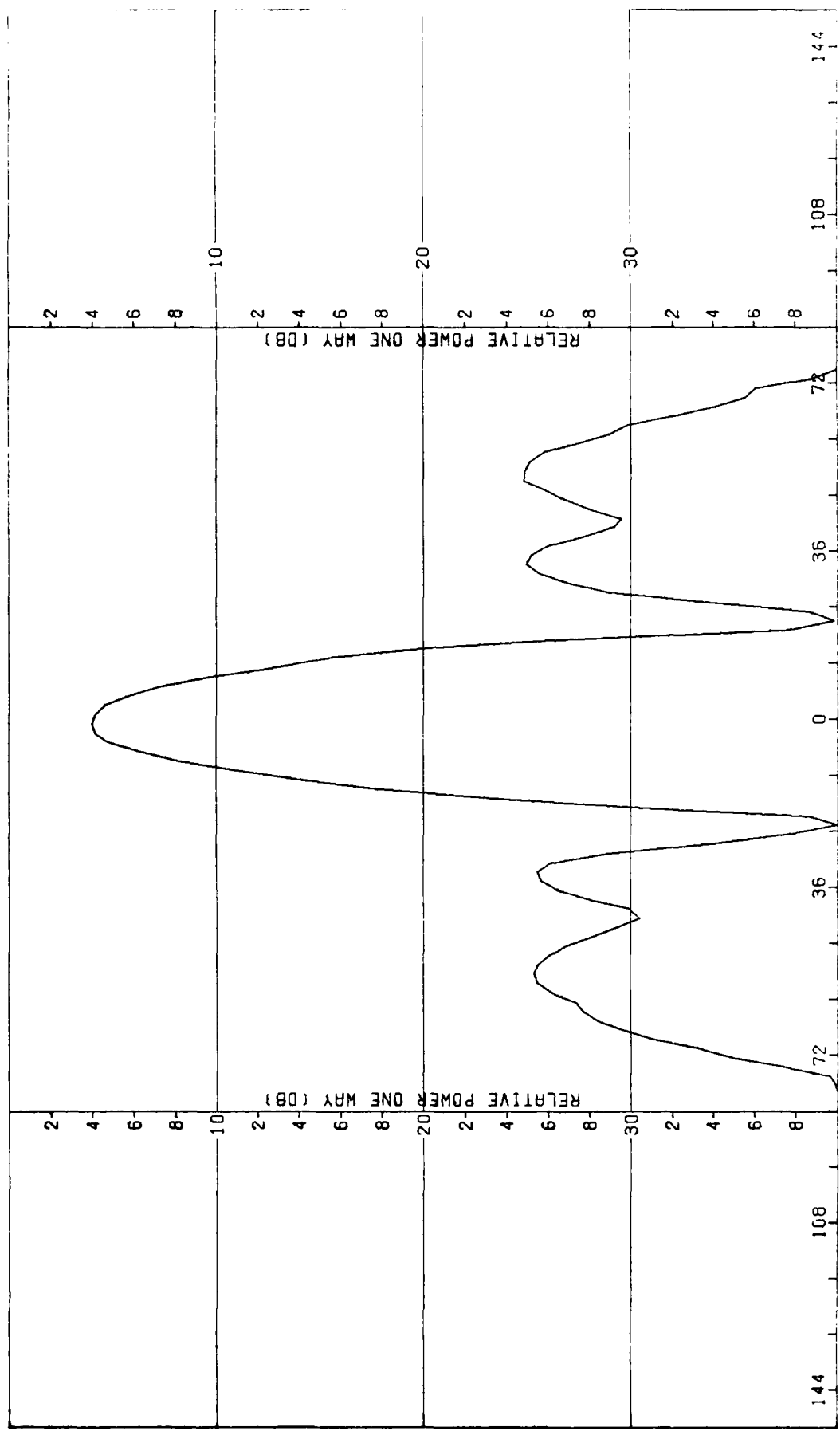


Figure B-16. Pattern of Medium Array:  $\psi = -45^\circ$  Plane, Sum,  $\phi$ -Component, No Radome

APPENDIX C

Antenna Patterns of Large Array Without Radome

PRECEDING PAGE BLANK-NOT FILMED

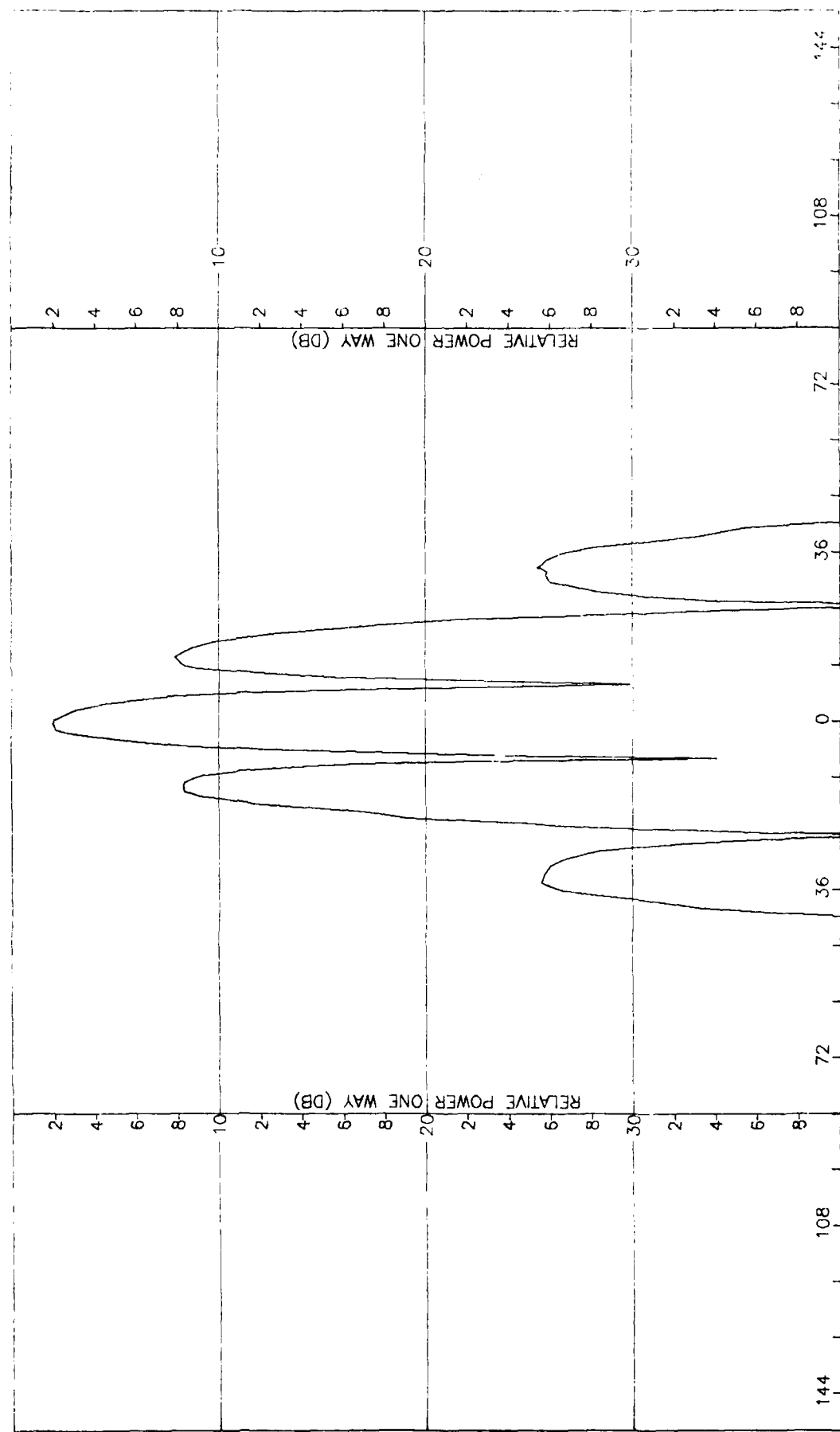


Figure C-1. Pattern of Large Array: H-Plane Sum,  $\phi$ -Component, No Radome

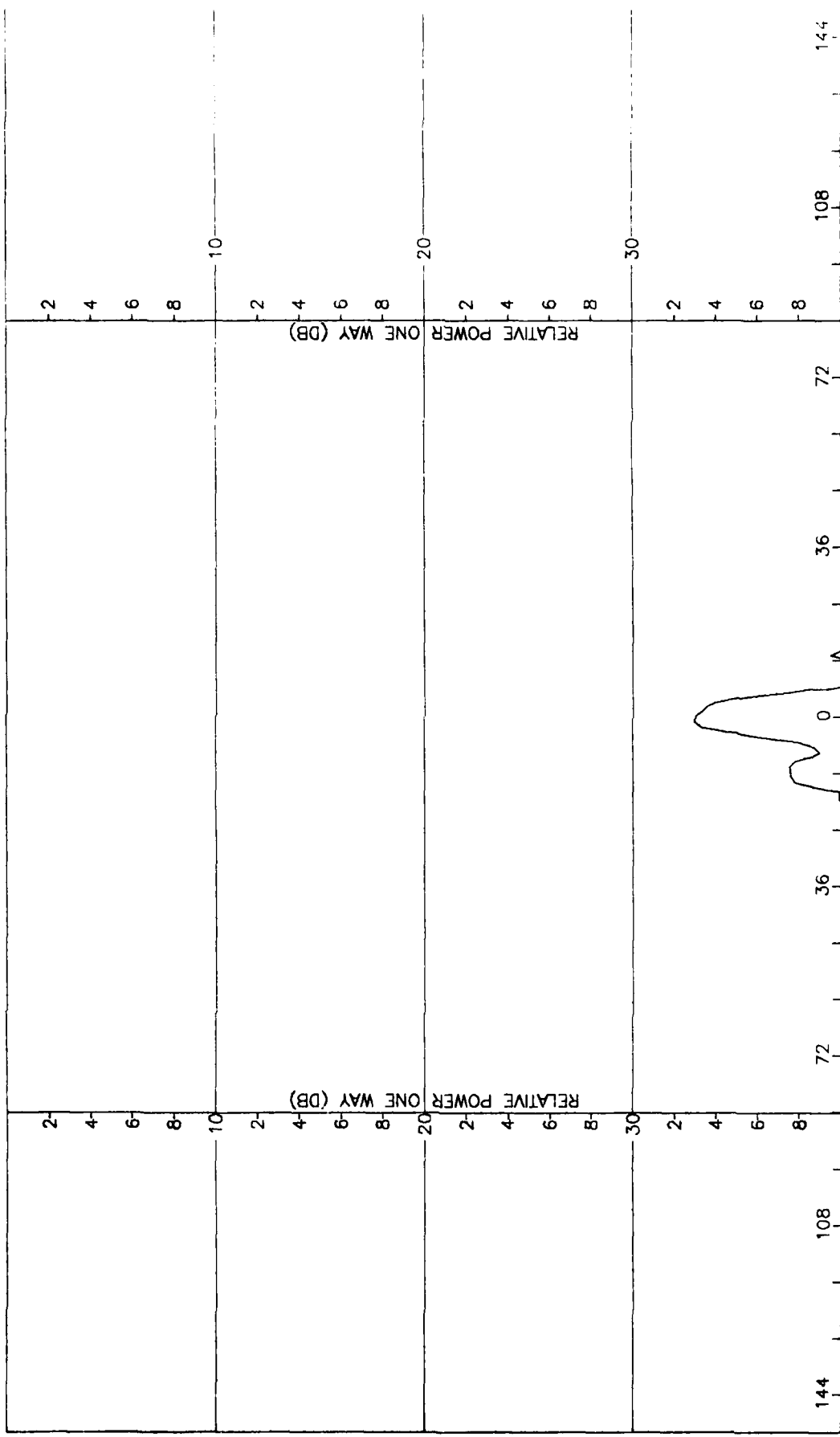


Figure C-2. Pattern of Large Array: H-Plane Sum,  $\theta$ -Component, No Radome

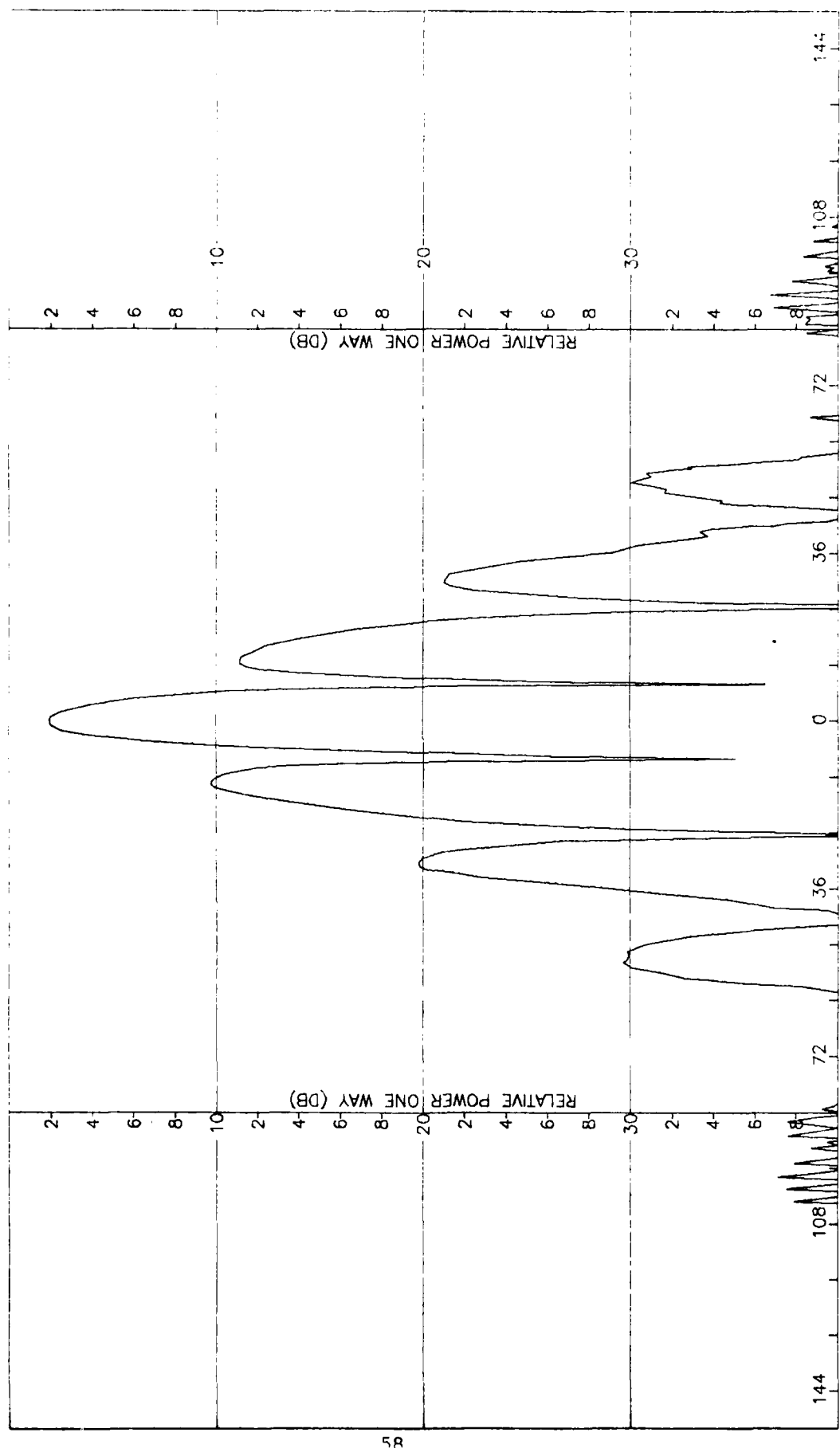


Figure C-3. Pattern of Large Array: E-Plane, Sum,  $\theta$ -Component, No Radome

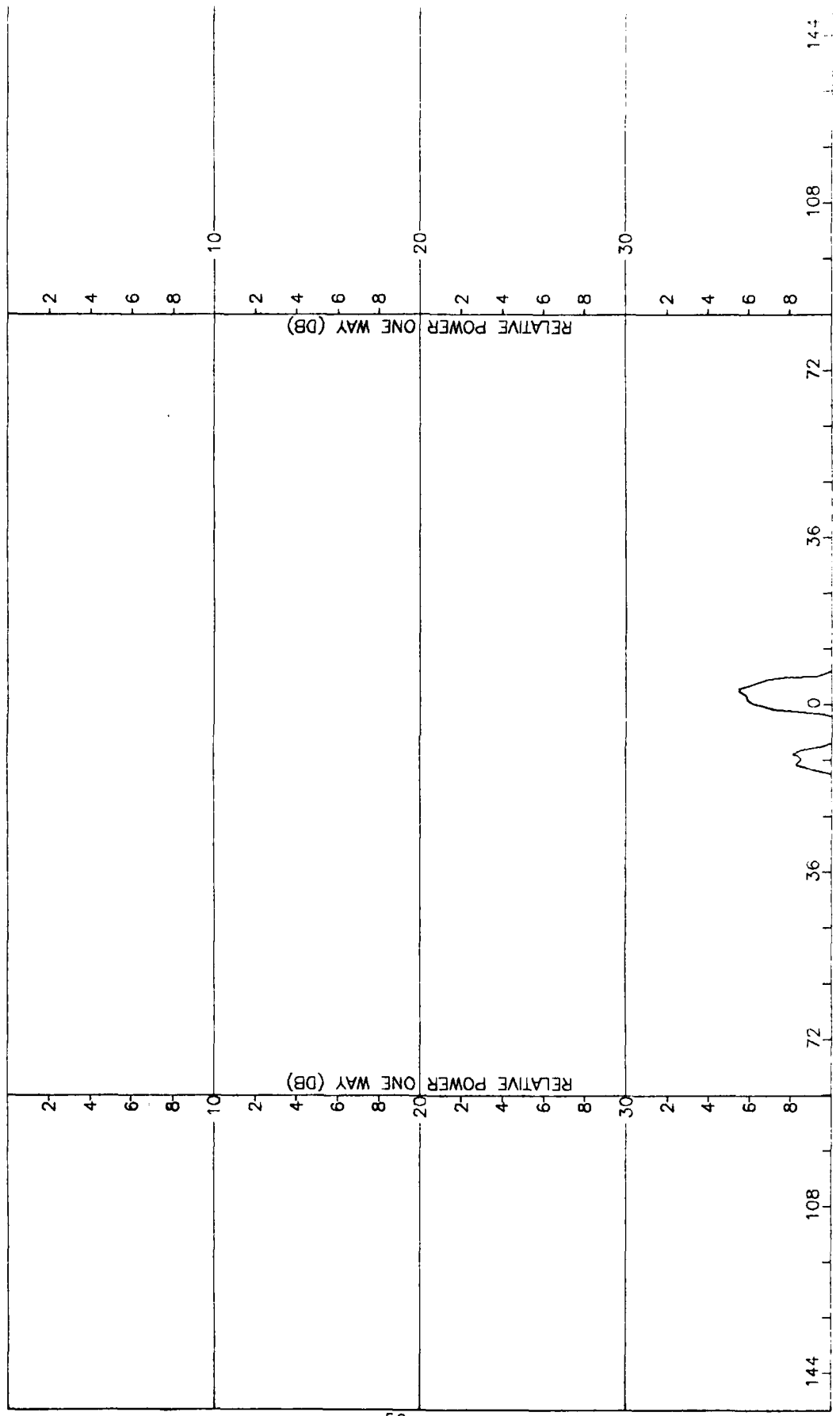


Figure C-4. Pattern of Large Array: E-Plane, Sum,  $\hat{e}$ -Component, No Radome

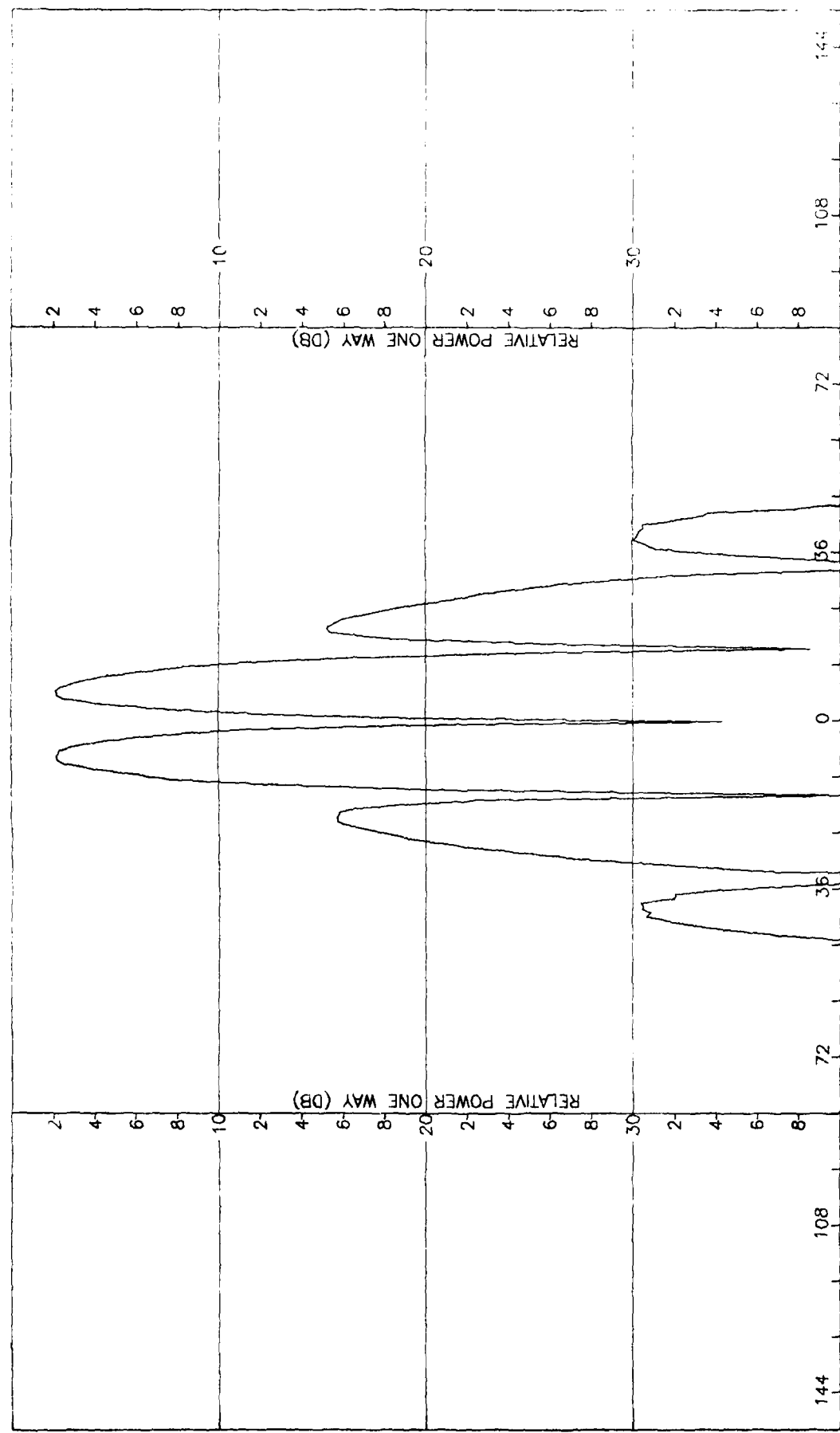


Figure C-5. Pattern of Large Array: H-Plane, Azimuth Difference,  $\phi$ -Component, No Radome

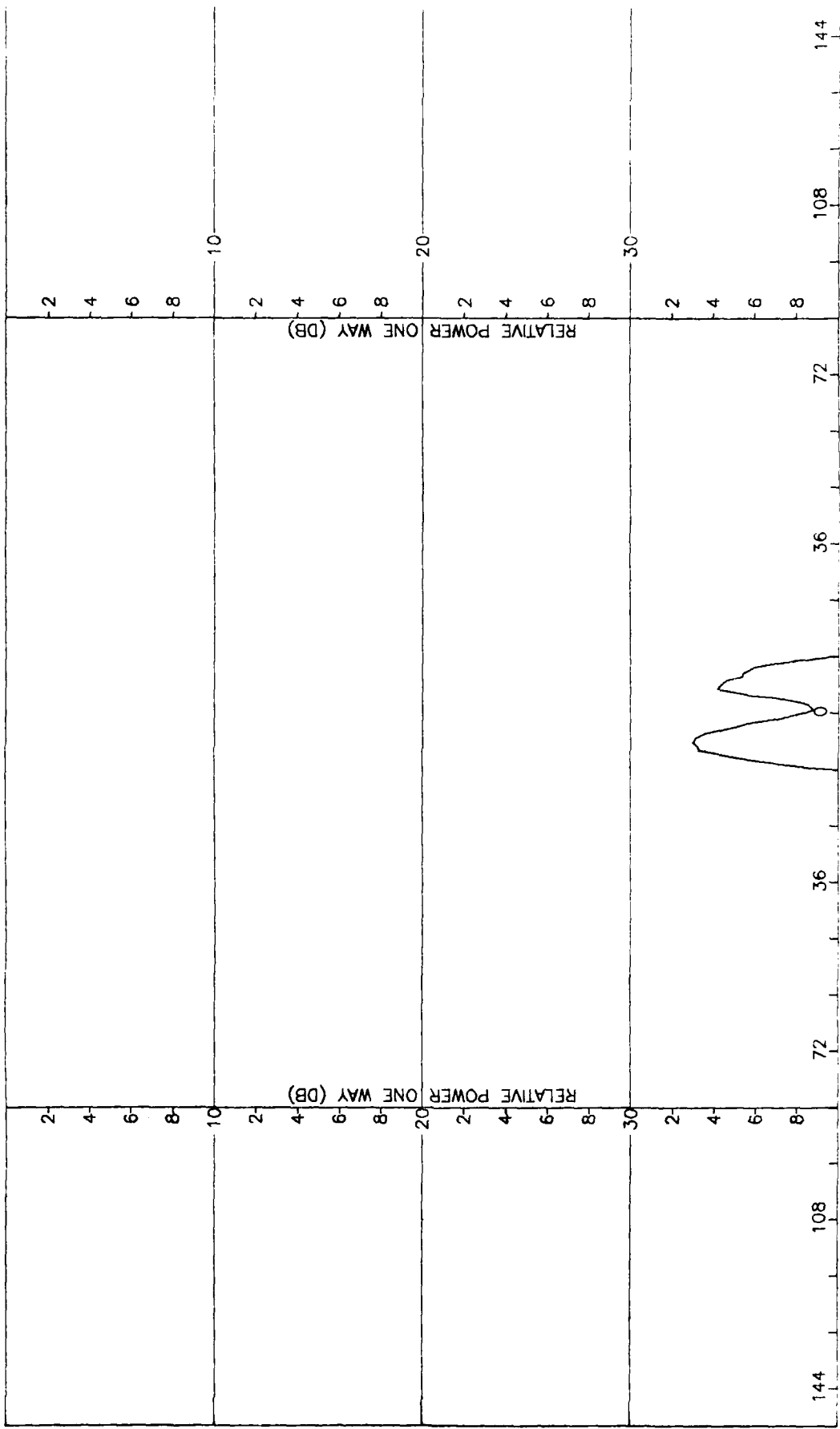


Figure C-6. Pattern of Large Array: H-Plane, Azimuth Difference,  $\frac{1}{4}$ -Component, No Radome

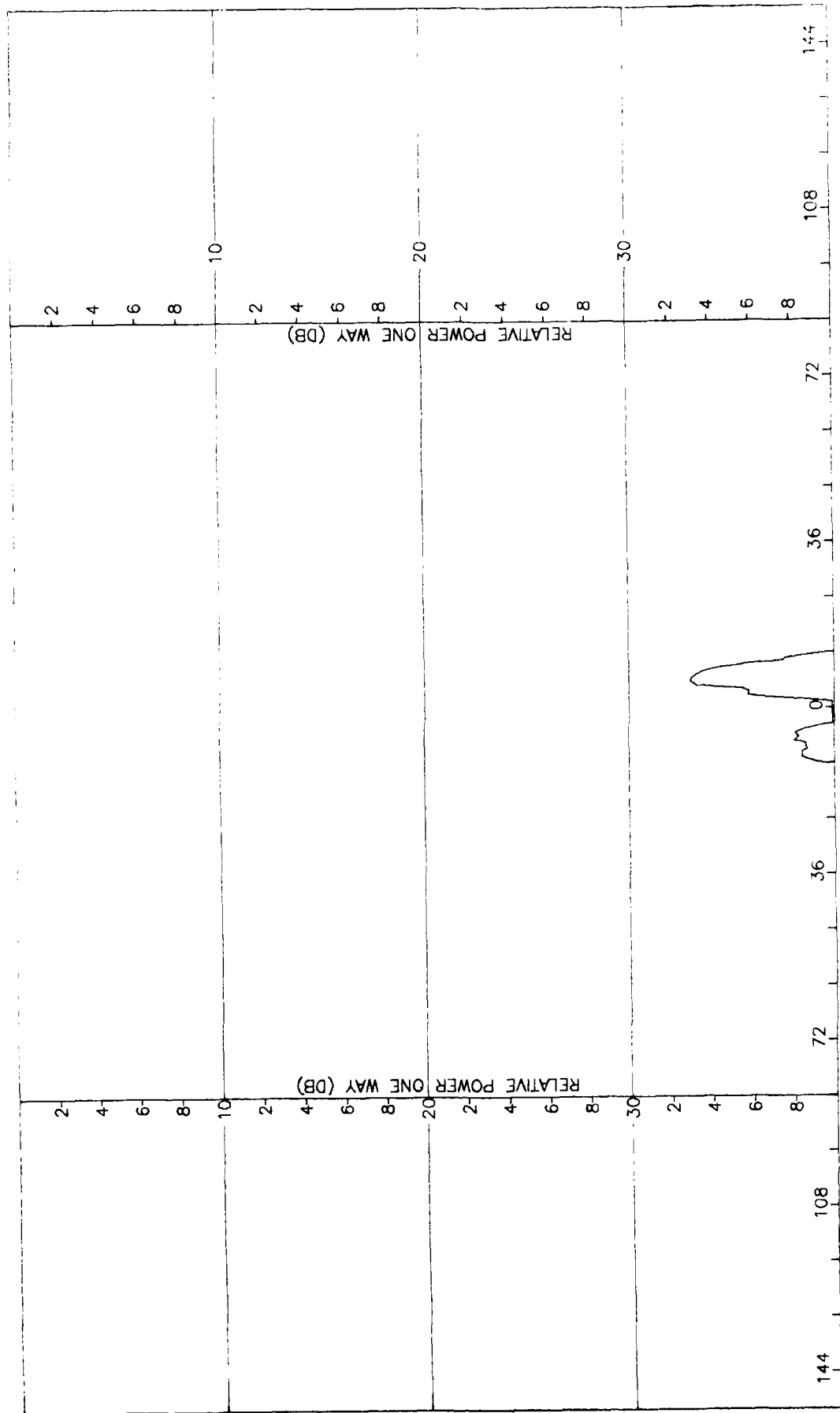


Figure C-7. Pattern of Large Array: E-Plane, Azimuth Difference,  $\phi$ -Component, No Radome

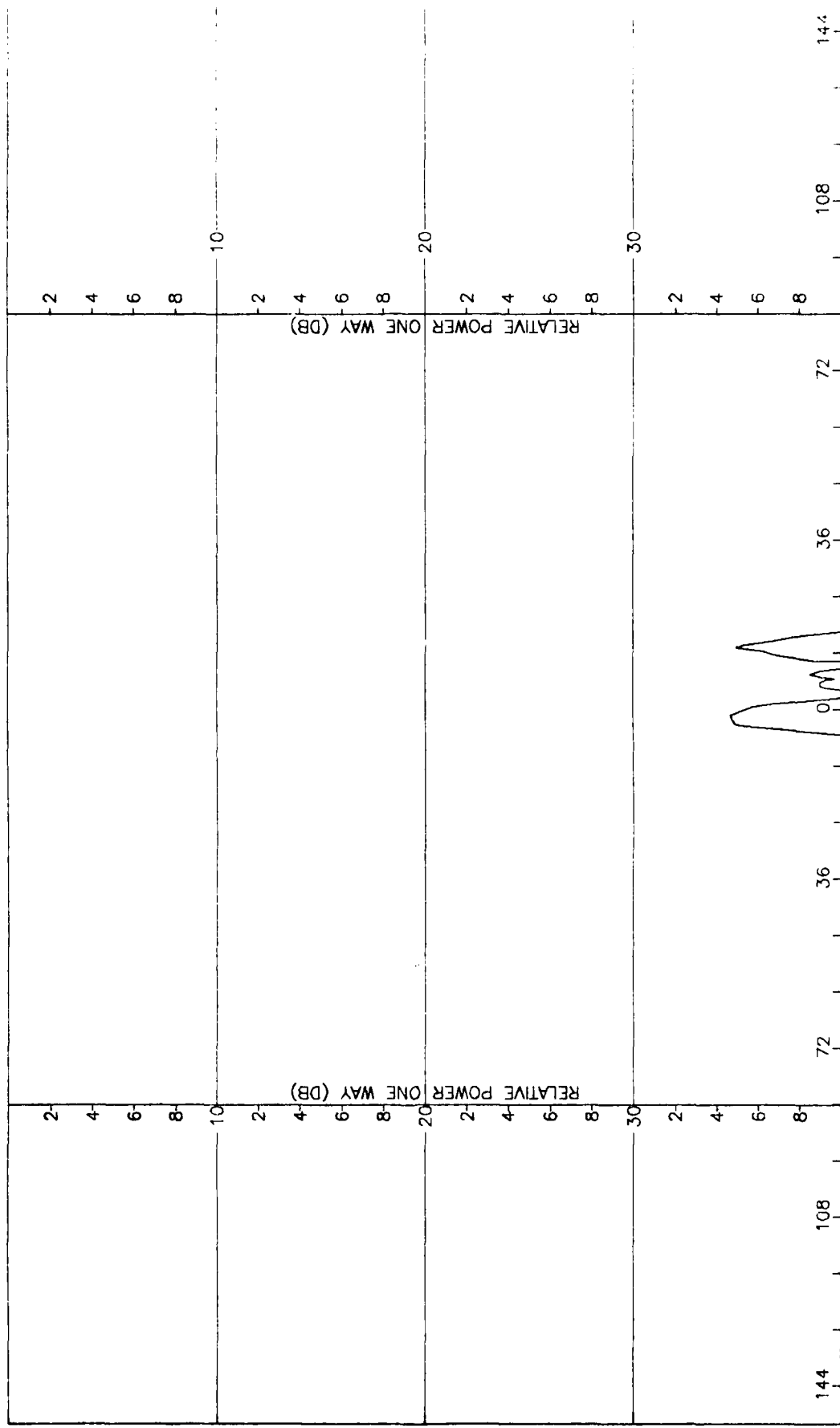


Figure C-8. Pattern of Large Array: E-Plane, Azimuth Difference,  $\phi$ -Component, No Radome

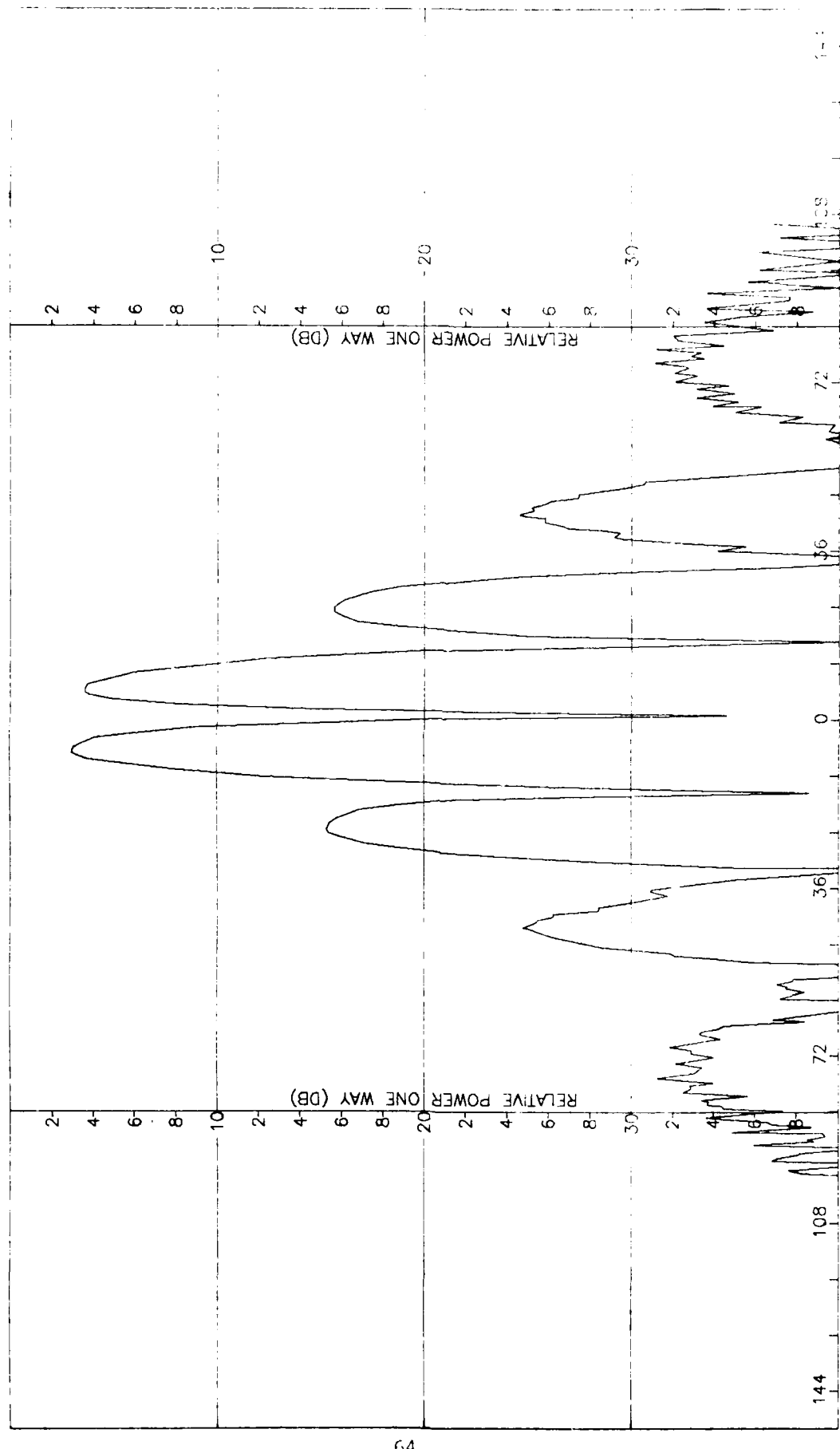


Figure C-9. Pattern of Large Array: E-Plane, Elevation Difference,  $\rho$ -Component, No Radome

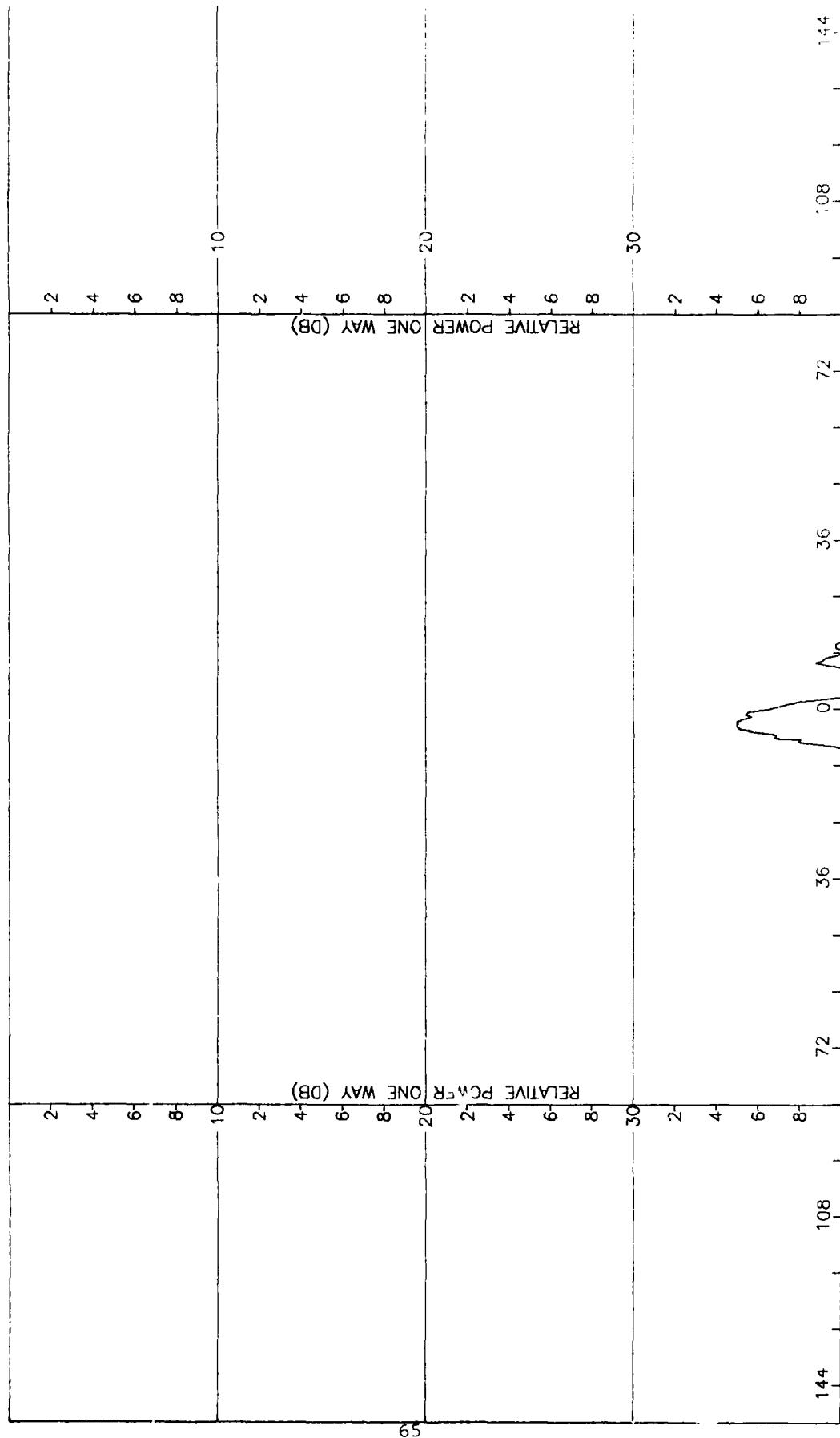


Figure C-10. Pattern of Large Array: E-Plane, Elevation Difference,  $\pm$ -Component, No Radome

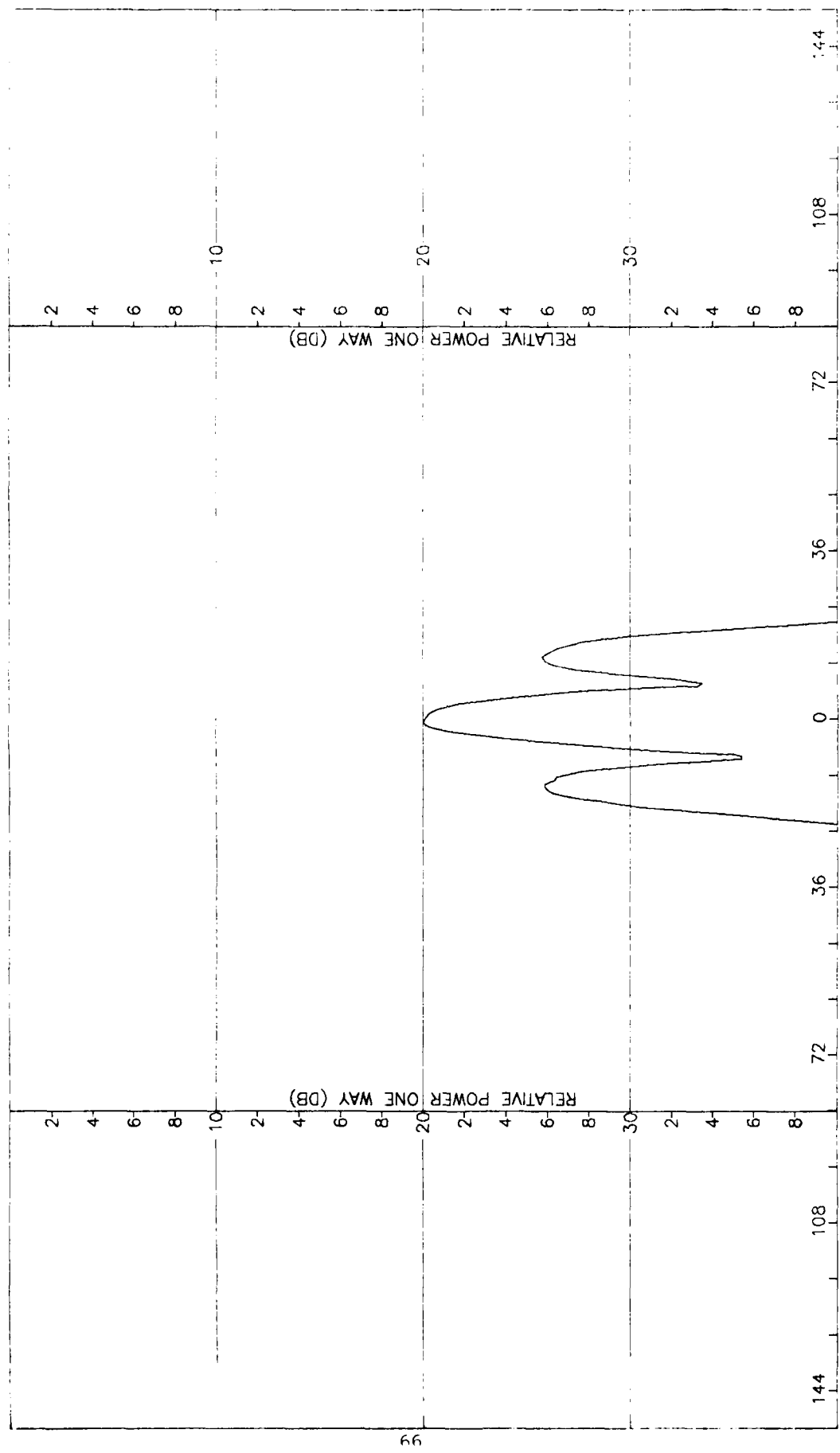


Figure C-11. Pattern of Large Array: H-Plane, Elevation Difference,  $\phi$ -Component, No Radome

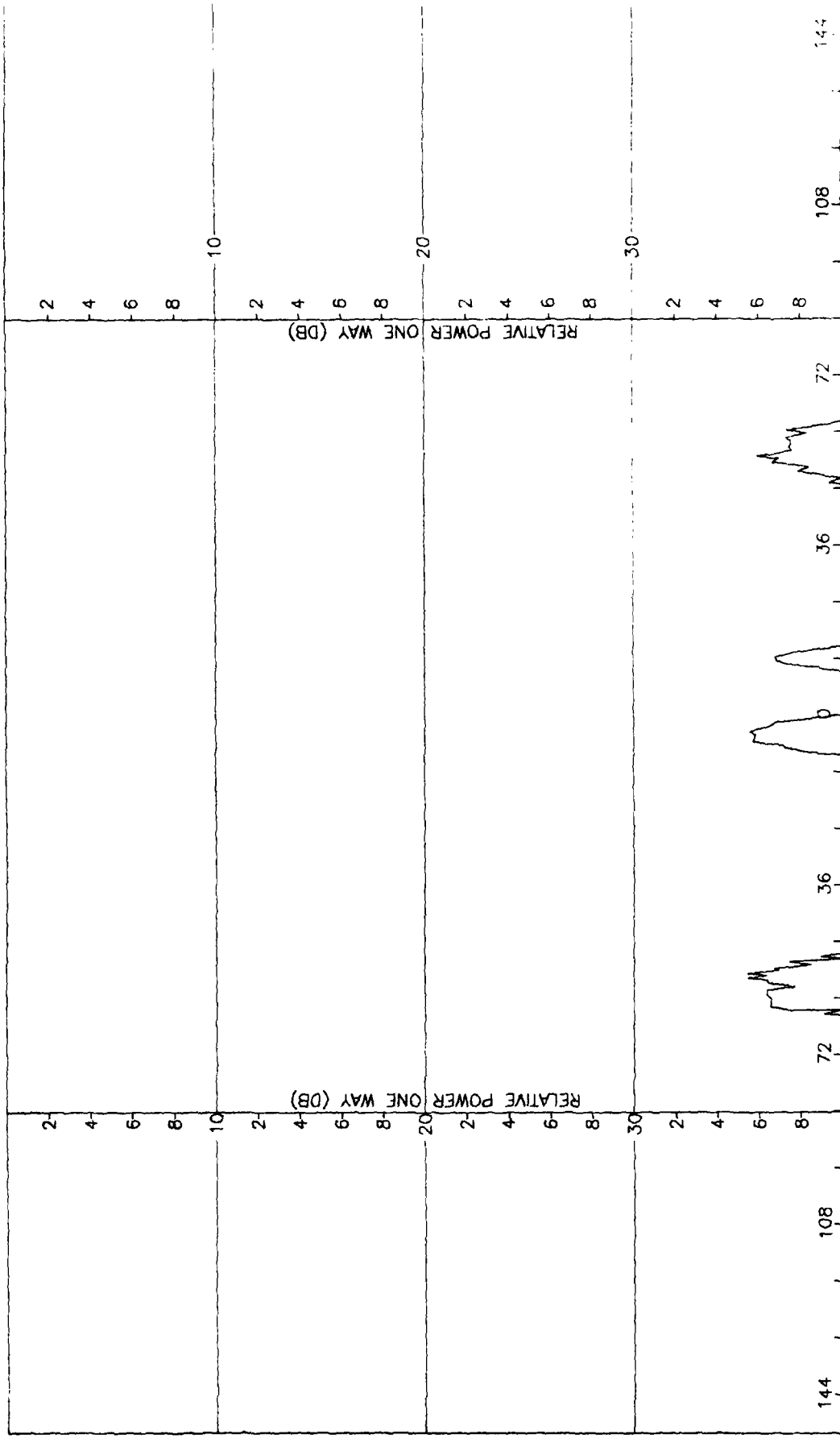


Figure C-12. Pattern of Large Array: H-Plane, Elevation Difference, a-Component, N, Radome

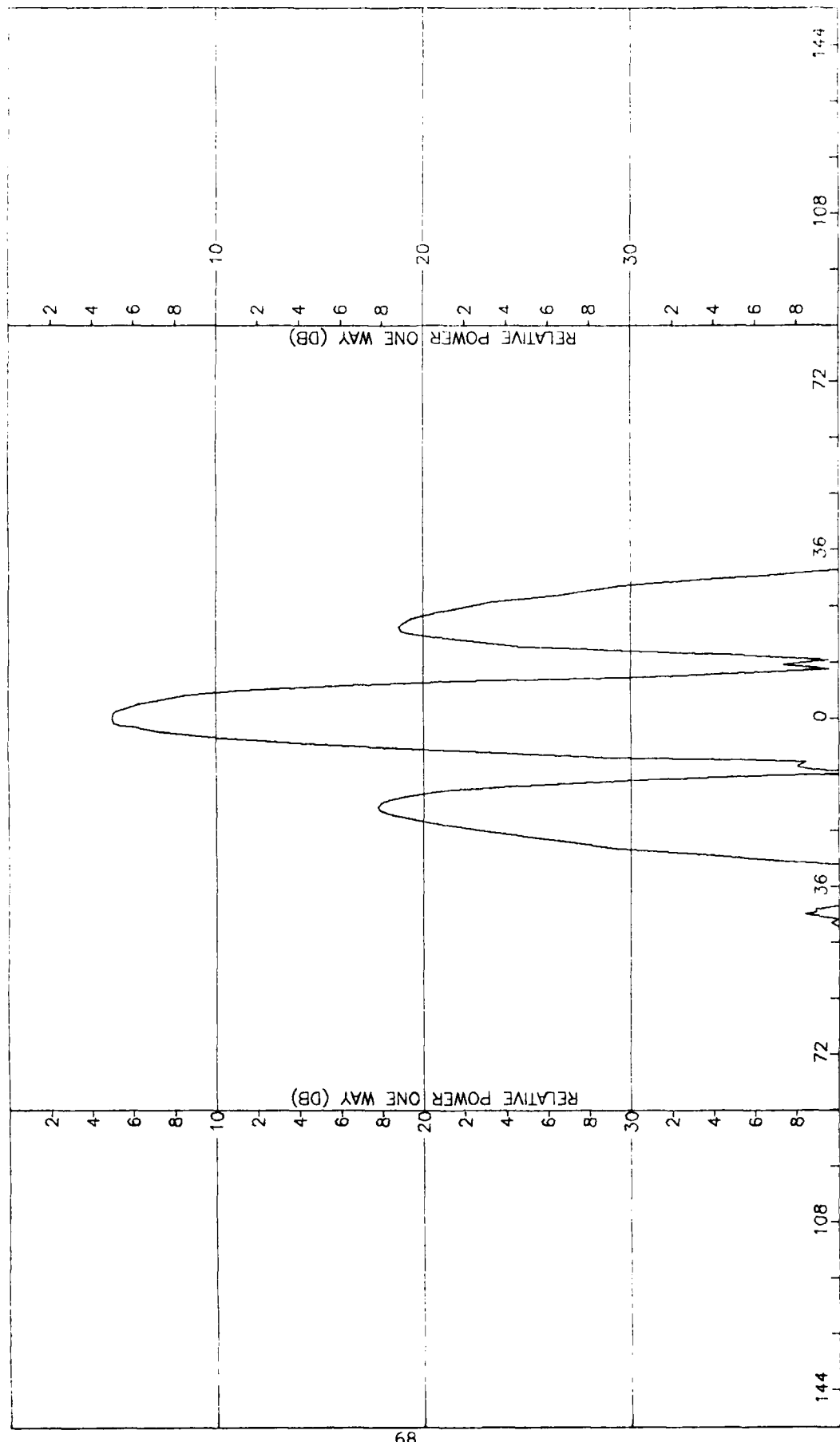


Figure C-13. Pattern of Large Array:  $\phi=45^\circ$  Plane, Sum,  $\theta$ -Component, No Radome

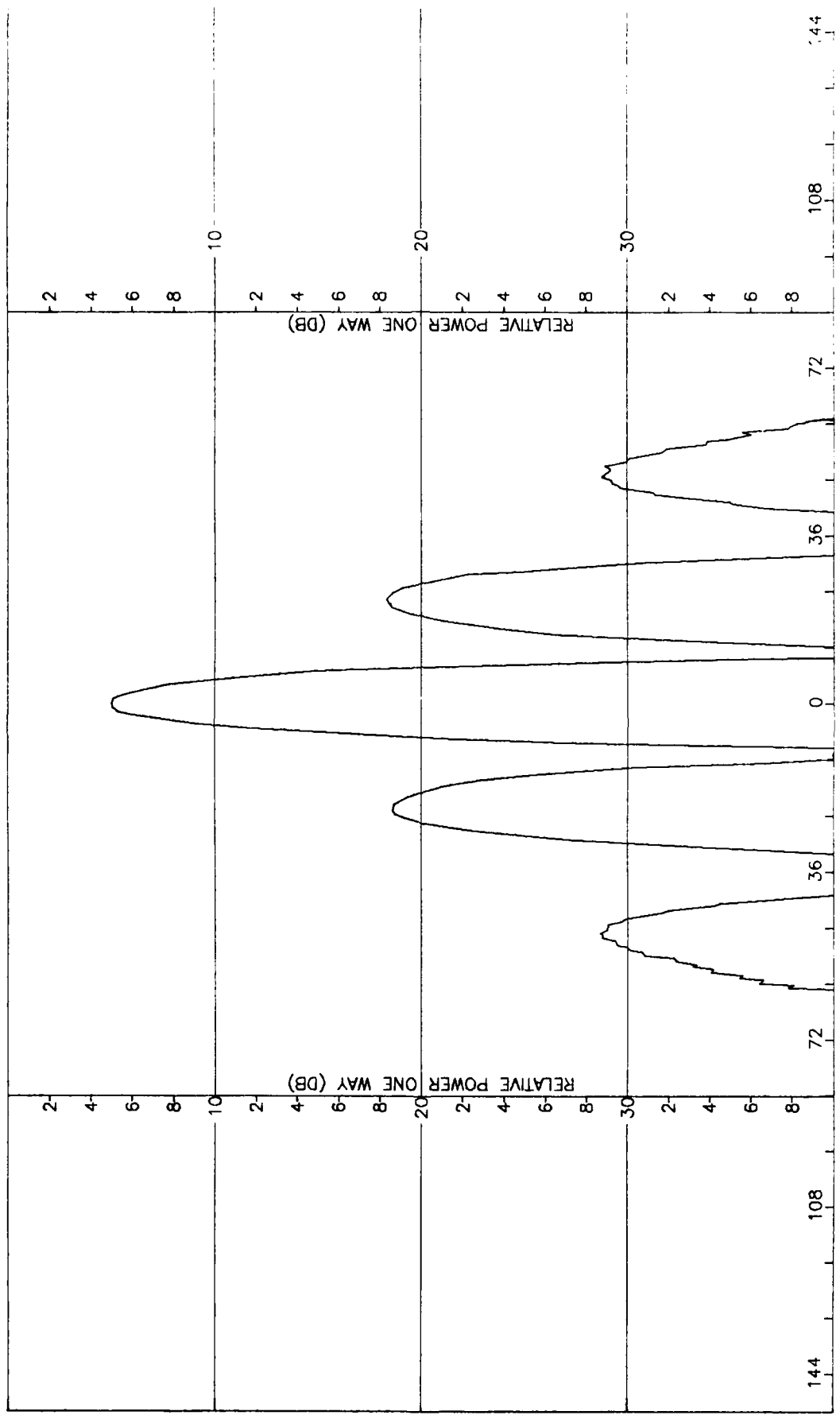


Figure C-14. Pattern of Large Array:  $\phi=45^\circ$  Plane, Sum,  $\phi$ -Component, No Radome

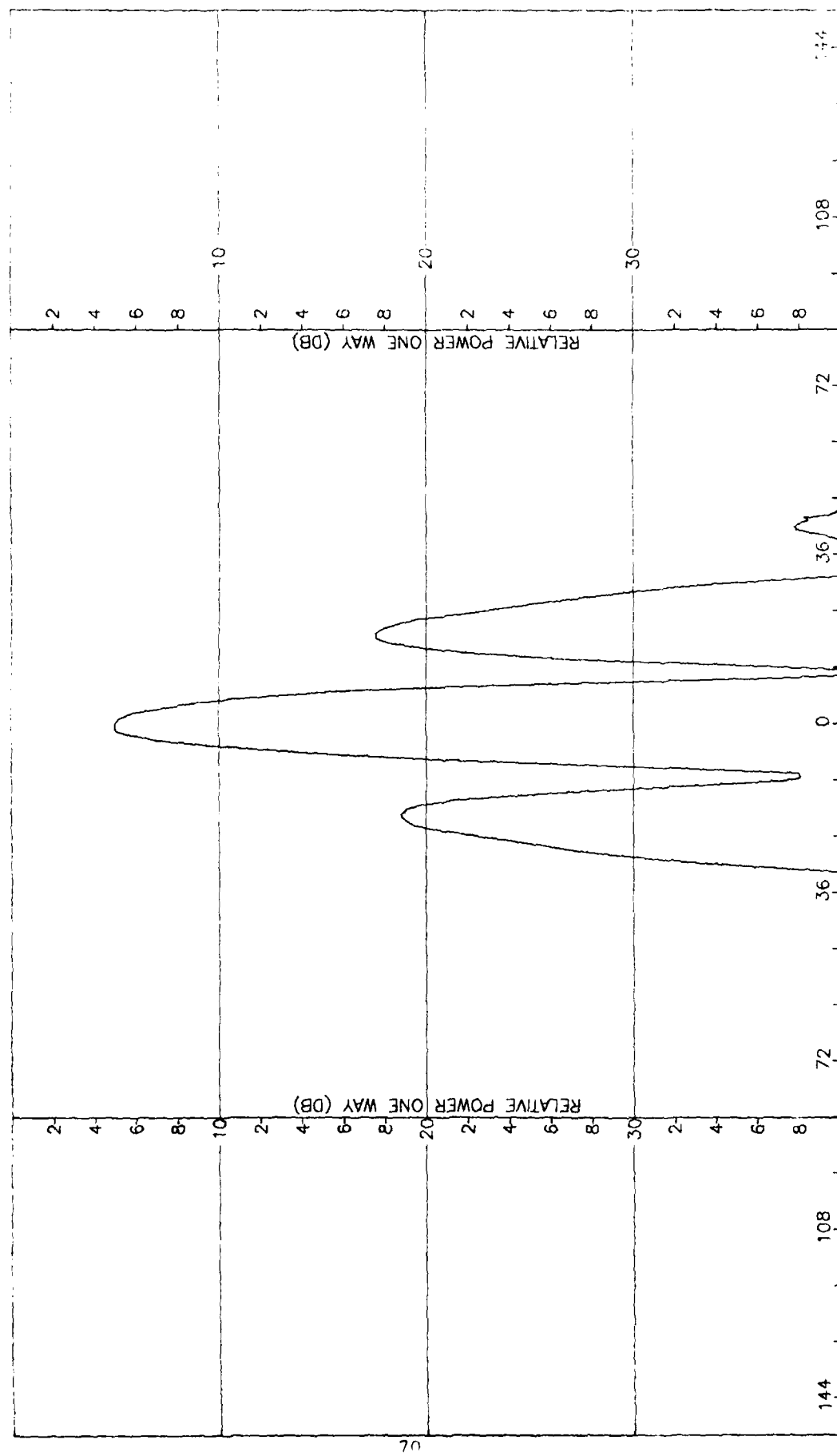


Figure C-15. Pattern of Large Array:  $\phi = -45^\circ$  Plane, Sum,  $\theta$ -Component, No Radome

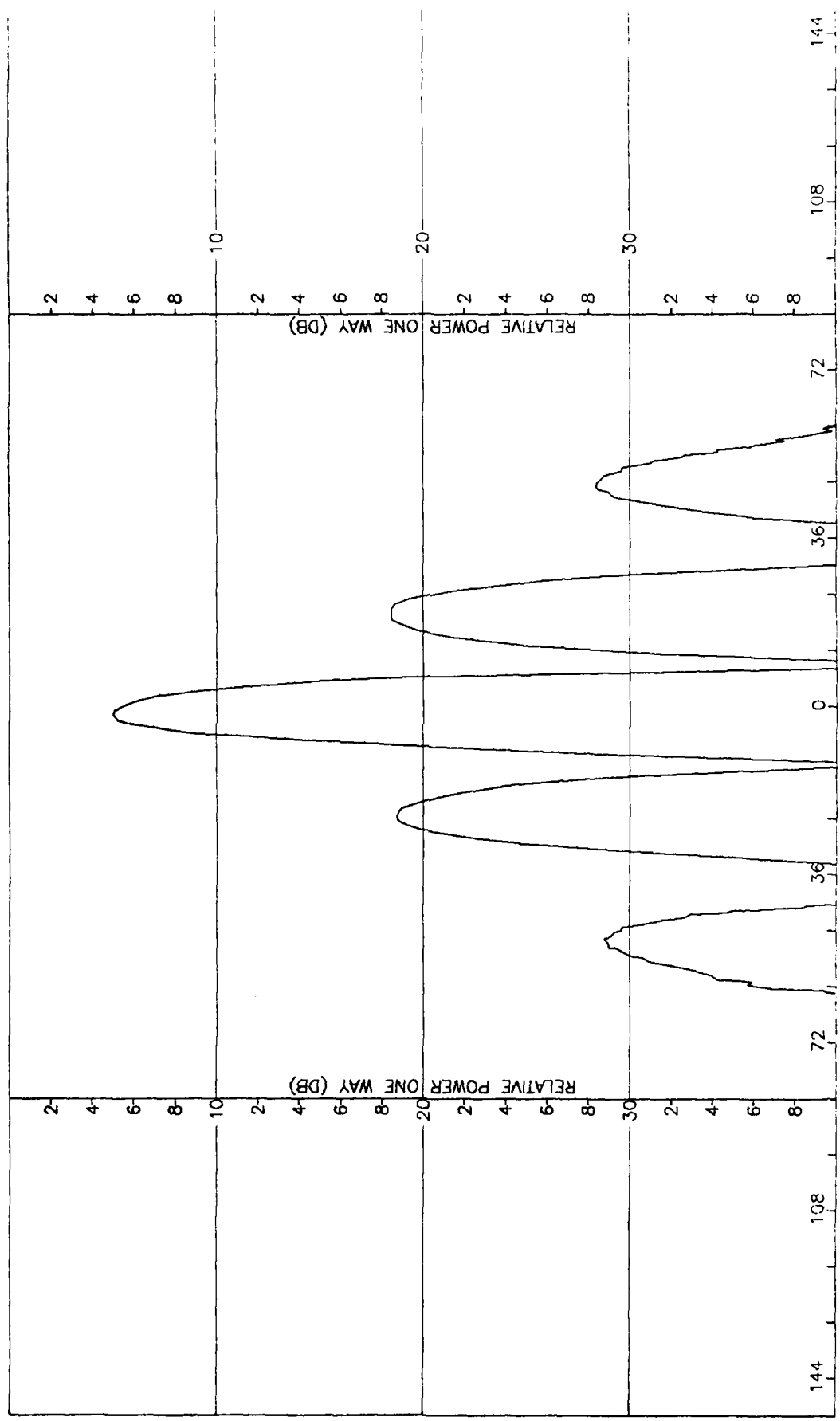


Figure C-16. Pattern of Large Array:  $\phi = -45^\circ$  Plane, Sum.  $\phi$ -Component, No Radome

APPENDIX D

Antenna Patterns of Small Array with Small (F=1) Radome

PRECEDING PAGE BLANK-NOT FILMED

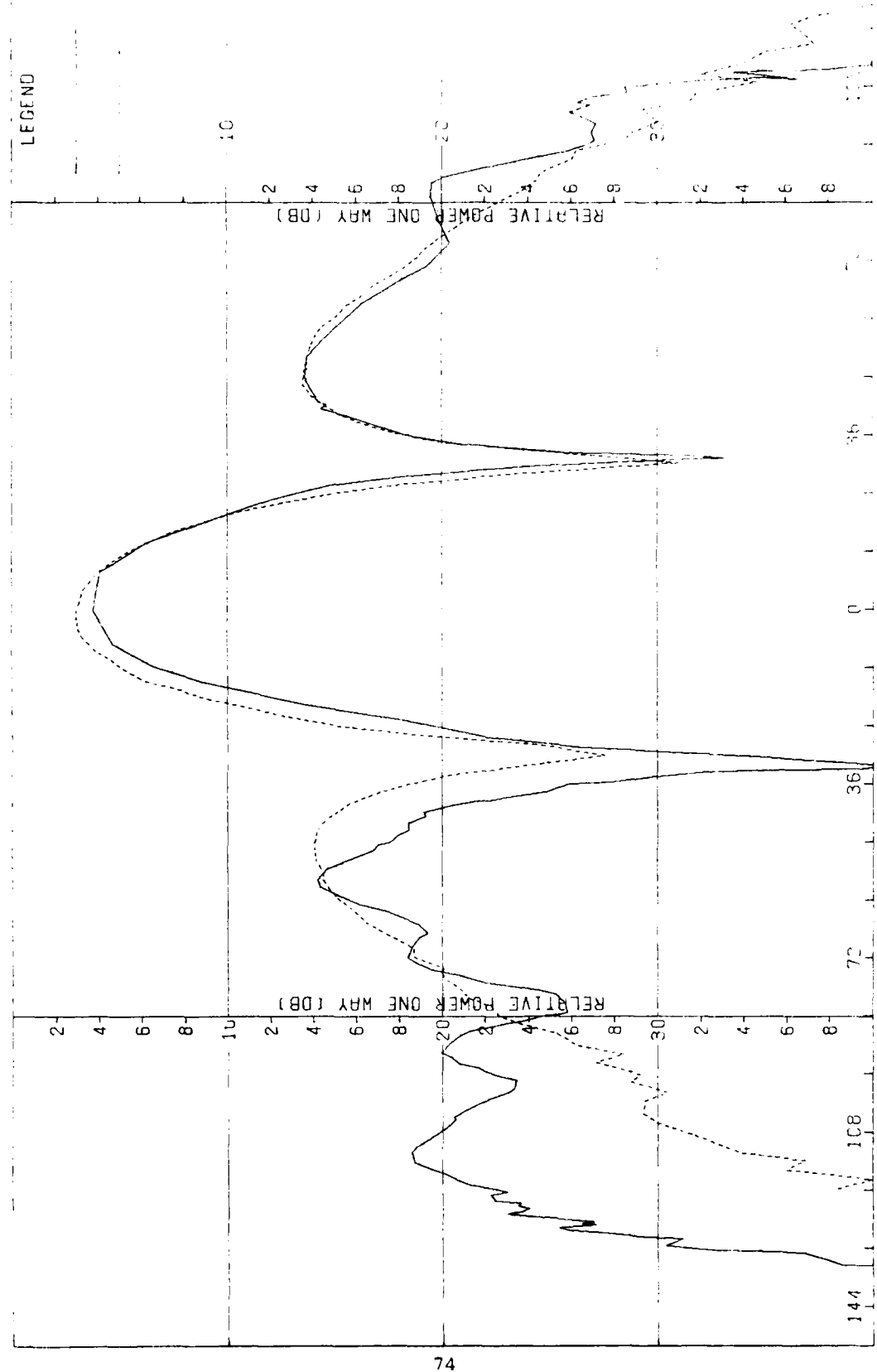


Figure D-1. Pattern of Small Array: H-Plane, Sum,  $\phi$ -Component, Small Radome

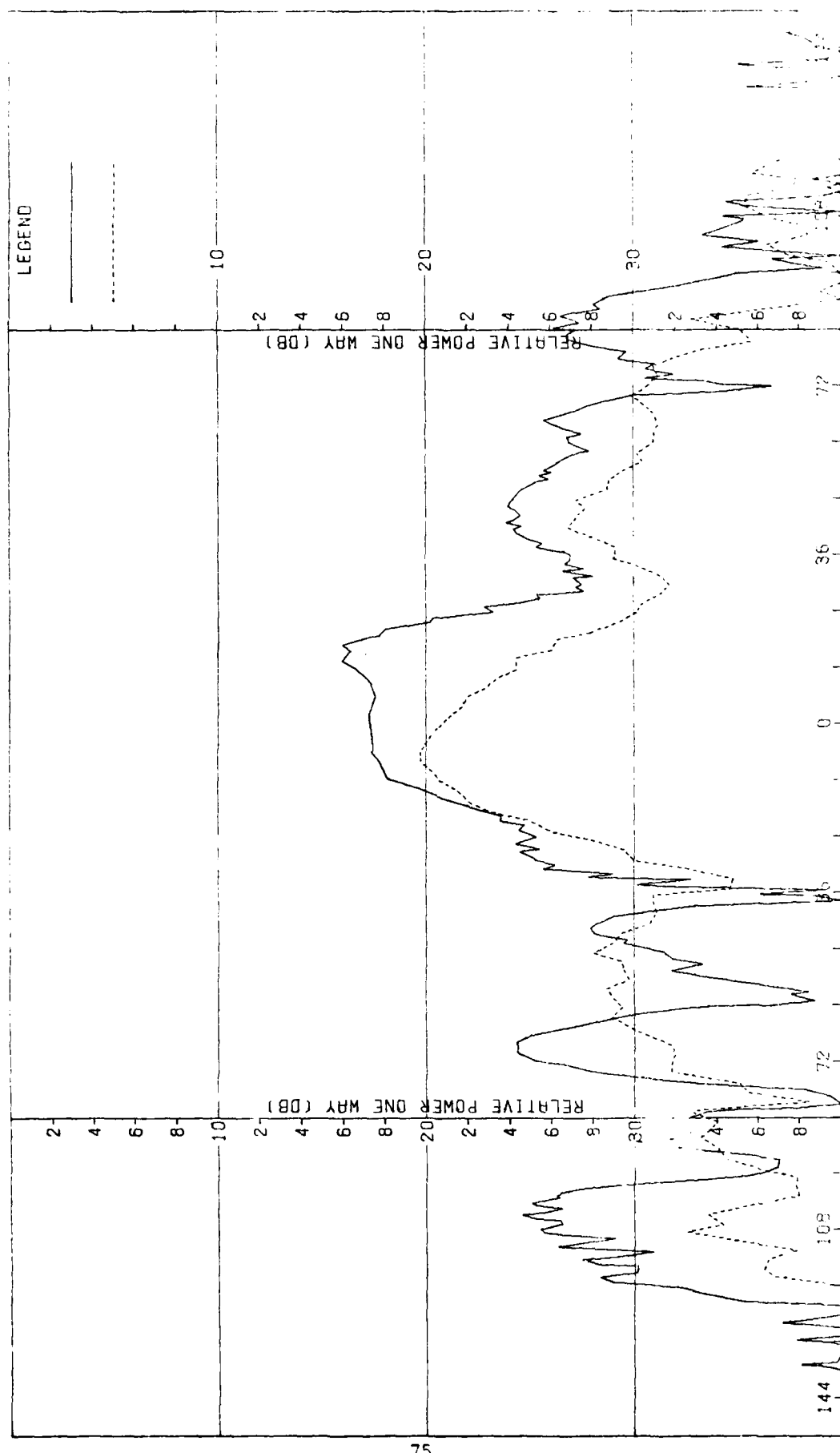


Figure D-2. Pattern of Small Array: H-Plane, Sum,  $\hat{E}$ -Component, Small Radome

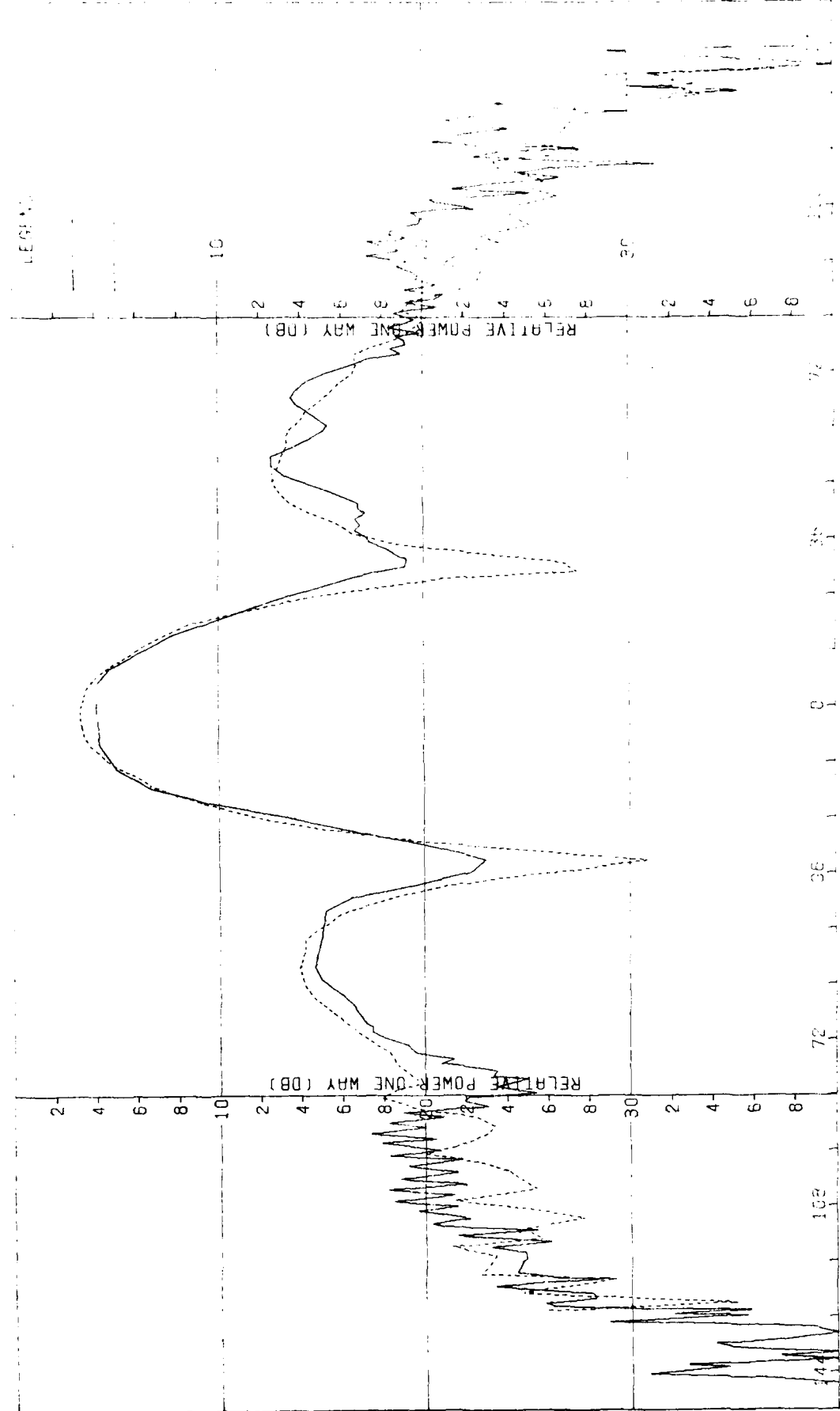


Figure D-3. Pattern of Small Array: E-Plane, Sum, 6-Component, Small Radome.

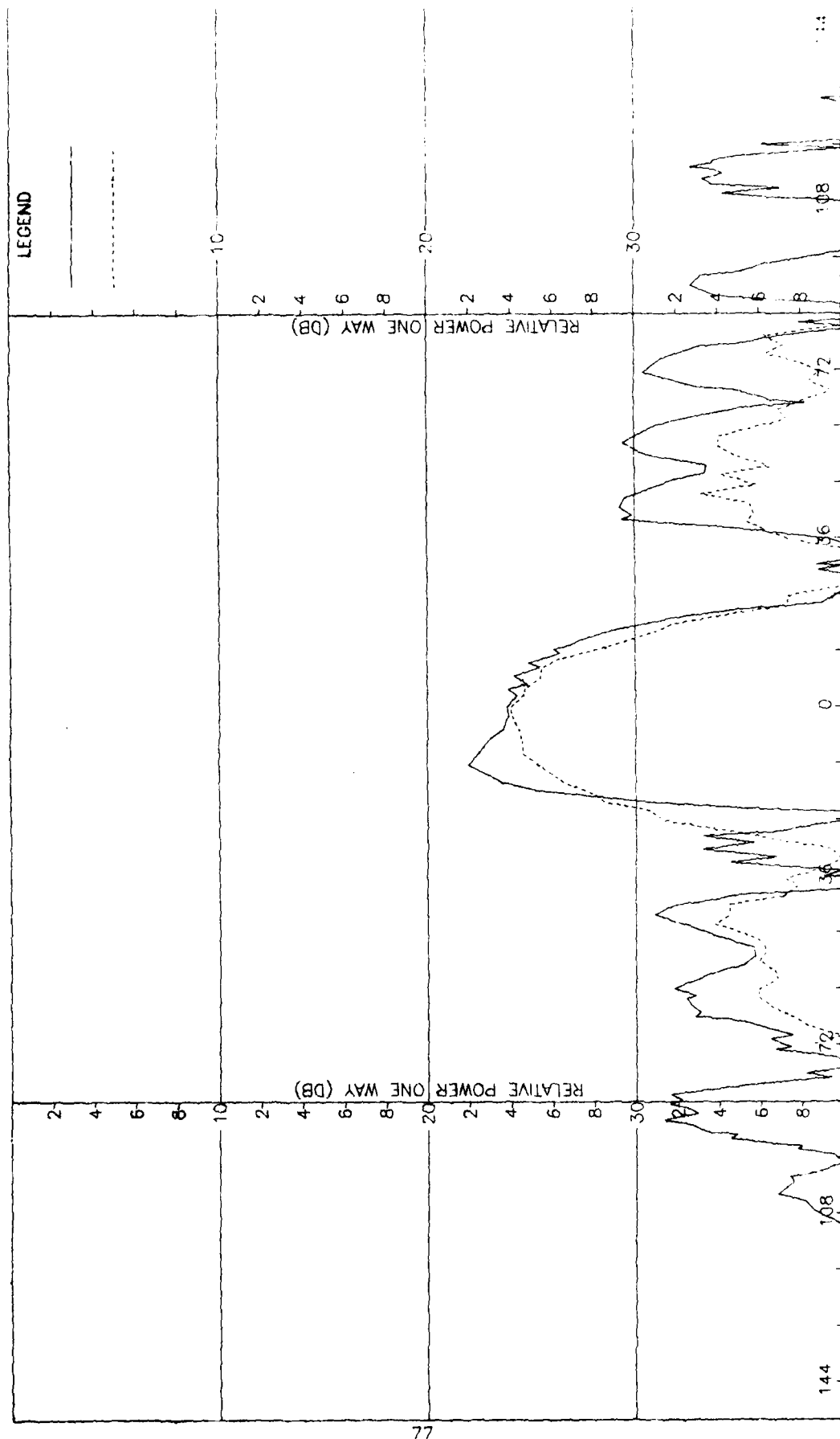


Figure D-4. Pattern of Small Array: Y-plane, X-plane, Sum,  $\hat{\alpha}$ -Component, Small Radome.

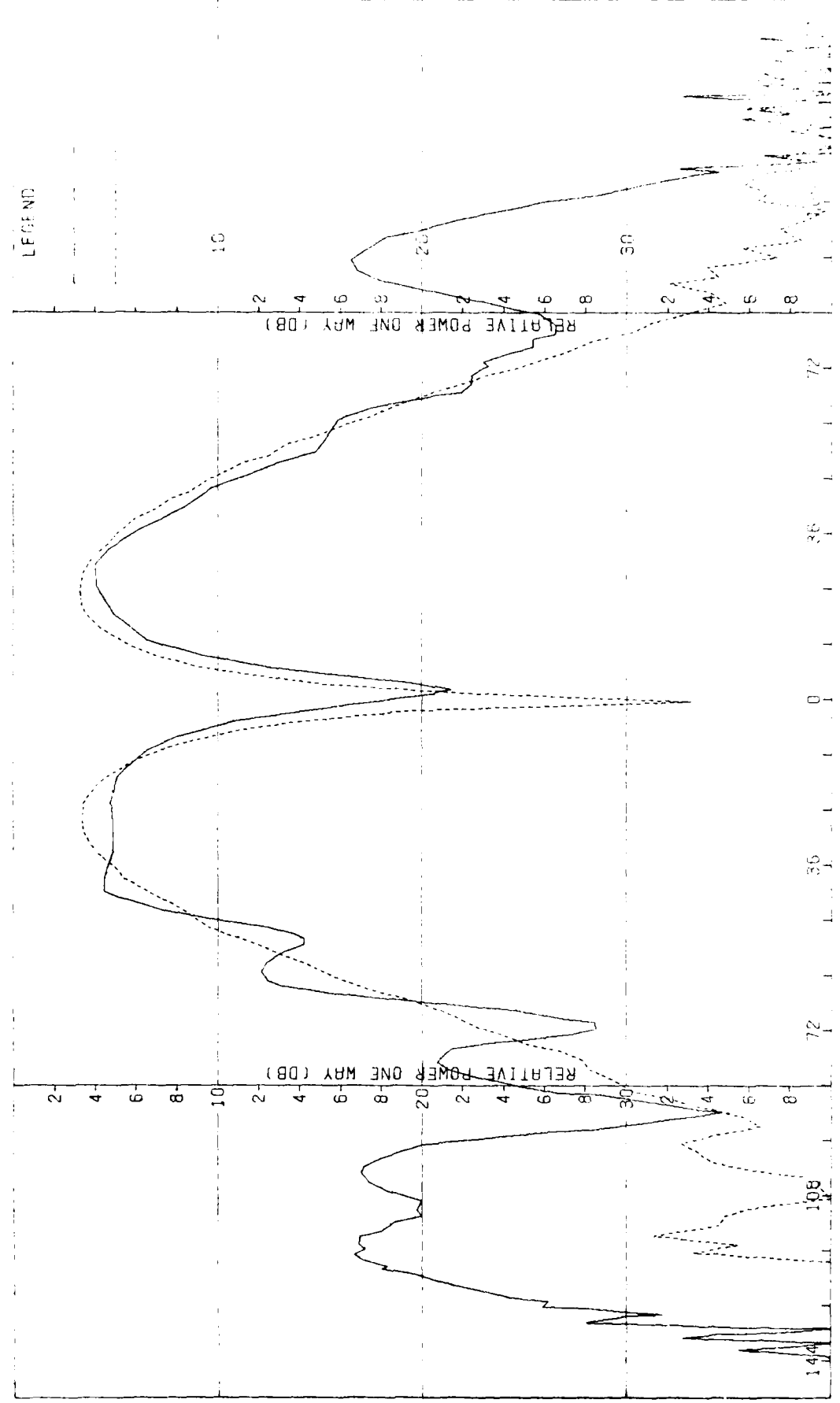


Figure D-5. Pattern of Small Array: H-Plane, Azimuth Difference,  $\phi$ -Component, Small Radome.

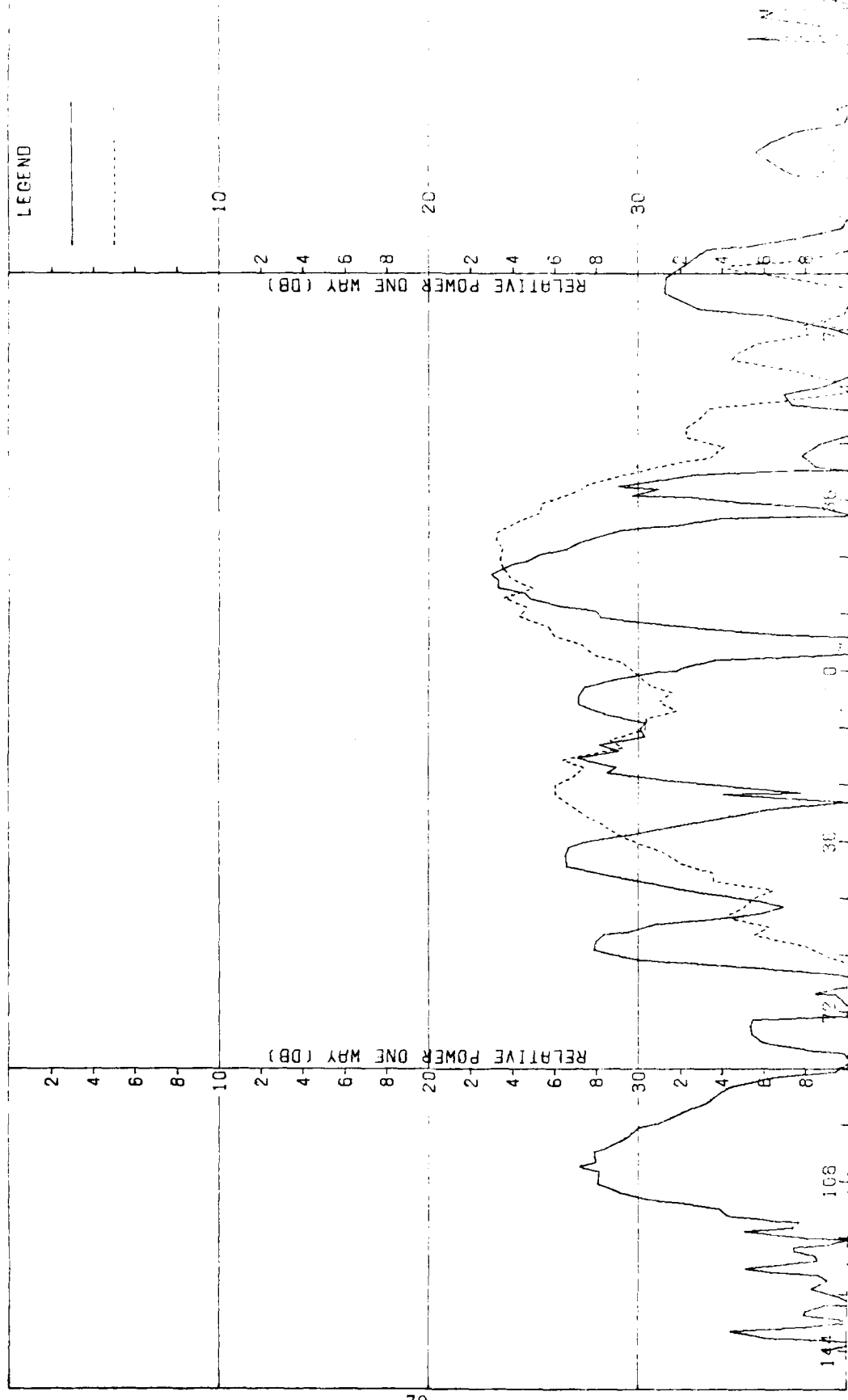


Figure D-6. Pattern of Small Array: H-Plane, Azimuth Difference,  $\theta$ -Component, Small Radome.

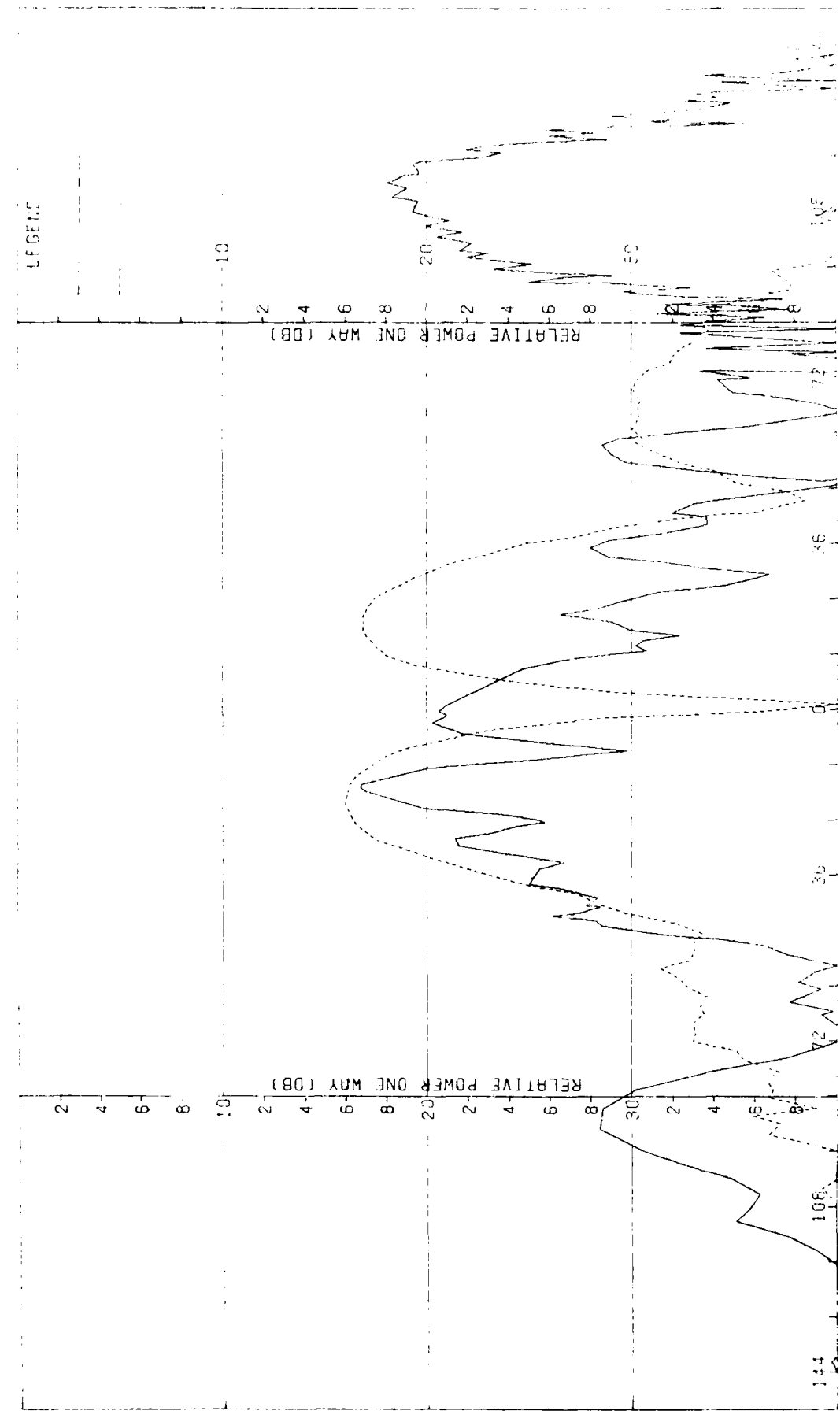
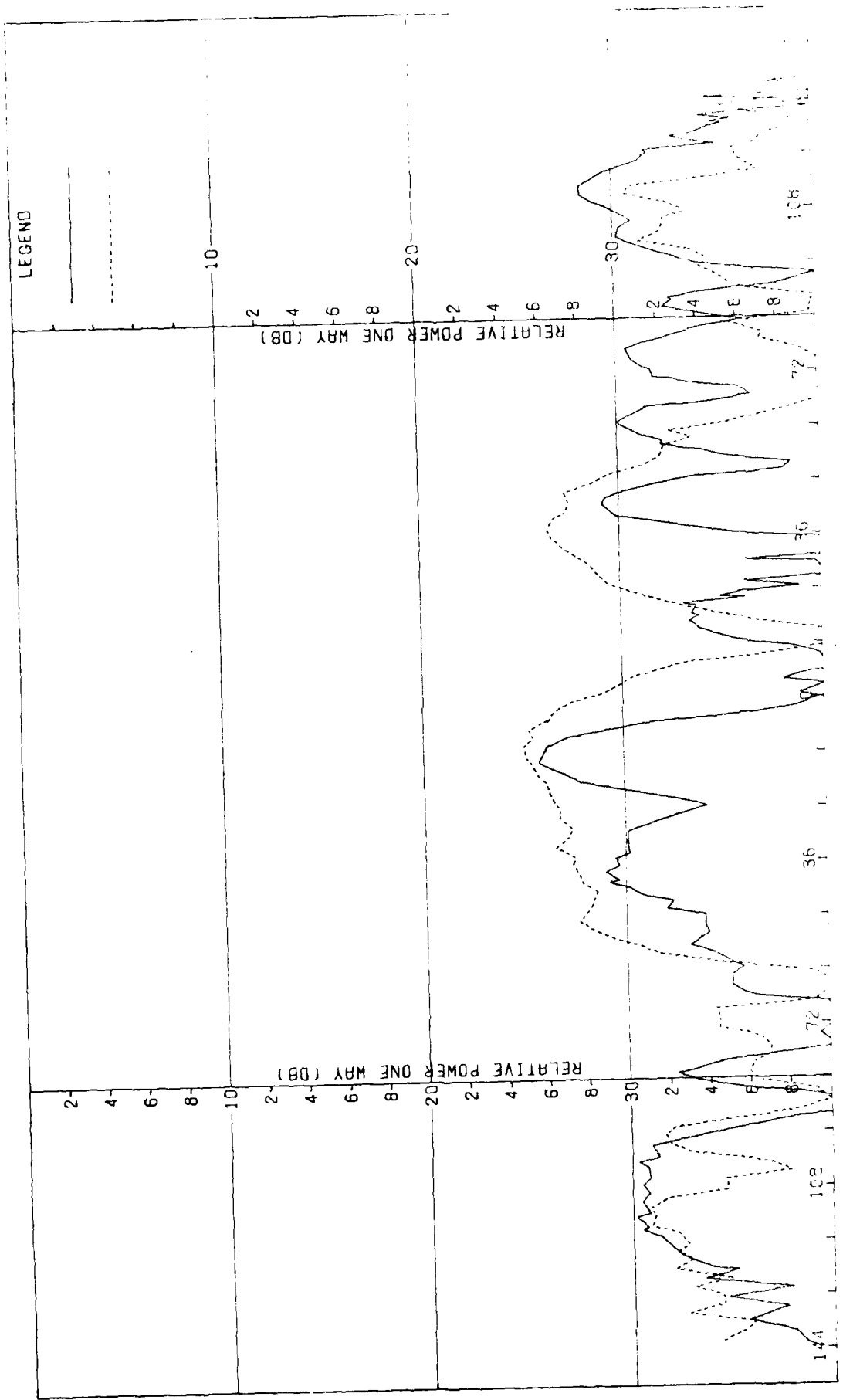


Figure D-7. Pattern of Small Array: E-Plane, Azimuth Difference, 0-Component, Small Radome.



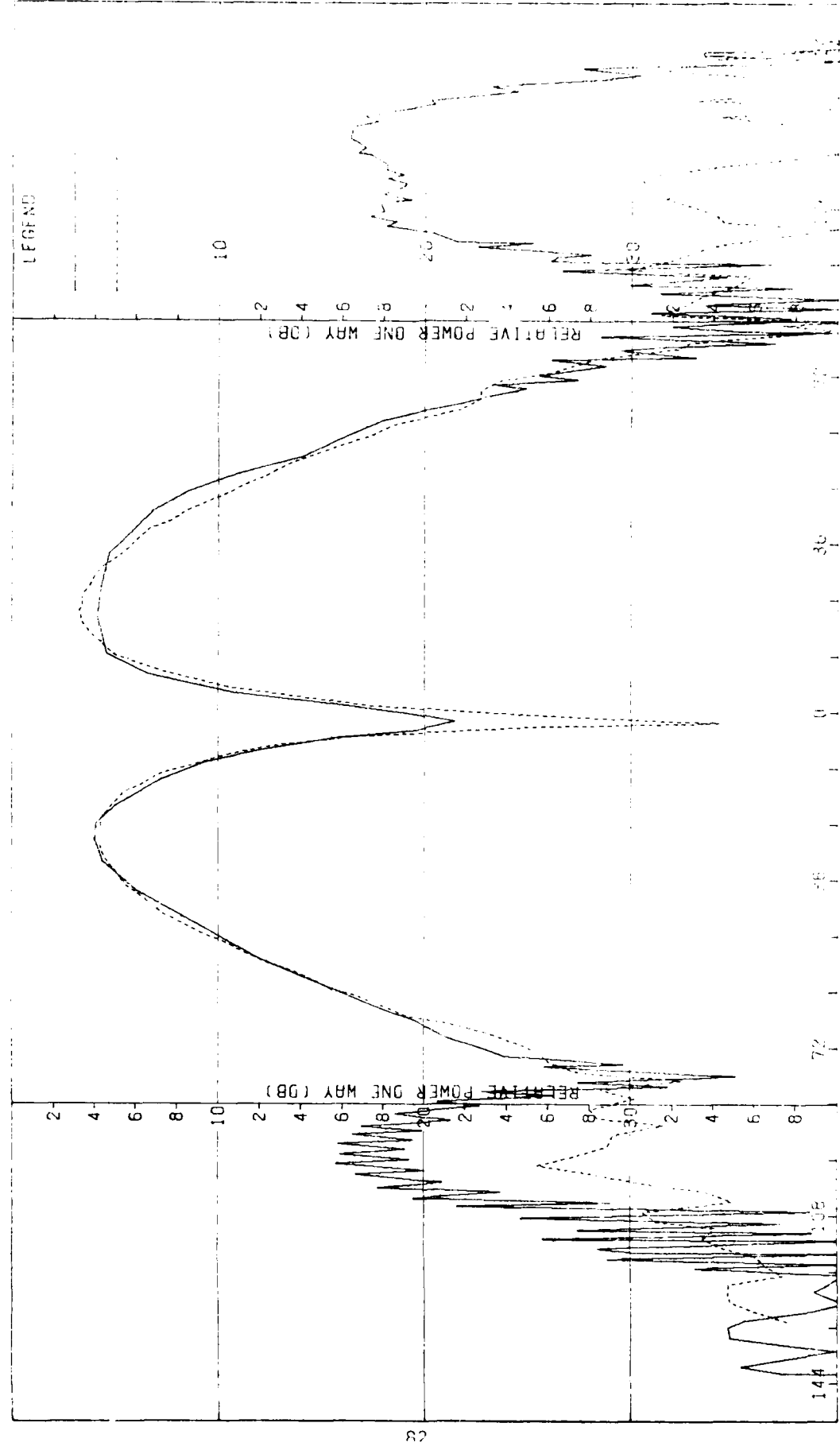


Figure D-9. Pattern of Small Array: E-plane, Elevation difference,  $n$ -Component, Small Radome.

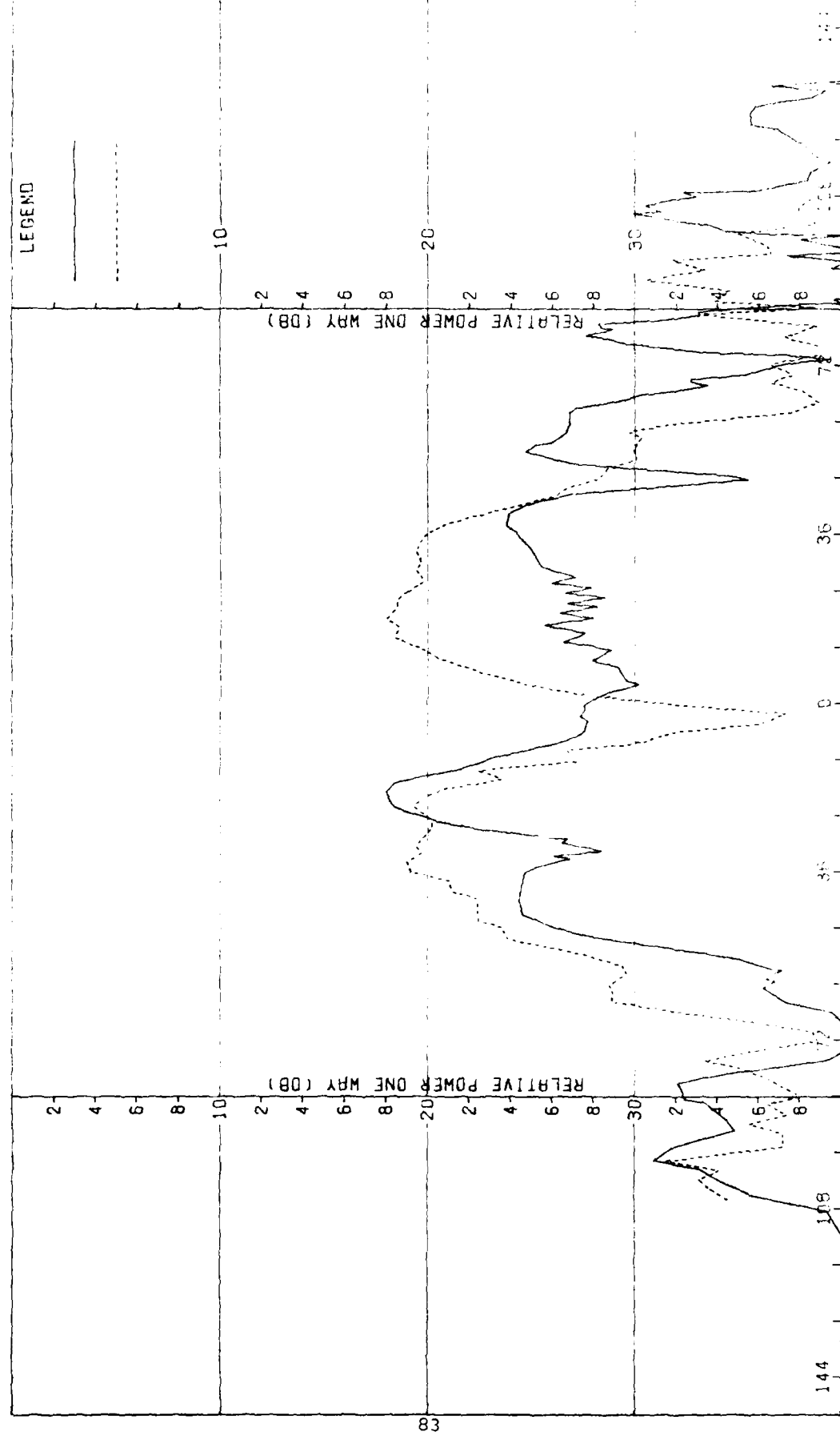


Figure D-10. Pattern of Small Array; E-Plane, Elevation difference,  $\phi$ -Component, Small Radome.

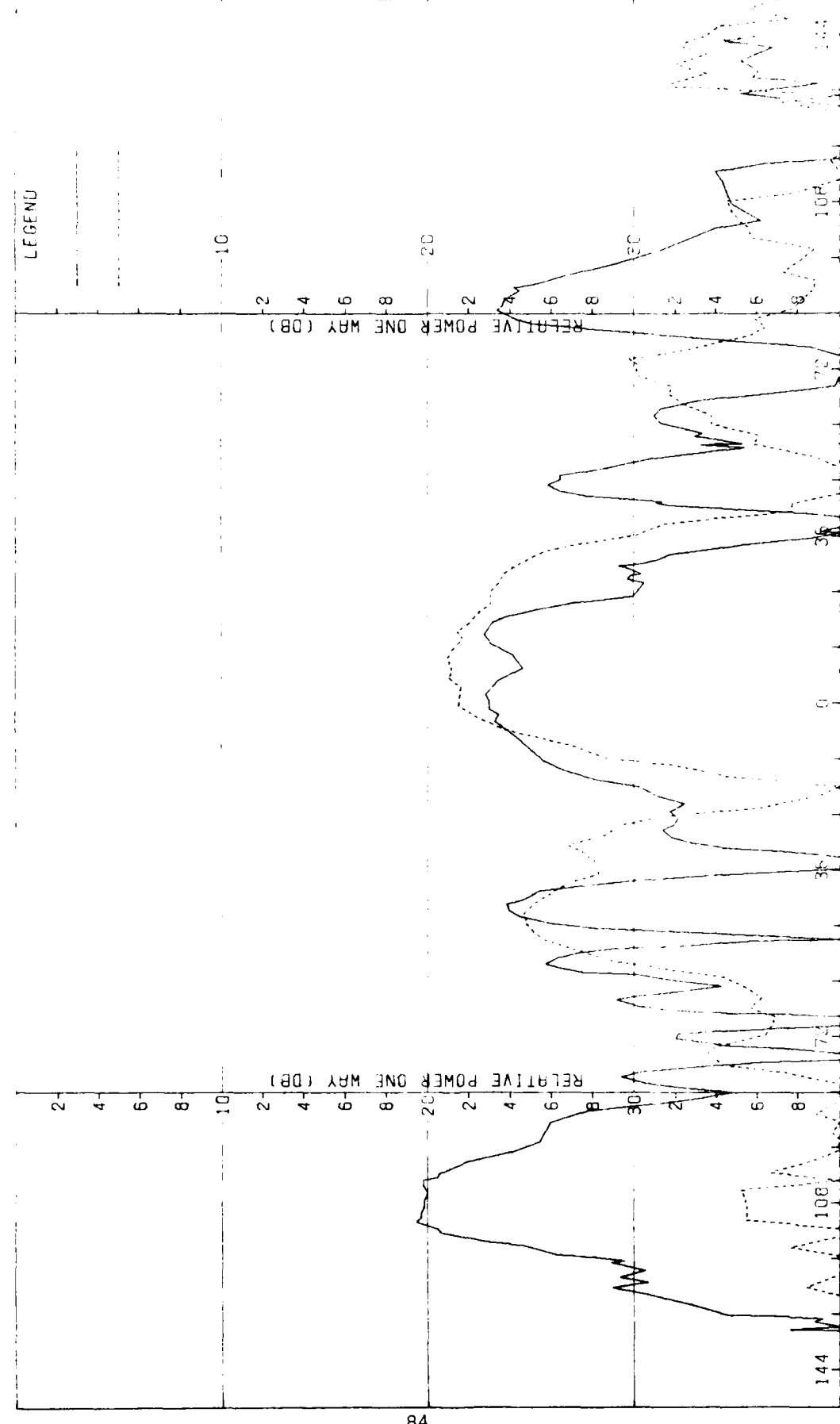


Figure D-11. Pattern of Small Array: H-Plane, Elevation difference,  $i$ -Component, Small Radome.

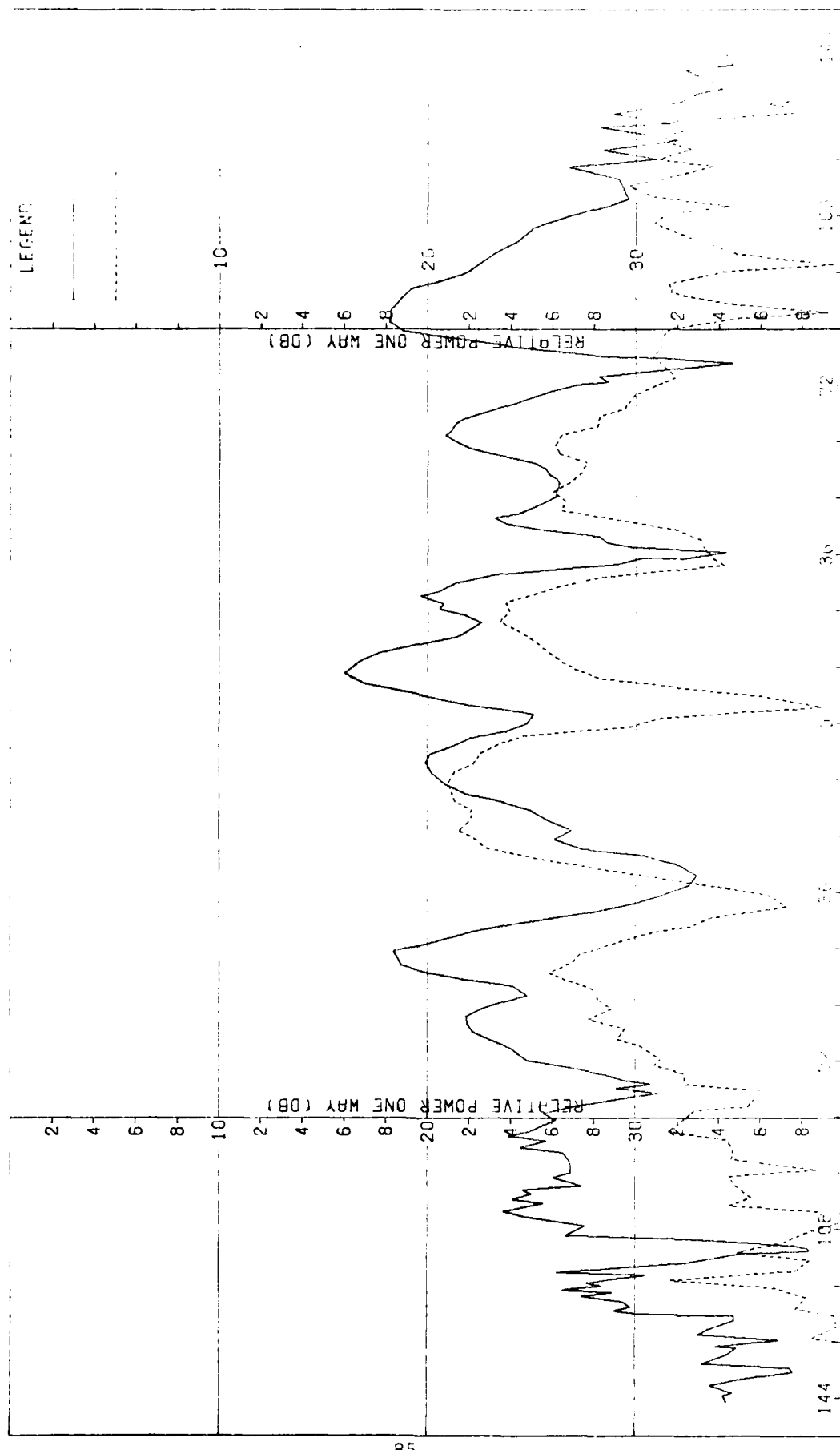


Figure D-12. Pattern of Small Array Radiation Pattern Difference, 2-Component, Small Radiant.

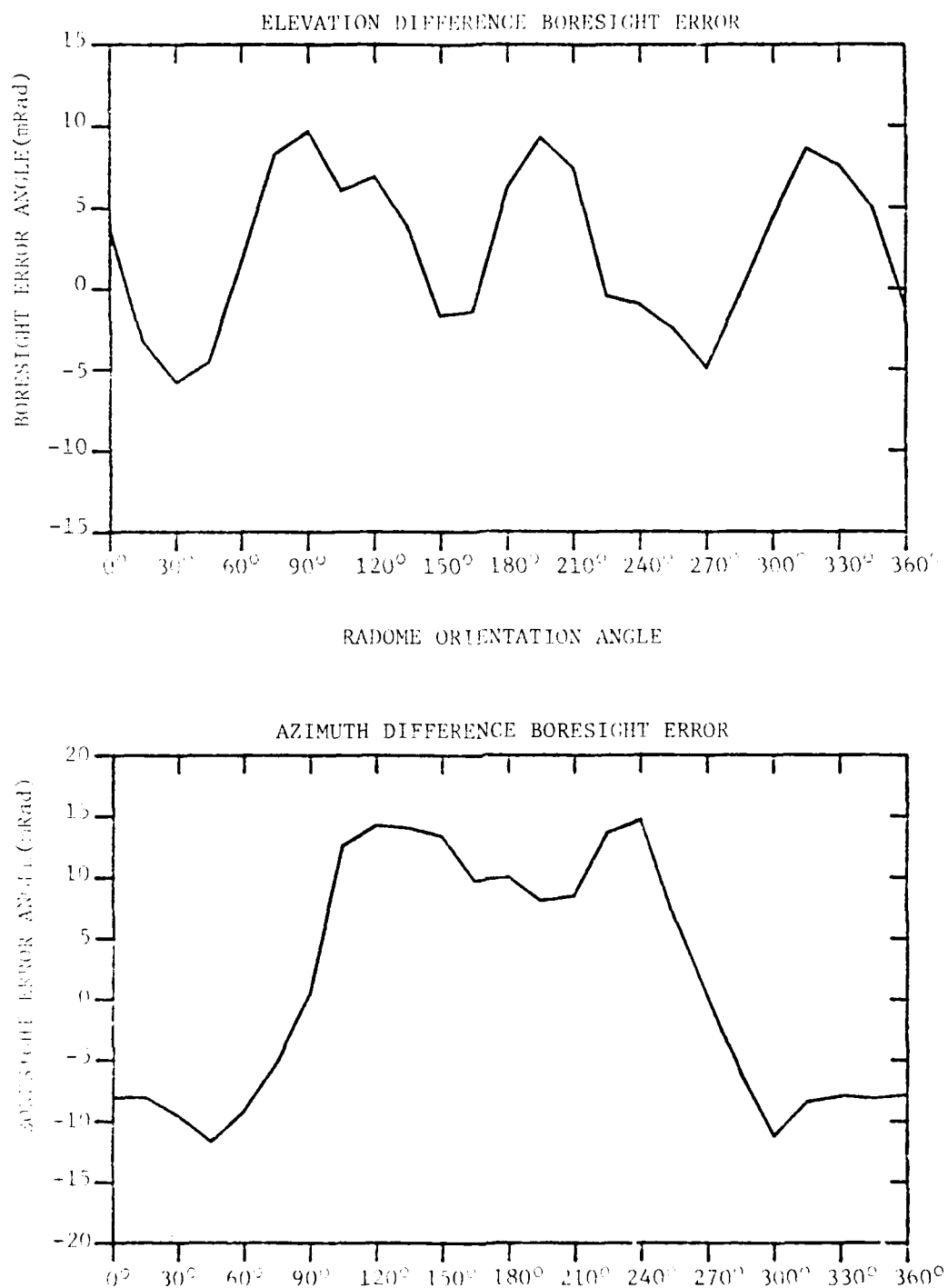


FIGURE D-13. BORESIGHT ERRORS OF SMALL ARRAY AND SMALL ( $F=1$ ) RADOME.

APPENDIX E

Antenna Patterns of Small Array with Medium (F=1) Radome

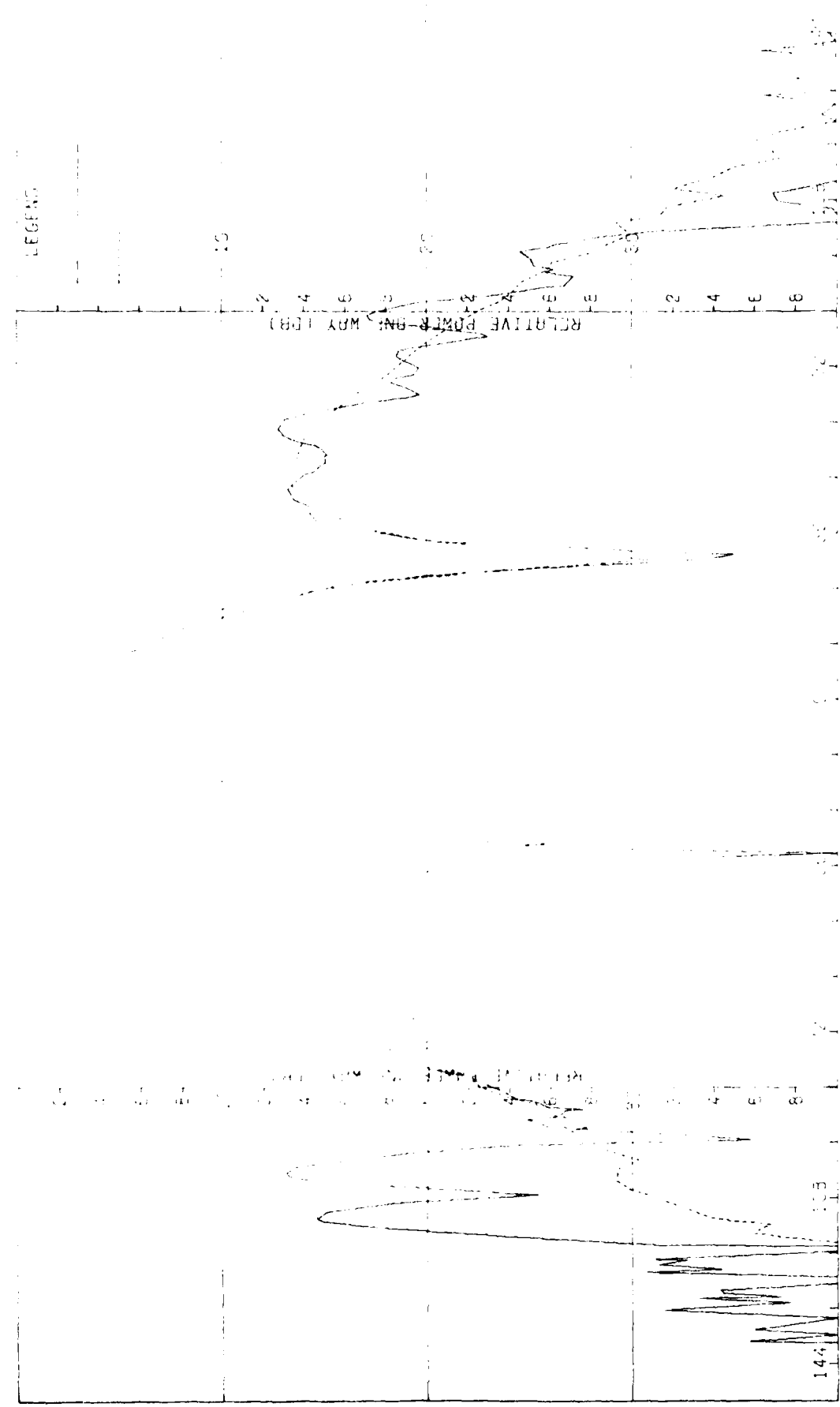


Figure E-1. Pattern of Small Array: H-Plane, Sum,  $f$ -component, Medium ( $F=1$ ) Radome

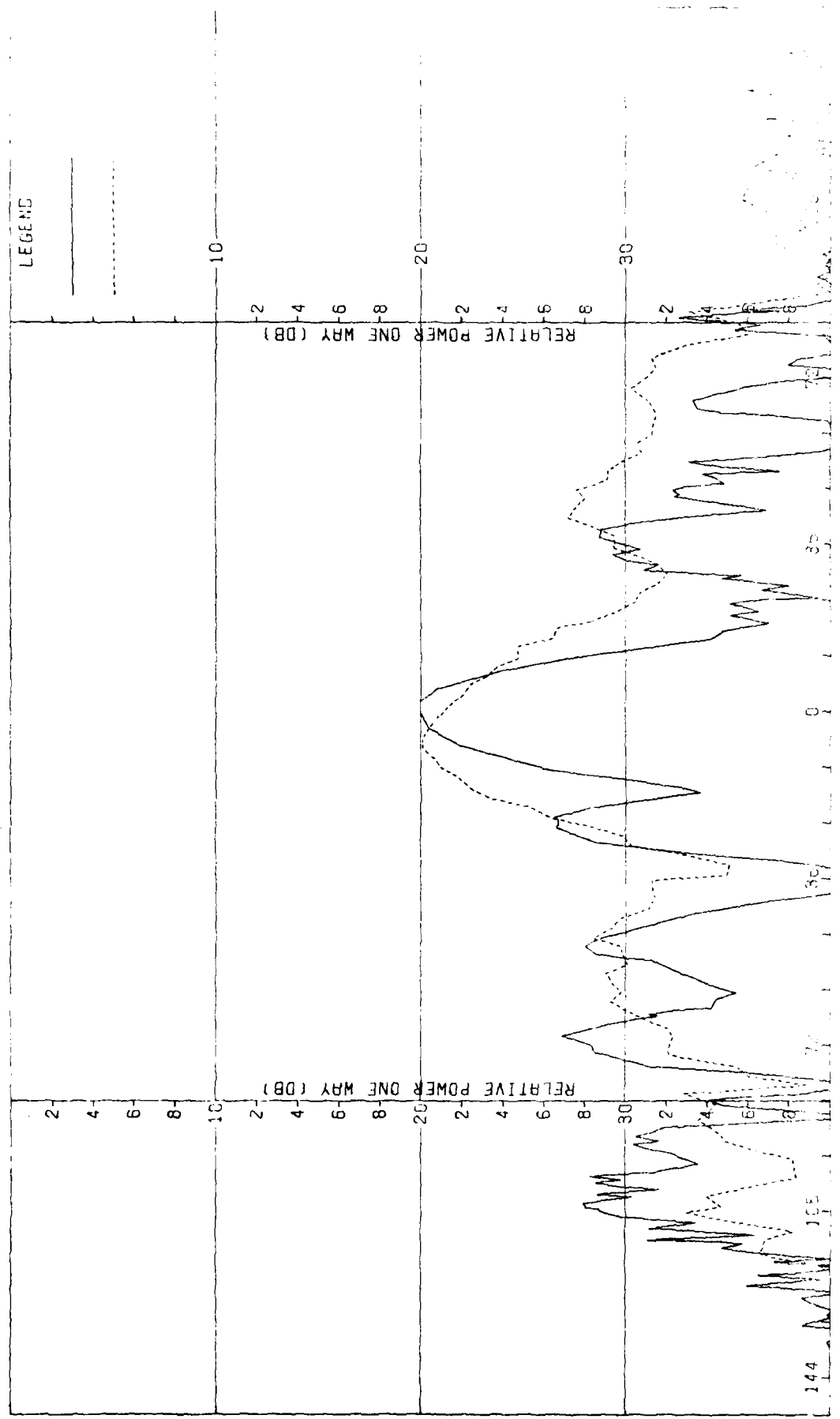


Figure E-2. Pattern of Small Array: H-Plane, Sum, & Component, Medium (F=1) Radome

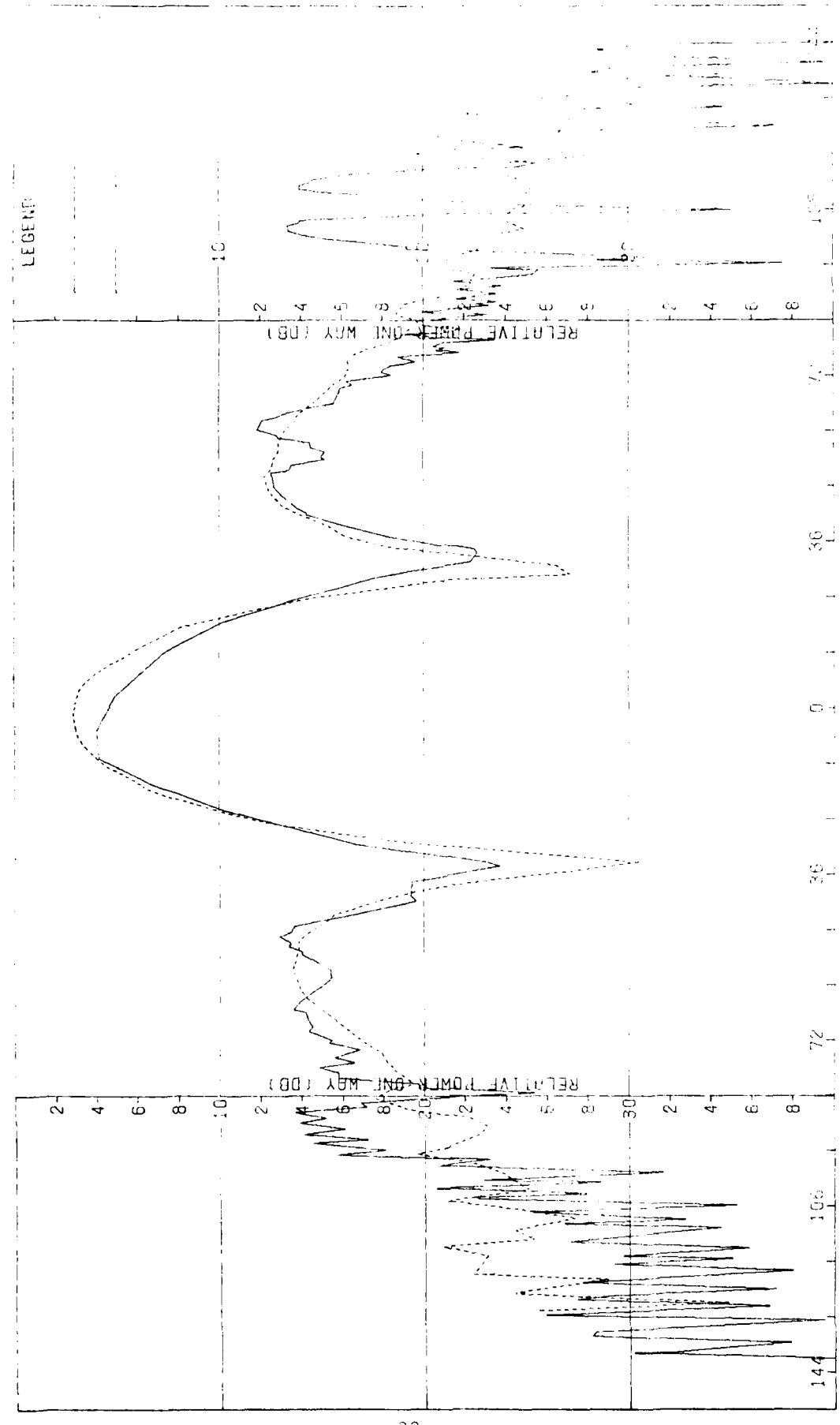


Figure E-3. Pattern of Small Array: E-Plane, Sum, H-Component, Medium (F=1) Radome

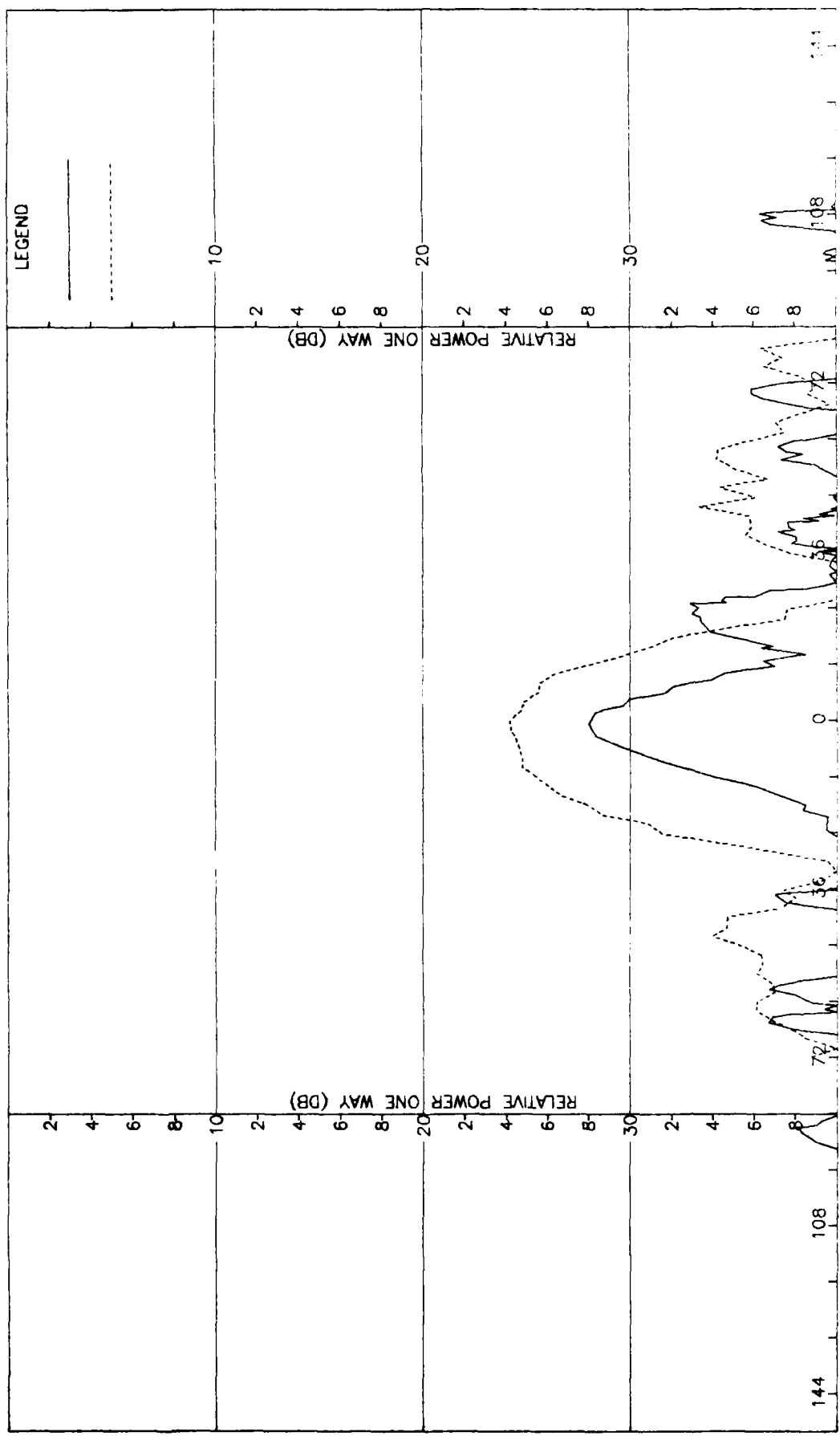


Figure E-4. Pattern of Small Array: E-plane, Azimuth Difference,  $p$ -component, Medium ( $F=1$ ) Radome

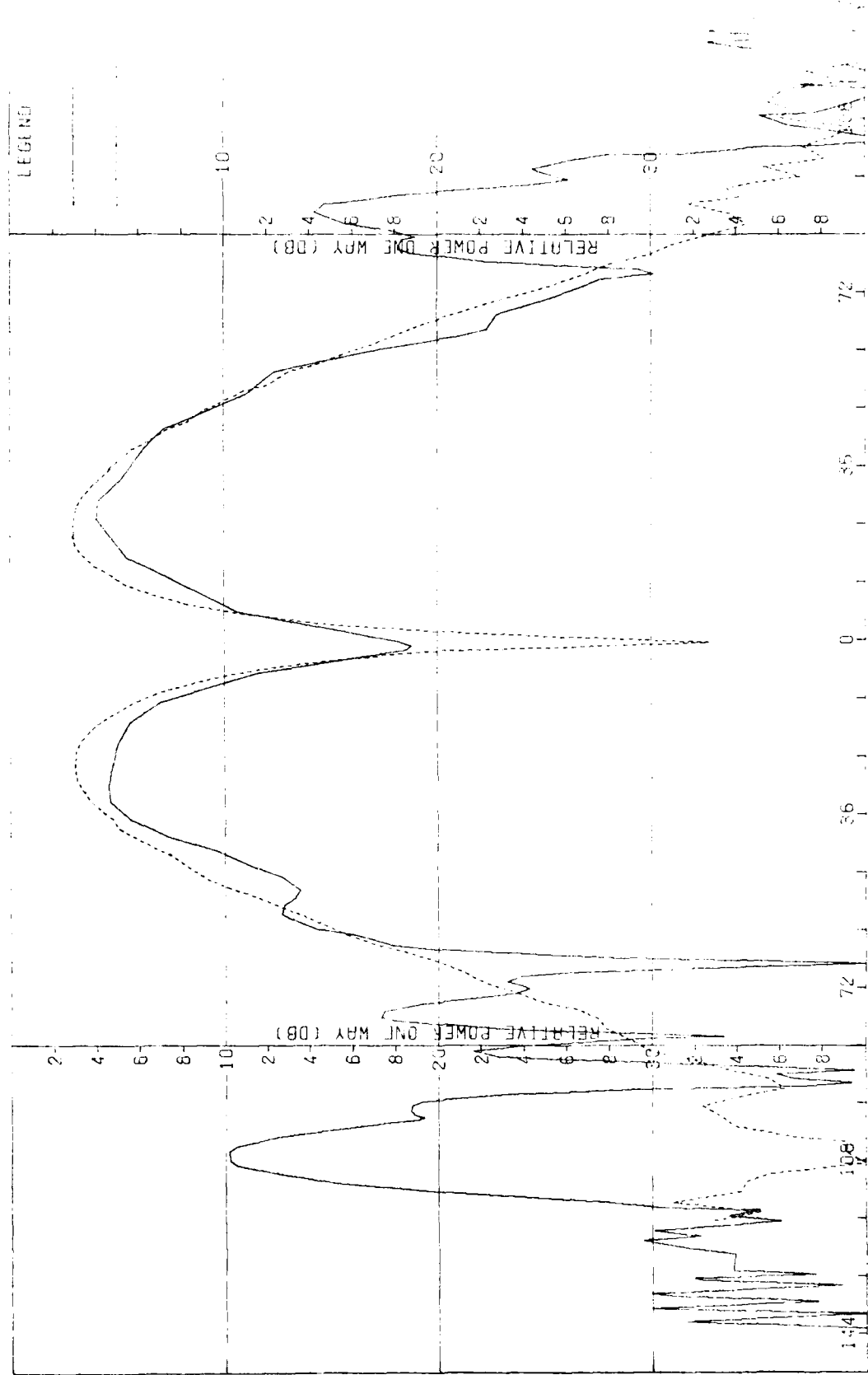
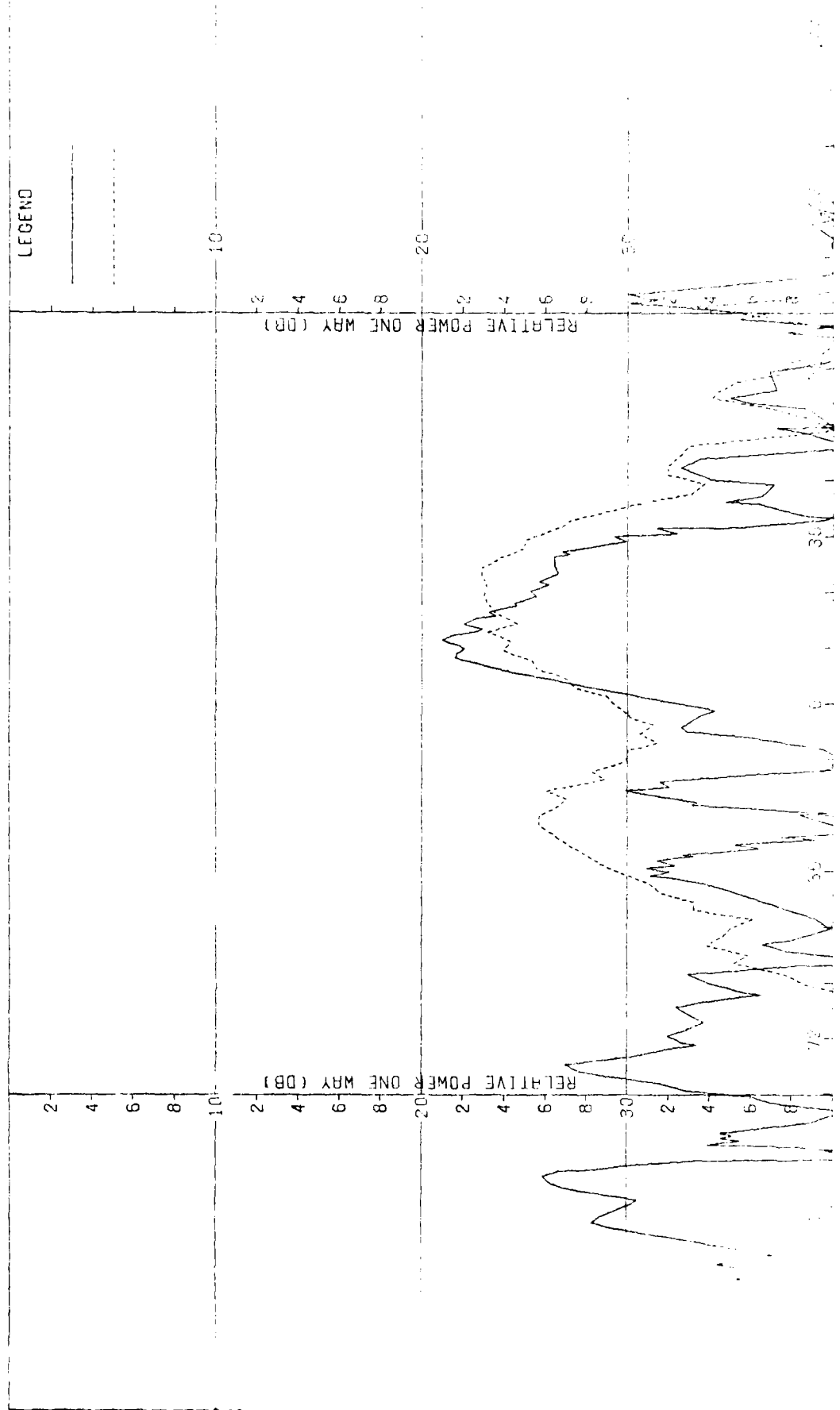


Figure E-5. Pattern of Small Array: H-Plane, Azimuth Difference,  $\frac{1}{4}$ -Component, Medium ( $F=1$ ) Radome



Pattern of Small Array: H-Plane, Azimuth Difference,  $\theta$ -Component, Medium ( $F=1$ ) Radome

AD-A100 017

GEORGIA INST OF TECH ATLANTA  
PARAMETRIC INVESTIGATION OF RADOME ANALYSIS METHODS. VOLUME IV.--ETC(U)  
FEB 81 H L BASSETT, J M NEWTON, W ADAMS AFOSR-77-3469

AFOSR-TR-81-0462

F/6 17/9

1

2

3

4

5

6

7

8

9

0

1

2

3

4

5

6

7

8

9

0

1

2

3

4

5

6

7

8

9

0

1

2

3

4

5

6

7

8

9

0

1

2

3

4

5

6

7

8

9

0

1

2

3

4

5

6

7

8

9

0

1

2

3

4

5

6

7

8

9

0

1

2

3

4

5

6

7

8

9

0

1

2

3

4

5

6

7

8

9

0

1

2

3

4

5

6

7

8

9

0

1

2

3

4

5

6

7

8

9

0

1

2

3

4

5

6

7

8

9

0

1

2

3

4

5

6

7

8

9

0

1

2

3

4

5

6

7

8

9

0

1

2

3

4

5

6

7

8

9

0

1

2

3

4

5

6

7

8

9

0

1

2

3

4

5

6

7

8

9

0

1

2

3

4

5

6

7

8

9

0

1

2

3

4

5

6

7

8

9

0

1

2

3

4

5

6

7

8

9

0

1

2

3

4

5

6

7

8

9

0

1

2

3

4

5

6

7

8

9

0

1

2

3

4

5

6

7

8

9

0

1

2

3

4

5

6

7

8

9

0

1

2

3

4

5

6

7

8

9

0

1

2

3

4

5

6

7

8

9

0

1

2

3

4

5

6

7

8

9

0

1

2

3

4

5

6

7

8

9

0

1

2

3

4

5

6

7

8

9

0

1

2

3

4

5

6

7

8

9

0

1

2

3

4

5

6

7

8

9

0

1

2

3

4

5

6

7

8

9

0

1

2

3

4

5

6

7

8

9

0

1

2

3

4

5

6

7

8

9

0

1

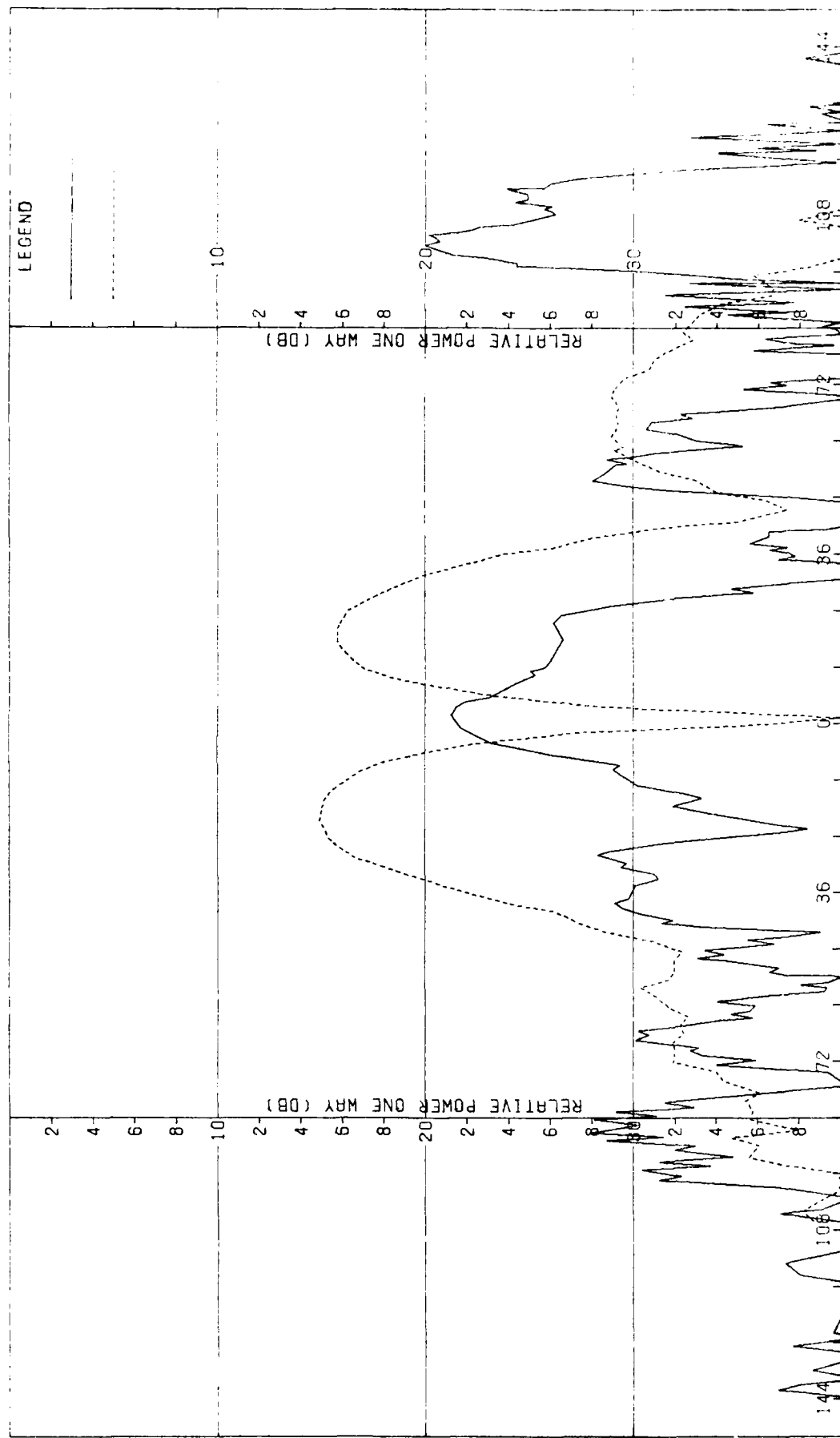


Figure E-7. Pattern of Small Array: E-Plane, Azimuth Difference,  $\theta$ -Component, Medium (F=1) Radome

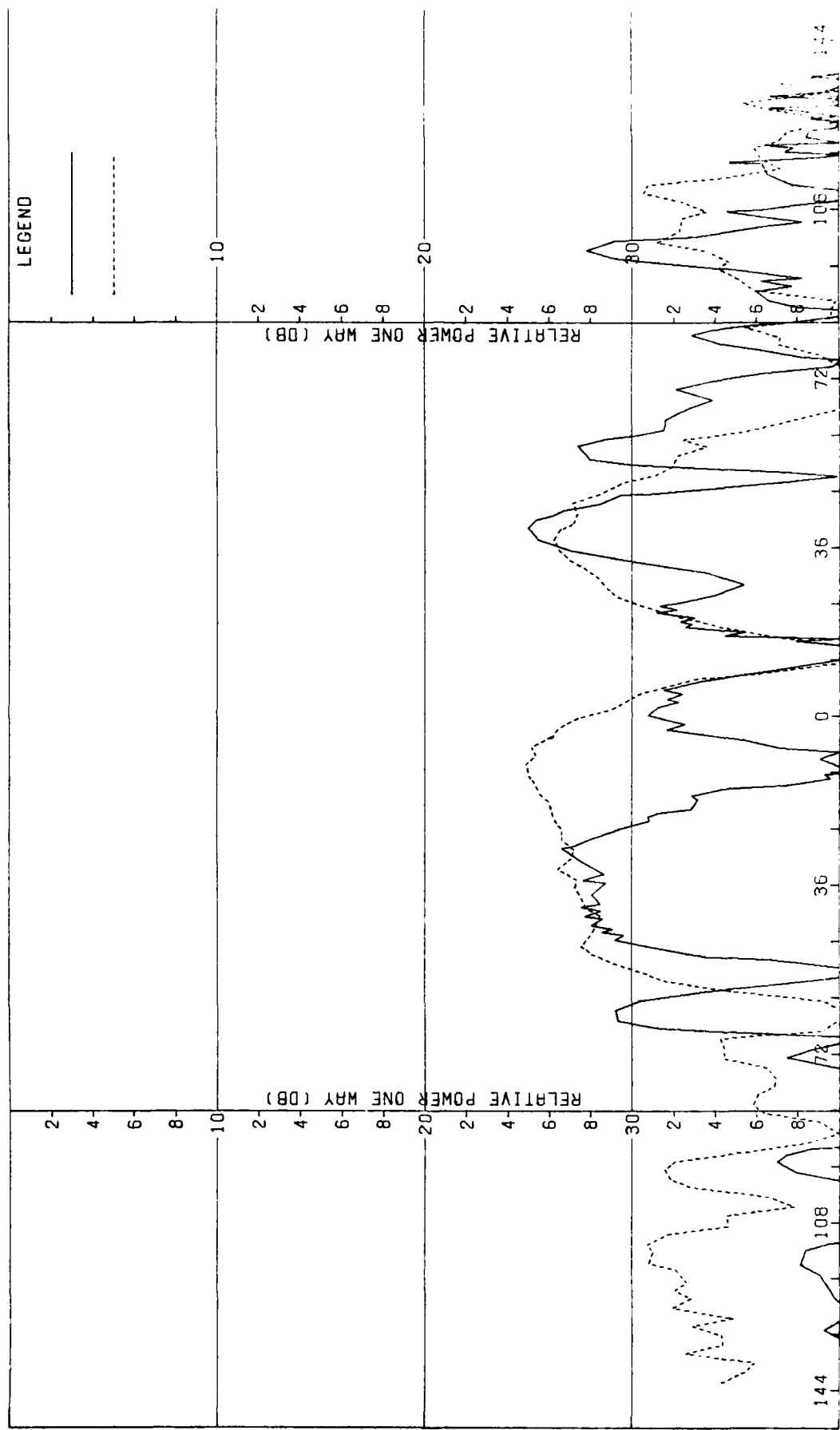


Figure E-8. Pattern of Small Array: E-Plane, Elev. Difference,  $\phi$ -Component, Medium ( $F=1$ ) Radome

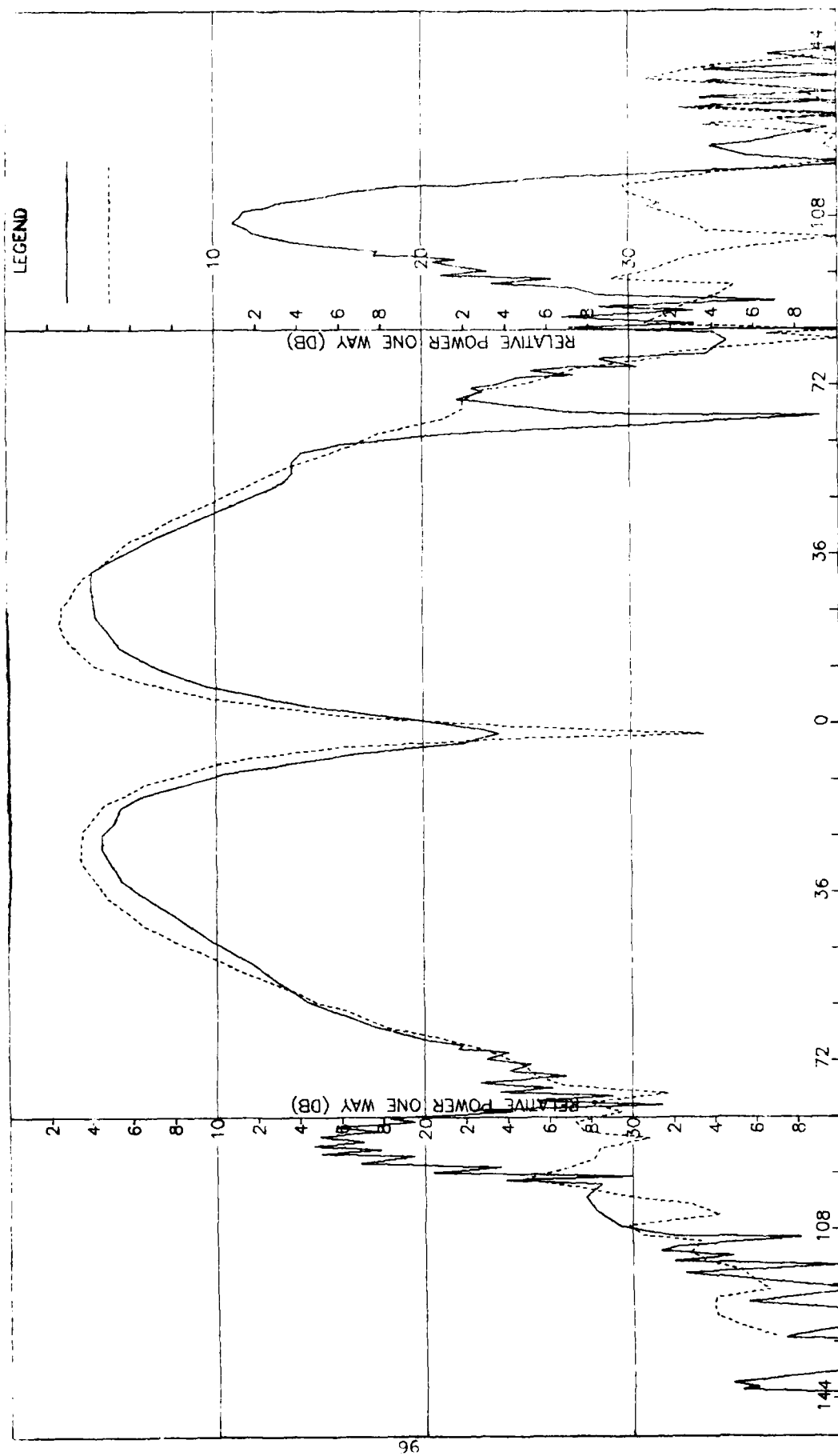


Figure E-9. Pattern of Small Array: E-Plane, Elev. Difference,  $\alpha$ -Component, Medium ( $F=1$ ) Radome

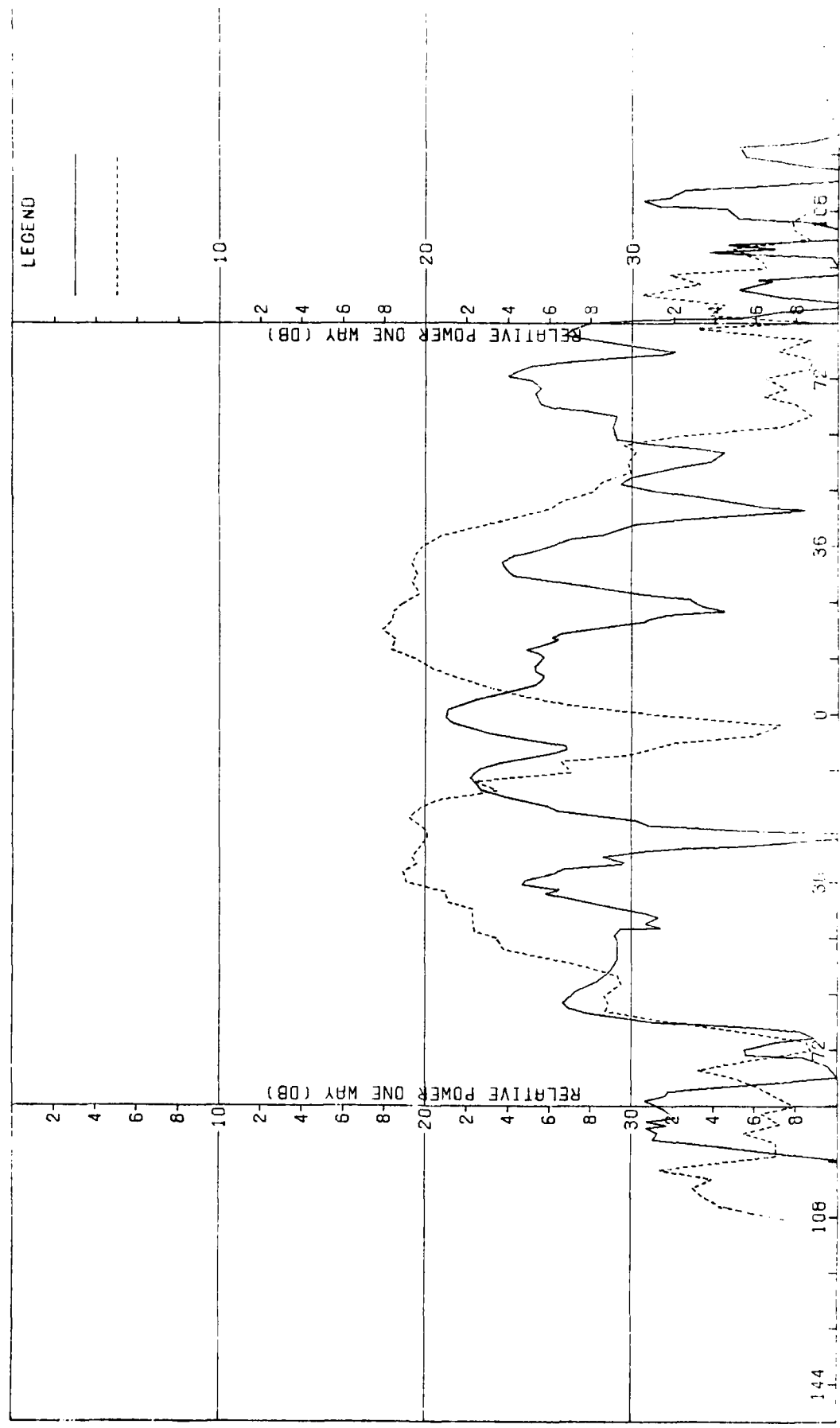


Figure E-10. Pattern of Small Array: E-Plane, Elev. Difference,  $\phi$ -Component, Medium ( $F=1$ ) Radome

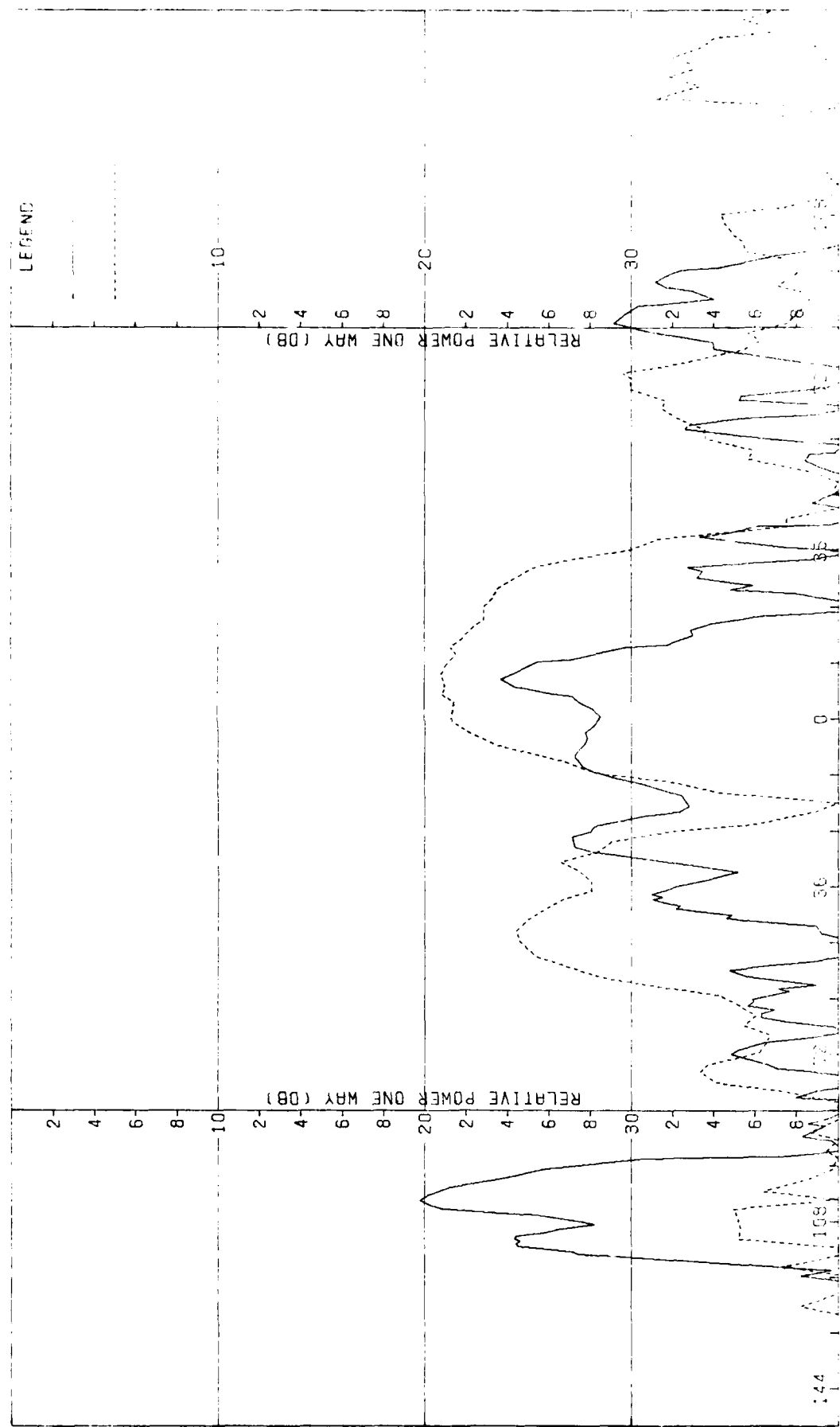


Figure E-11. Pattern of Small Array: H-Plane, Elev. Difference,  $\frac{1}{4}$ -Component, Medium ( $F=1$ ) Radome

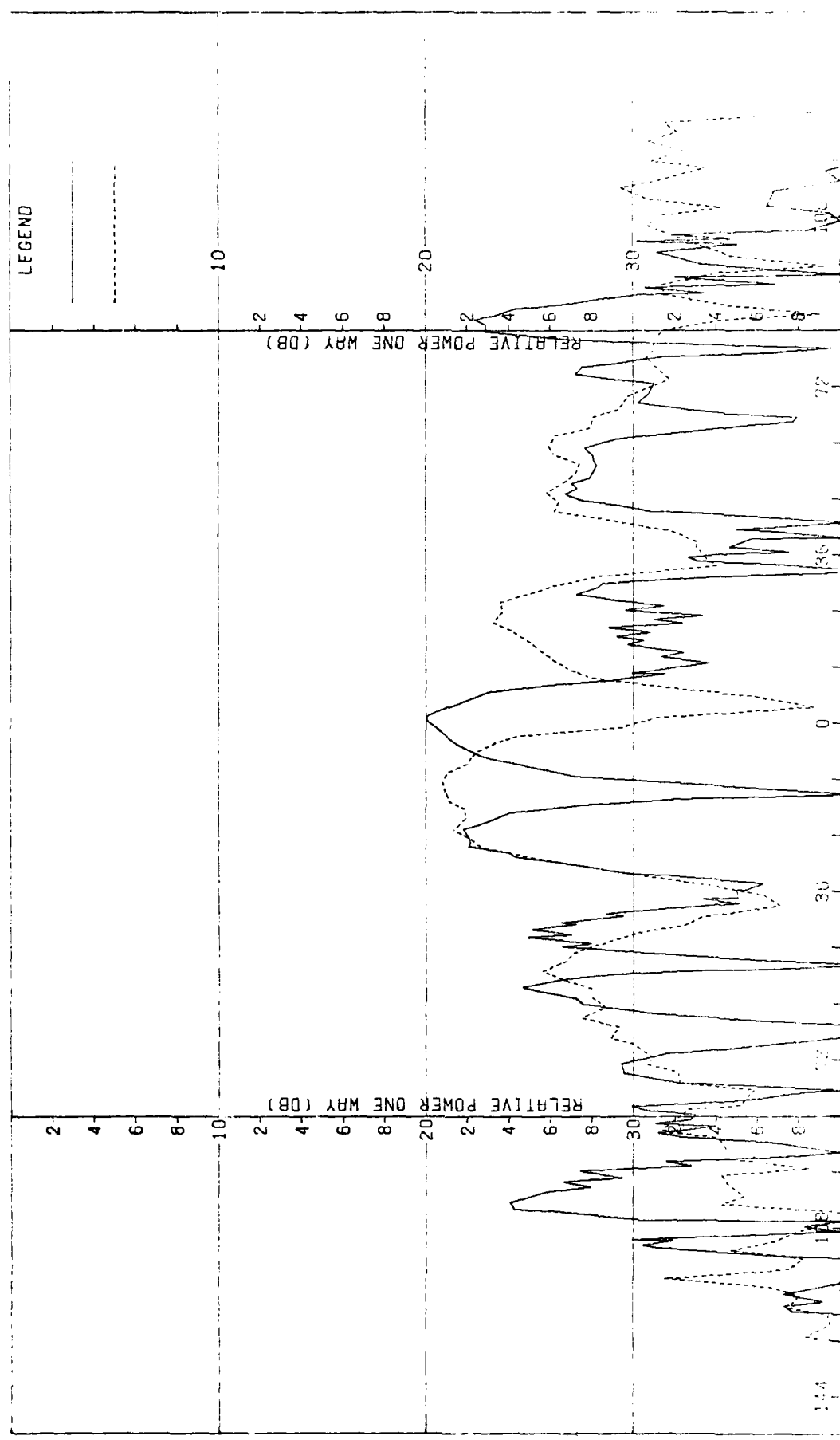


Figure E-12. Patterns of Small Array: H-plane, Elevation, Difference,  $\alpha$ -Component, Medium ( $F=1$ ) Radome

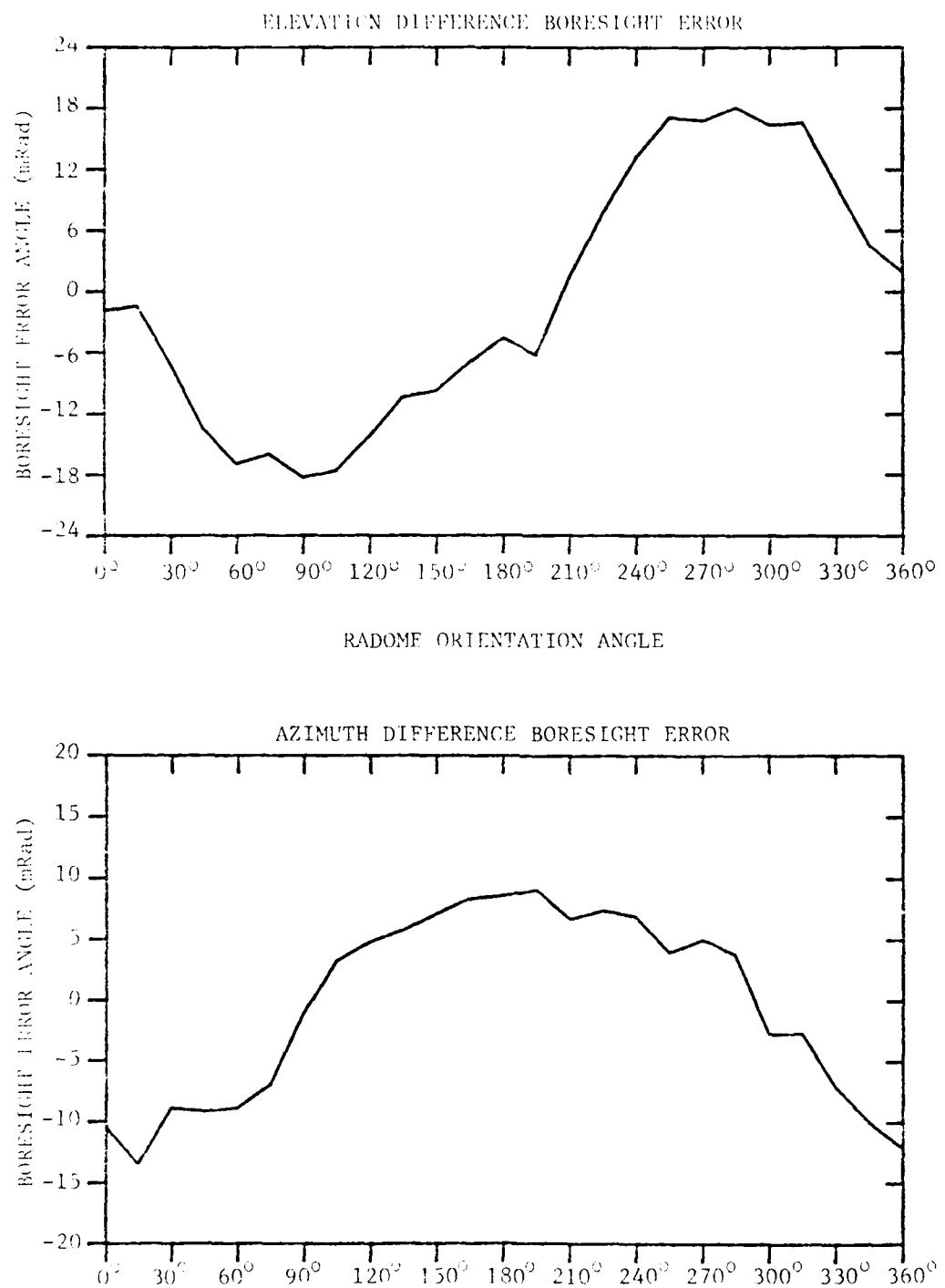


FIGURE E-13. BORESIGHT ERRORS OF SMALL ARRAY AND MEDIUM ( $F=1$ ) RADOME.

APPENDIX F

Antenna Patterns of Small Array with Large (F=1) Radome

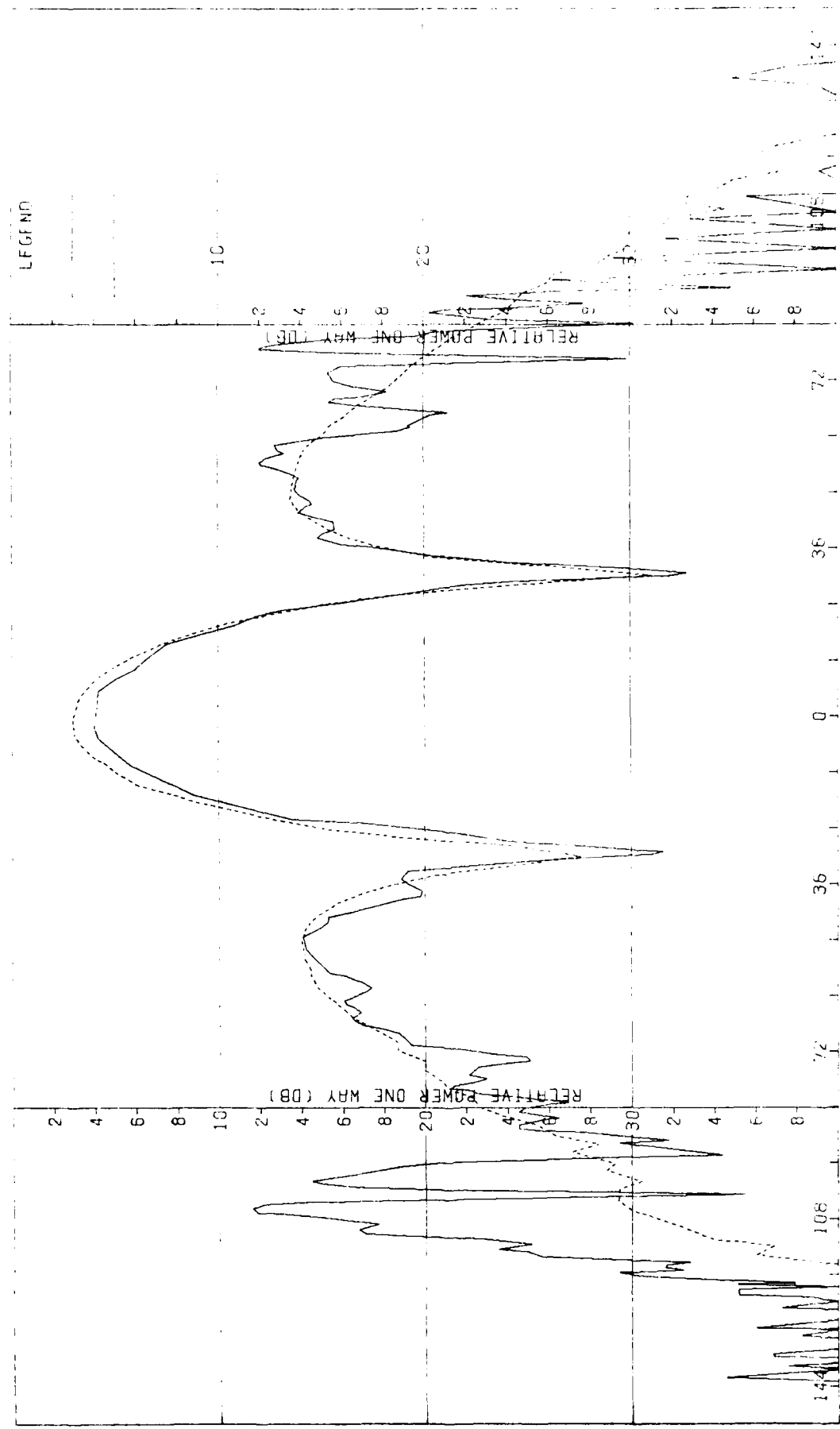


Figure F-1. Pattern of Small Array: H-Plane, Sum,  $\phi$ -Component, Large ( $F=1$ ) Radome

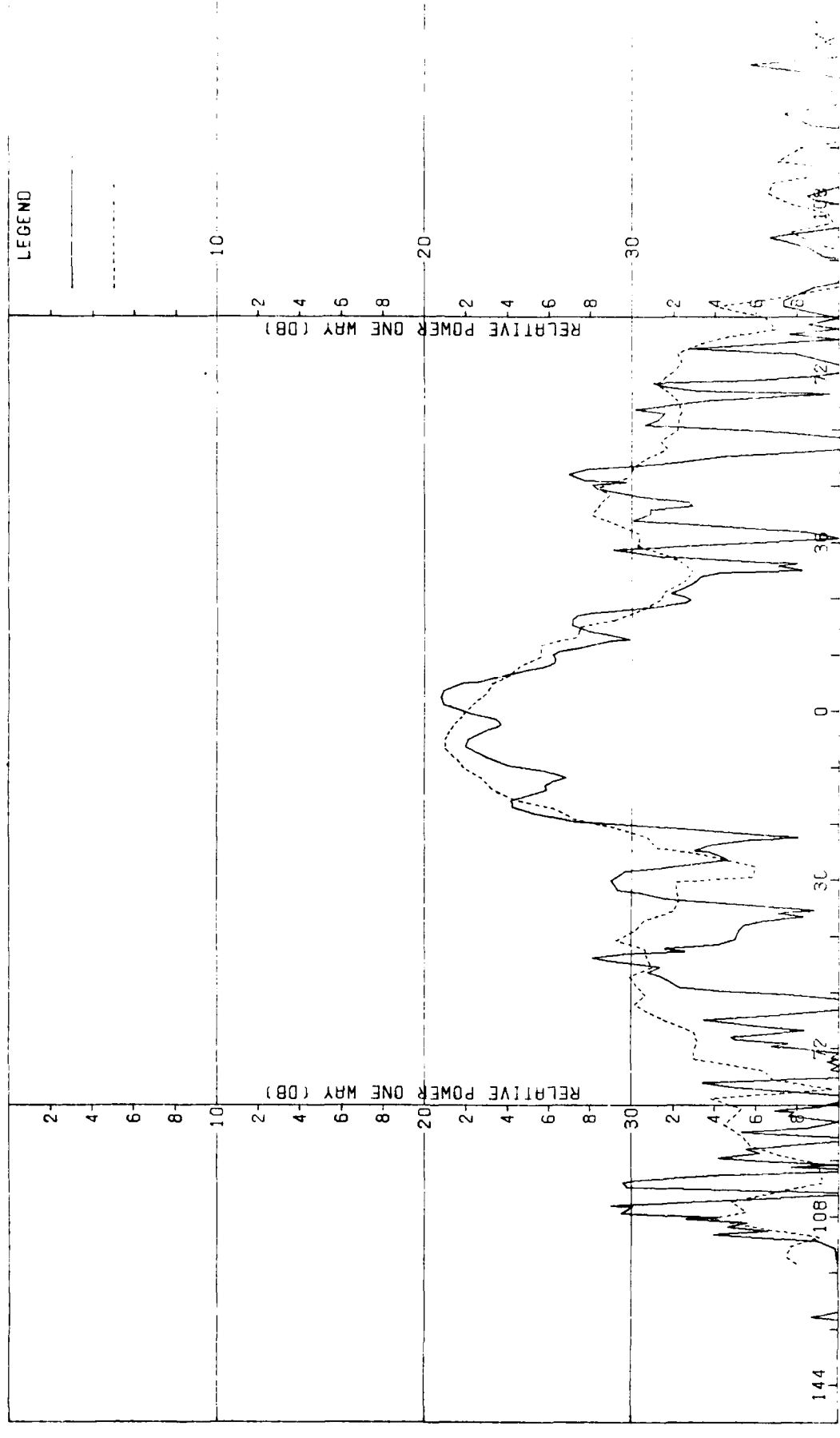


Figure F-2. Pattern of Small Array: H-Plane, Sum, A-Component, Large (F=1) Radome

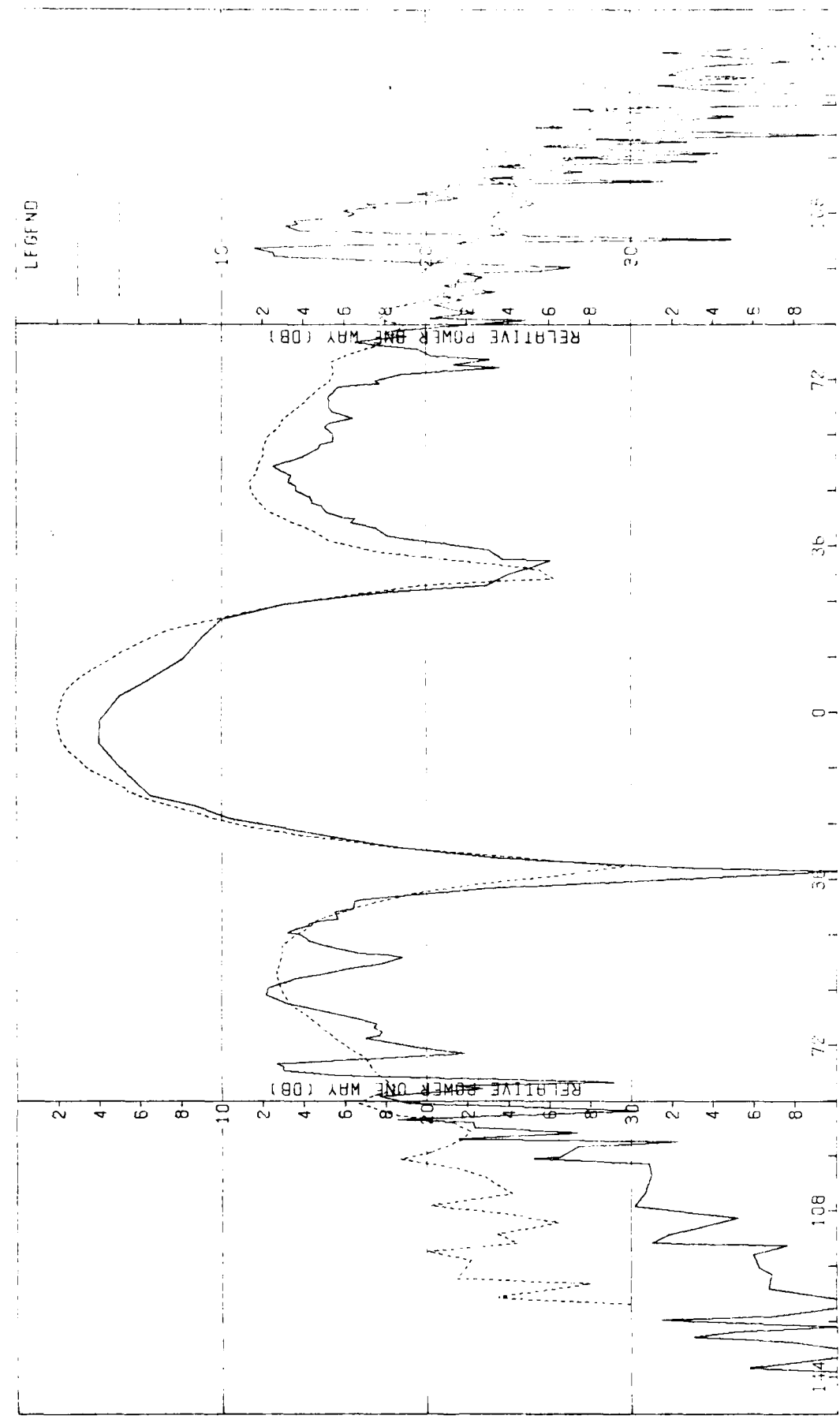


Figure E-3. Pattern of Small Array: E-Plane, Sum, Component, Large (F=1) Radome

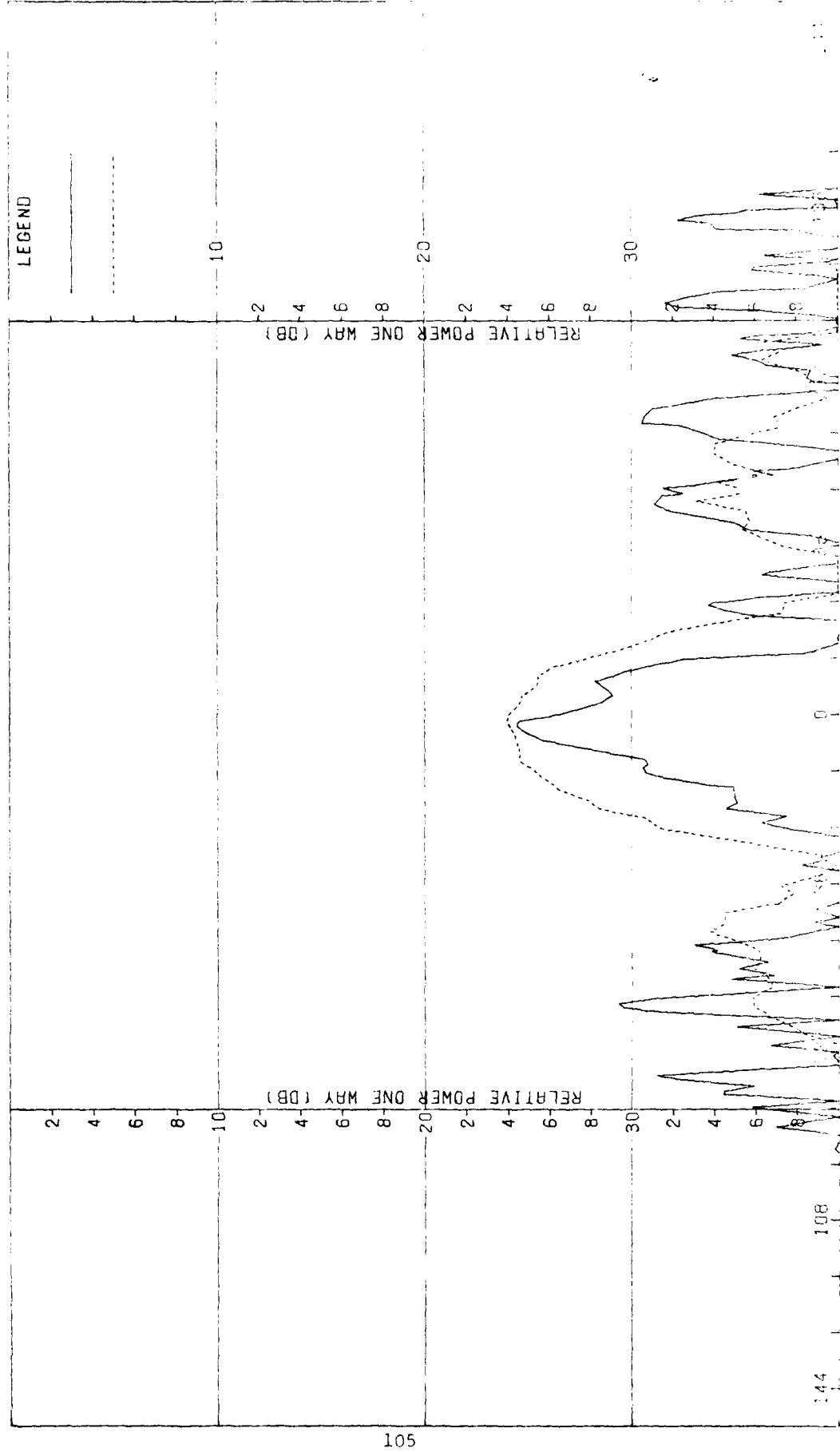


Figure F-4. Pattern of Small Array: E-plane, Sum,  $\phi$ -Component, Large (F=1) Radome

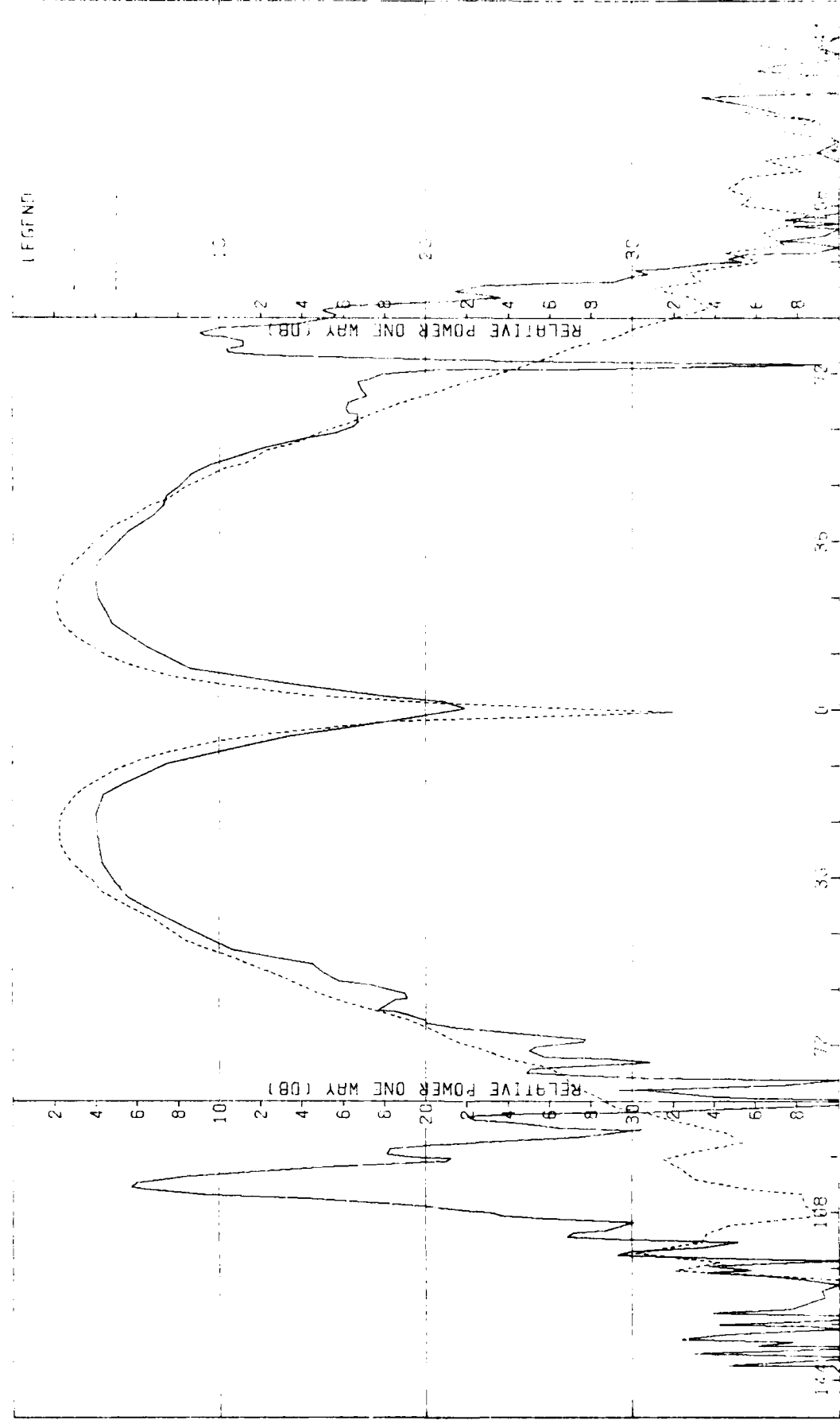


Figure F-5. Pattern of Small Array: H-plane, Azimuth Diff.,  $\phi$ -Component, Large ( $F=1$ ) Radome

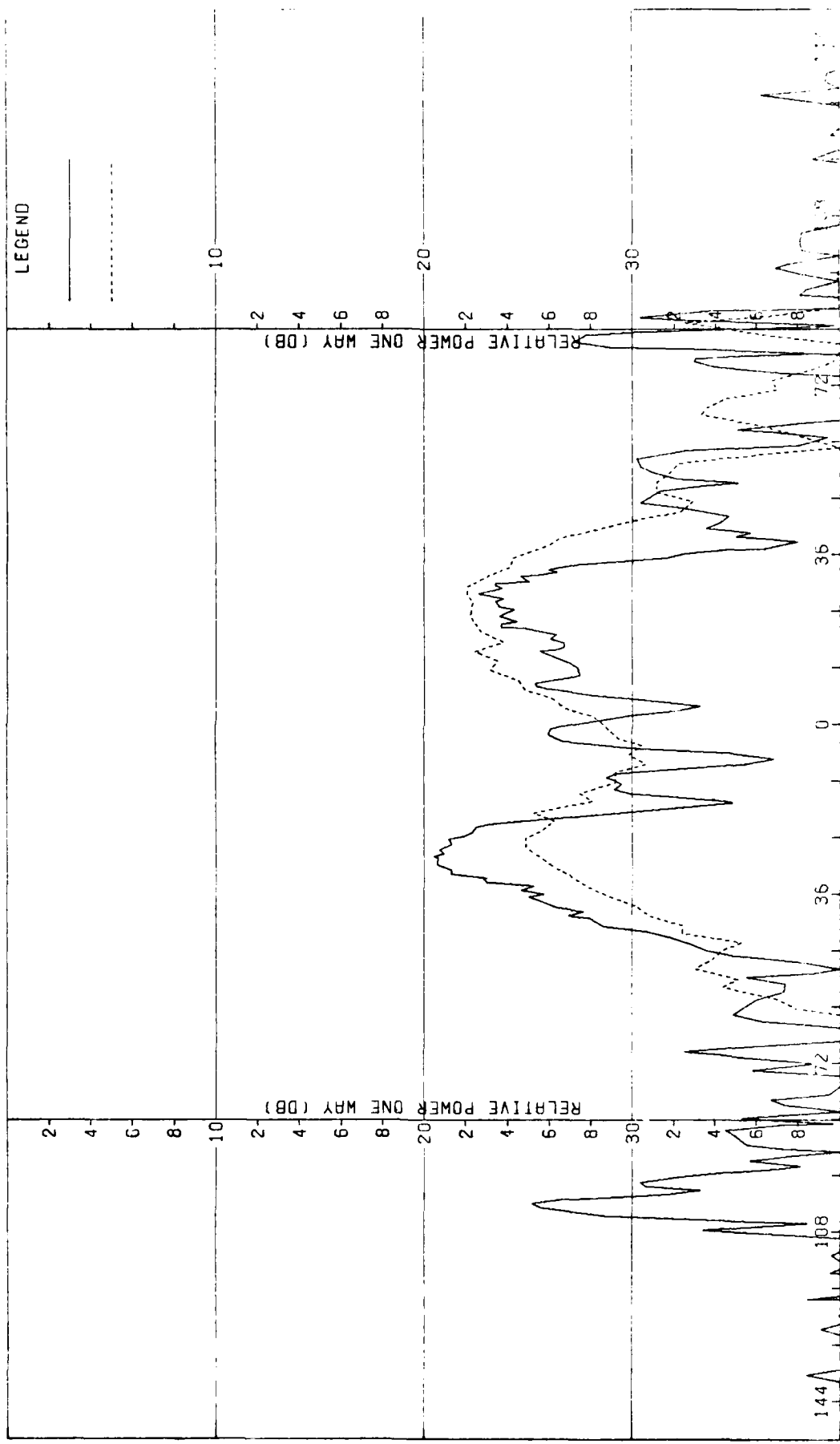


Figure F-6. Pattern of Small Array: H-Plane, Azimuth Diff.,  $\lambda$ -Component, Large ( $F=1$ ) Radome

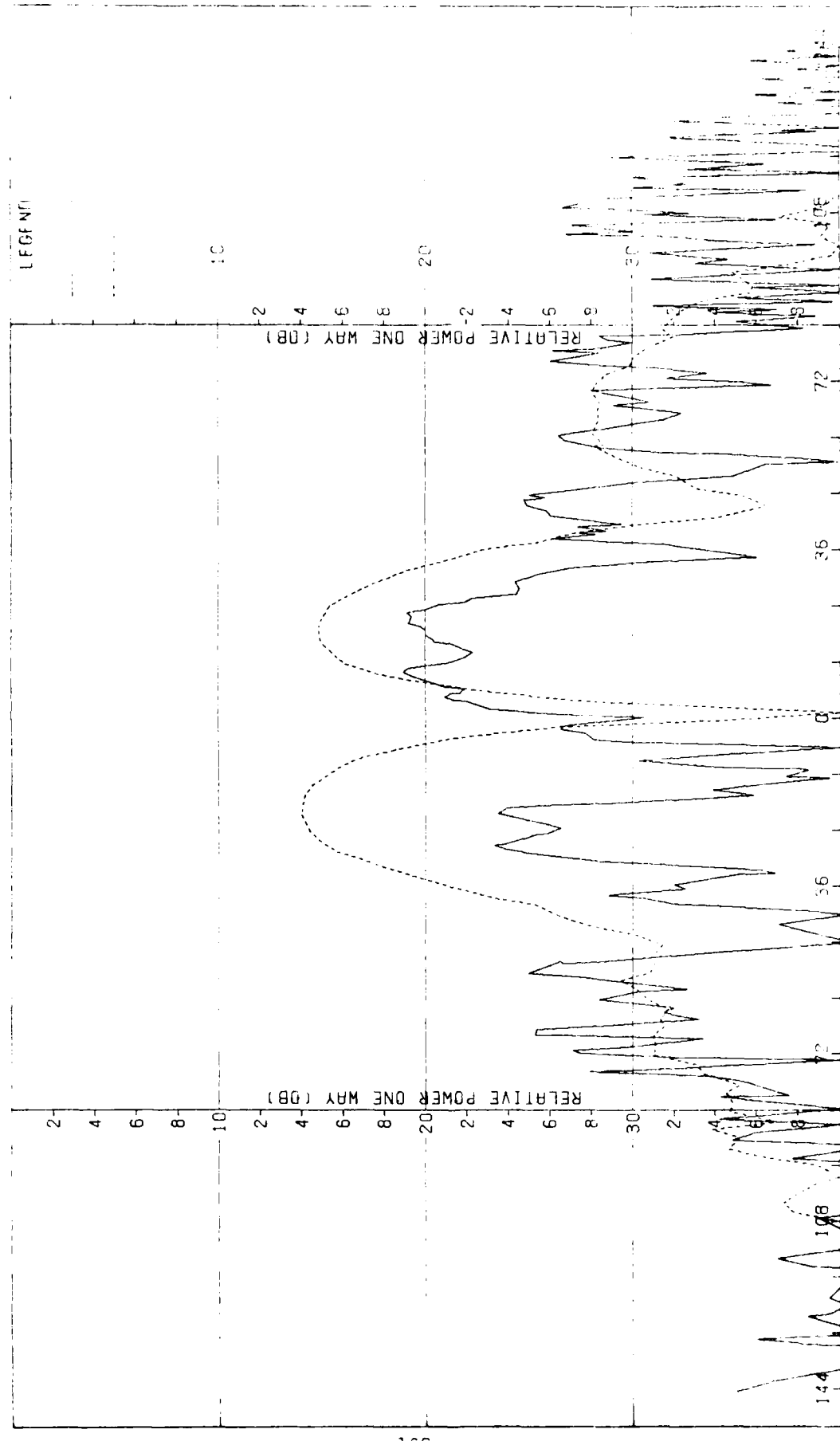


Figure F-7. Pattern of Small Array: E-Plane, Azimuth Diff.,  $\theta$ -Component, Large (F=1) Radome

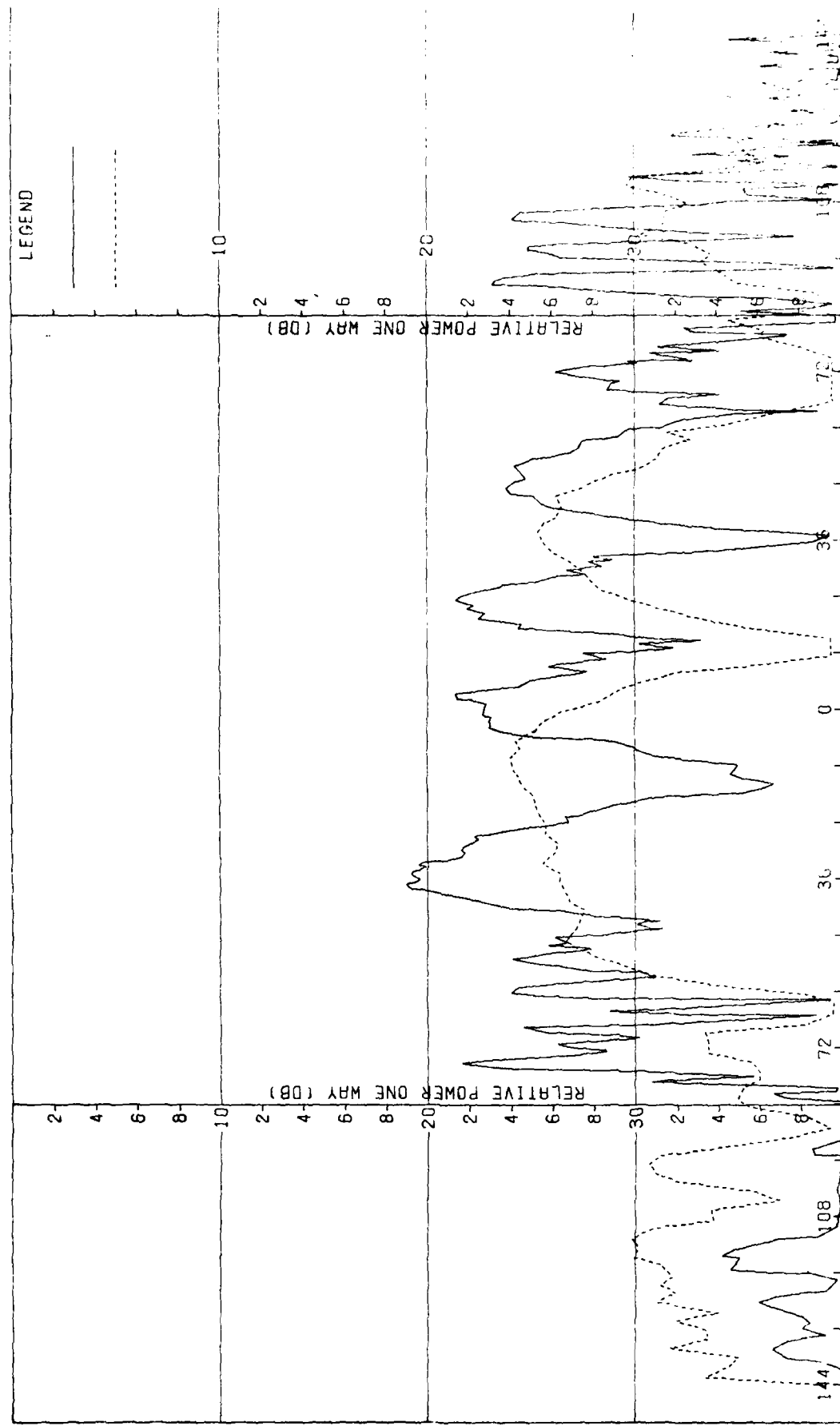


Figure F-8. Pattern of Small Array: E-Plane, Azimuth Diff.,  $\phi$ -Component, Large ( $F=1$ ) Radome

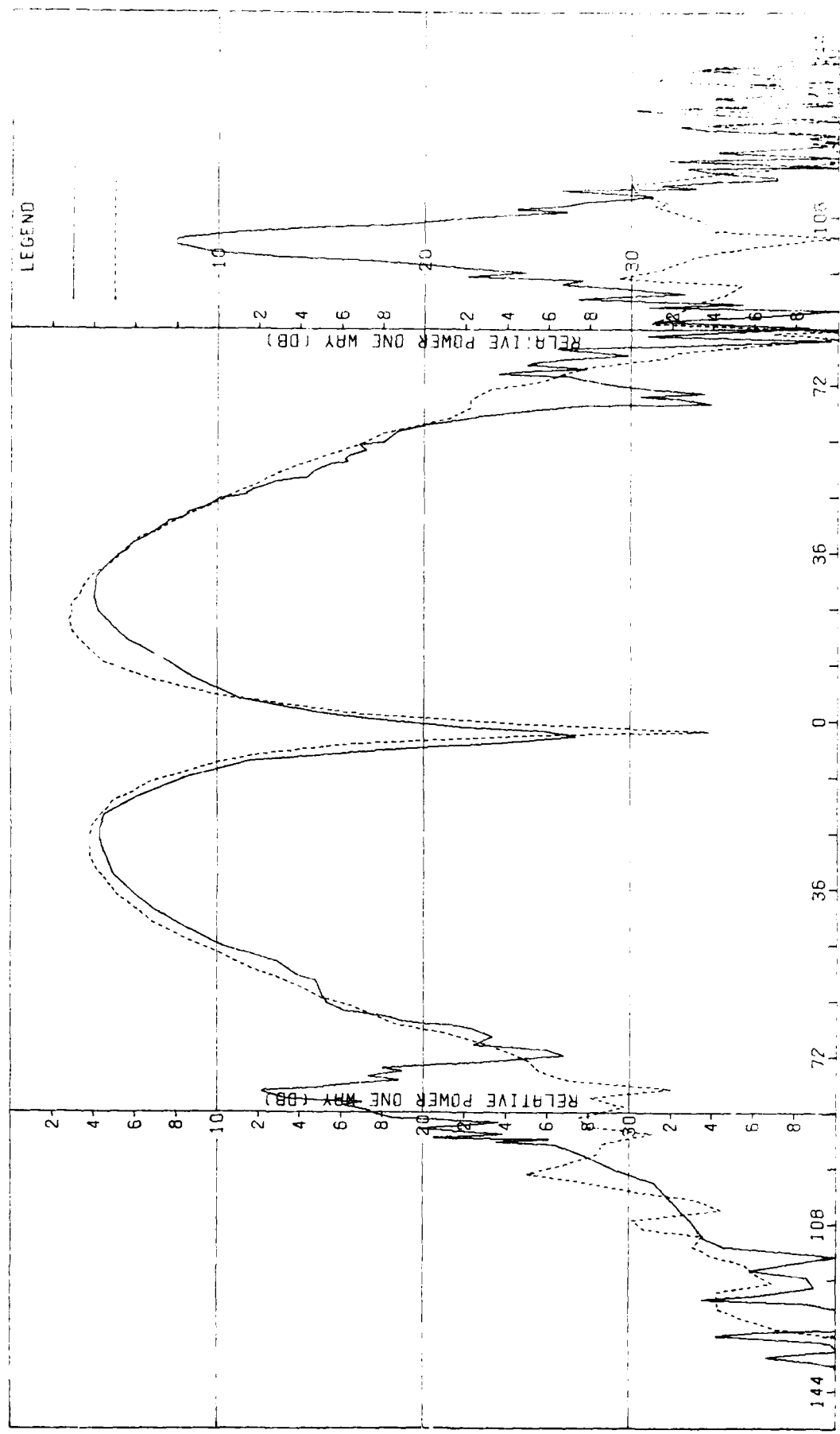


Figure F-9. Pattern of Small Array: E-Plane, Elev. Difference,  $c$ -Component, Large ( $F=1$ ) Radome

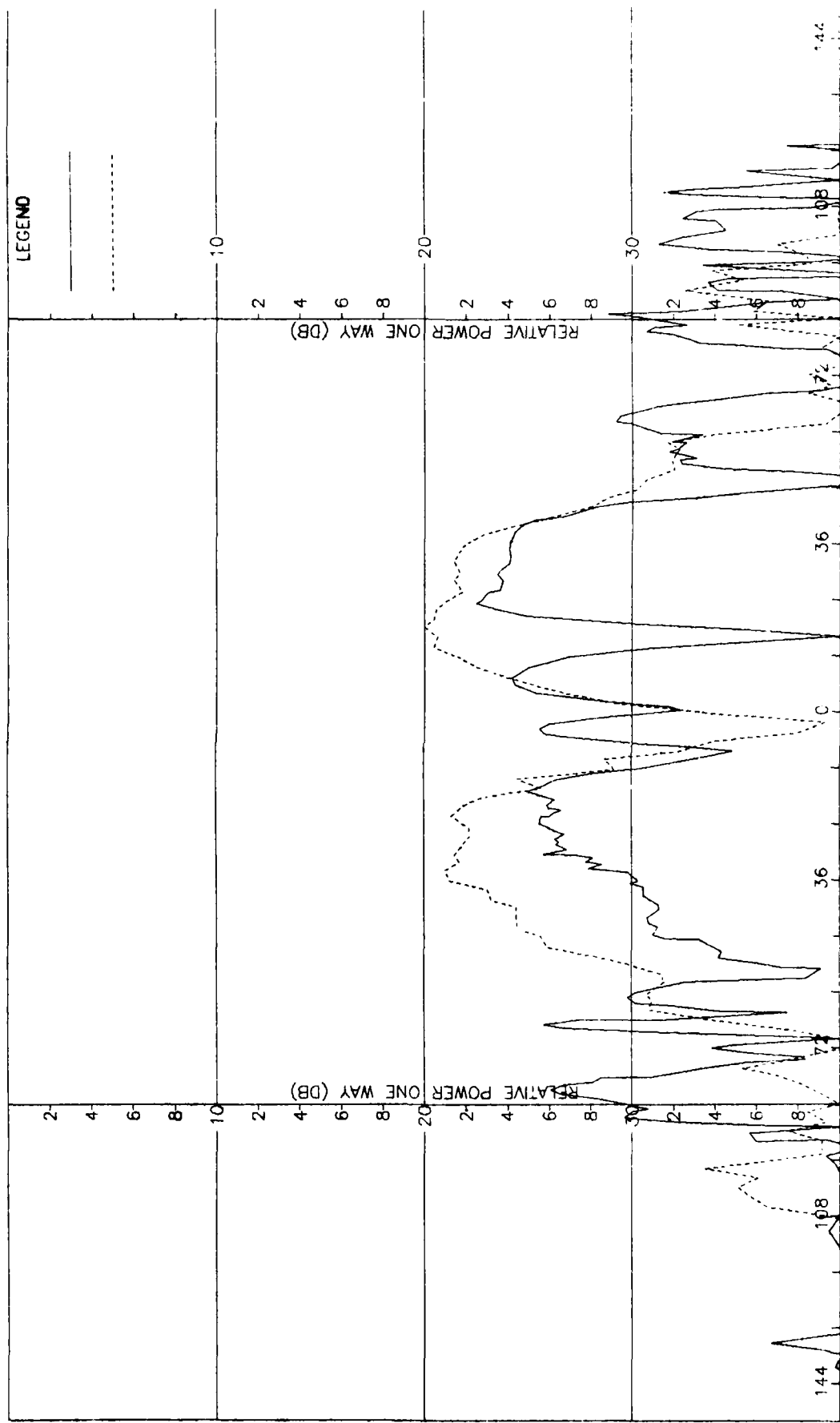


Figure F-10. Pattern of Small Array: E-Plane, Elev. Difference,  $\phi$ -Component, Large ( $F=1$ ) Radome

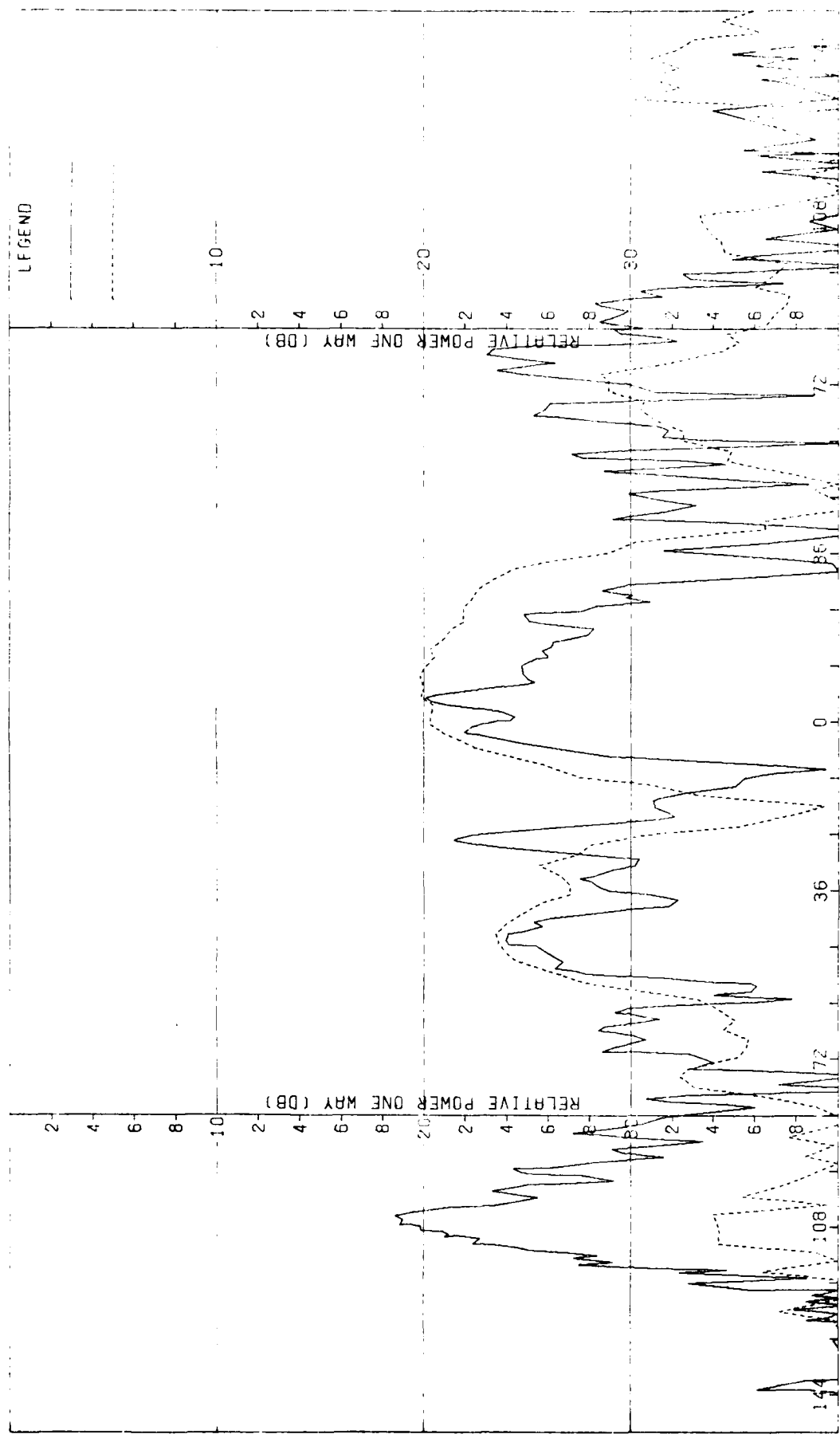


Figure F-11. Pattern of Small Array: H-Plane, Elevation Diff.,  $\phi$ -Component, Large (F=1) Radome

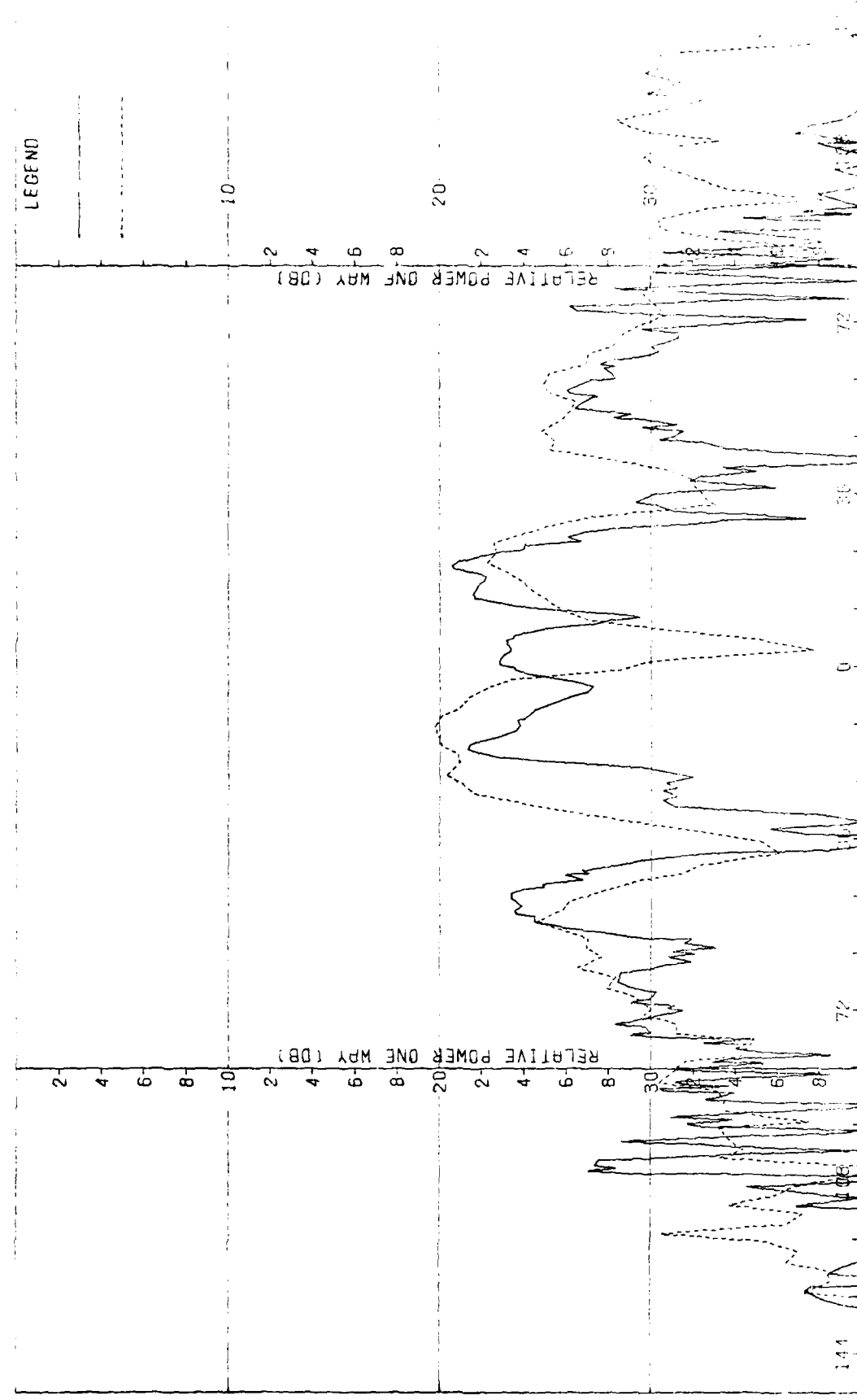


Figure F-12. Pattern of Small Array: H-Plane, Elev. Difference, z-component, Large ( $F=1$ ) Radiome

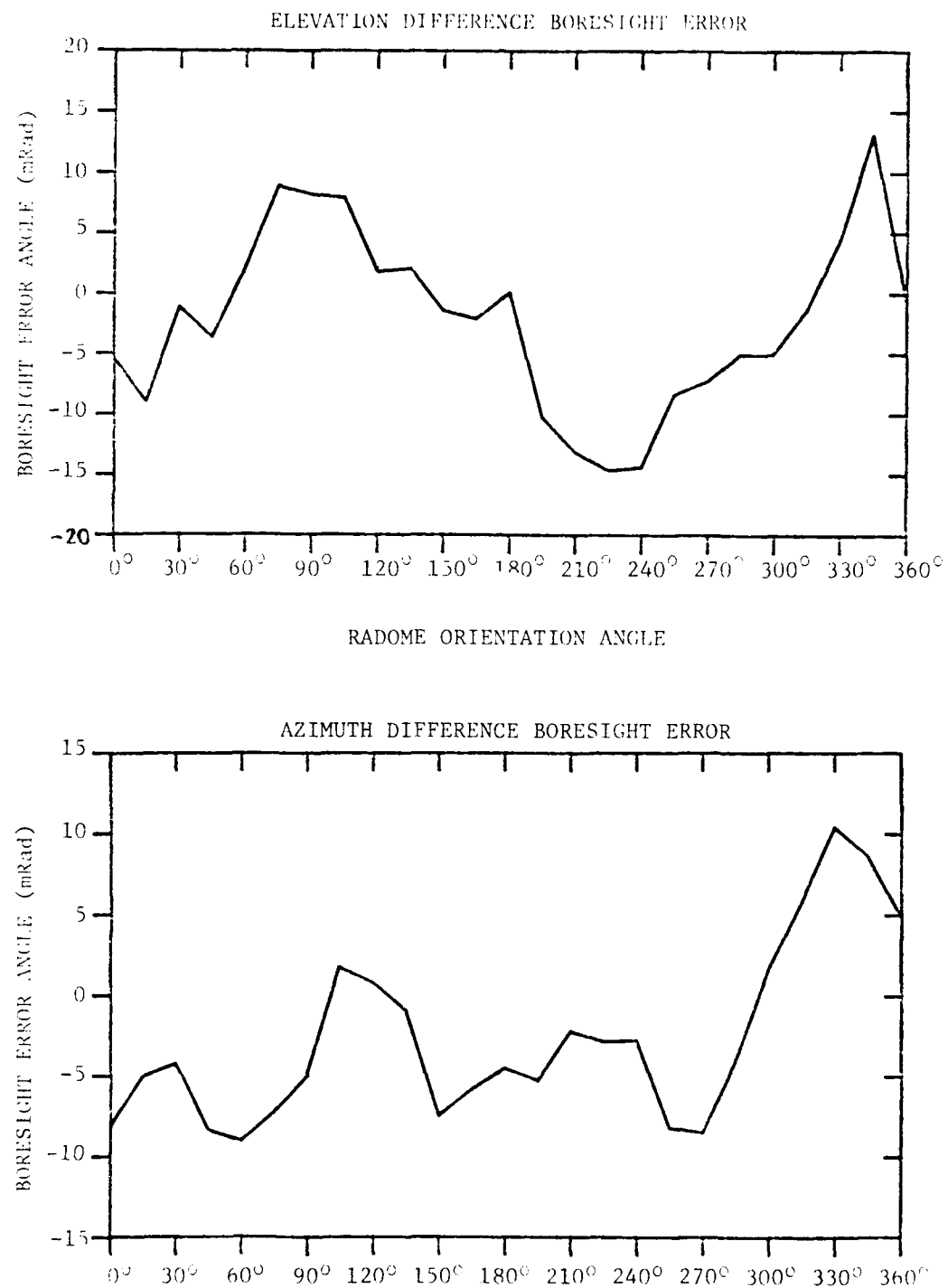


FIGURE F-13. BORESIGHT ERRORS OF SMALL ARRAY AND LARGE RADOME.

APPENDIX G

Antenna Patterns of Medium Array with Medium ( $F=1$ ) Radome

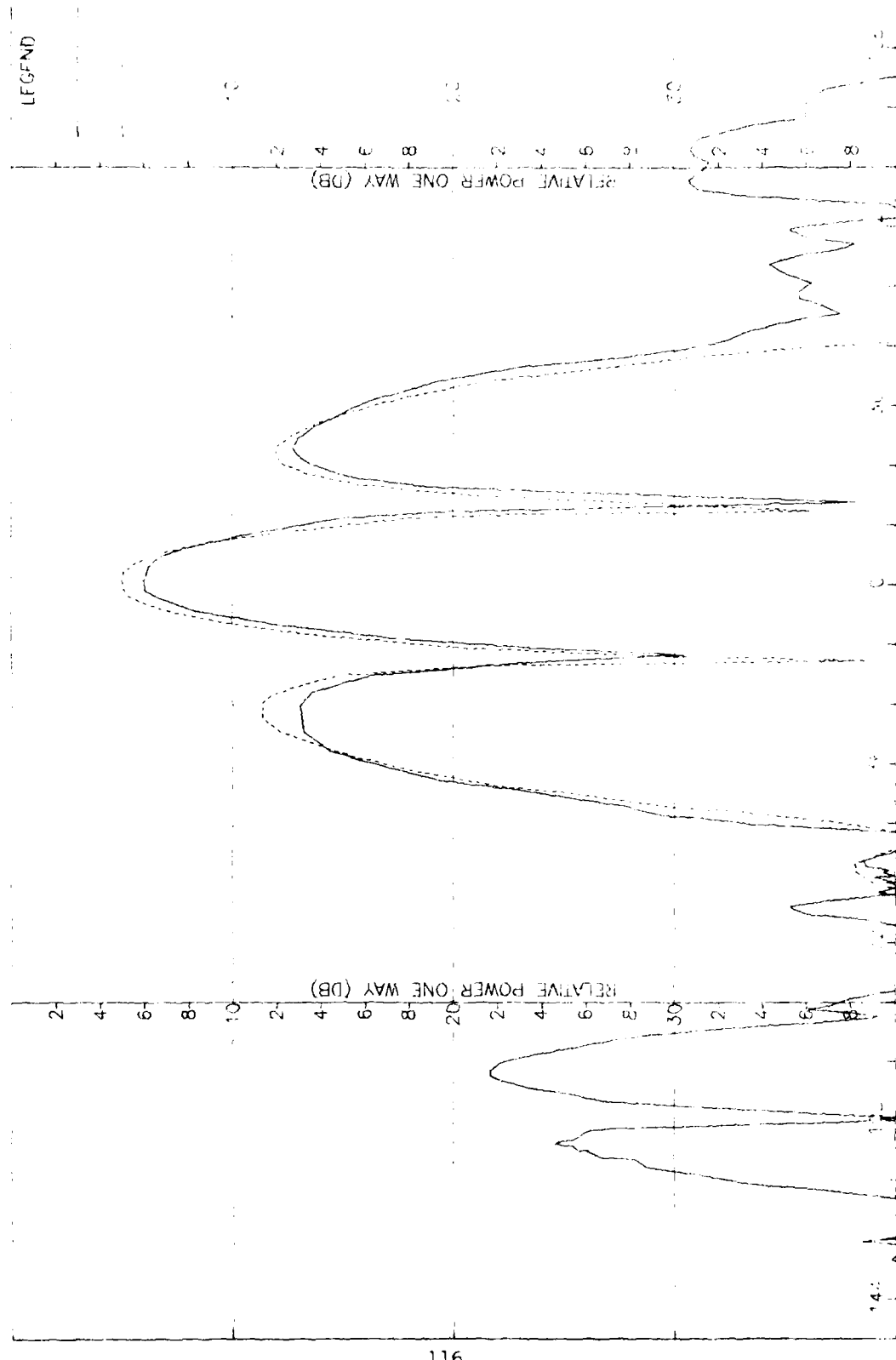


Figure G-1. Pattern of Medium Array: H-Plane, Sum,  $\psi$ -Component, Medium ( $F=1$ ) Radome

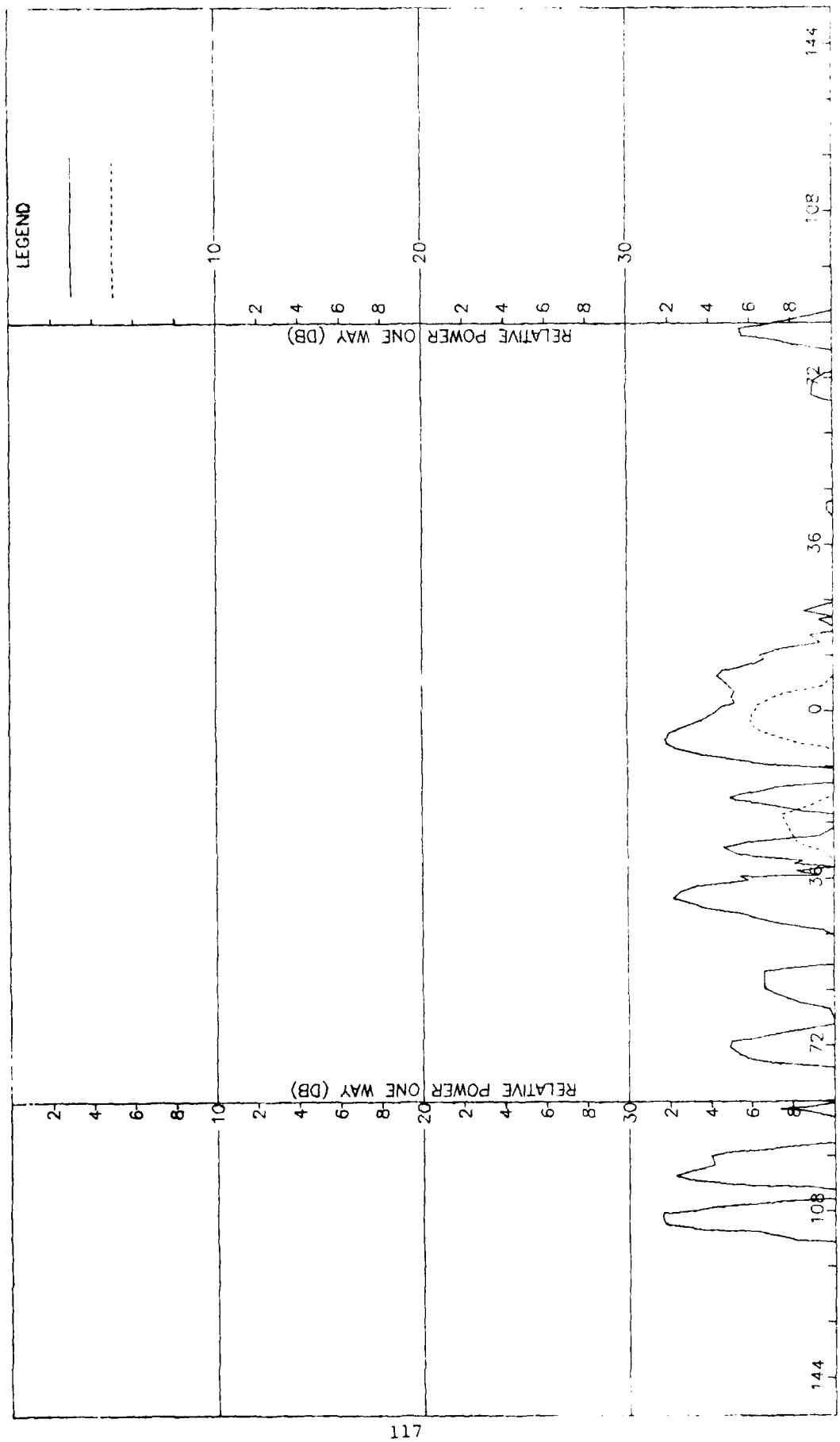


Figure 6-2. Pattern of Medium Array: H-Plane, Sum,  $\phi$ -Component, Medium ( $F=1$ ) Radome

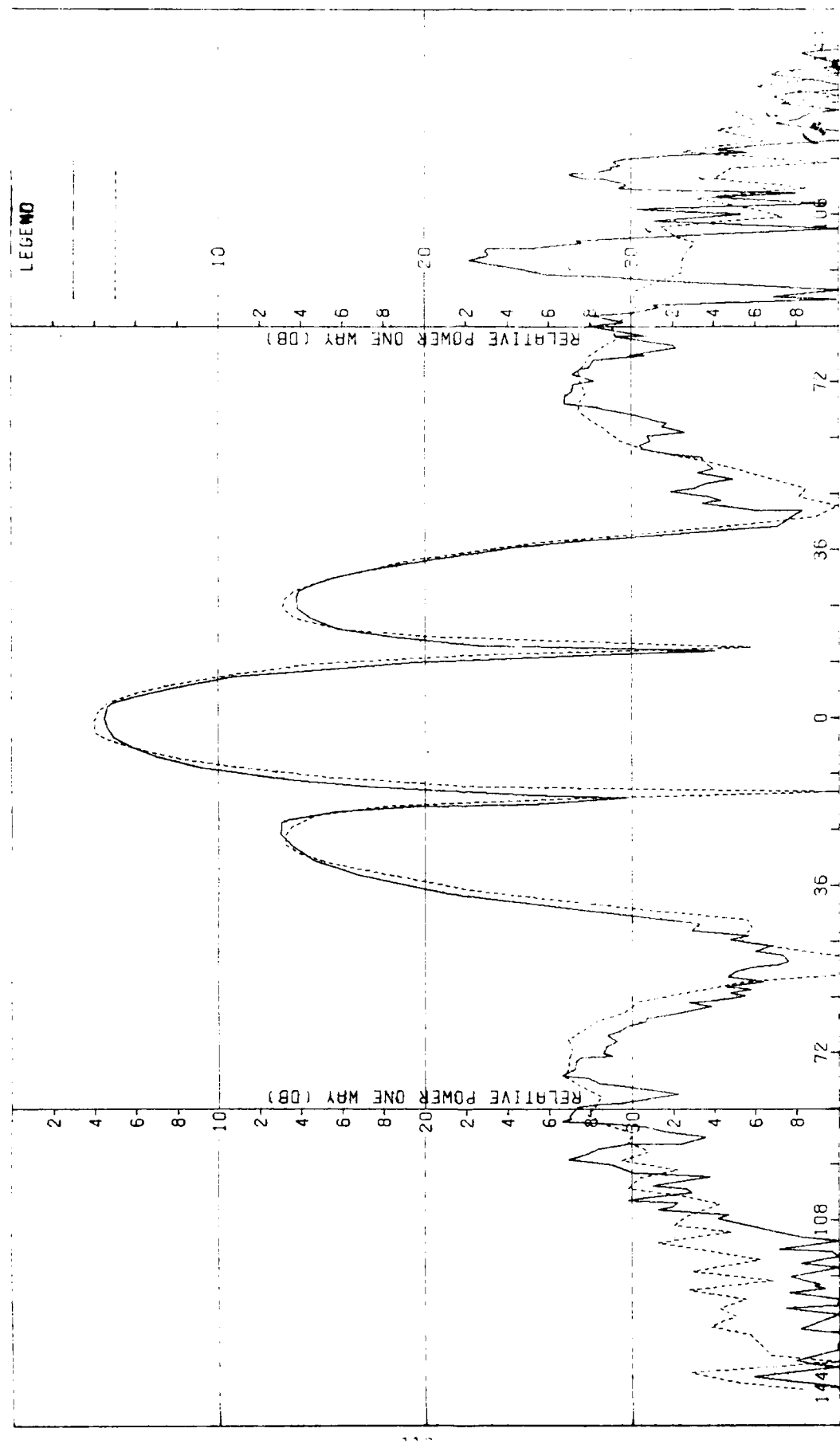


Figure G-3. Pattern of Medium Array: E-Plane, Sum,  $\alpha$ -Component, Medium ( $F=1$ ) Radome

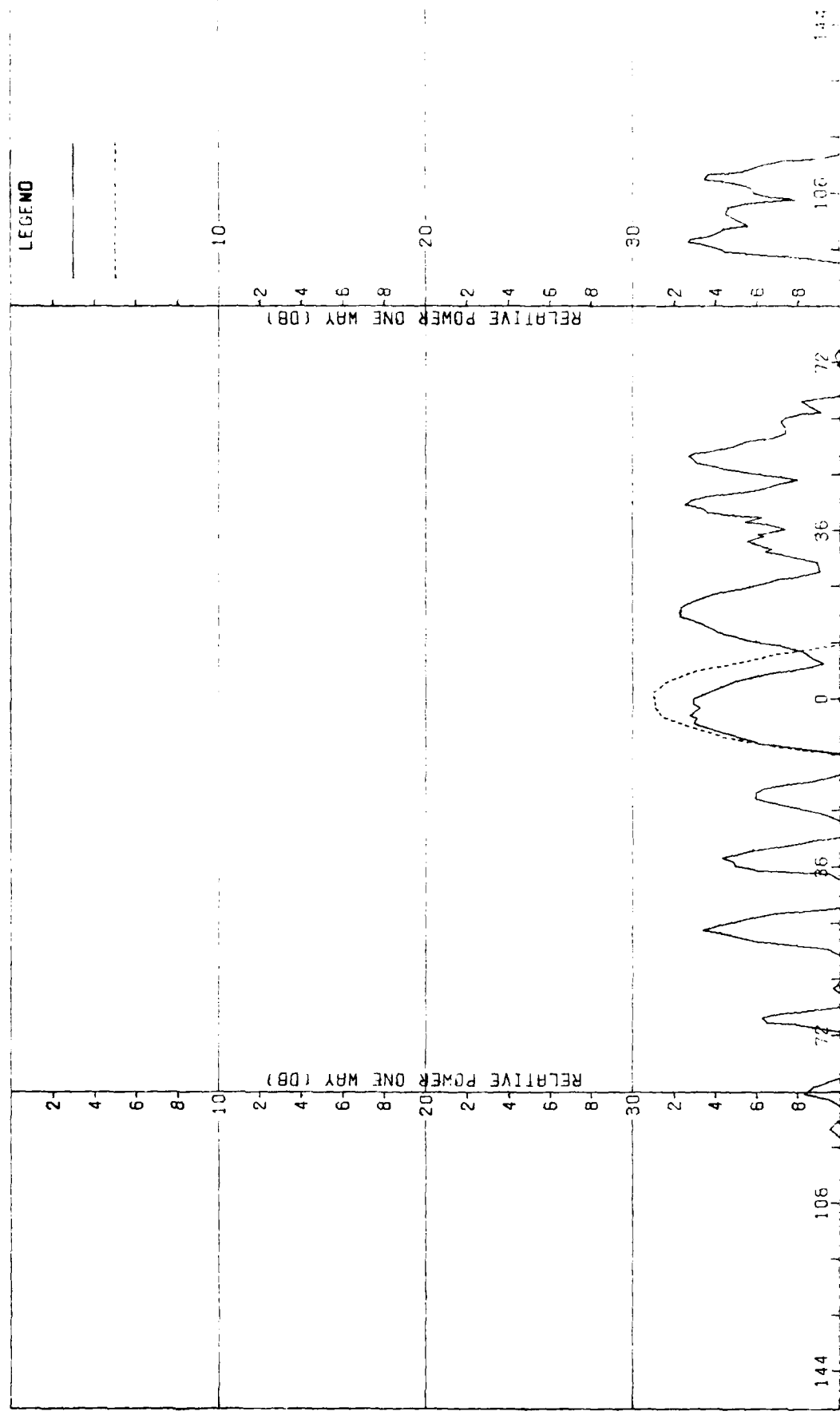


Figure 5-4. Pattern of Medium Array: E-Plane Sum, H-Plane Sum, Medium ( $F=1$ ) Radome

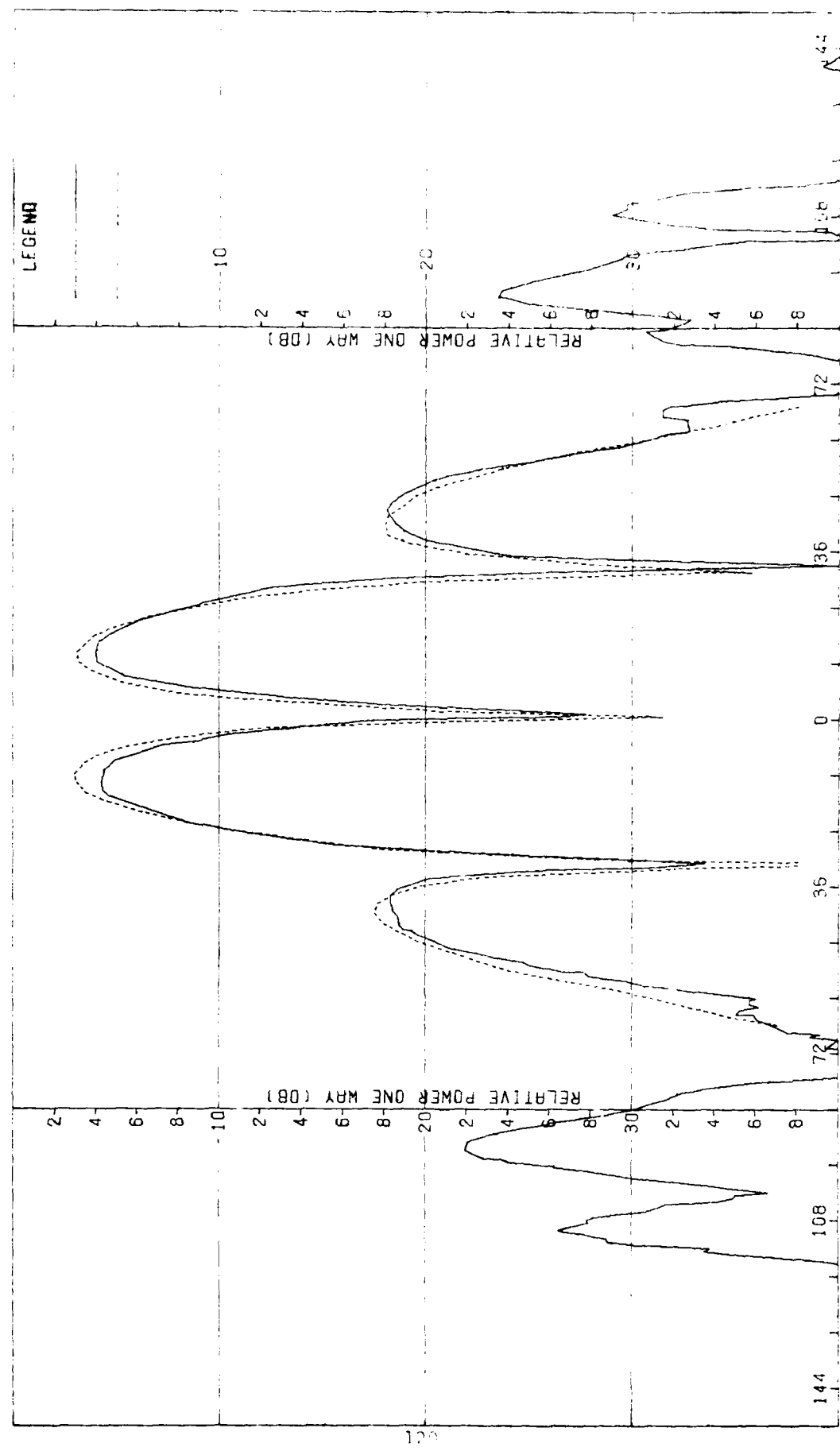


Figure G-5. Pattern of Medium Array: H-Plane, Azimuth Difference,  $\delta$ -Component, Medium ( $F=1$ ) Radiator

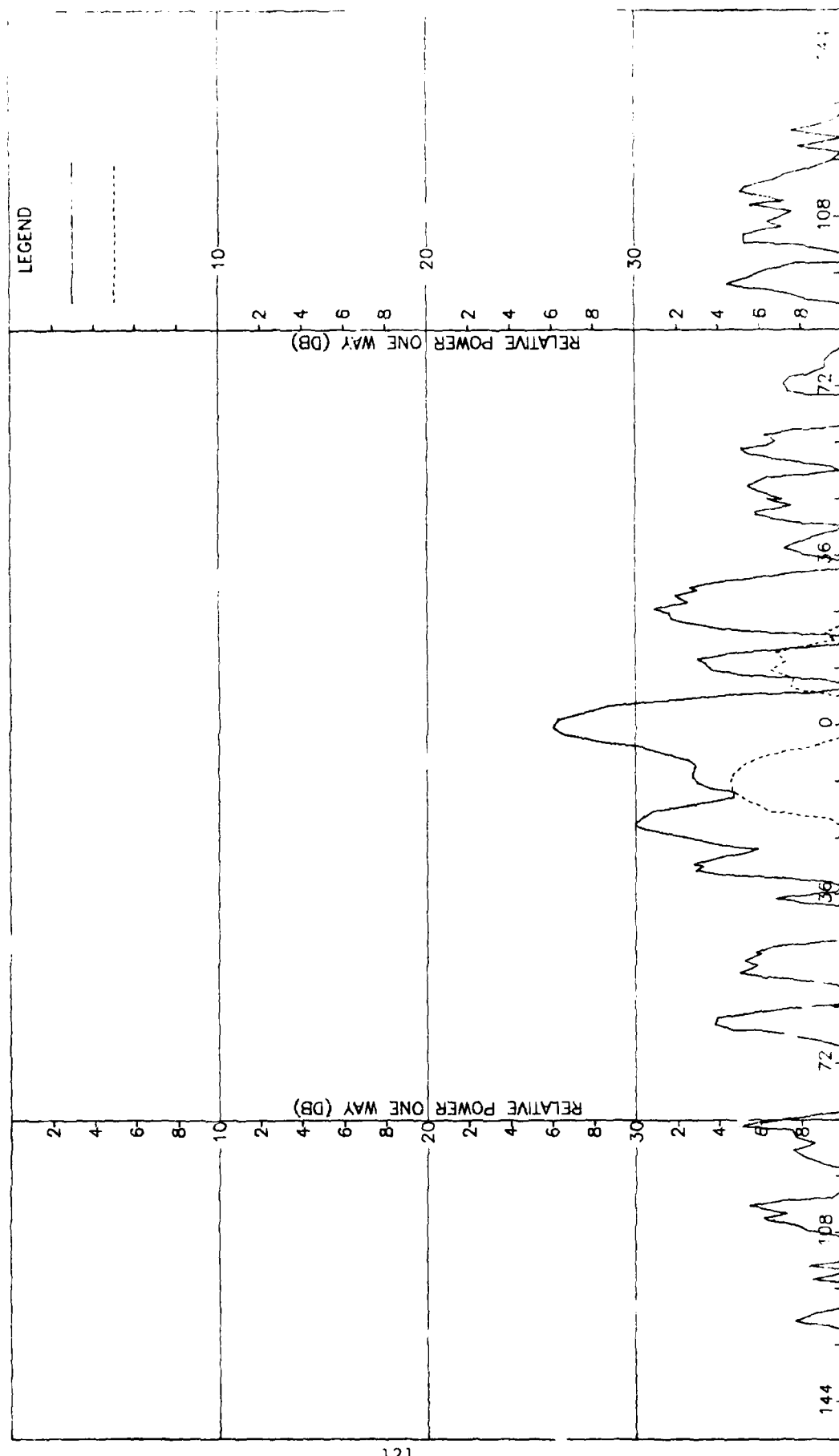


Figure 6-6. Pattern of Medium Array: H-Plane, Azimuth Difference, -Component, Medium (F=1) Radome

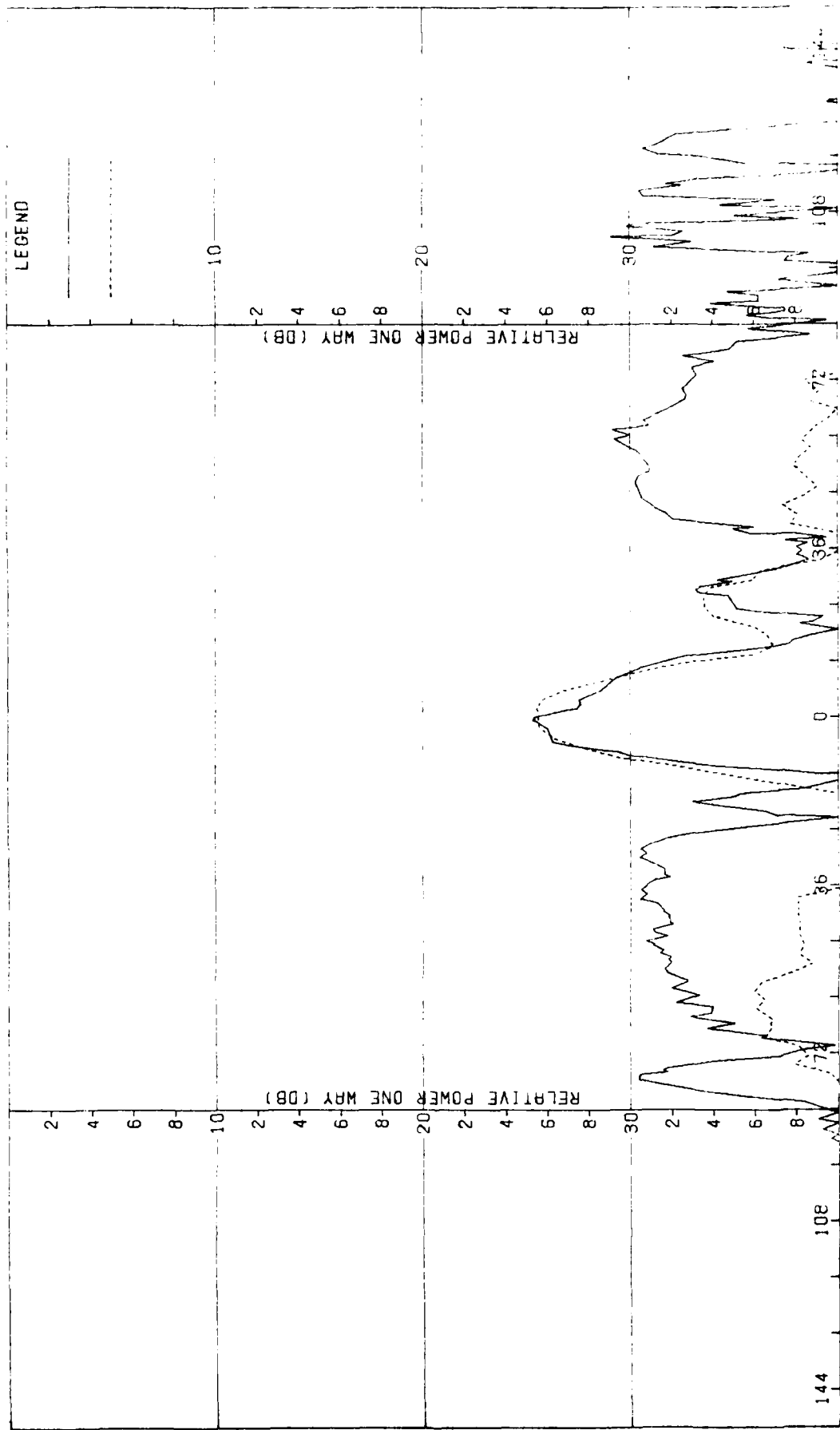


Figure 6-7. Pattern of Medium Array: E-Plane, Azimuth Difference,  $\theta$ -Component, Medium ( $F=1$ ) Radome

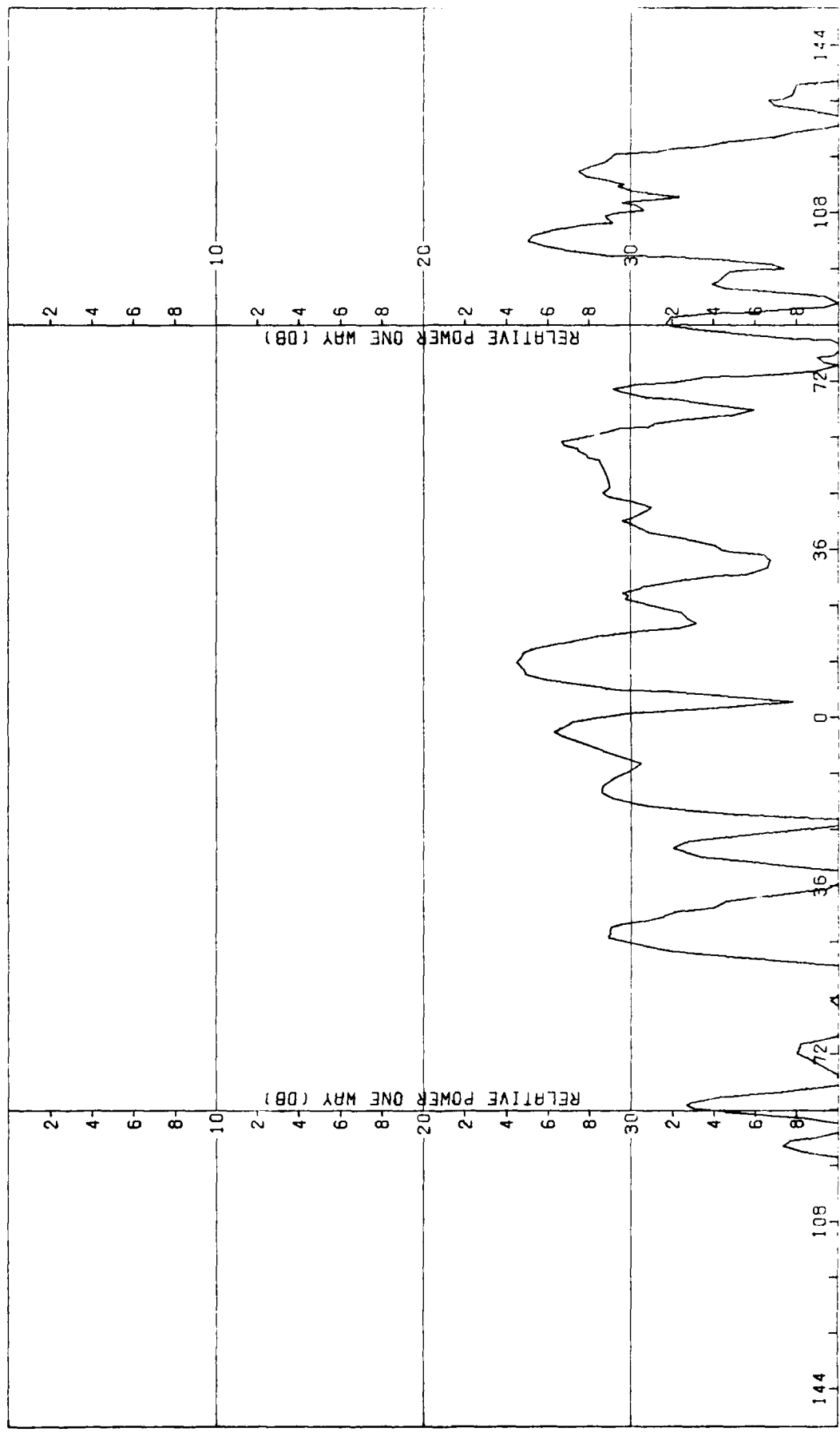


Figure G-8. Pattern of Medium Array: E-Plane, Azimuth Difference,  $\pm$ -Component, Medium ( $F=1$ ) Radome

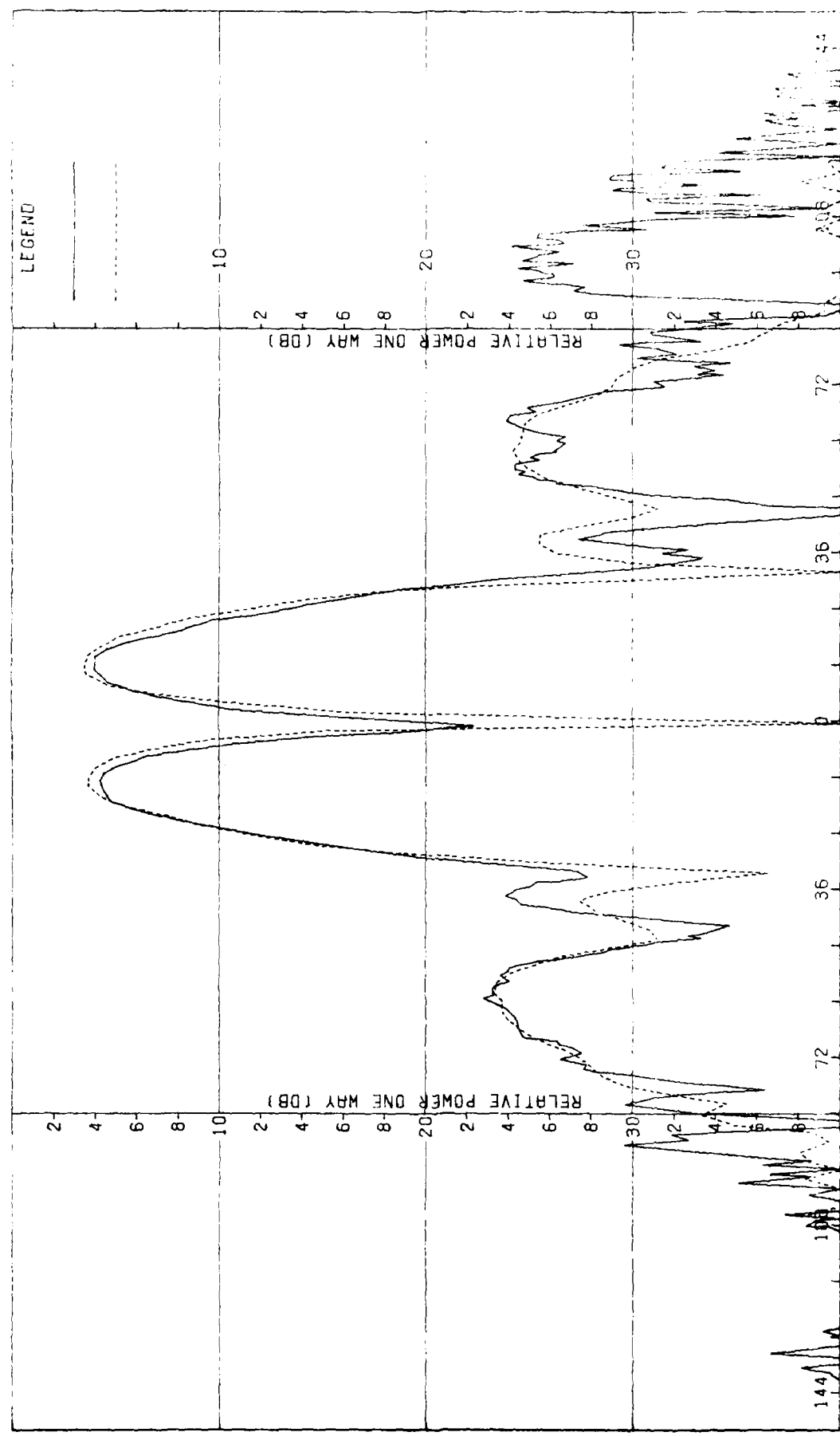
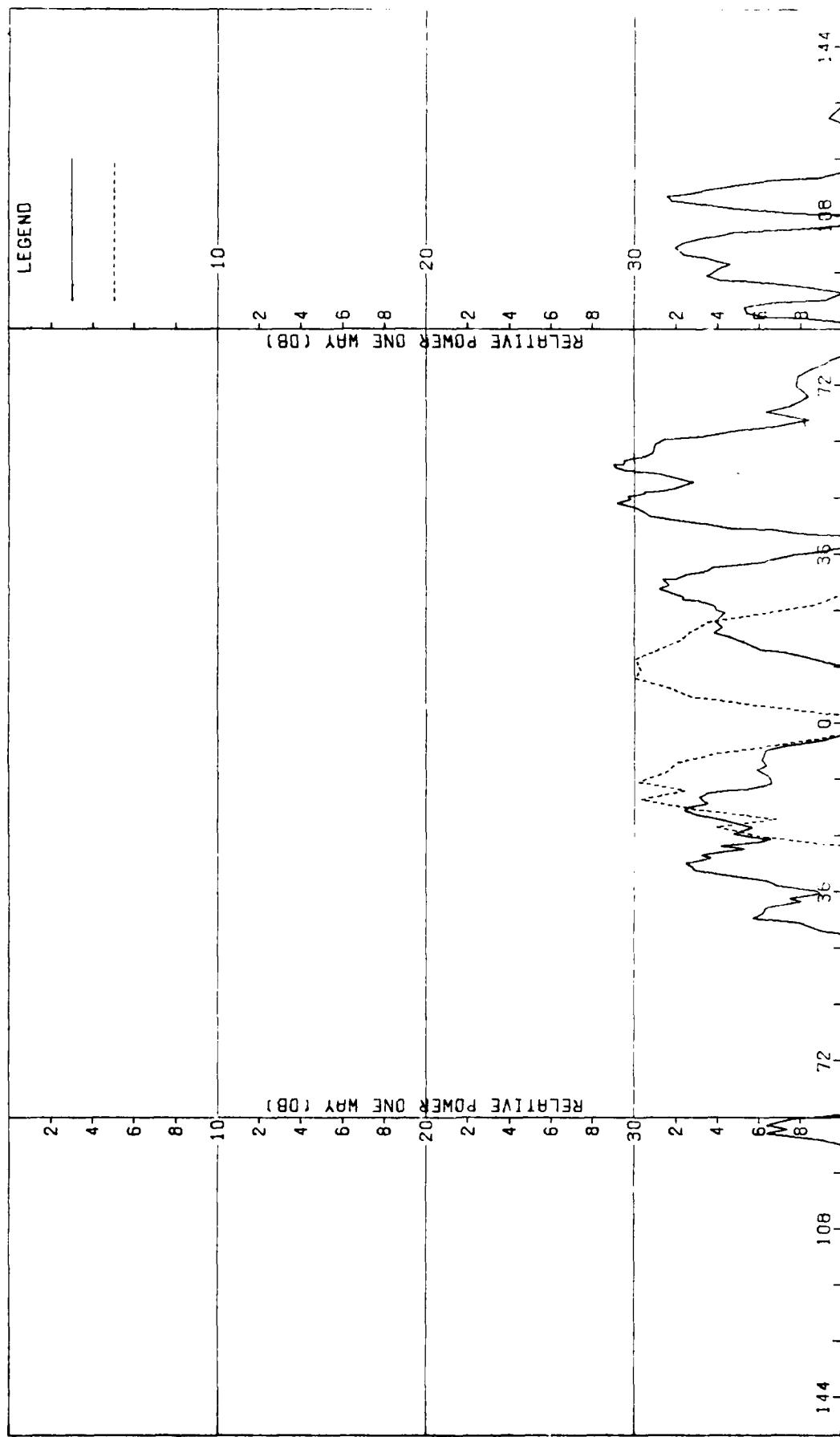


Figure 6-9. Pattern of Medium Array: E-Plane, Elevation Difference,  $\rho$ -Component, Medium (F=1) Radome



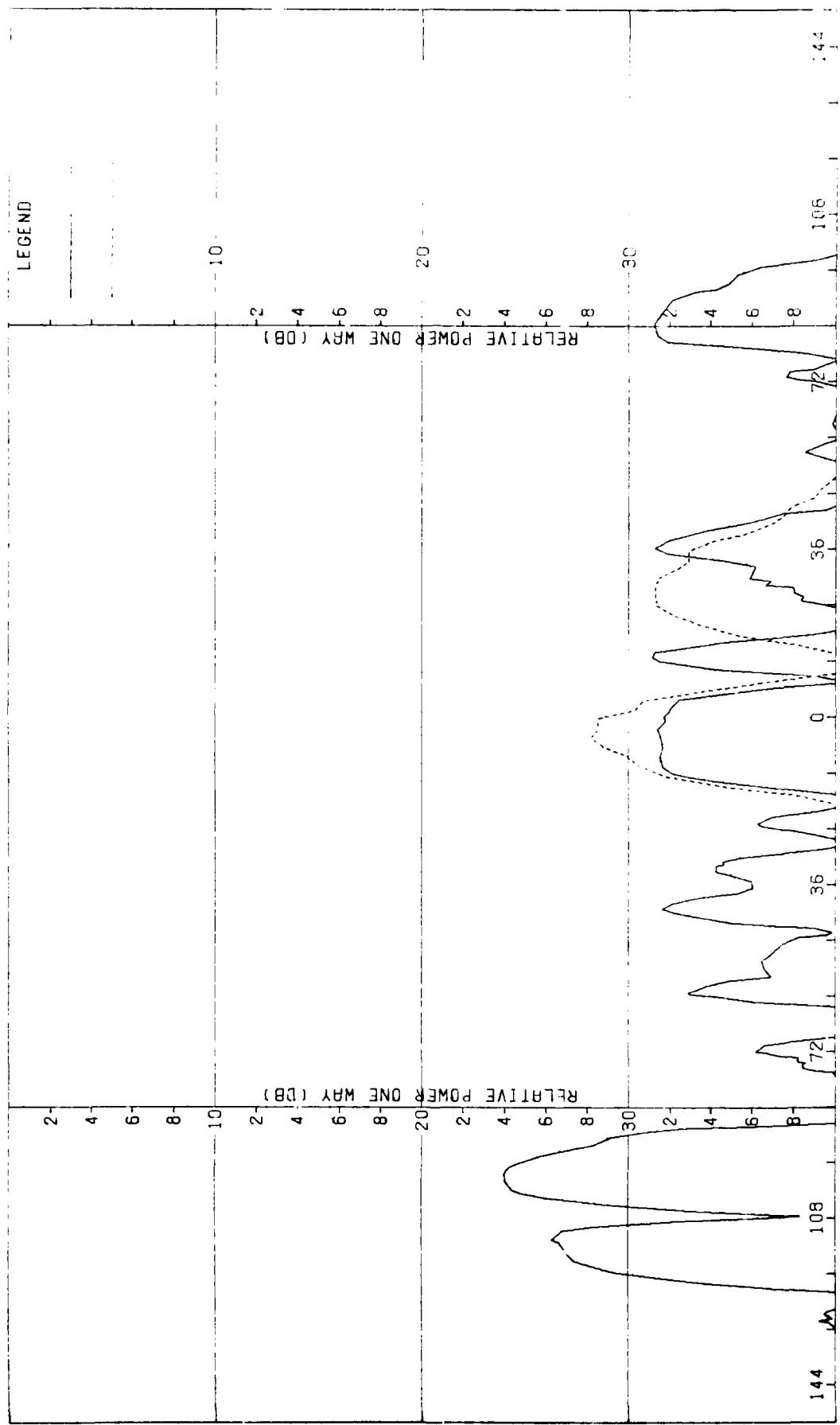


Figure G-11. Pattern of Medium Array: H-Plane, Elevation Difference,  $\lambda/2$ -Component, Medium ( $F=1$ ) Radome

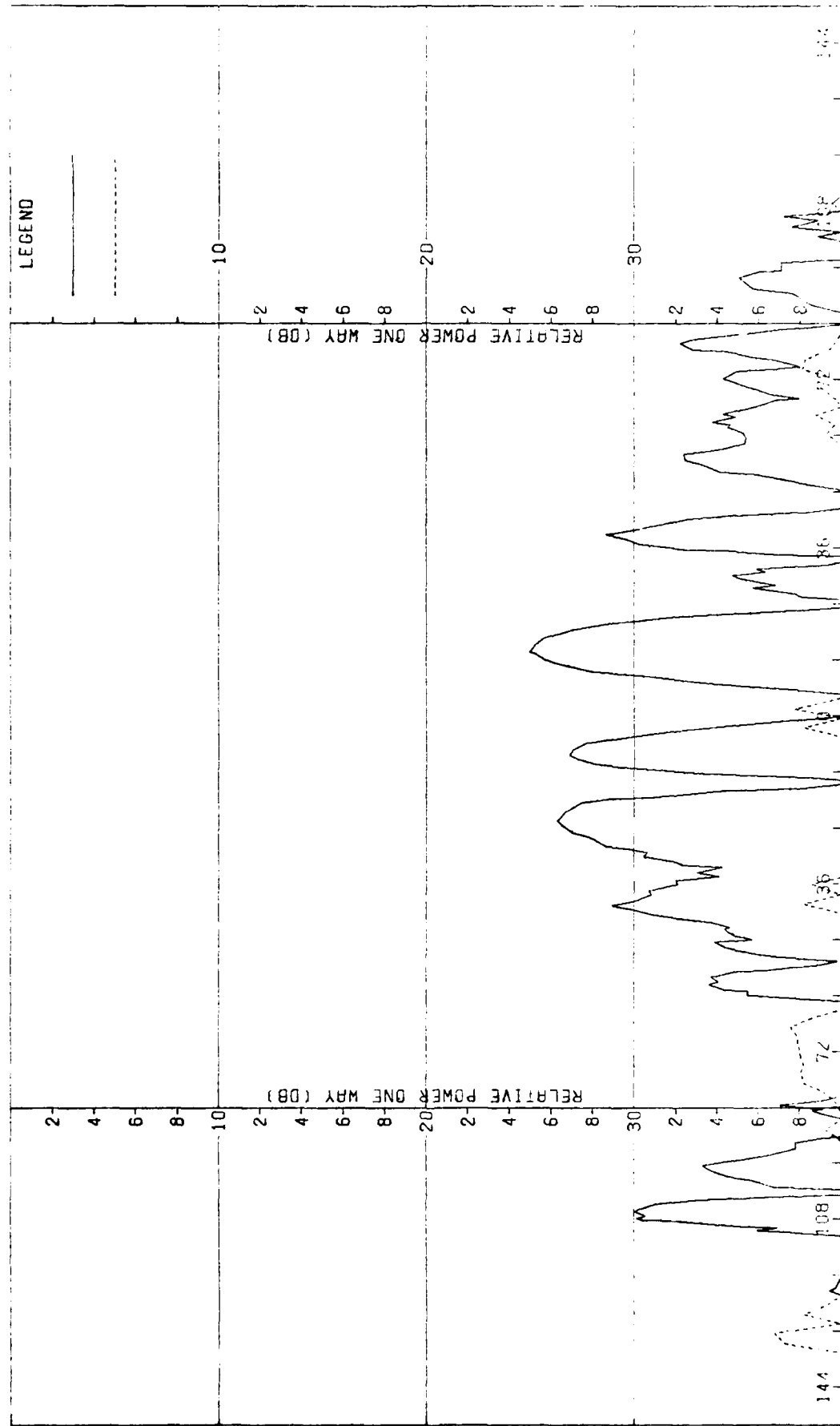
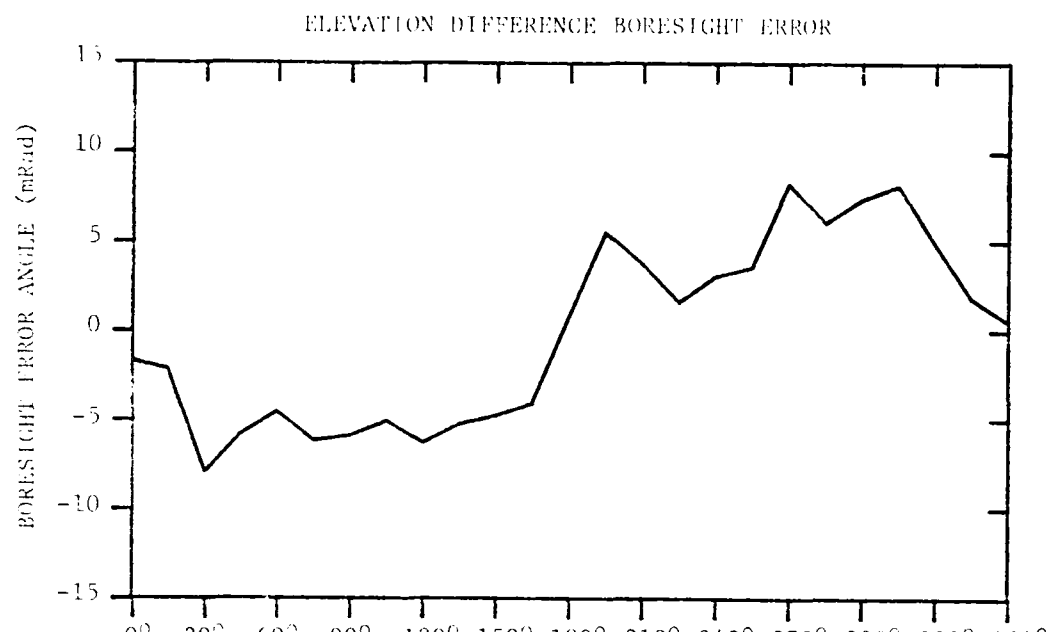


Figure 6-17. Pattern of Medium Array: H-plane, Elevation Difference, --Component, Medium ( $F=1$ ) Radar.



RADOME ORIENTATION ANGLE

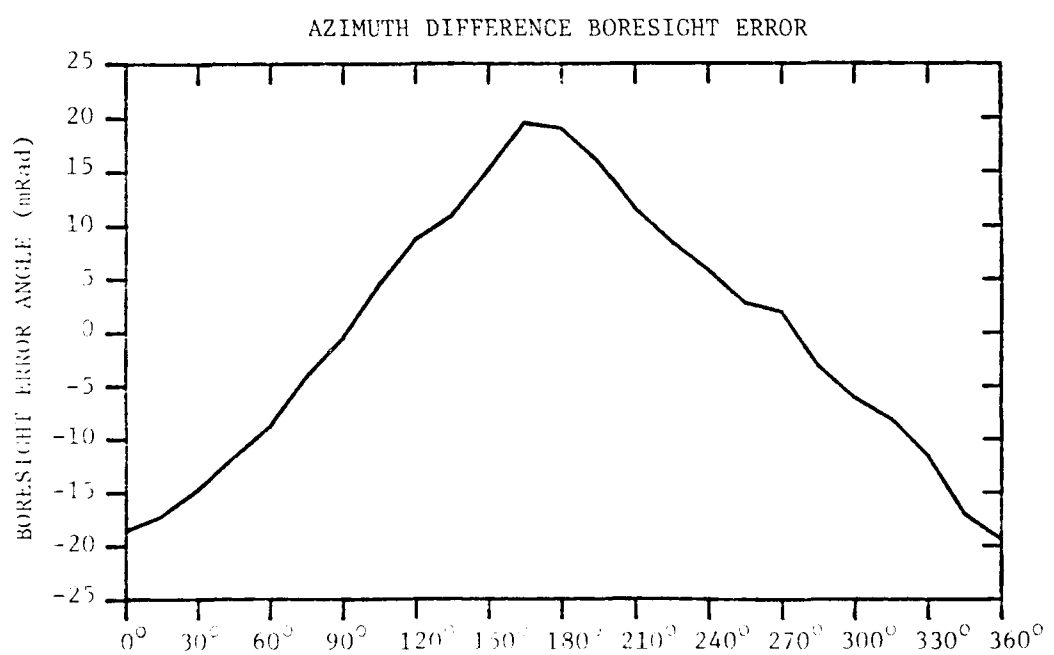


FIGURE G-13. BORESIGHT ERRORS OF MEDIUM ARRAY AND MEDIUM ( $F=1$ ) RADOME.

APPENDIX H

Antenna Patterns of Medium Array with Medium (F=1.5) Radome

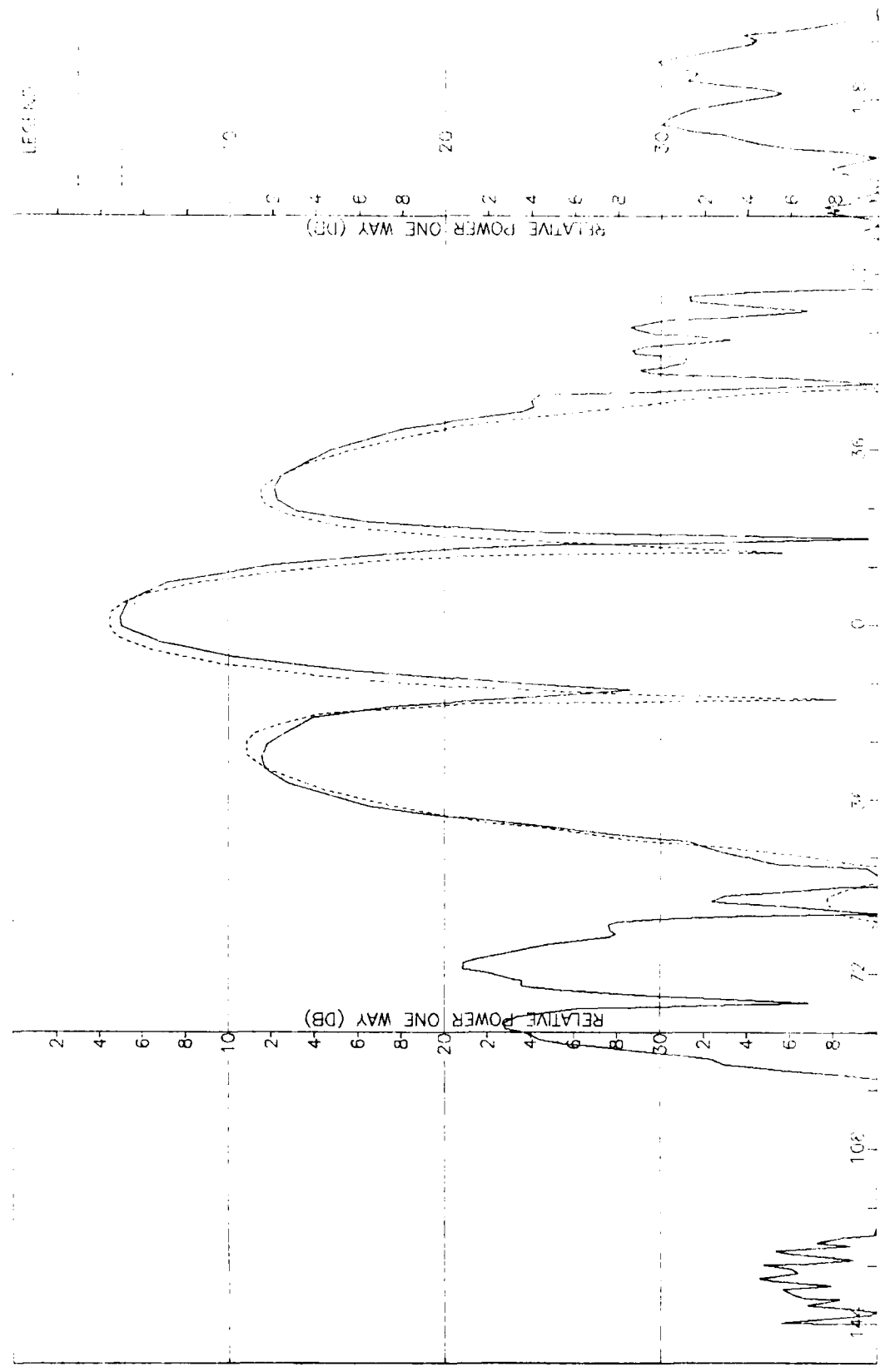


Figure H-1. Pattern of Medium Array: H-Plane, Sum,  $\pm$ -Component, Medium ( $F=1.5$ ) Radome

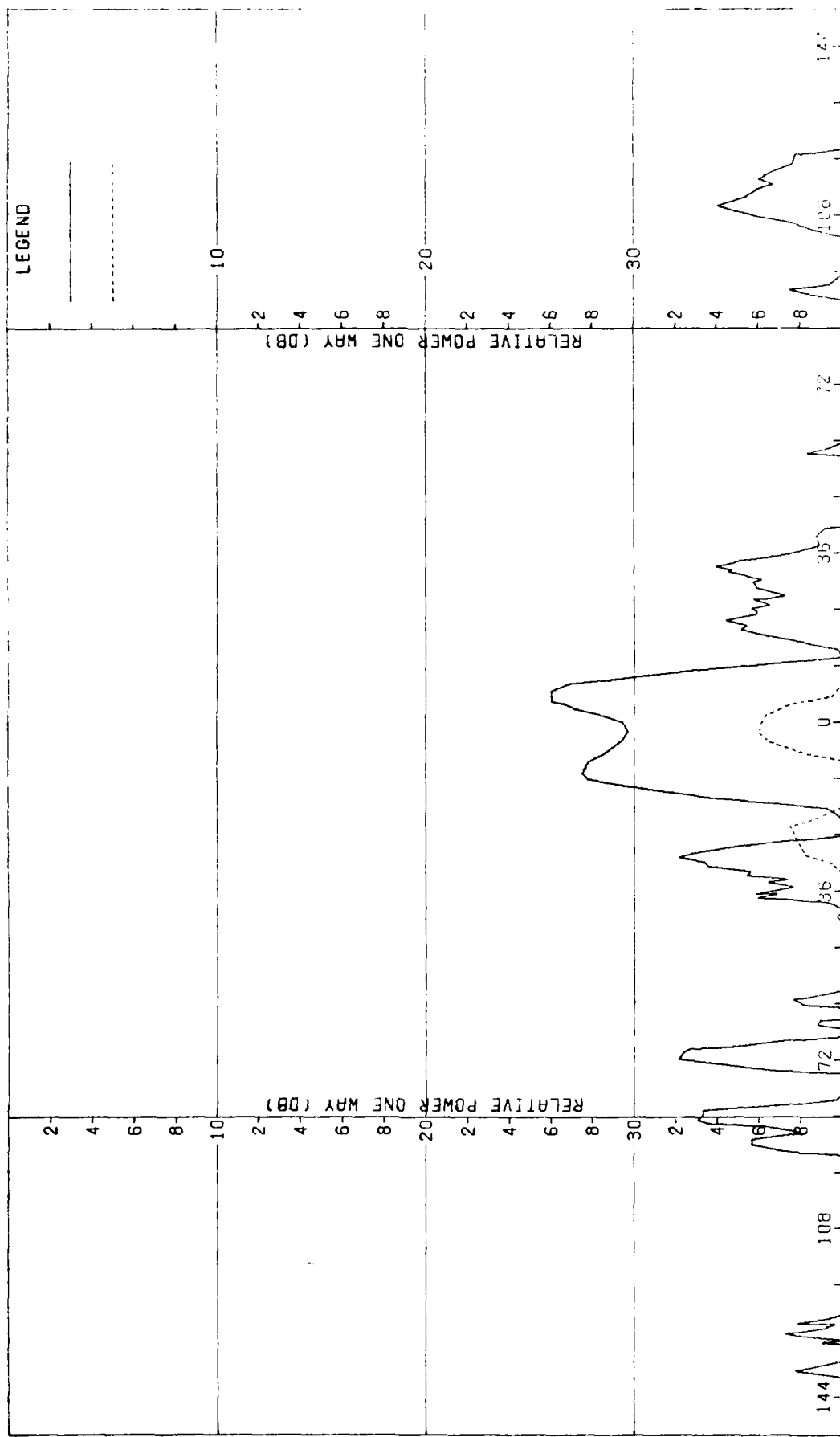
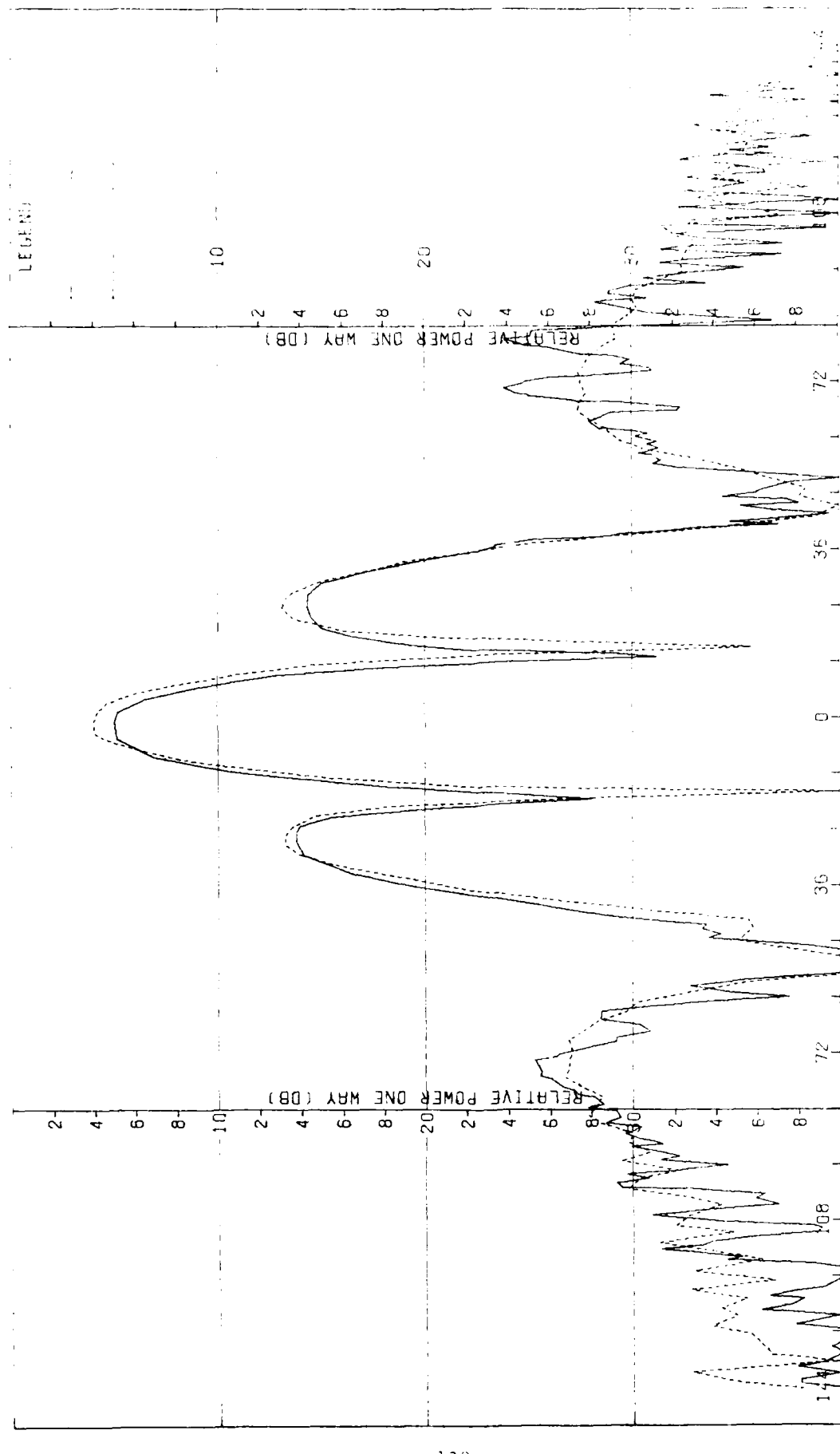


Figure H-2. Pattern of Medium Array: H-Plane, Sum,  $\alpha$ -Component, Medium ( $F=1.5$ ) Radome



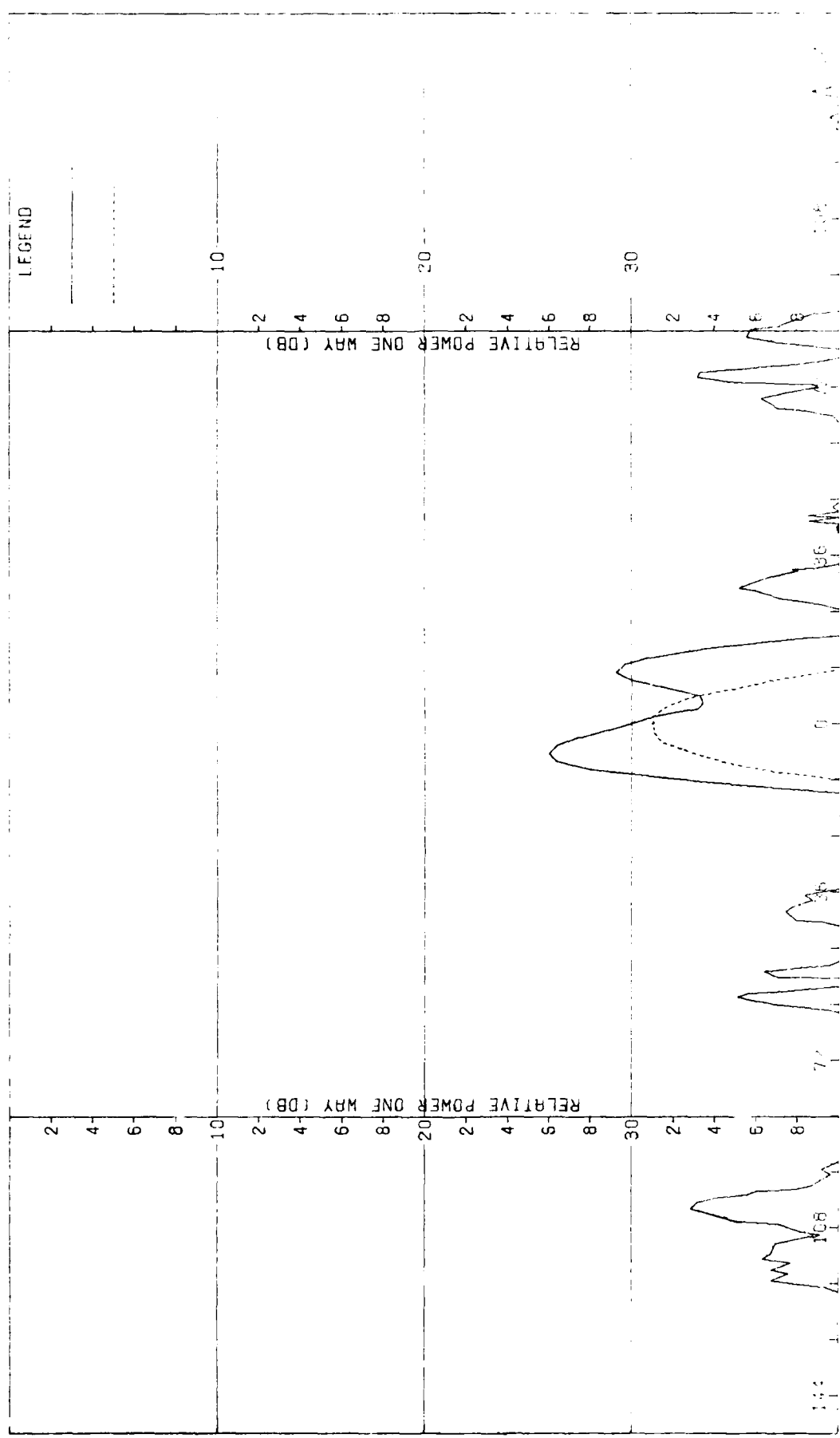


Figure H-4. Pattern of Medium Array: E-Plane, H-Plane, CP Component, Medium ( $\lambda = 1.5$ ) Radome.

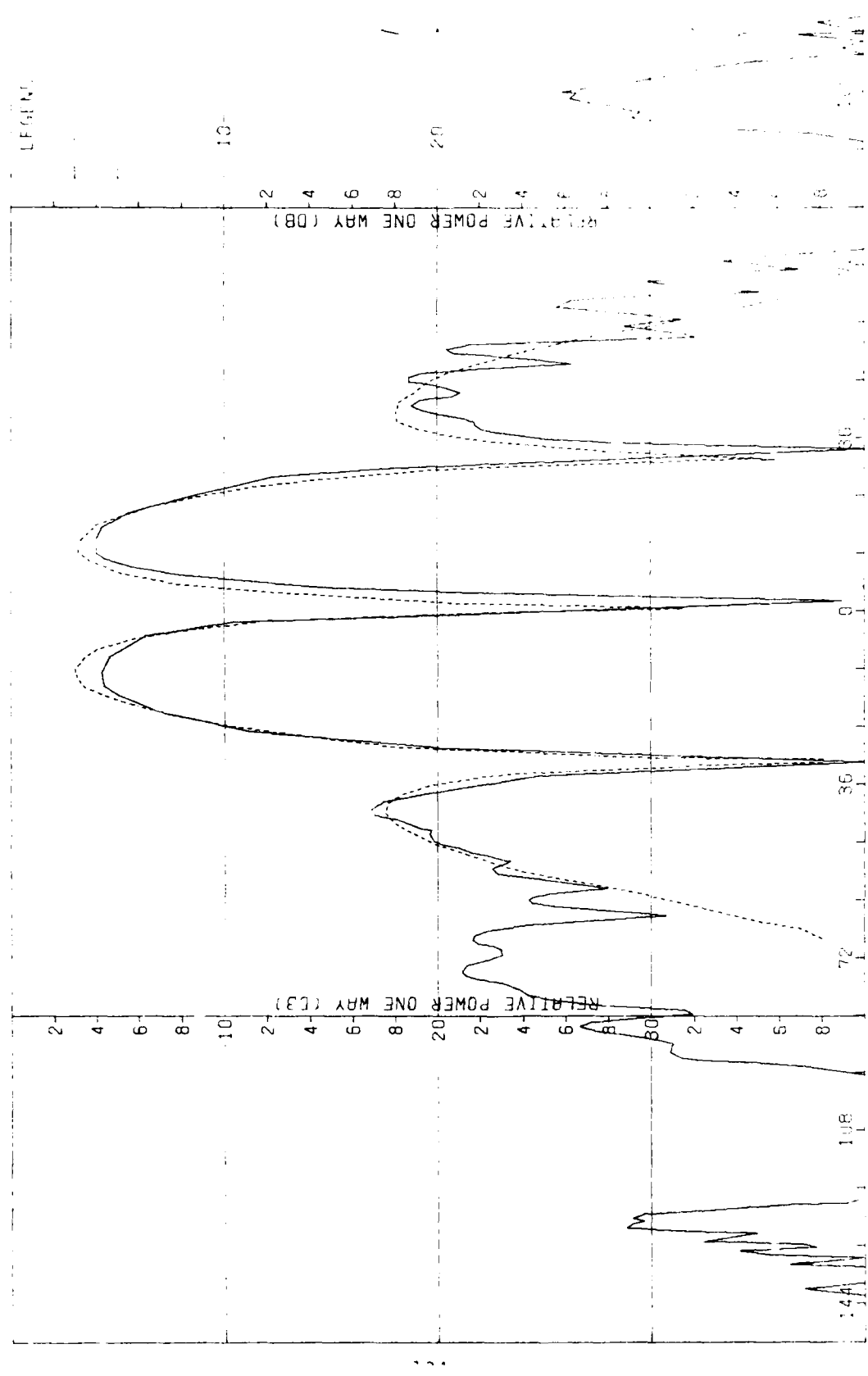


Figure H-5. Pattern of Medium array: H-Plane, Azimuth Diff.,  $\pm$ -Component, Medium (F.1.5) Radome

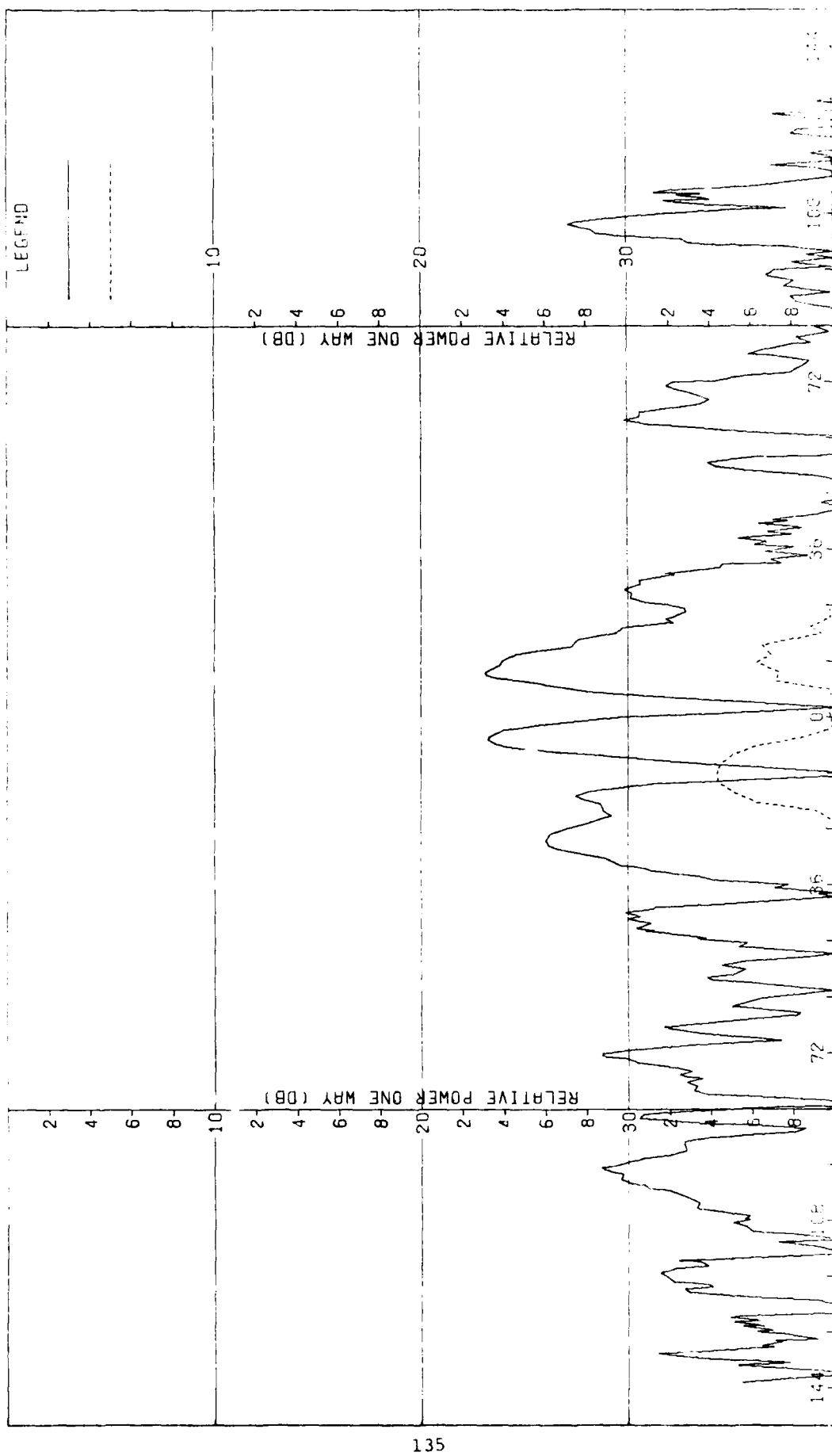


Figure H-6. Pattern of Medium Array: H-Plane, Azimuth Diff.,  $\theta$ -Component, Medium ( $F=1.5$ ) Radome

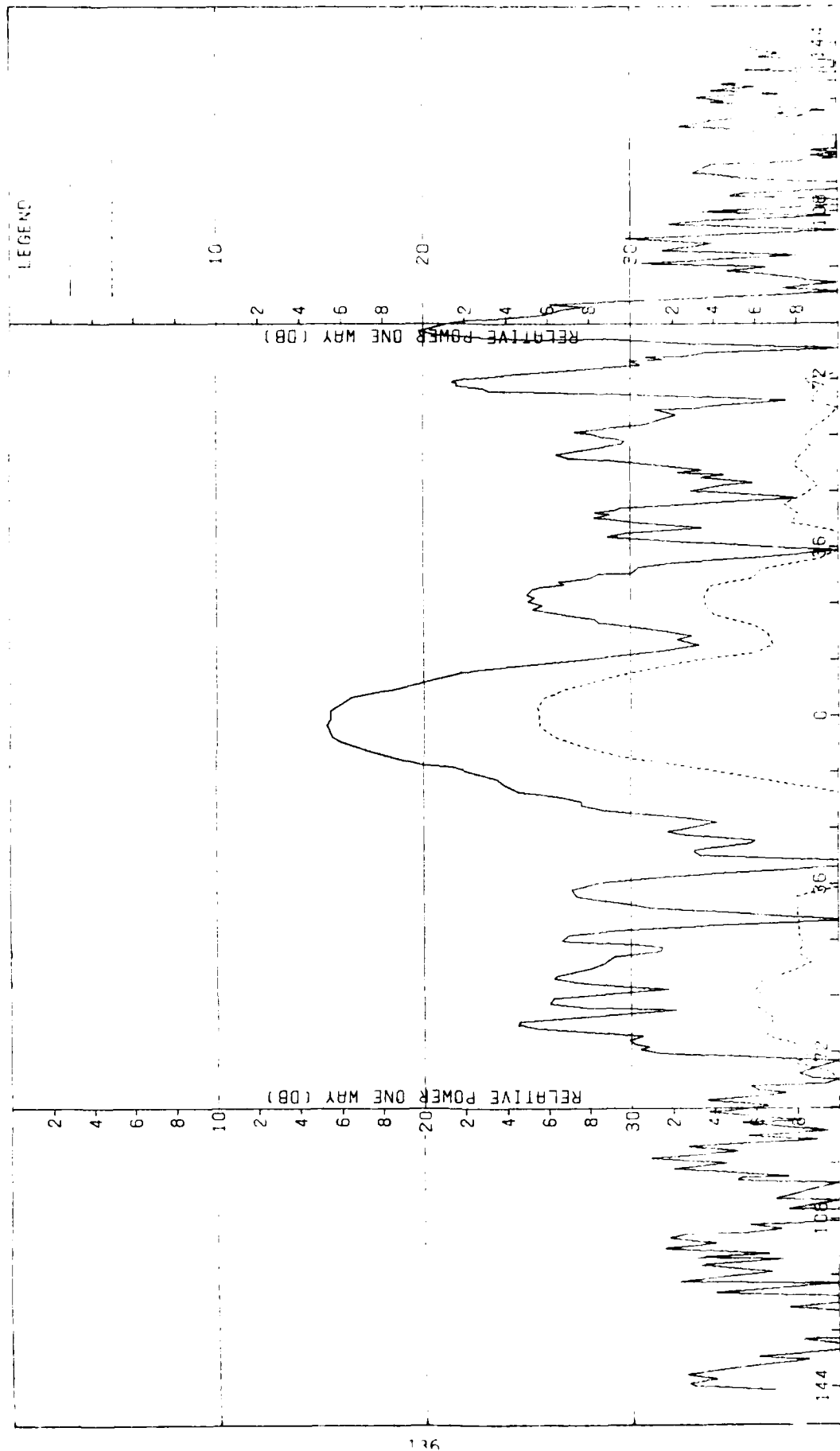


Figure H-7. Pattern of Medium Array: E-Plane, Azimuth Diff., H-Component, Medium ( $F=1.5$ ) Radome

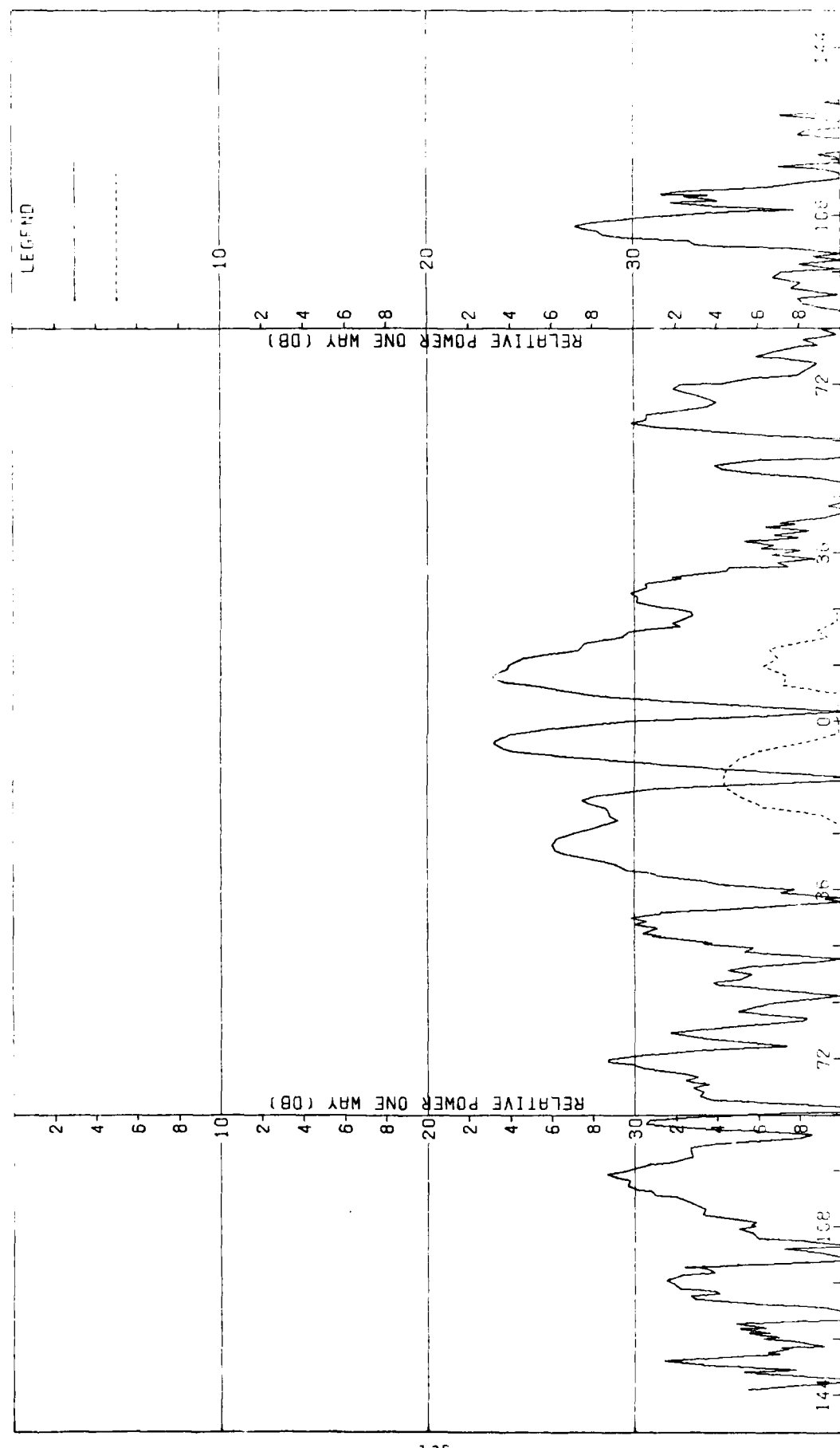


Figure H-6. Pattern of Medium Array: H-Plane, Azimuth Diff.,  $\beta$ -Component, Medium ( $F=1.5$ ) Radome

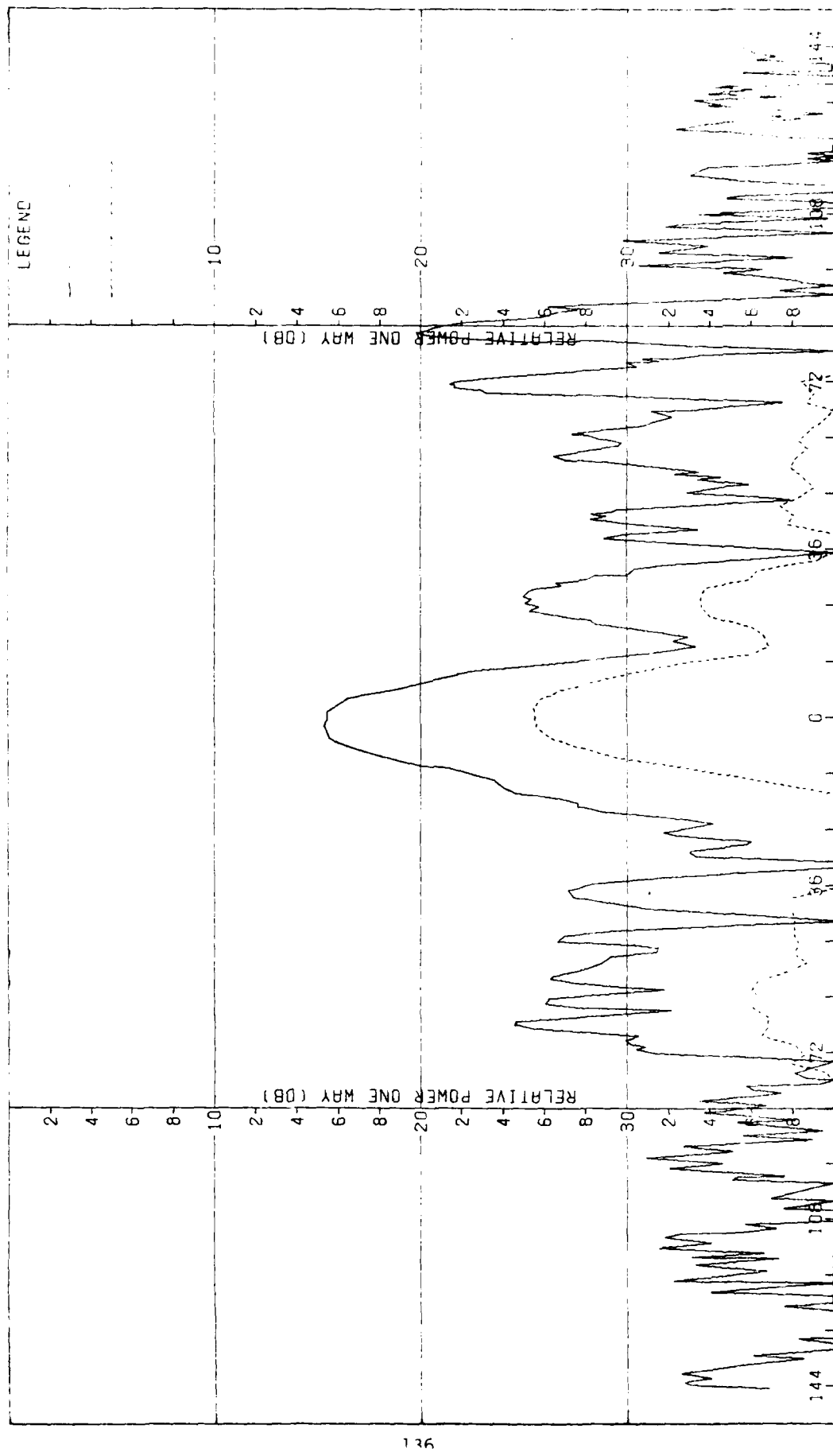


Figure H-7. Pattern of Medium Array: F-Plane, Azimuth Diff.,  $F$ -Component, Medium ( $F=1.5$ ) Radome

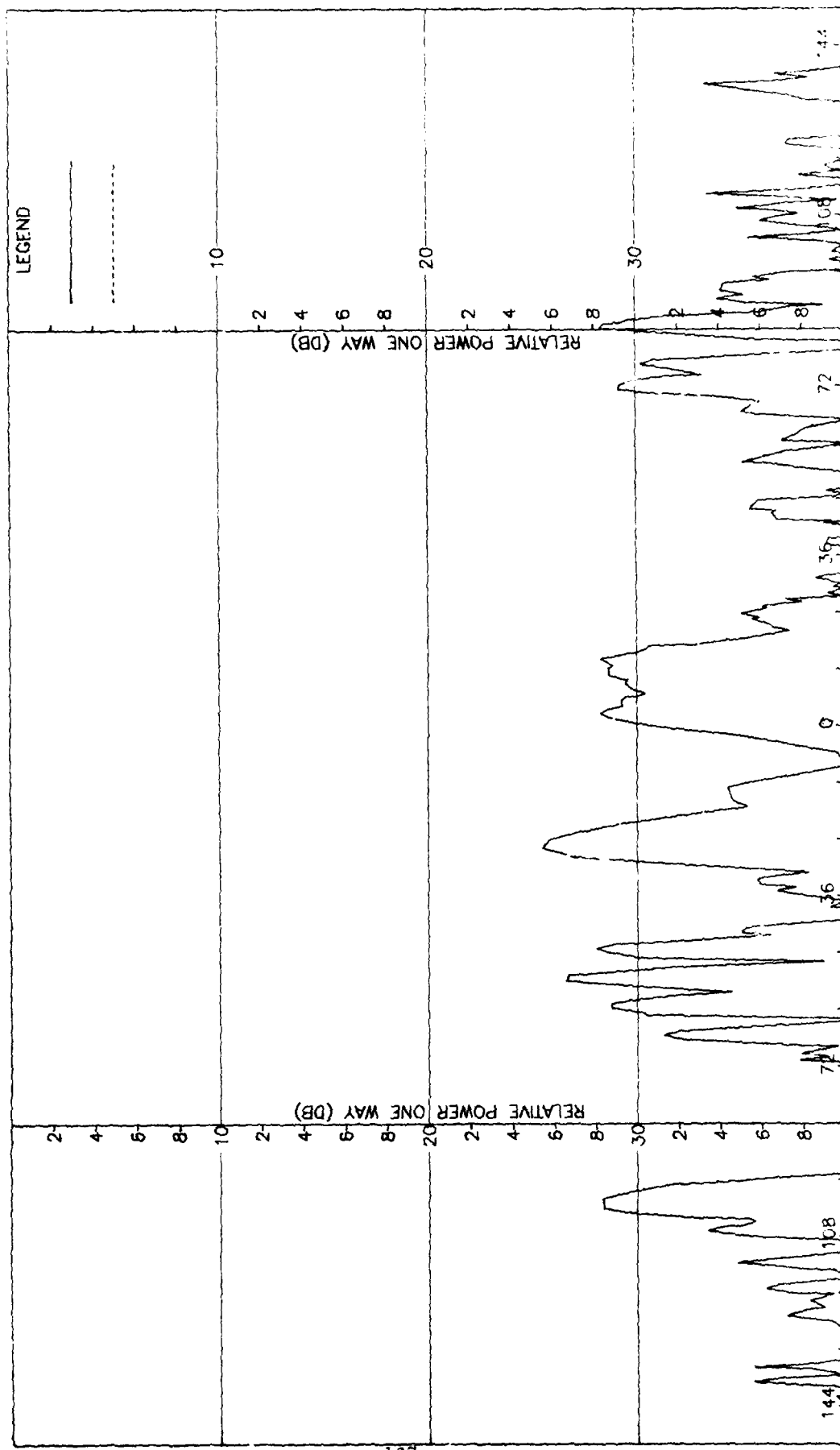


Figure H-8. Pattern of Medium Array: E-plane, Azimuth (degrees); -Component, Medium ( $F=1.5$ ) Radiome.

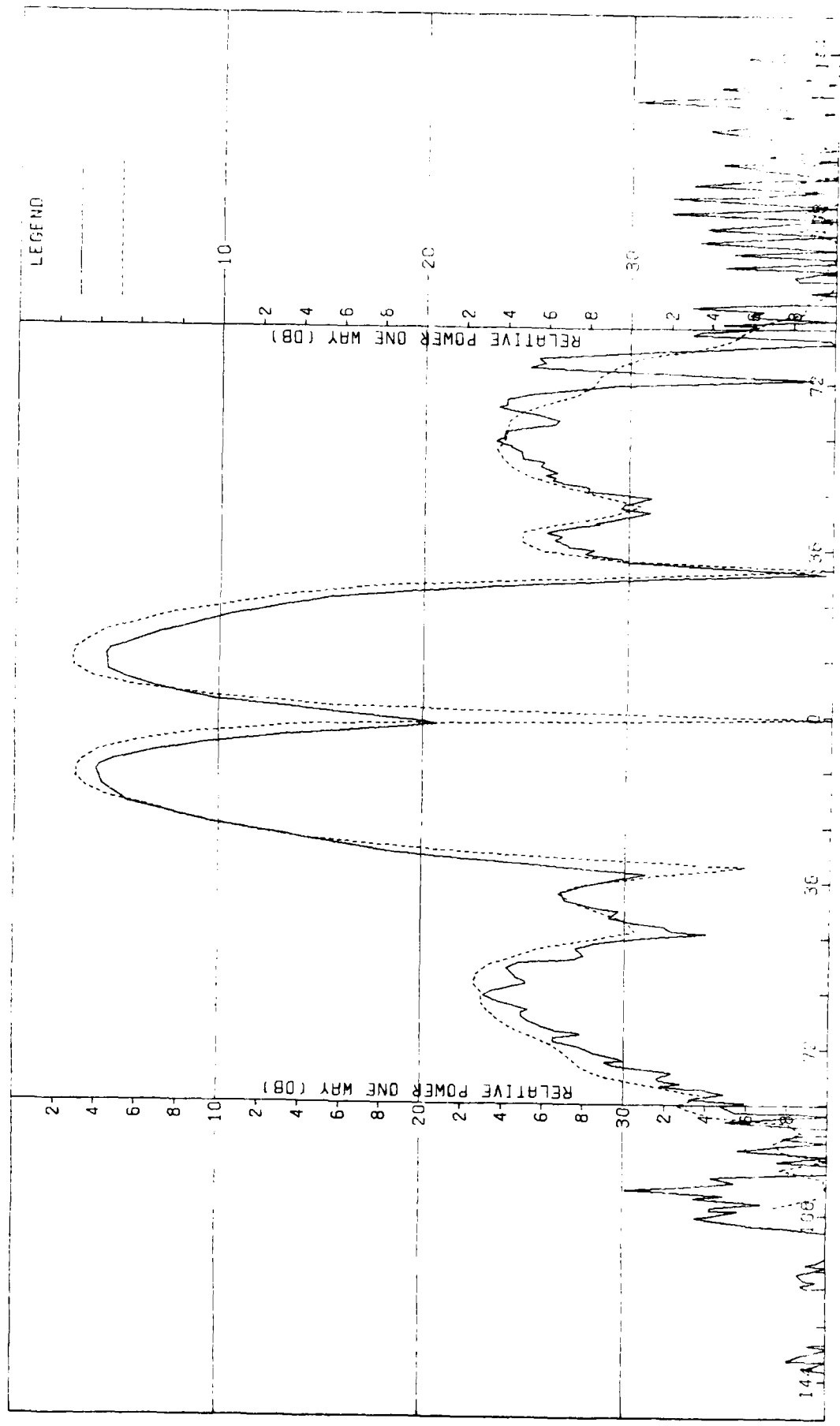


Figure H-9. Pattern of Medium Array: E-Plane, Elevation Diff.,  $n$ -Config, Medium ( $F=1.5$ ) Radome

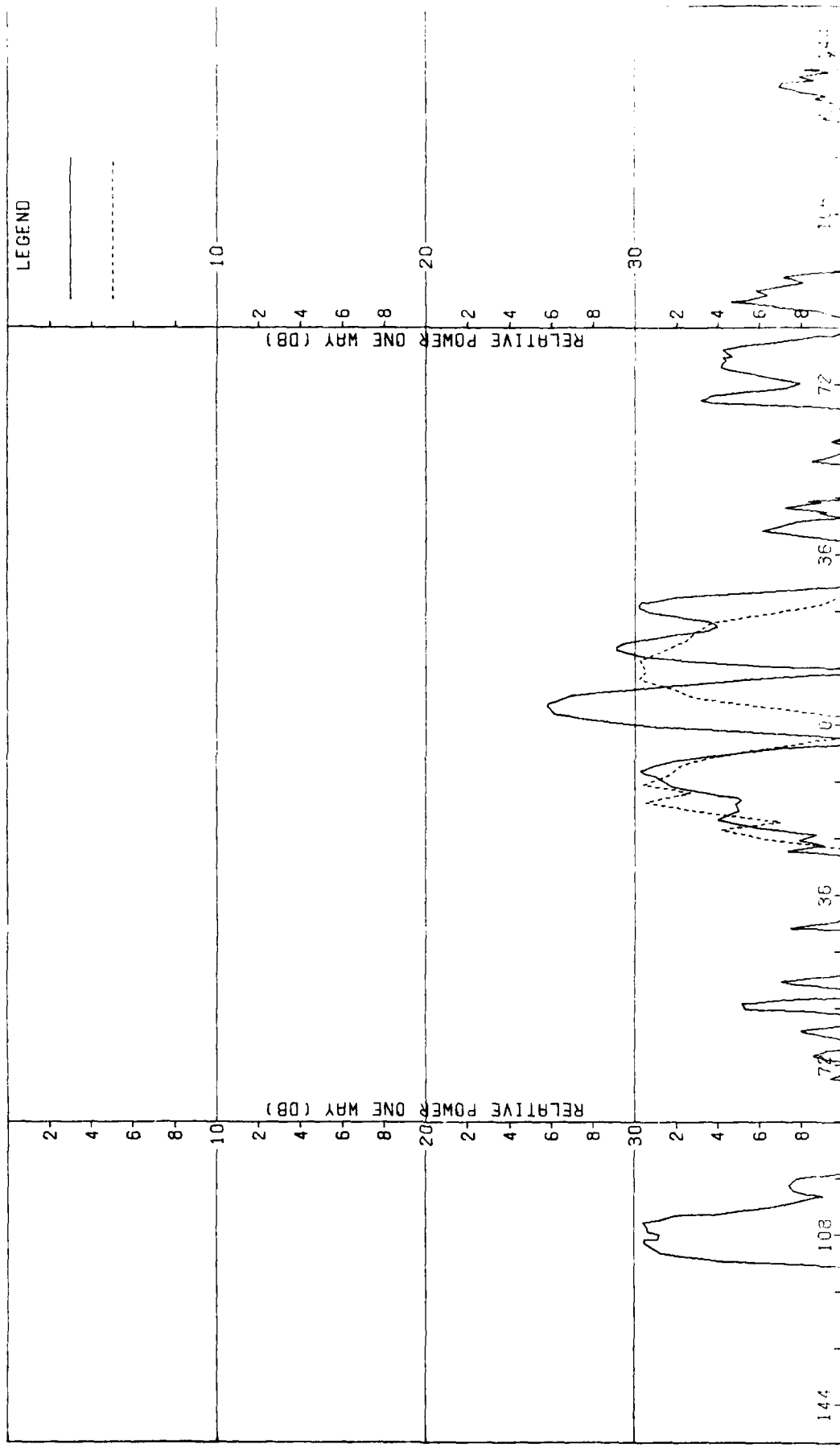


Figure H-10. Pattern of Medium Array: E-Plane, Elevation Diff.,  $\phi$ -Component, Medium ( $f=1$ ) Radome

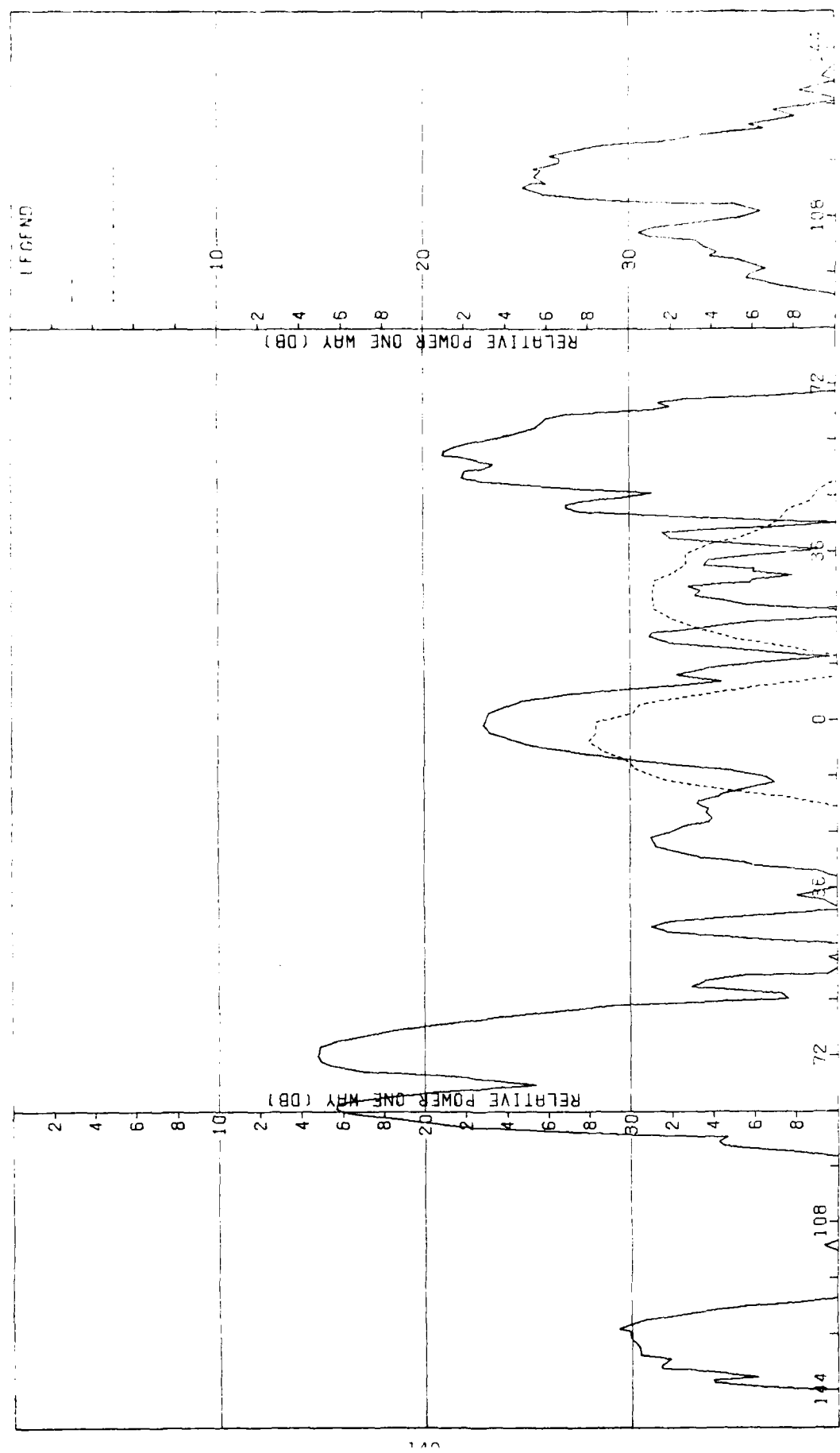


Figure H-11. Pattern of Medium Array: H-Plane, Elevation Diff.,  $\phi$ -Component. Medium ( $F=1.5$ ) Radome

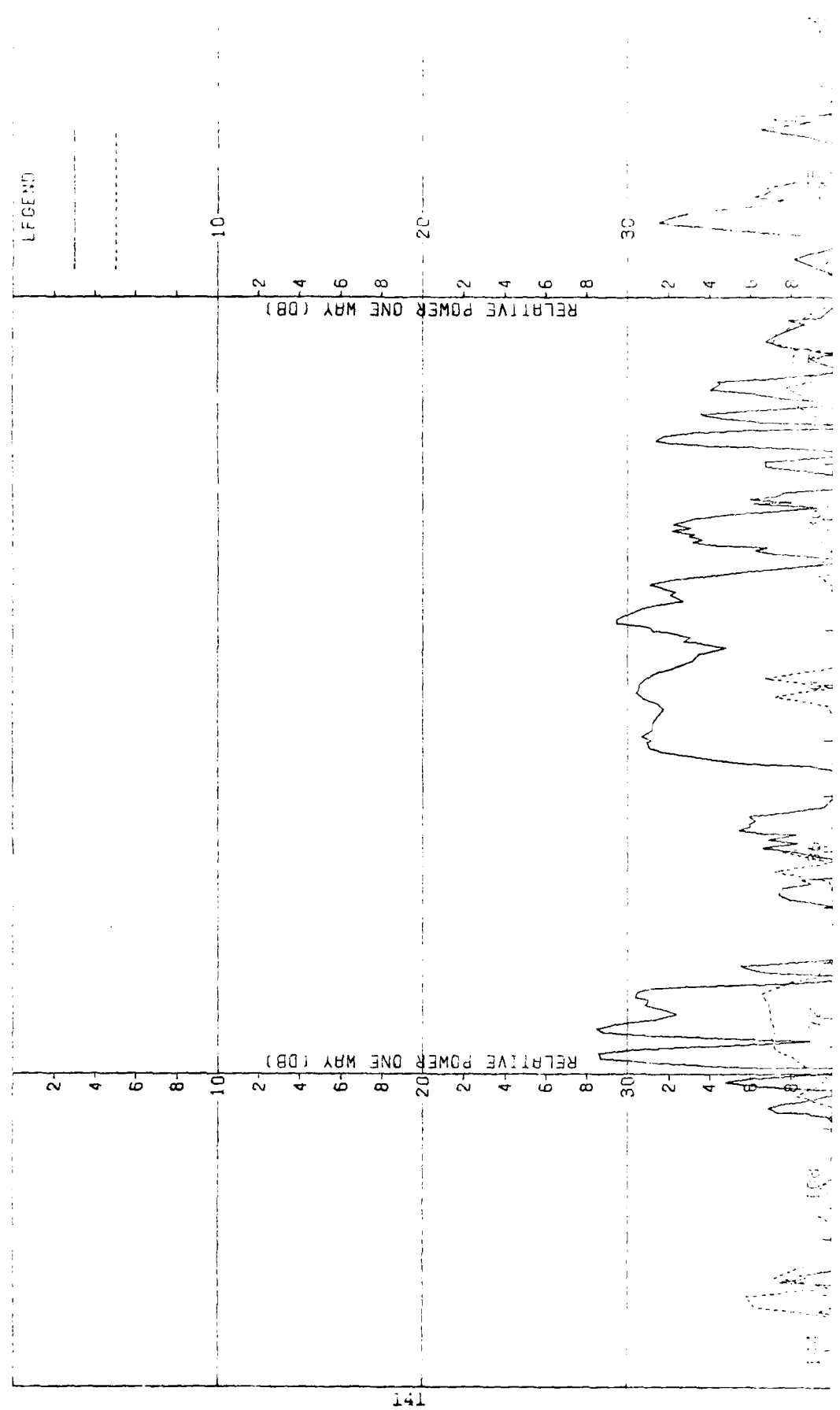
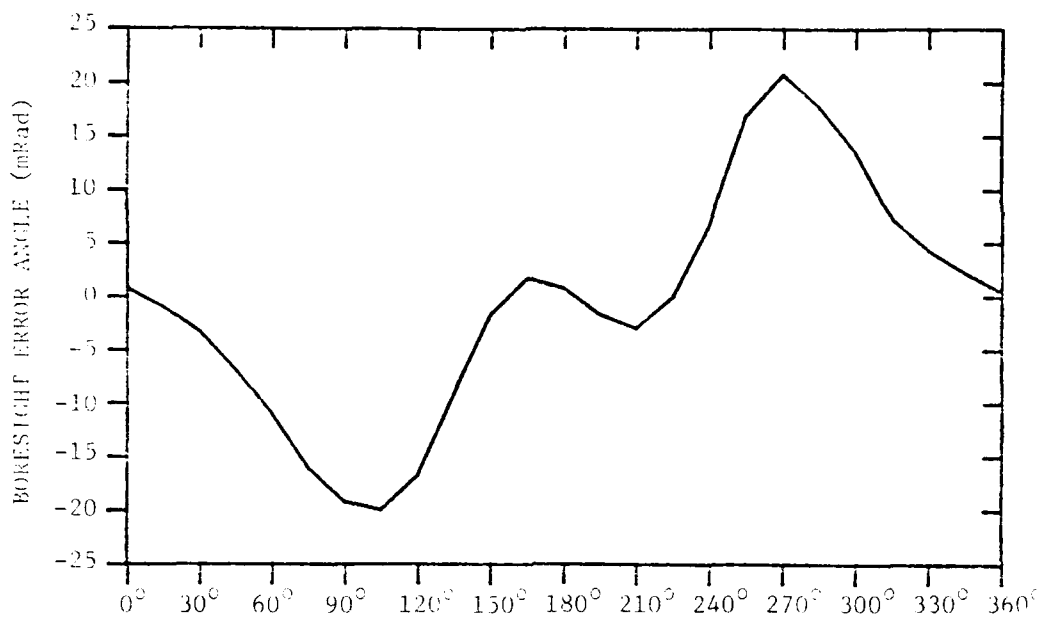


Figure H-12. Pattern of Medium Array: H-Plane, Fixation diff., - component, Medium ( $i = 1.0$ ) Radome

ELEVATION DIFFERENCE BORESIGHT ERROR



RADOME ORIENTATION ANGLE

AZIMUTH DIFFERENCE BORESIGHT ERROR

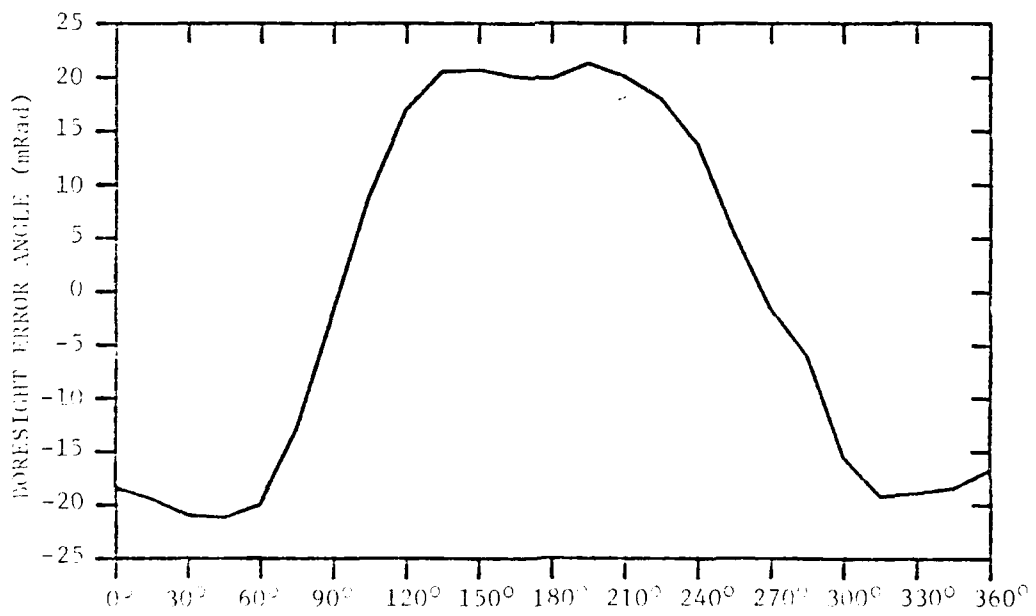


FIGURE H-13. BORESIGHT ERRORS OF MEDIUM ARRAY AND MEDIUM ( $F=1.5$ ) RADOME.

APPENDIX I

Antenna Patterns of Medium Array with Medium (F=2) Radome

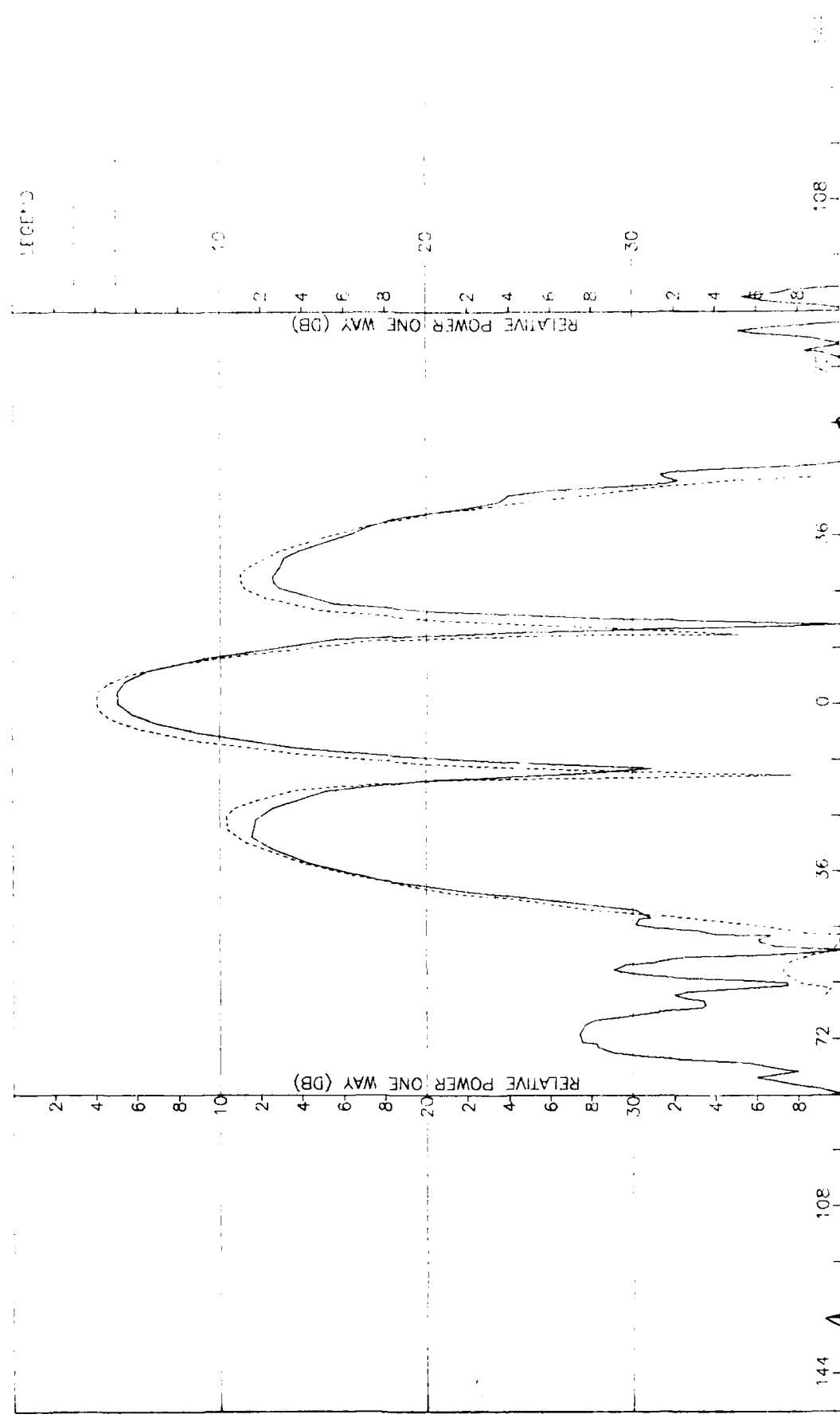


Figure 1-1. pattern of Medium Array: H-plane, Sum, z-component, Medium ( $|z| = 0$ ) Radome

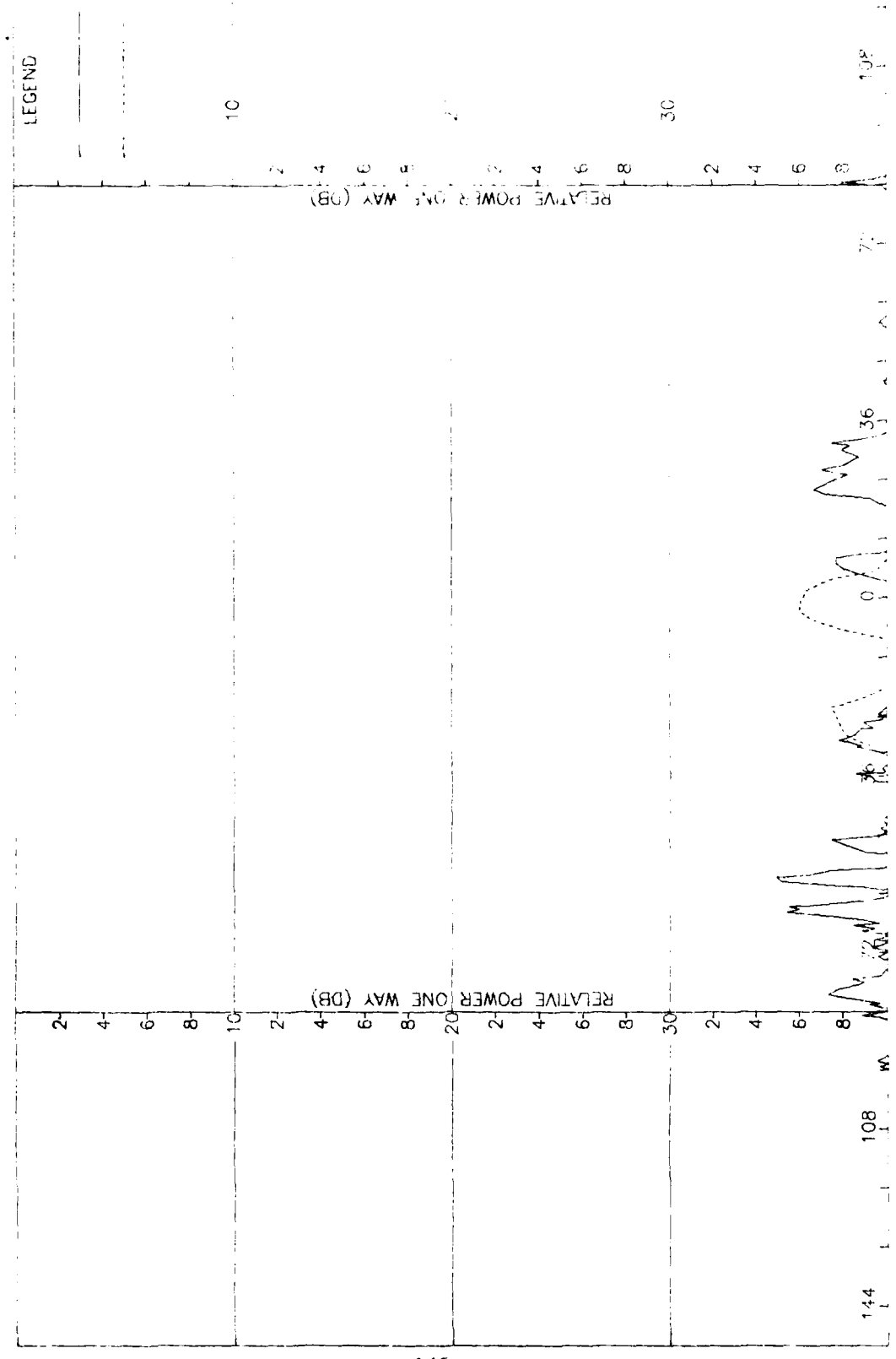


Figure I-2. Pattern of Medium Array: H-Plane, Sum,  $\psi$ -Component, Medium ( $\Gamma = 1.0$ ) Radome

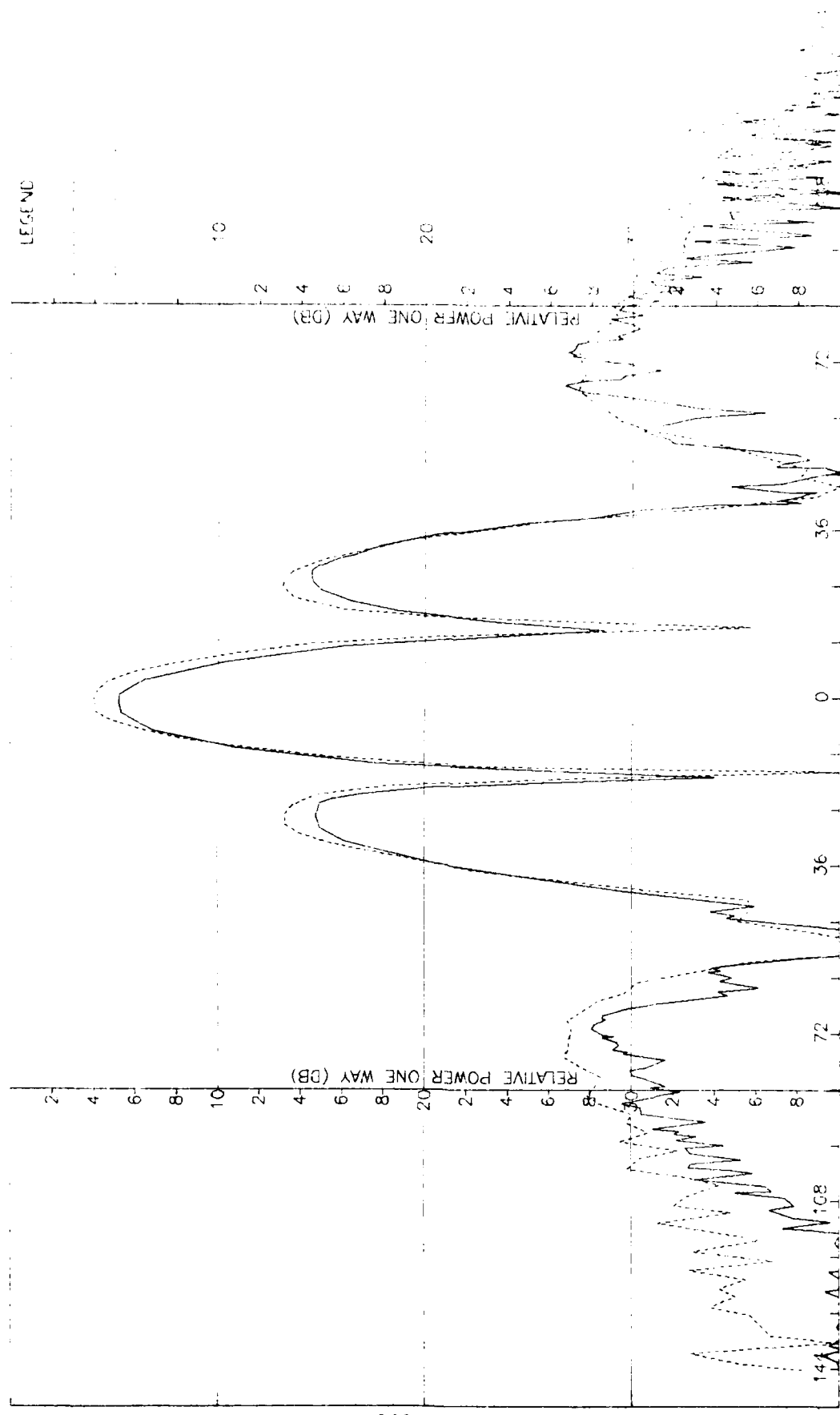


Figure 1-3. Pattern of Medium Array: E-Plane, Sum,  $\alpha$ -Component, Medium ( $F=1.0$ ) Ridome

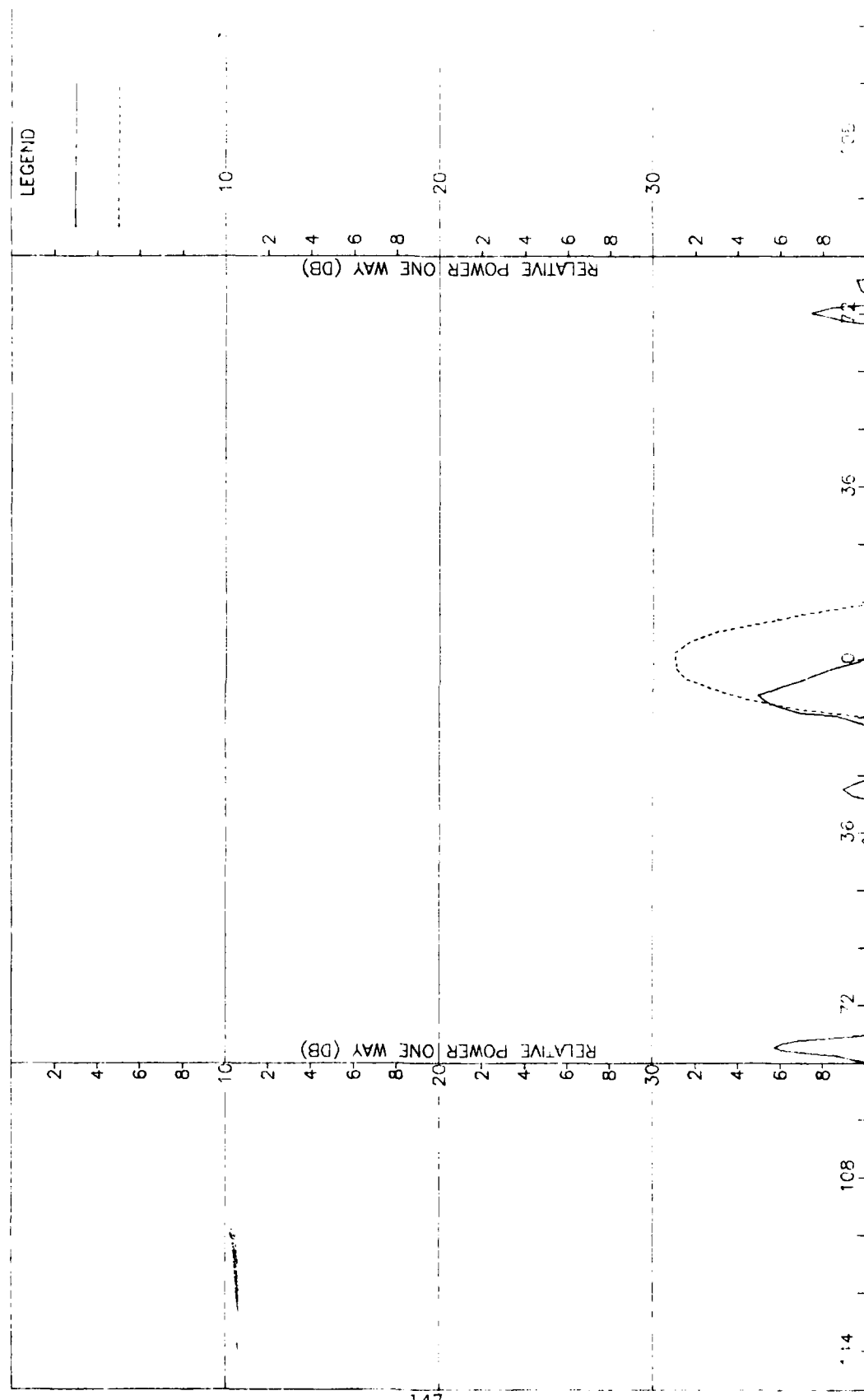


Figure 1-4. Pattern of Medium Array: E-Plane, Sum,  $\phi$ -Component, Medium ( $F=2.0$ ) Radome

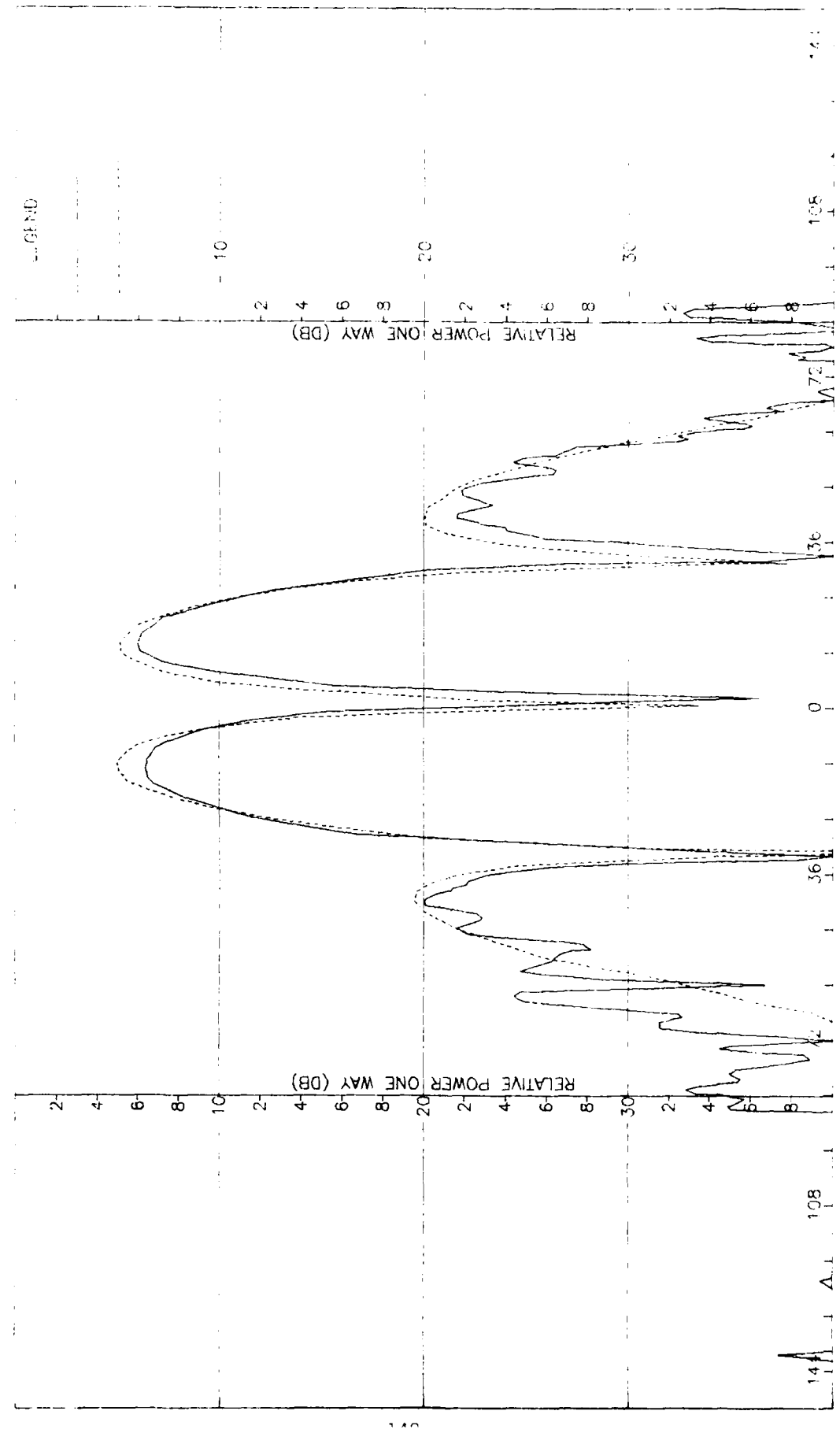


Figure I-5. Pattern of Medium Array: H-Plane, Azimuth Diff.,  $\lambda$ -Component, Medium ( $f=2.0$ ) Radome

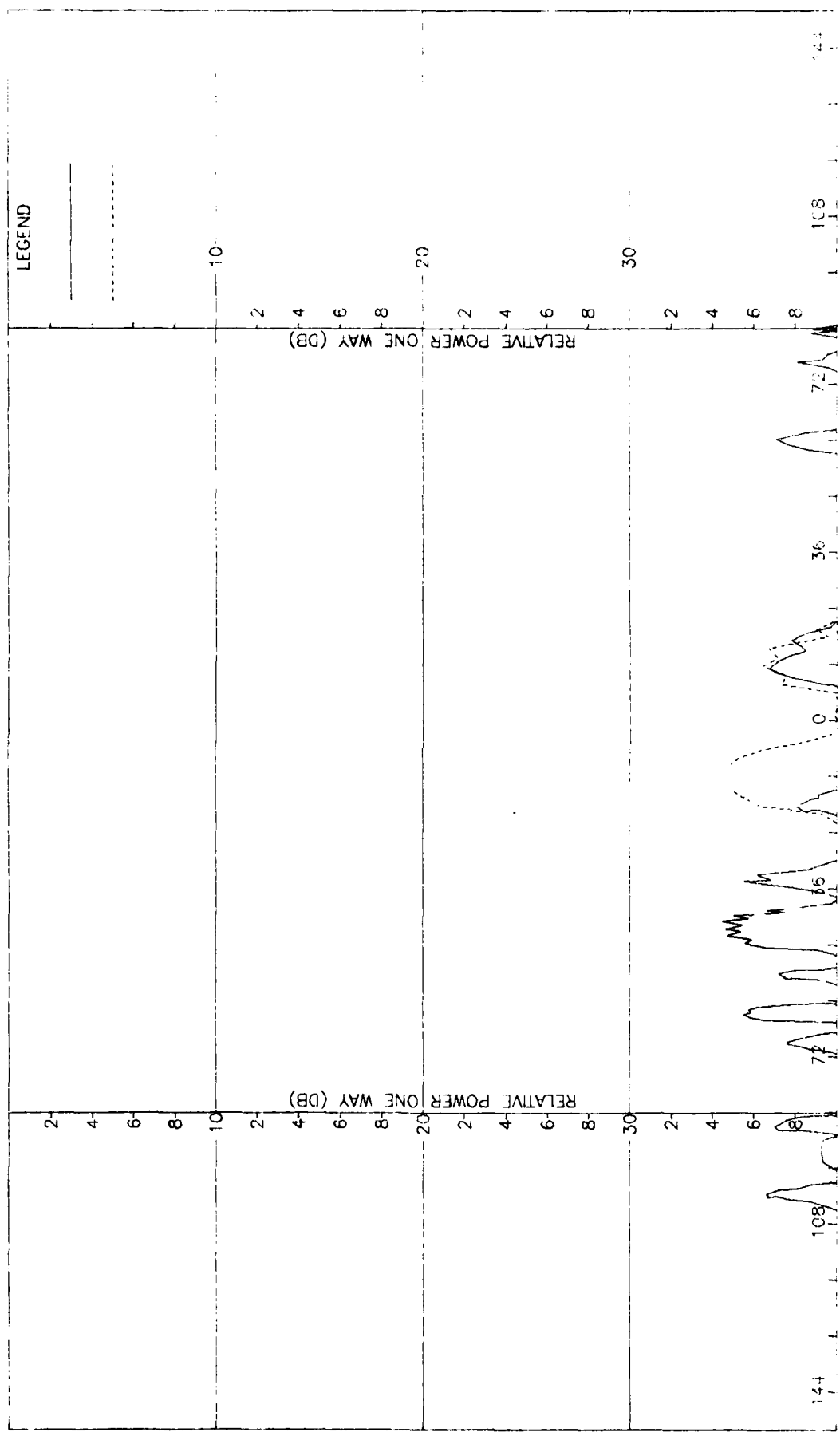
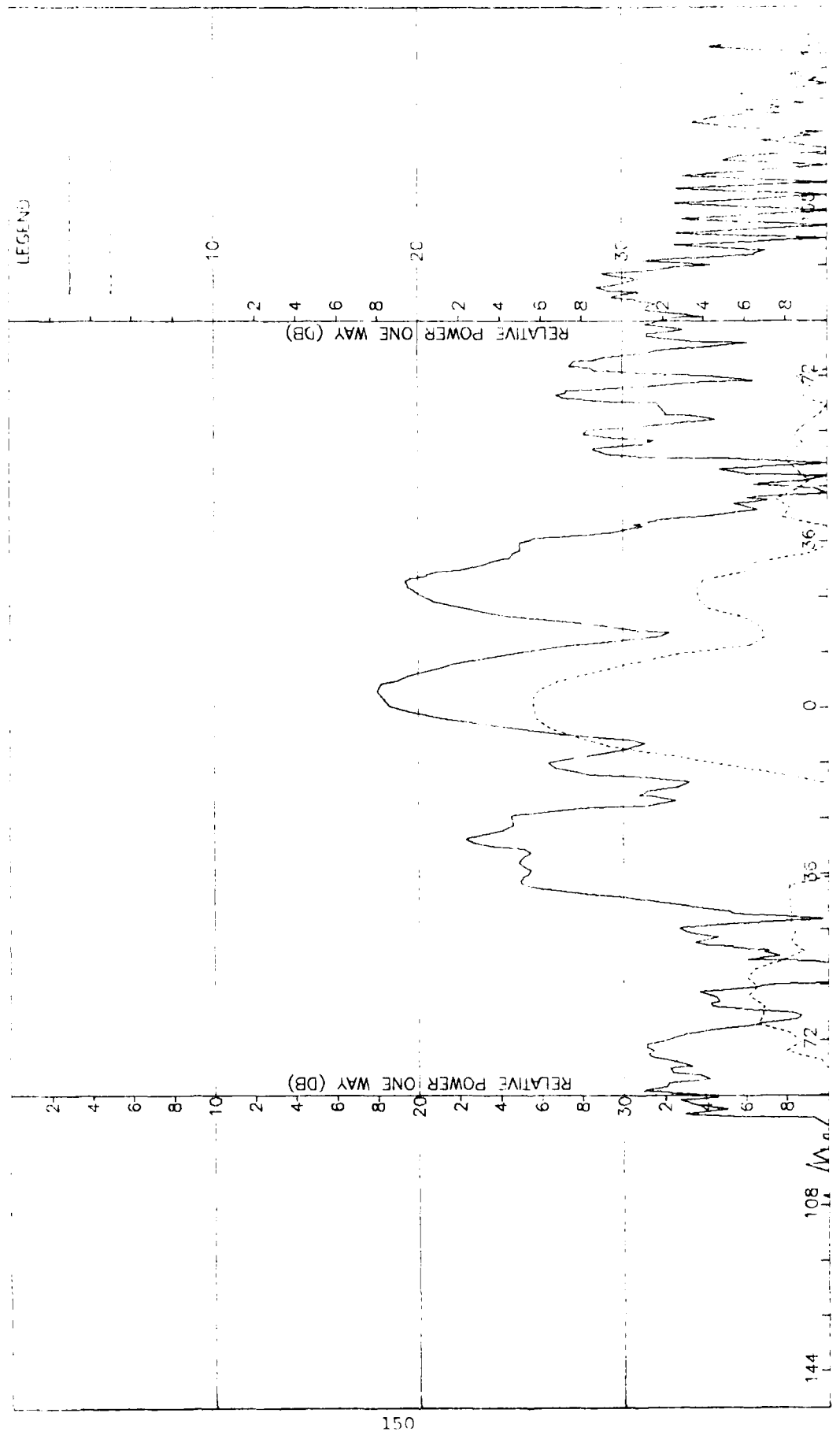


Figure I-6. Pattern of Medium Array: H-Plane, Azimuth Diff.,  $\epsilon$ -Component, Medium ( $F=2.0$ ) Radome



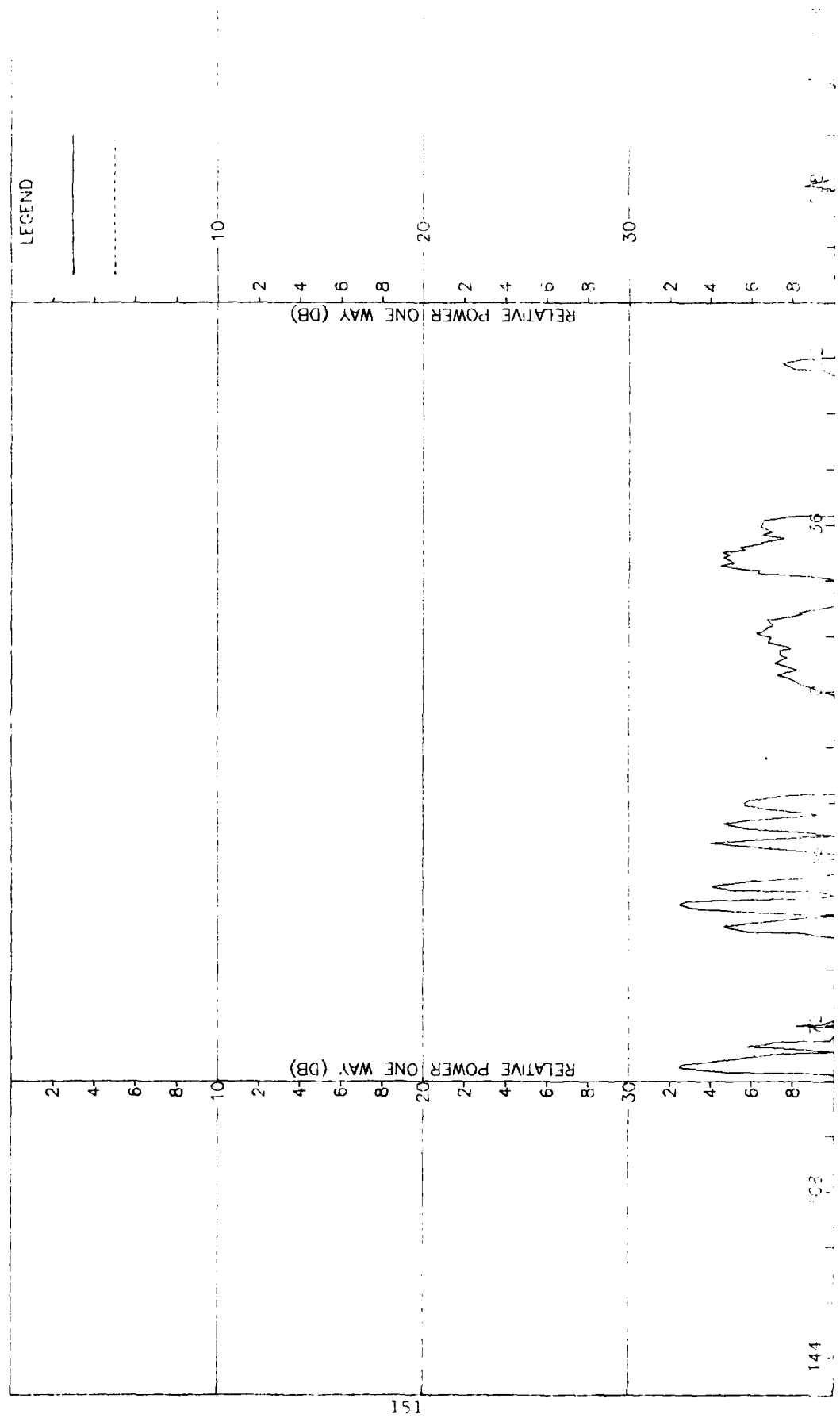


Figure 1-8. Pattern of Medium Array: E-Plane, Azimuth Diff.,  $\varphi$ -Component, Medium ( $\Gamma=2.0$ ) Radome

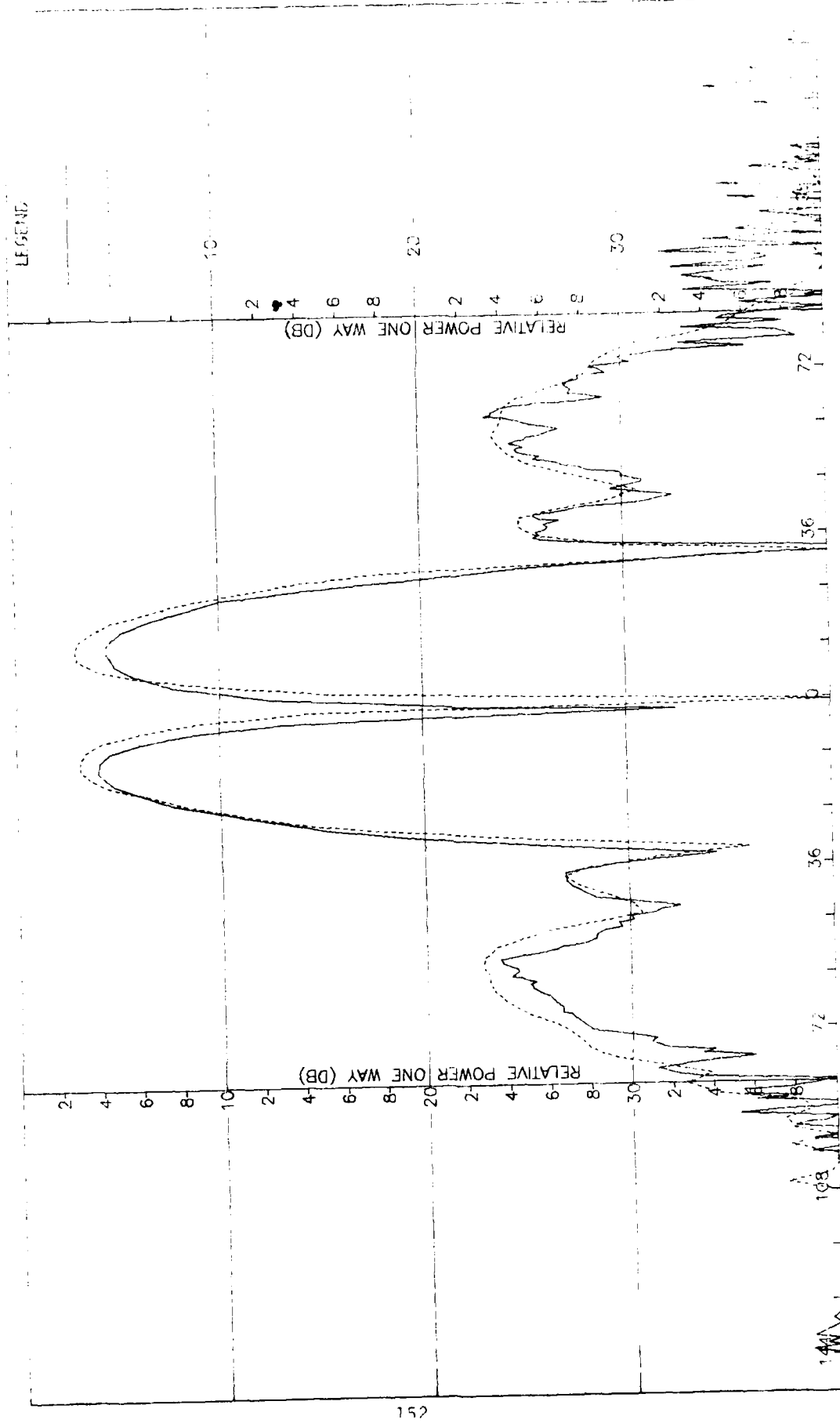


Figure I-9. Pattern of Medium Array: E-Plane, Flevation Diff.,  $f$ -component, Medium ( $F=2.0$ ) Radome

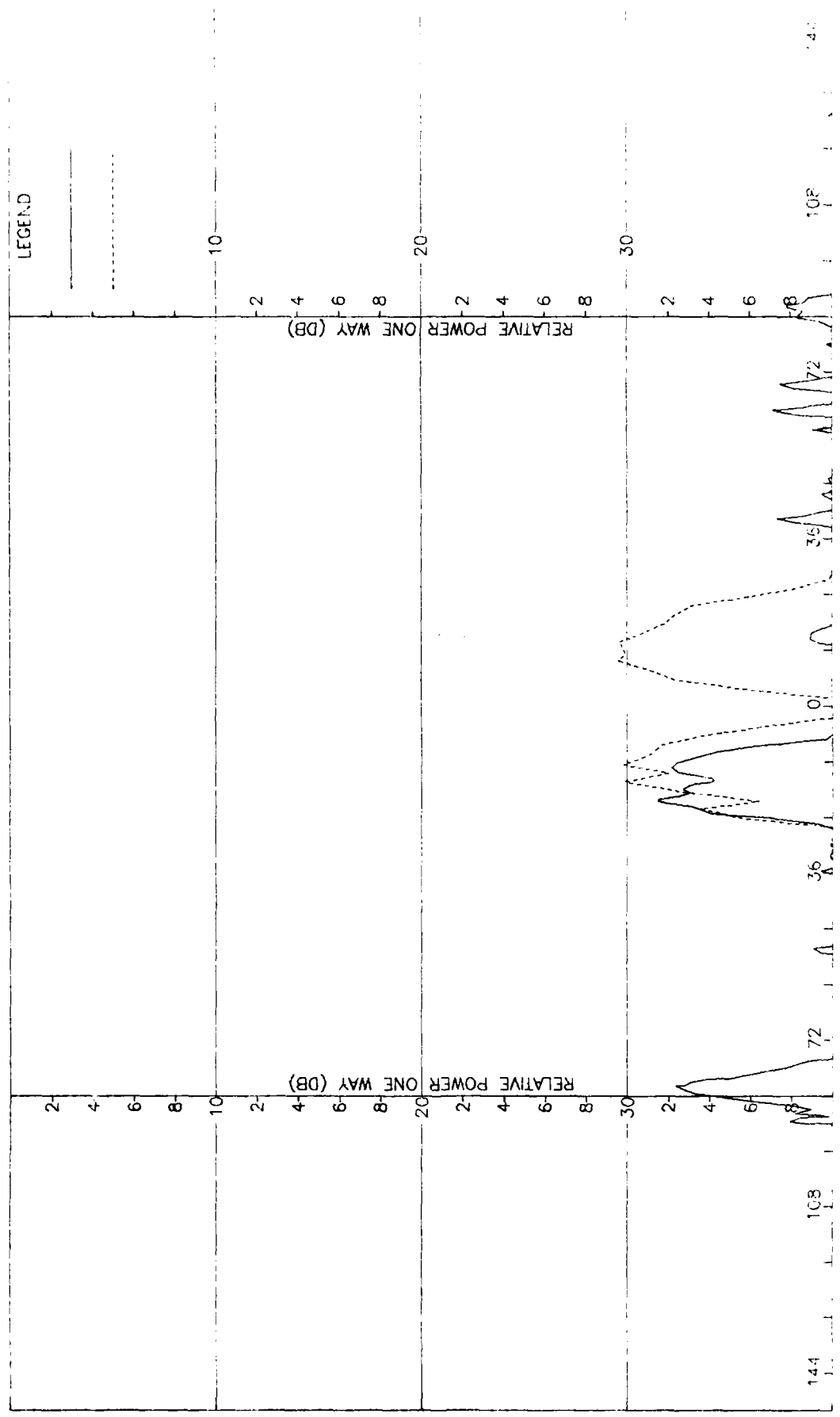


Figure I-10. Pattern of Medium Array: E-Plane, Elevation Diff.,  $\varphi$ -Component, Medium ( $F=2.0$ ) Radome

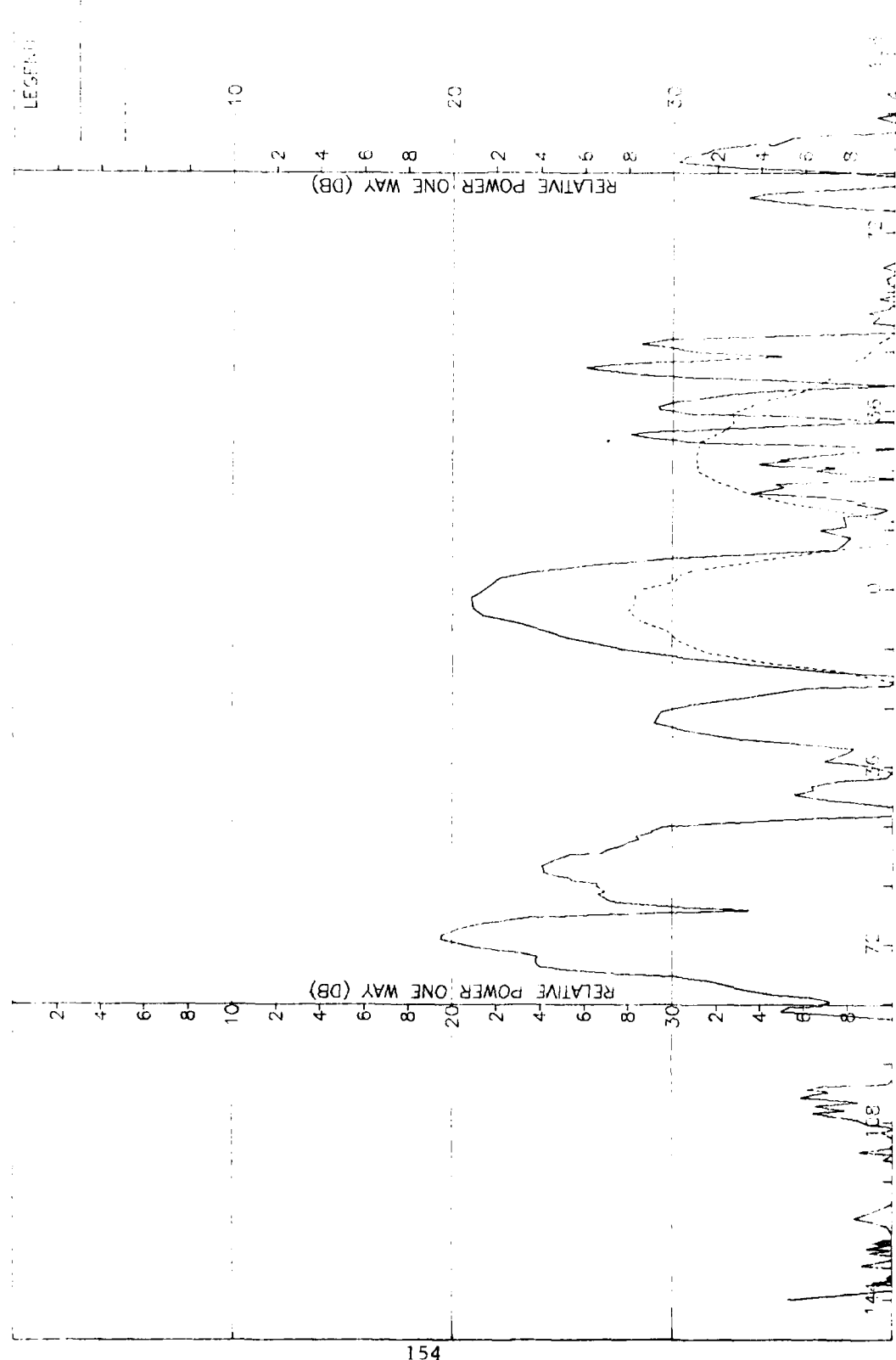


Figure I-11. Pattern of Medium Array: H-Plane, Elevation Diff.,  $\phi$ -Component, Medium ( $F=2.0$ ) Radome

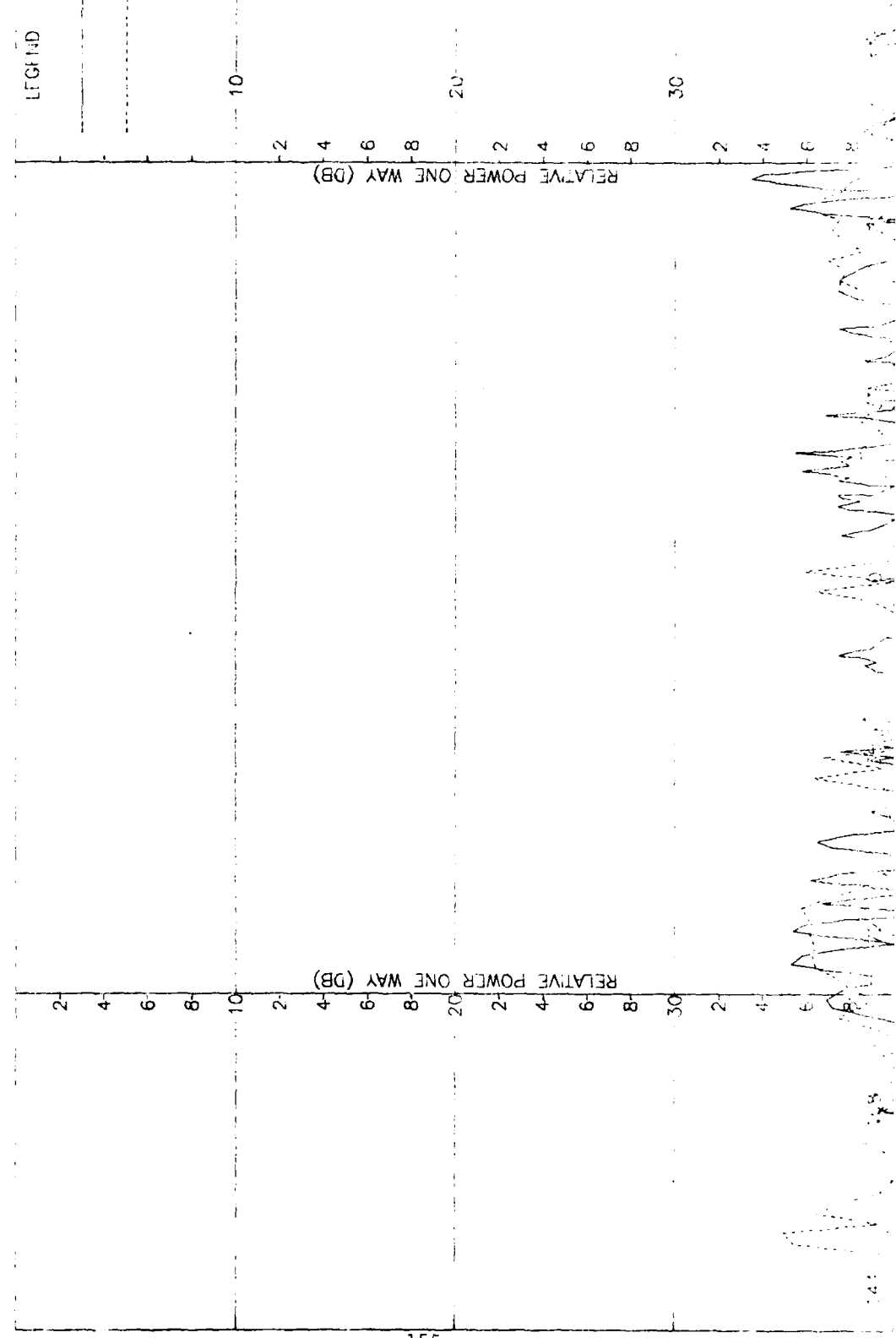


Figure 1-13. Pattern of Medium Array: H-Plane, Elevation Diff.,  $\alpha$ -Component, Medium ( $\Gamma = 2.0$ ) Radome

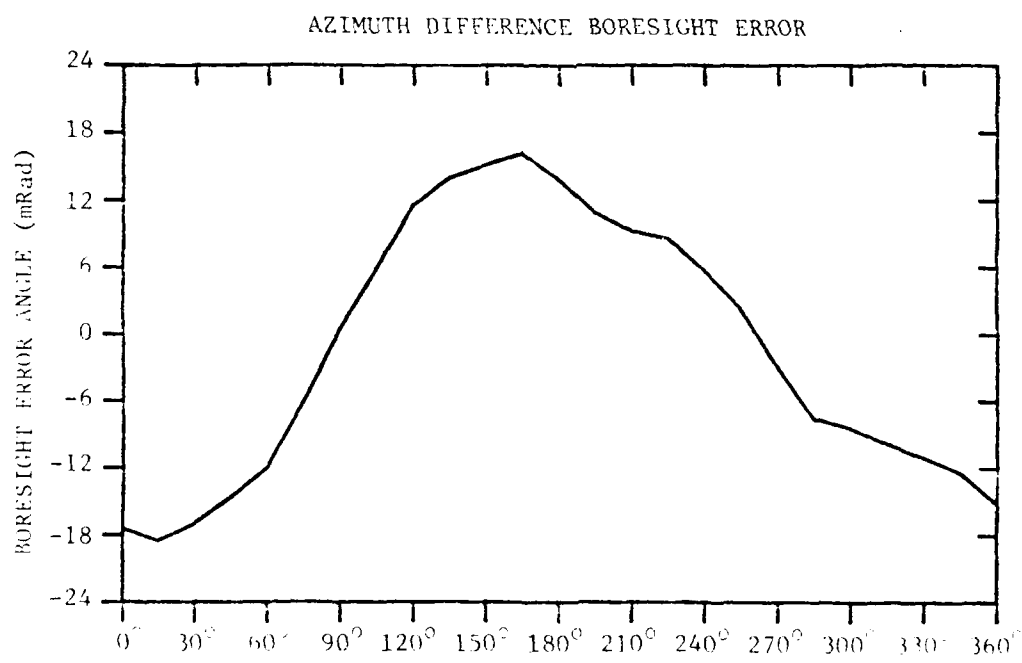
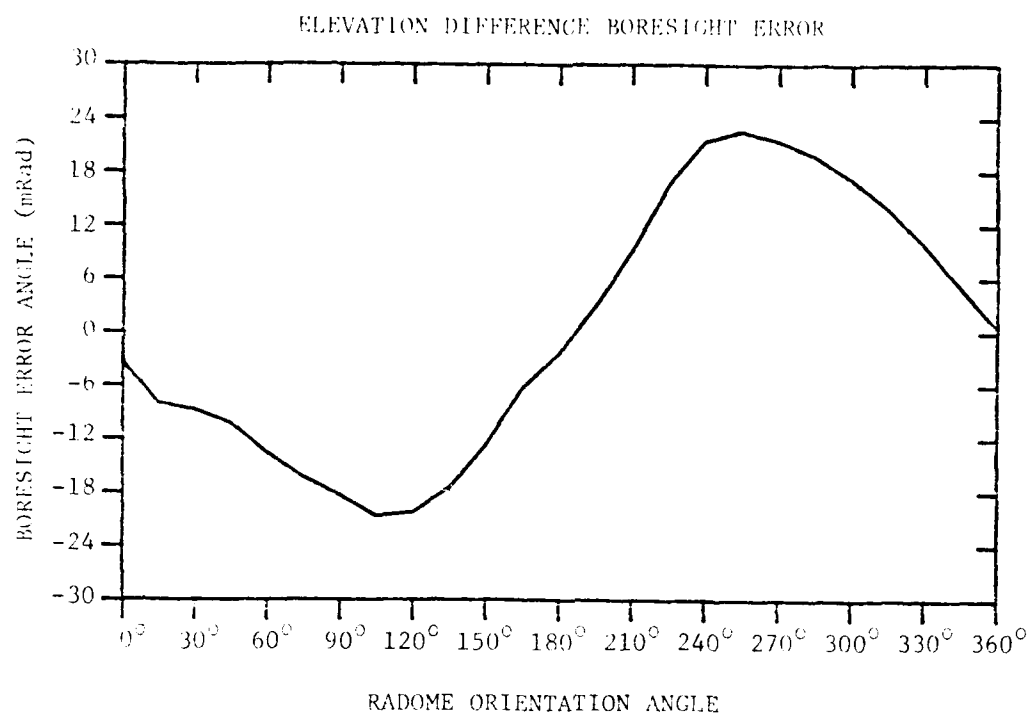


FIGURE I-13. BORESIGHT ERRORS OF MEDIUM ARRAY AND MEDIUM ( $F=2$ ) RADOME.

APPENDIX J

Antenna Patterns of Medium Array with Large (F=1) Radome

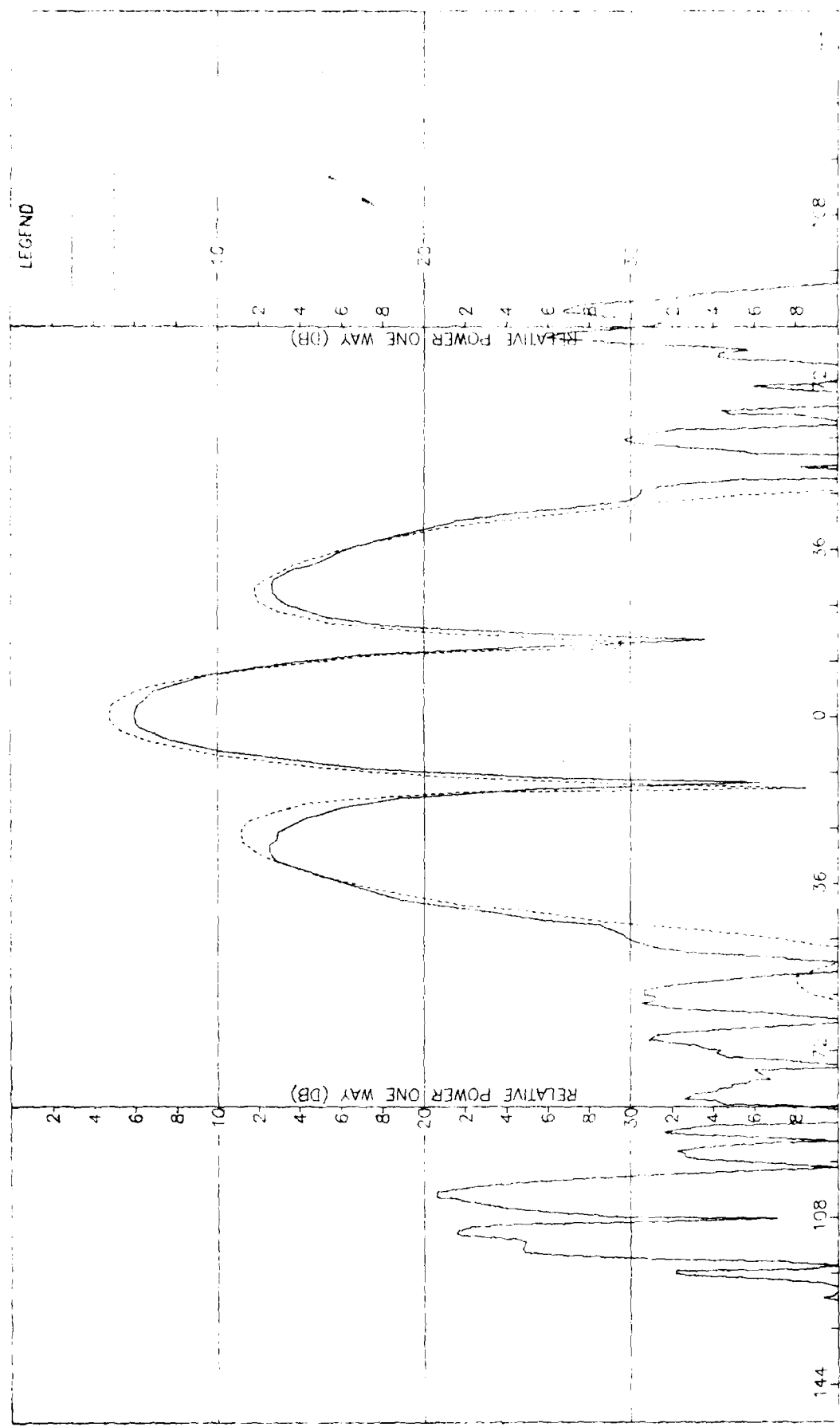


Figure J-1. Pattern of Medium Array: H-Plane, Sum,  $t$ -Component, large ( $F=1$ ) Radome

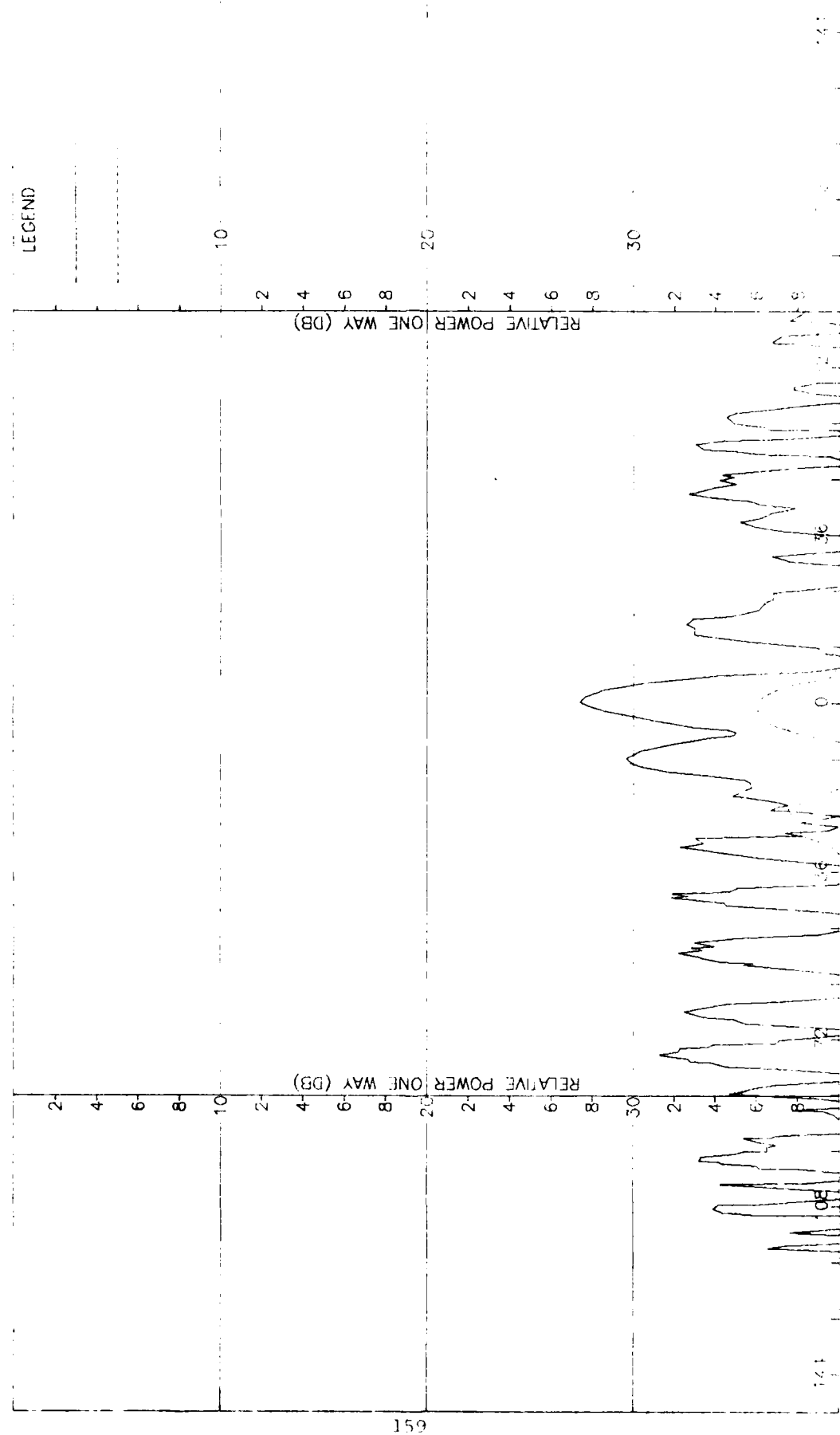


Figure J-2. Pattern of Medium Array: H-P plane, Sum,  $n$ -component, Large ( $F=1$ ) radome

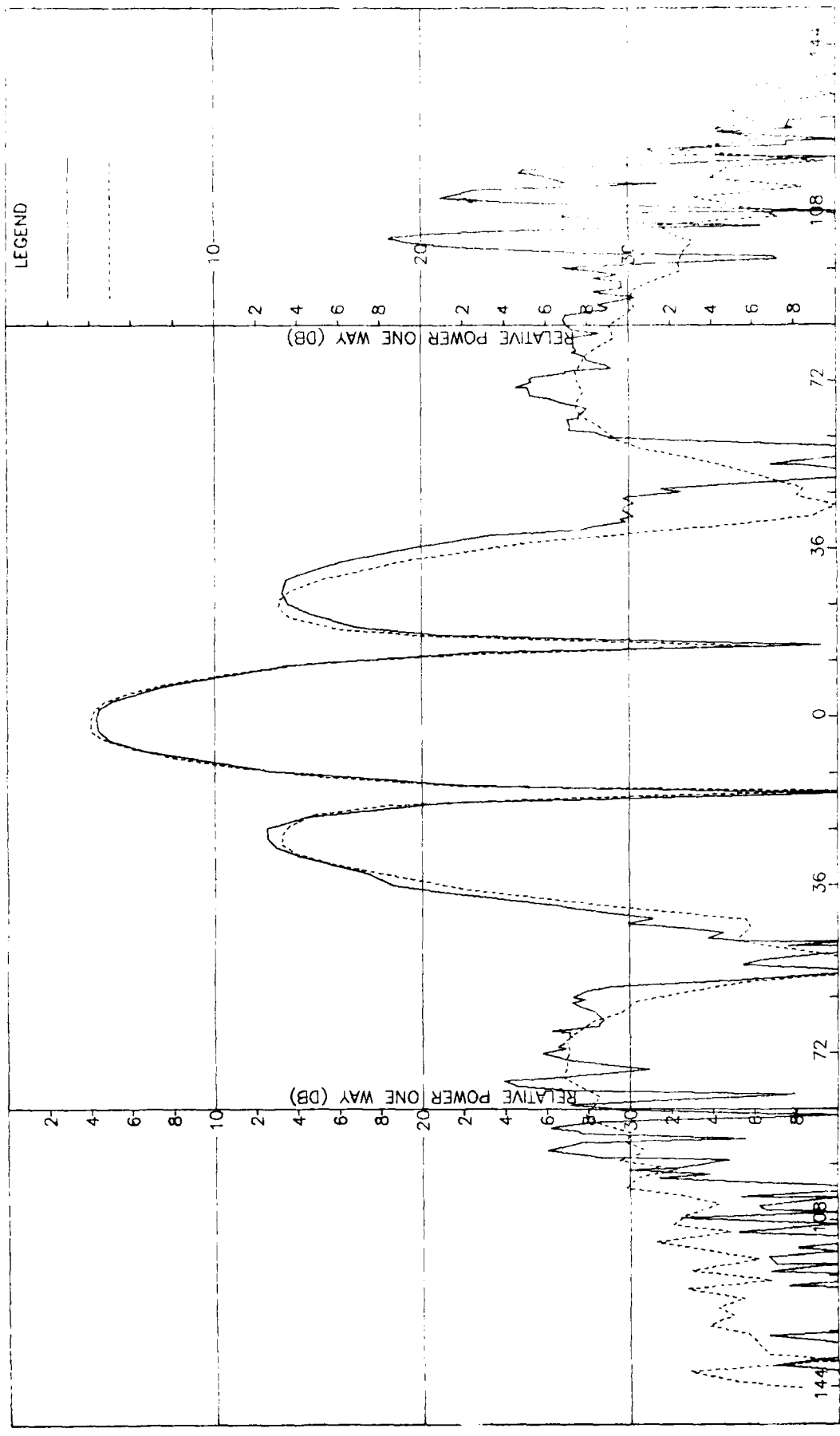


Figure J-3. Pattern of Medium Array: E-Plane, Sum,  $\theta$ -Component, Large ( $l=1$ ) Radome

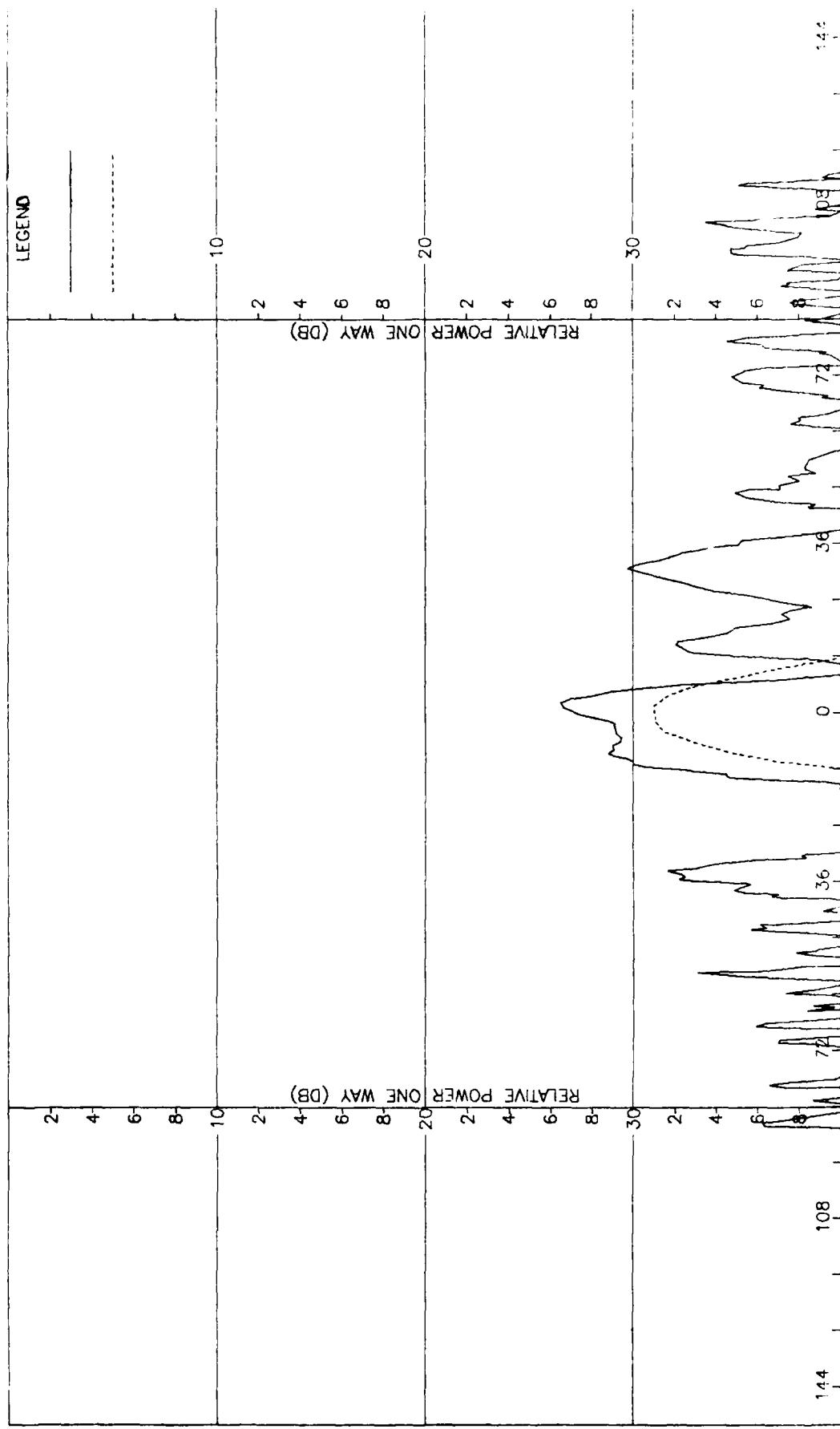


Figure J-4. Pattern of Medium Array: E-Plane, Sum,  $+$ -Component, Large ( $F=1$ ) Radome

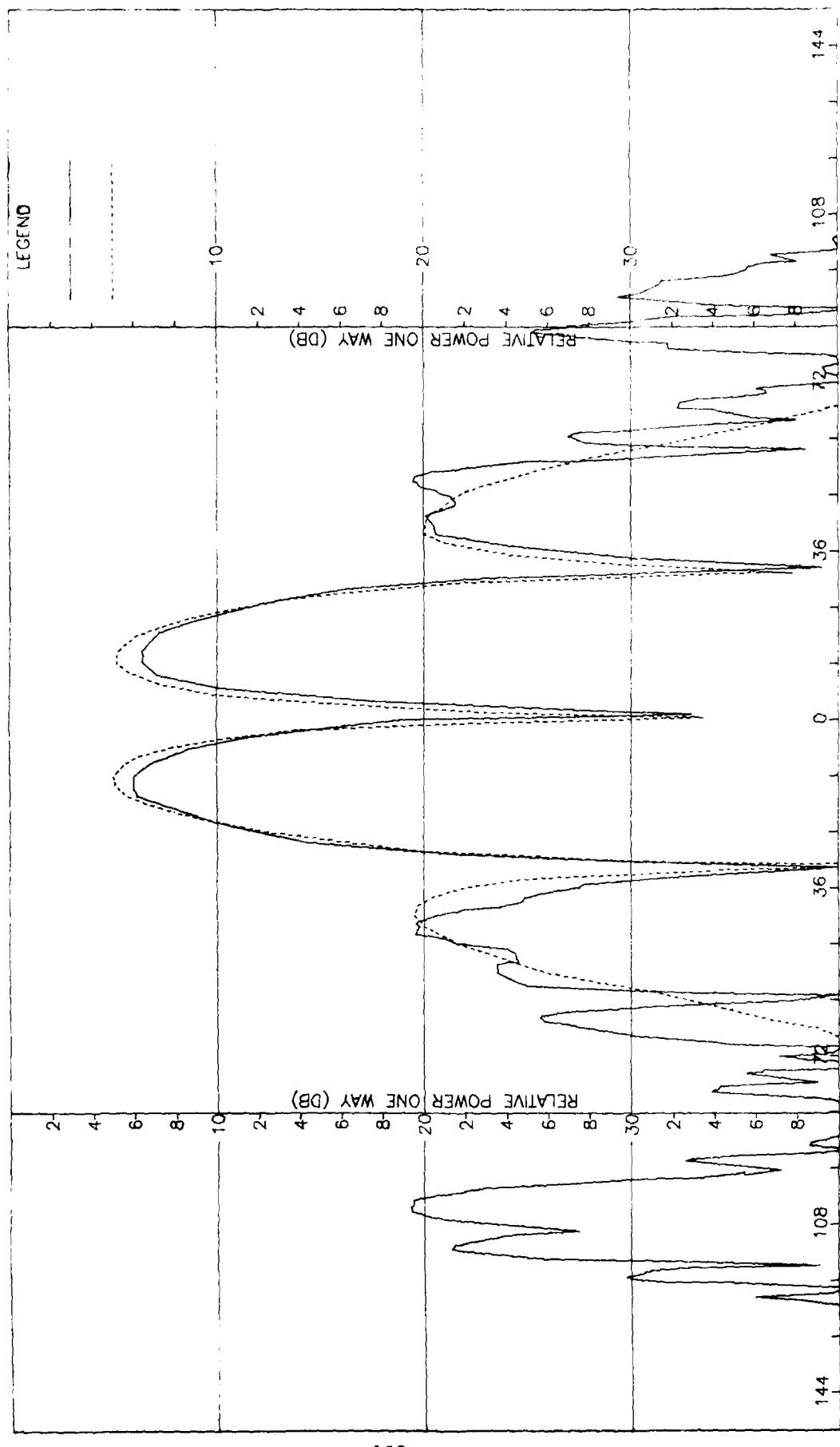


Figure J-5. Pattern of Medium Array: H-Plane, Azimuth Diff.,  $+$ -Component, Large (F=1) Radome

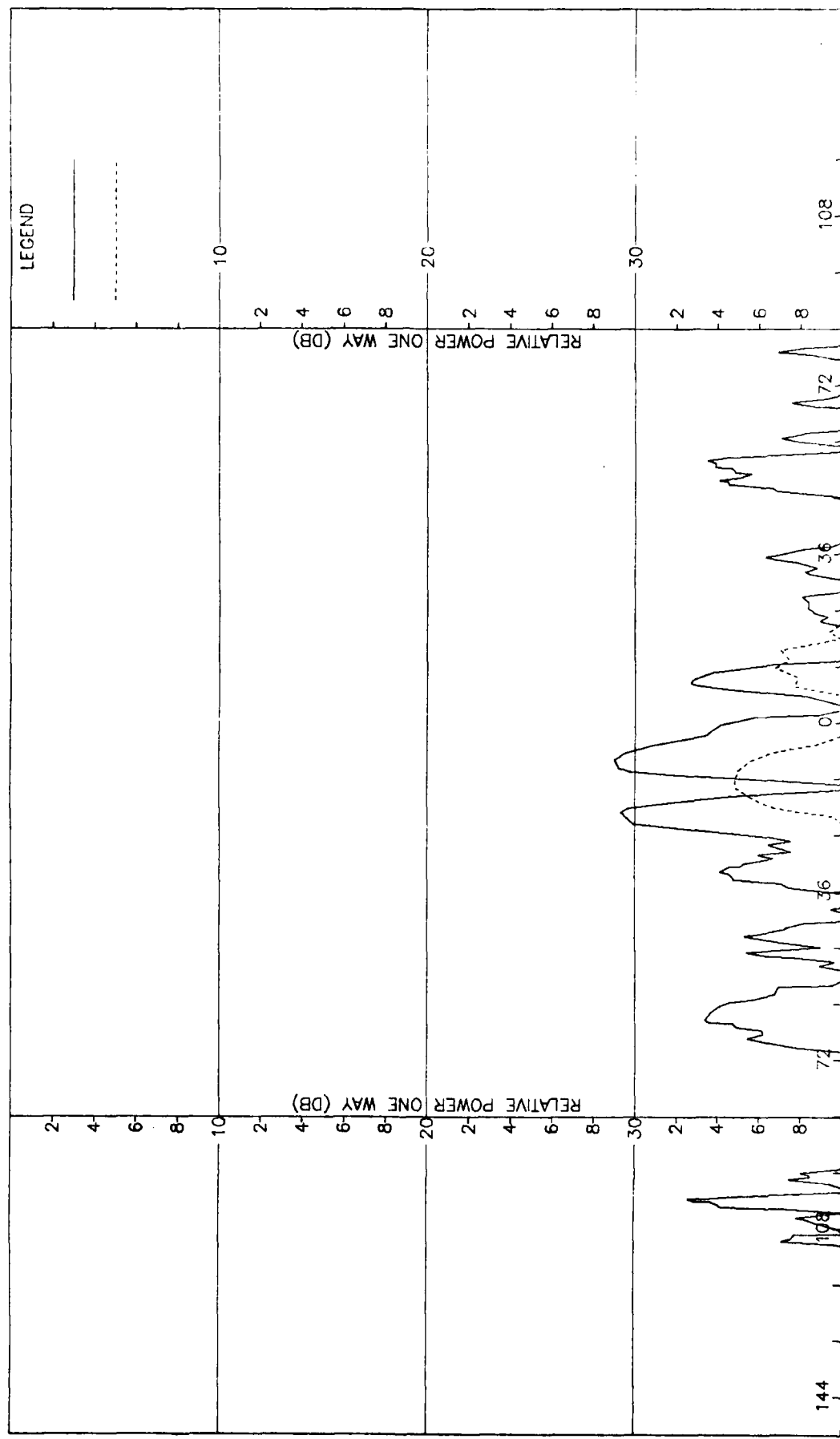


Figure J-6. Pattern of Medium Array: H-Plane, Azimuth diff.,  $\theta$ -Component, Large (F=1) Radome

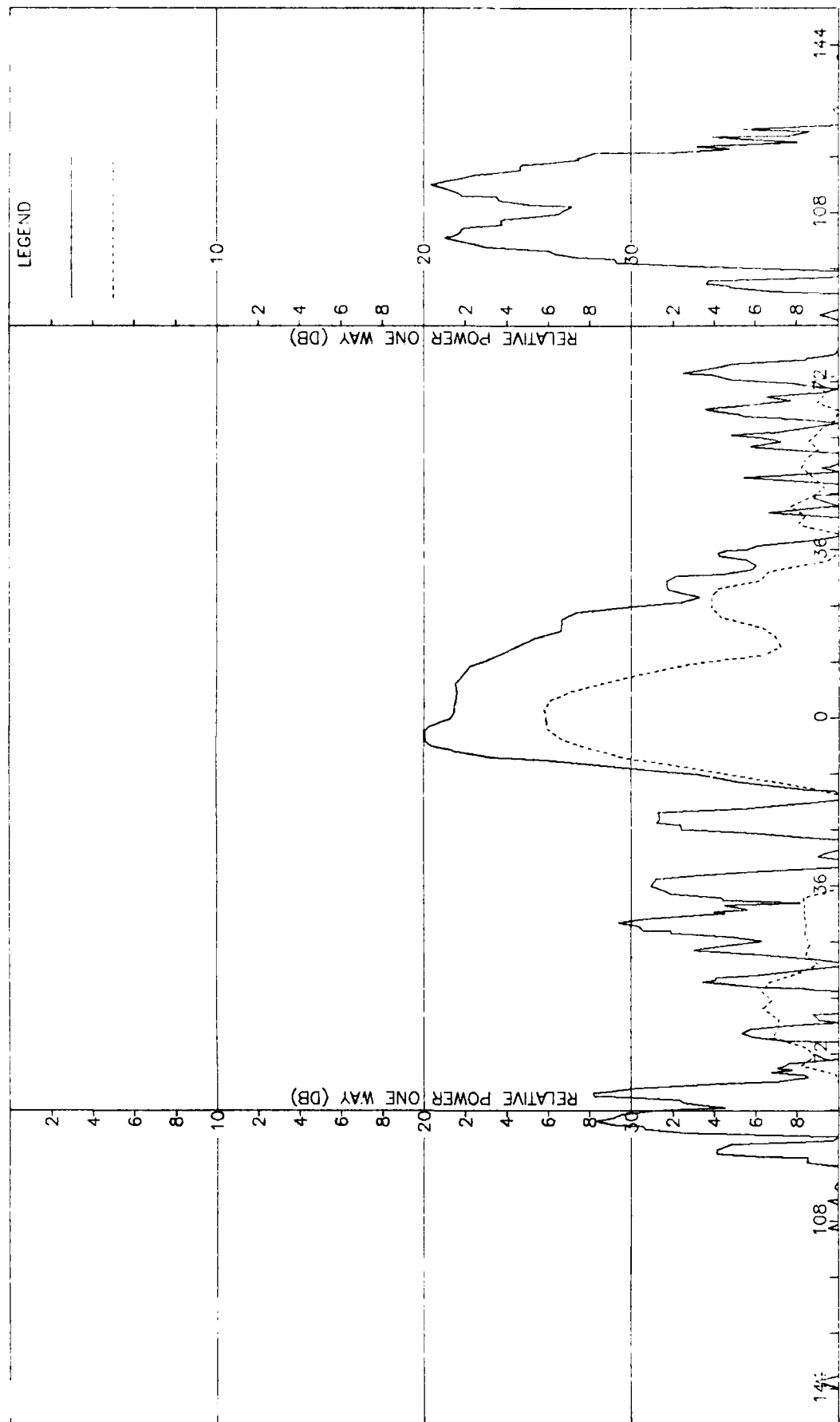


Figure J-7. Pattern of Medium Array: E-Plane, Azimuth Diff., ° - Component, Large (F=1) Radome

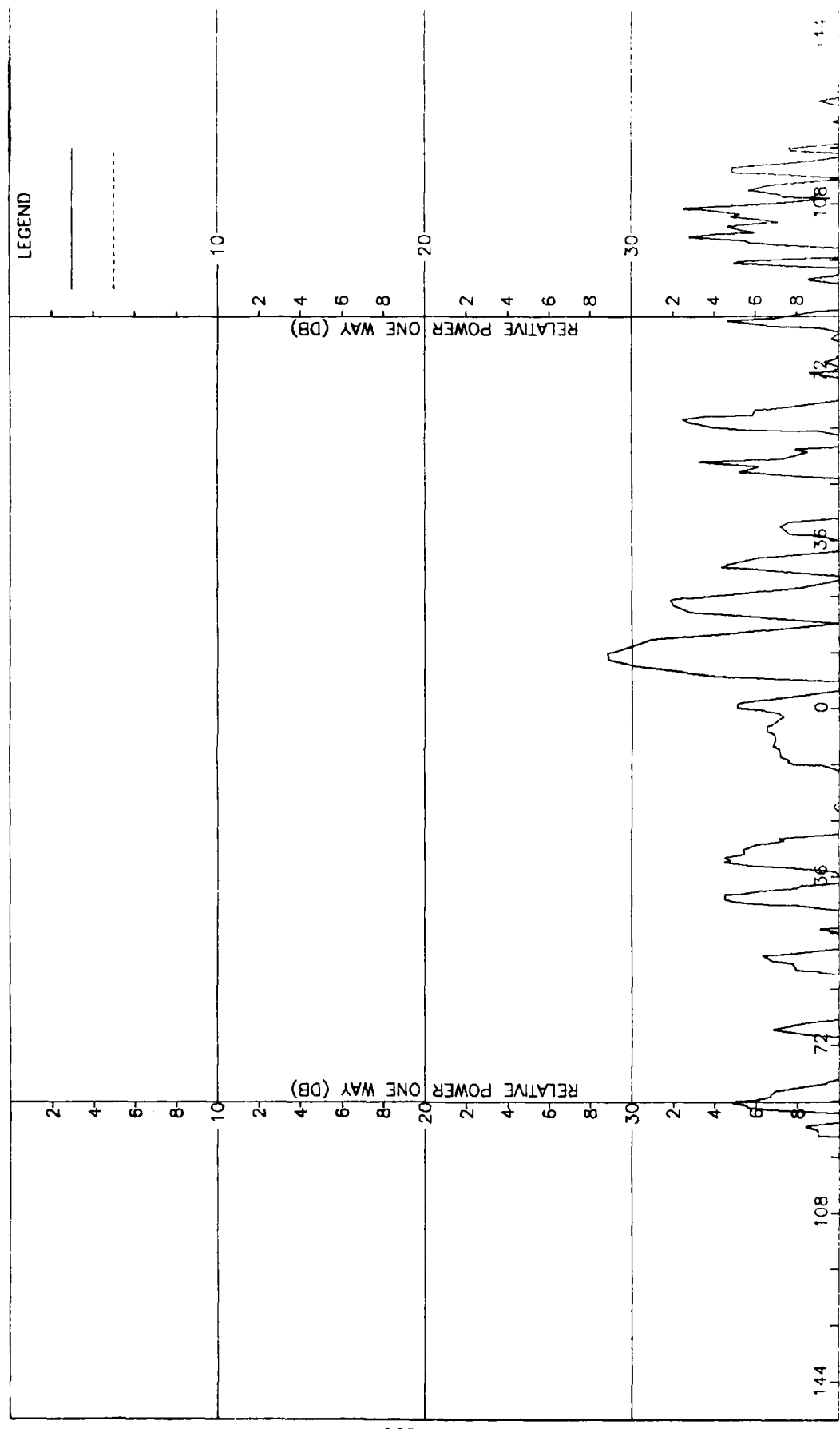


Figure J-8. Pattern of Medium Array: E-Plane, Azimuth Diff., H-Plane, Large (R=1) Radome

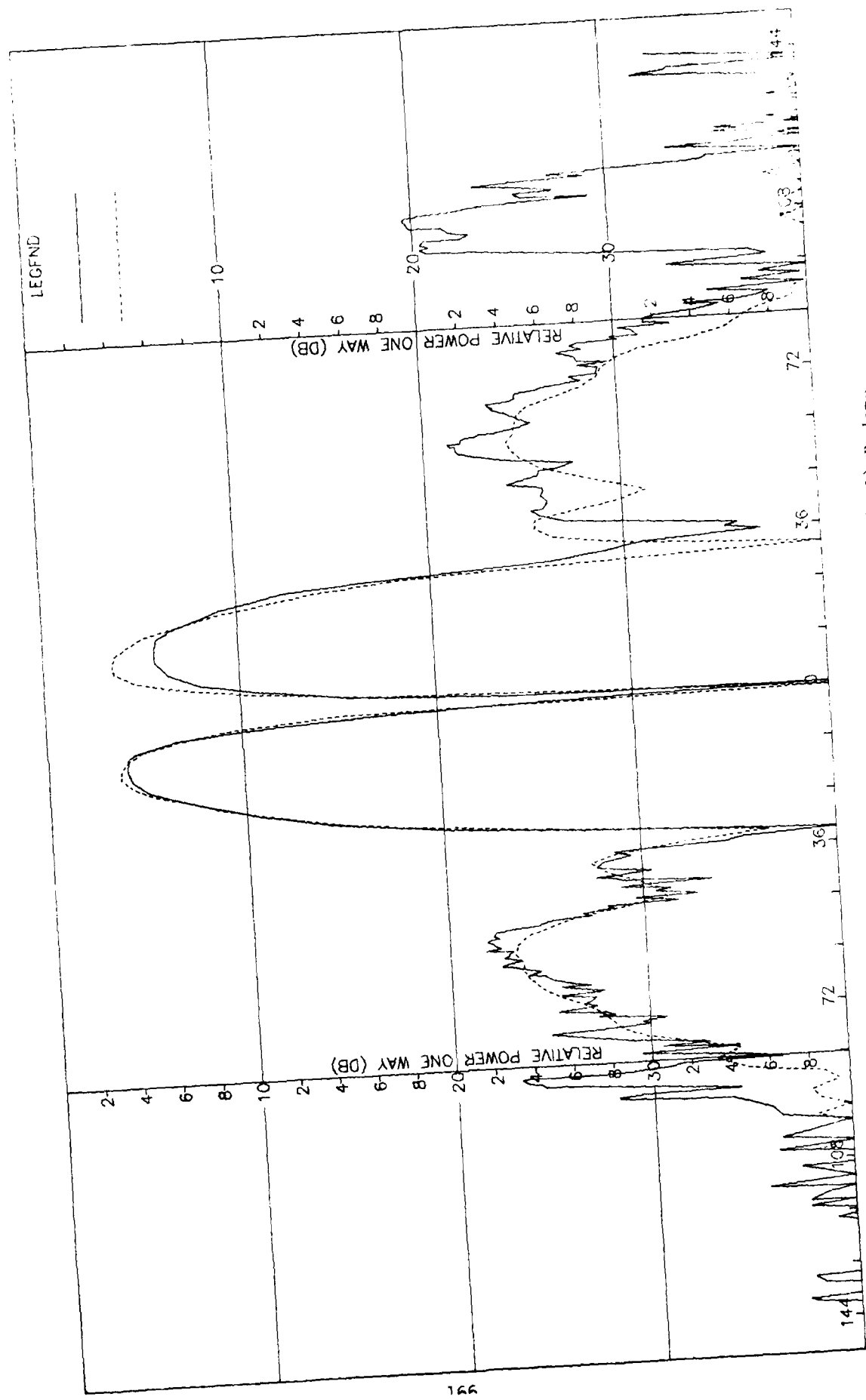


Figure J-9. Pattern of Medium Array: E-Plane,  $q$ -Component, Large (F=1) Radome

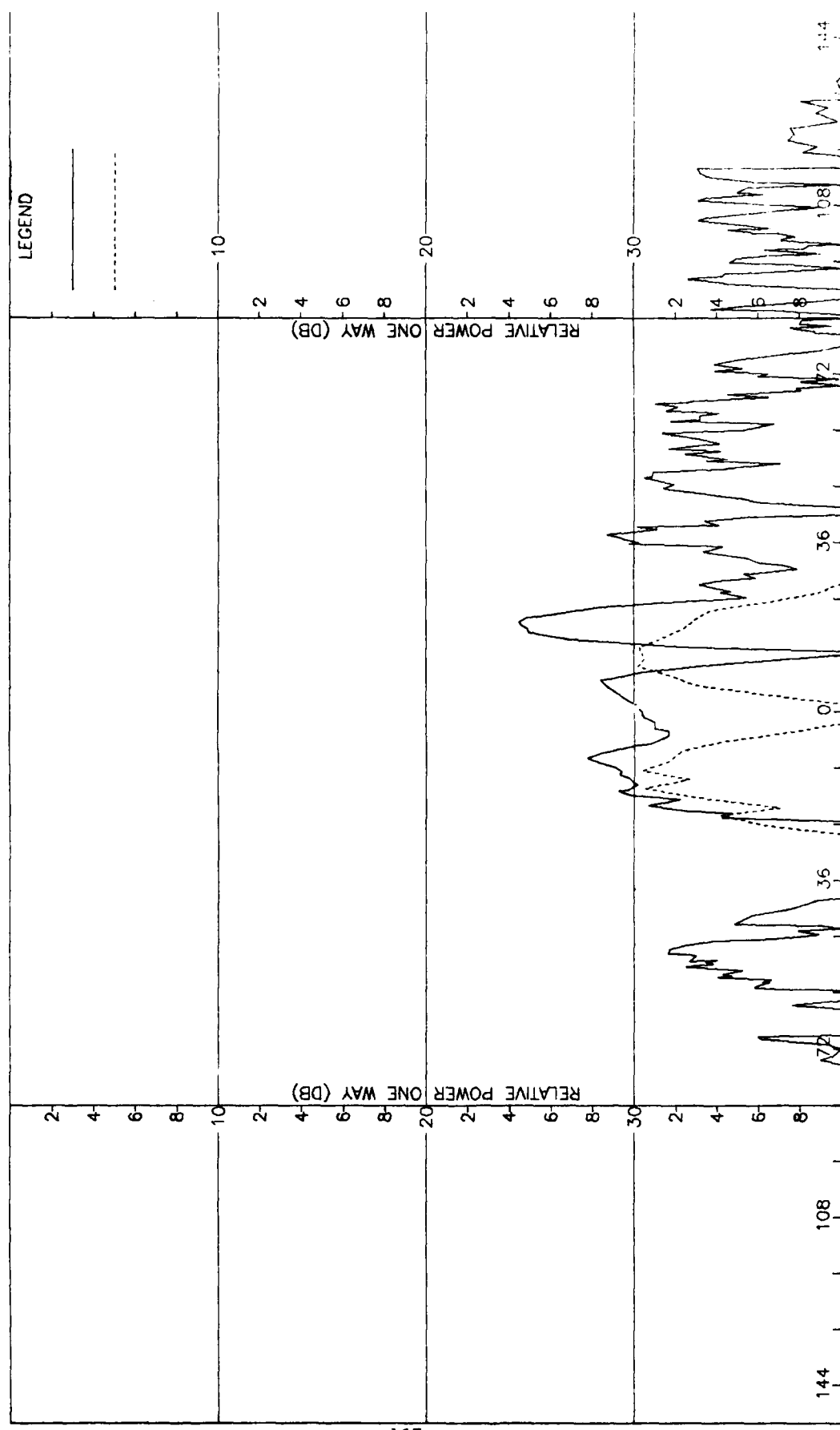


Figure J-10. Pattern of Medium Array: E-Plane, Elevation Diff.,  $\phi$ -Component, Large ( $F=1$ ) Radome

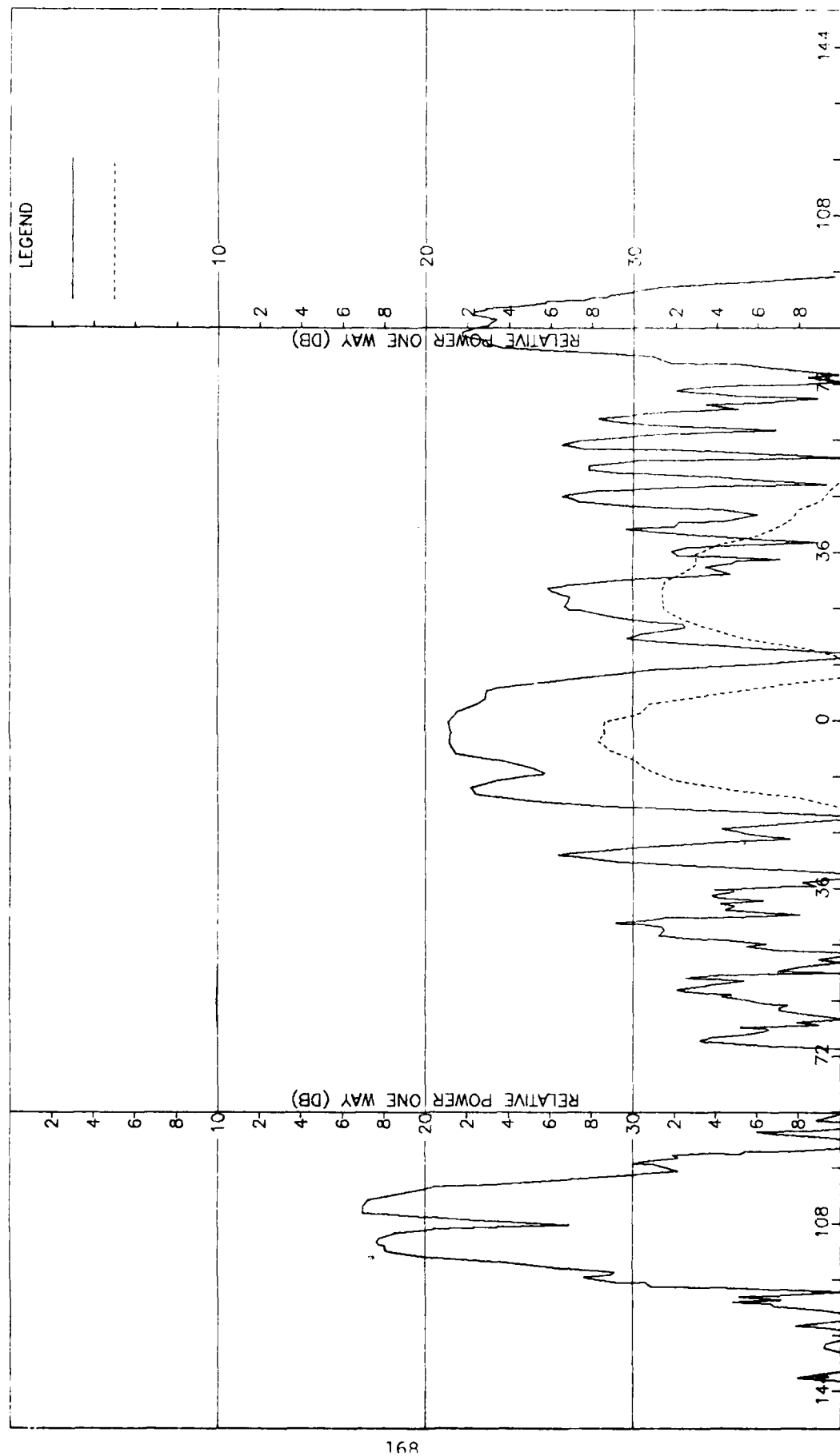


Figure J-11. Pattern of Medium Array: -Plane, Elevation Diff.,  $\phi$ -Component, Large ( $r=1$ ) Radome

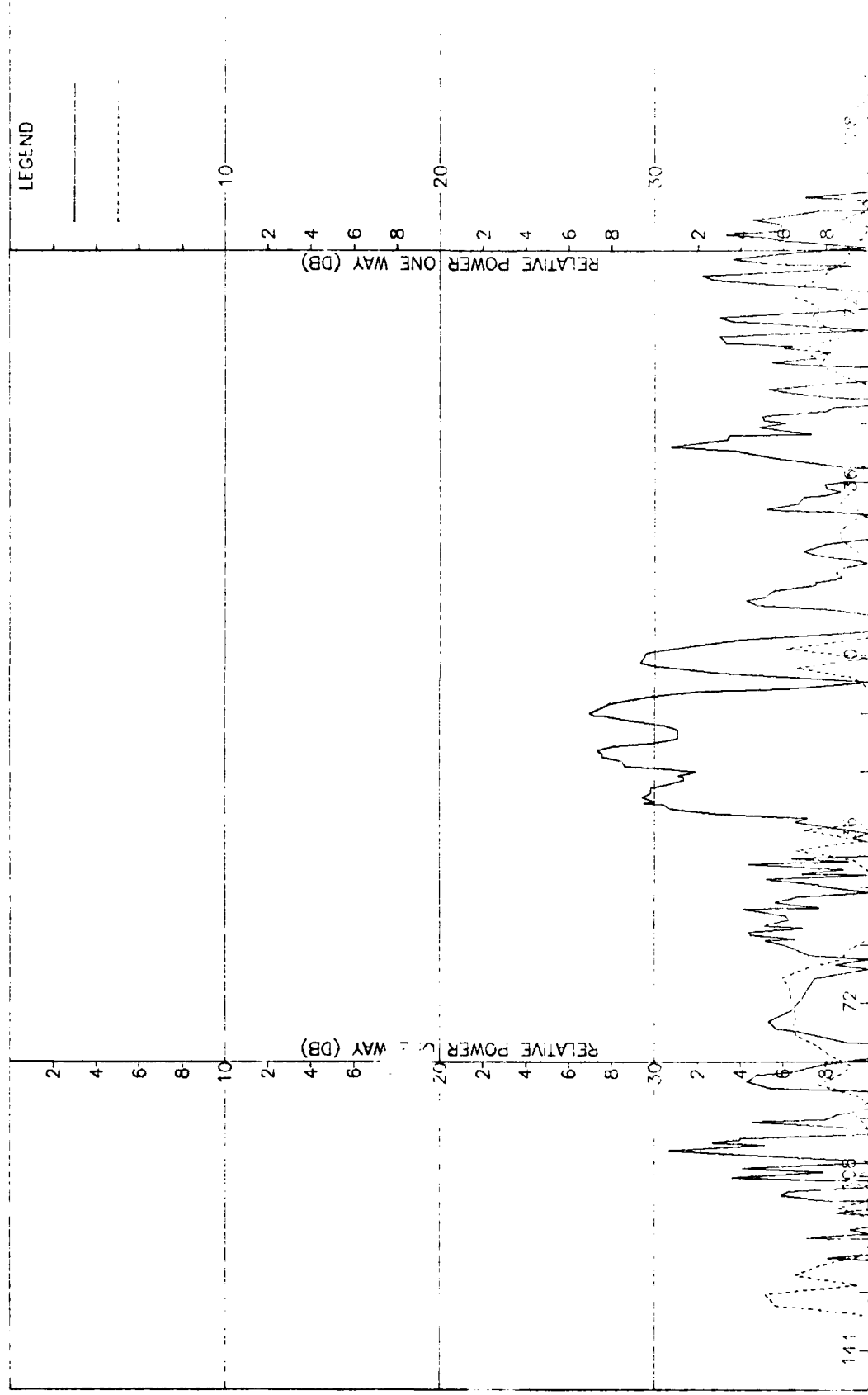


Figure J-12. Pattern of Medium Array: H-Plane, Elevation diff., E-Component, large (—) Small (---).

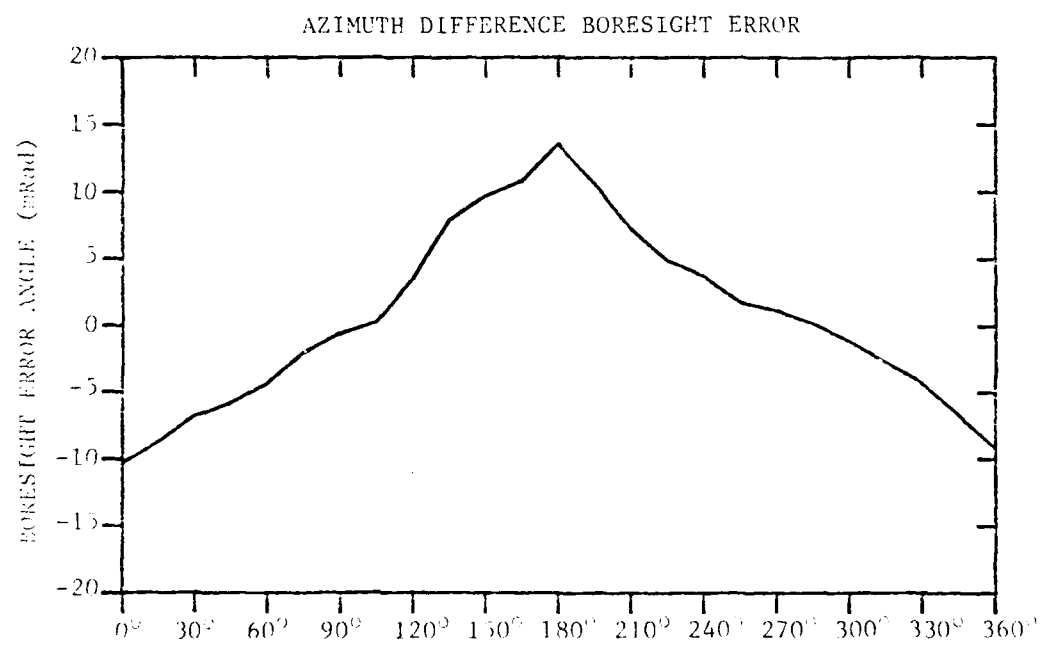
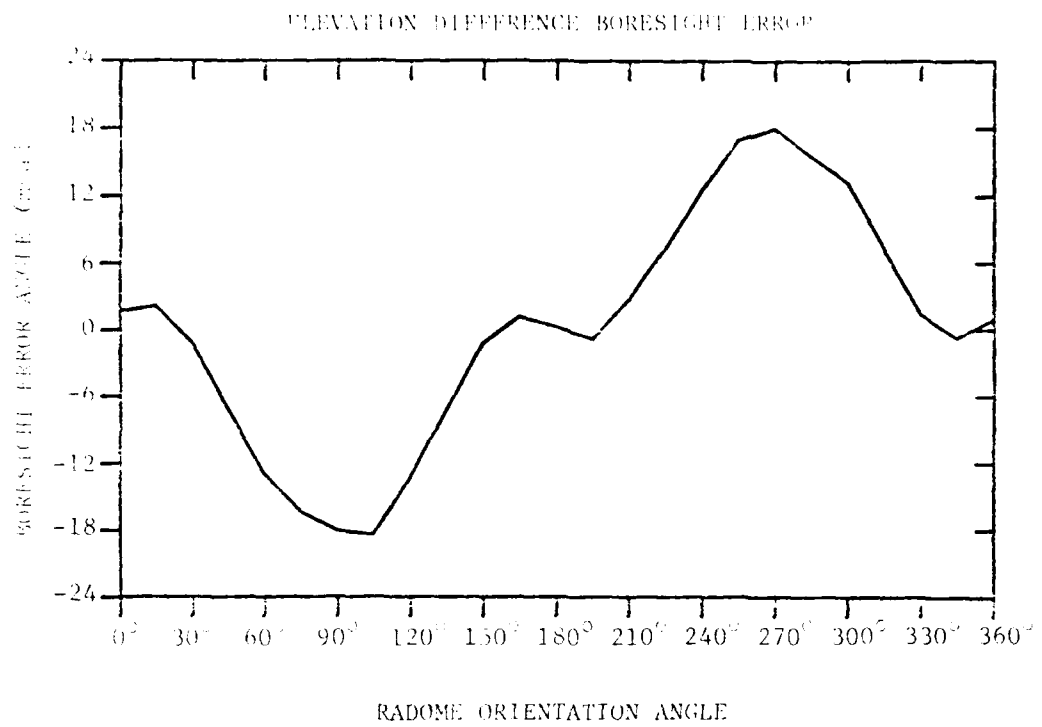


FIGURE J-13. BORESIGHT ERRORS OF MEDIUM ARRAY AND LARGE ( $F=1$ ) RADOME.

APPENDIX K

Antenna Patterns of Large Array with Large (F=1) Radome

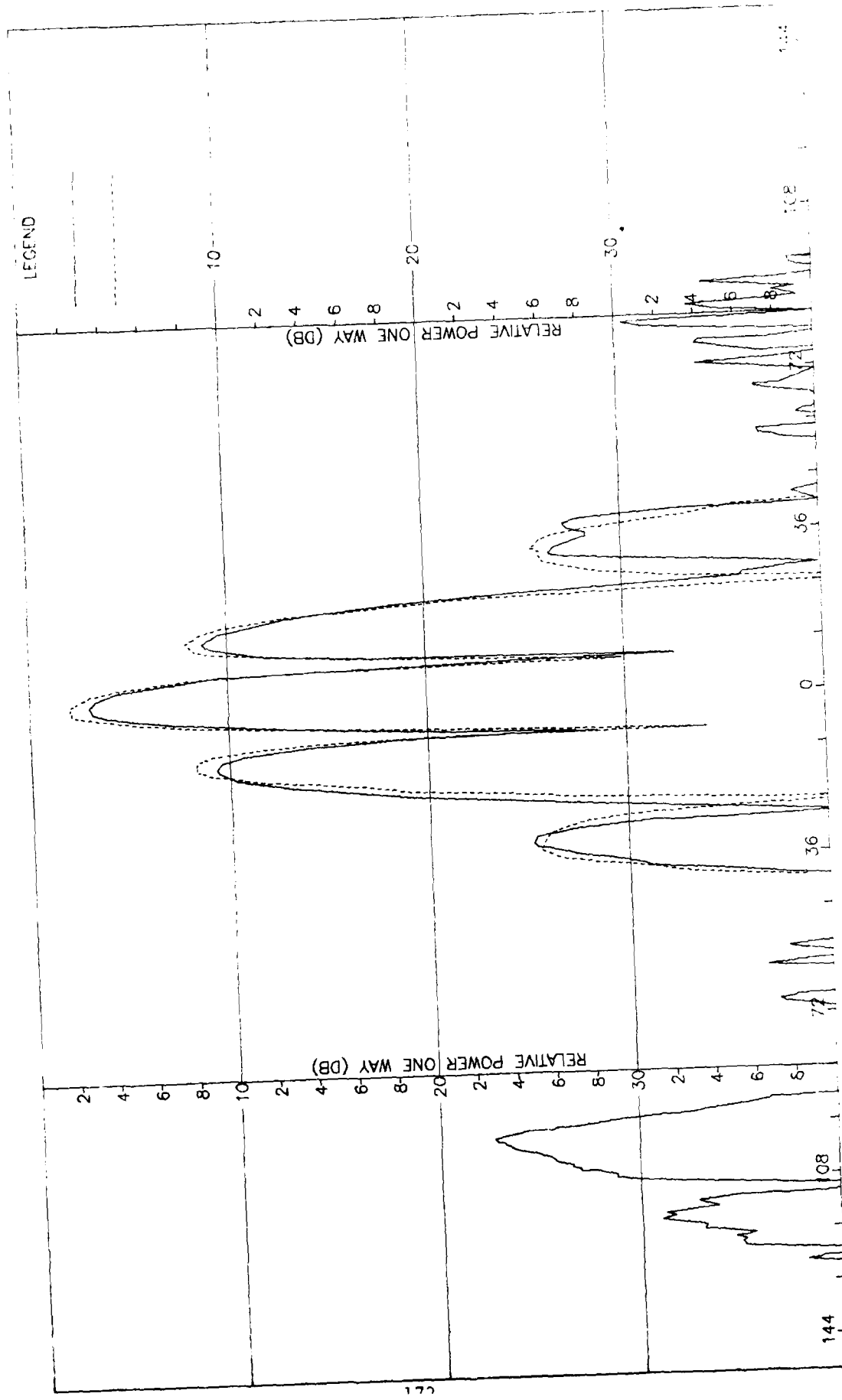


Figure K-1. Pattern of large array: H-plane, Sum,  $\phi$ -component, Large Radome

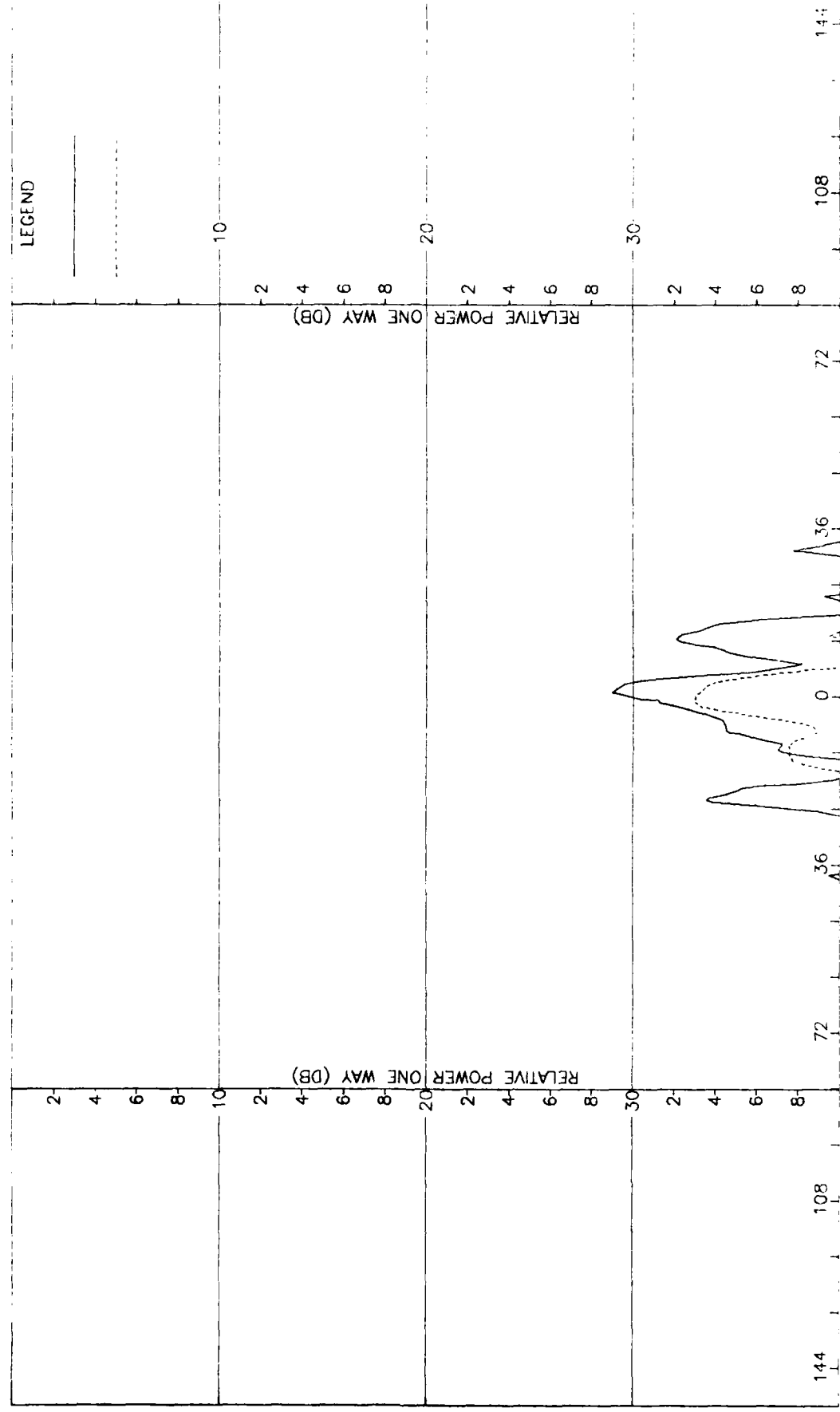


Figure K-2. Pattern of Large Array: H-Plane, Sum,  $\alpha$ -Component, Large Radome

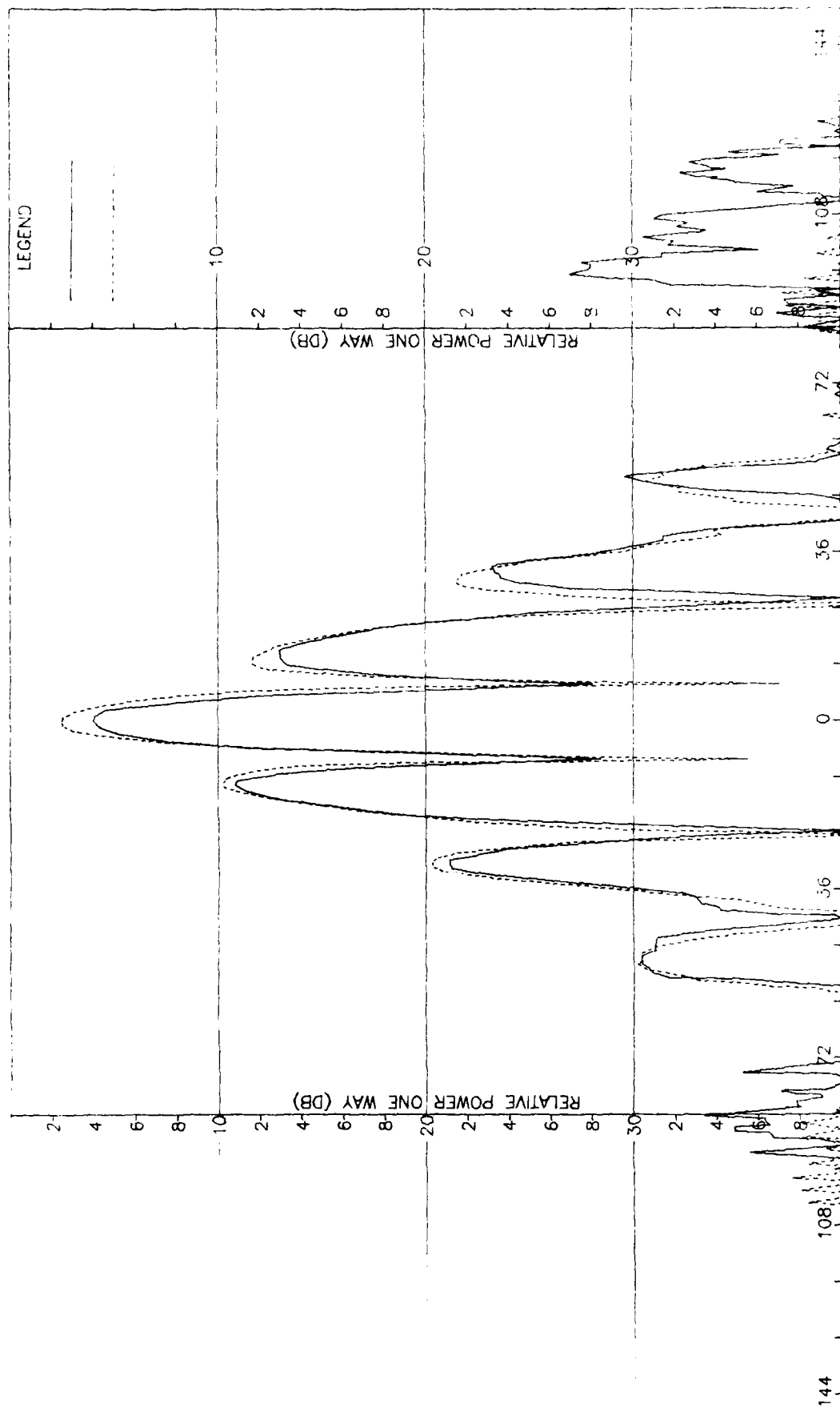


Figure K-3. Pattern of Large Array: E-Plane, Sum, -Component, Large Radome

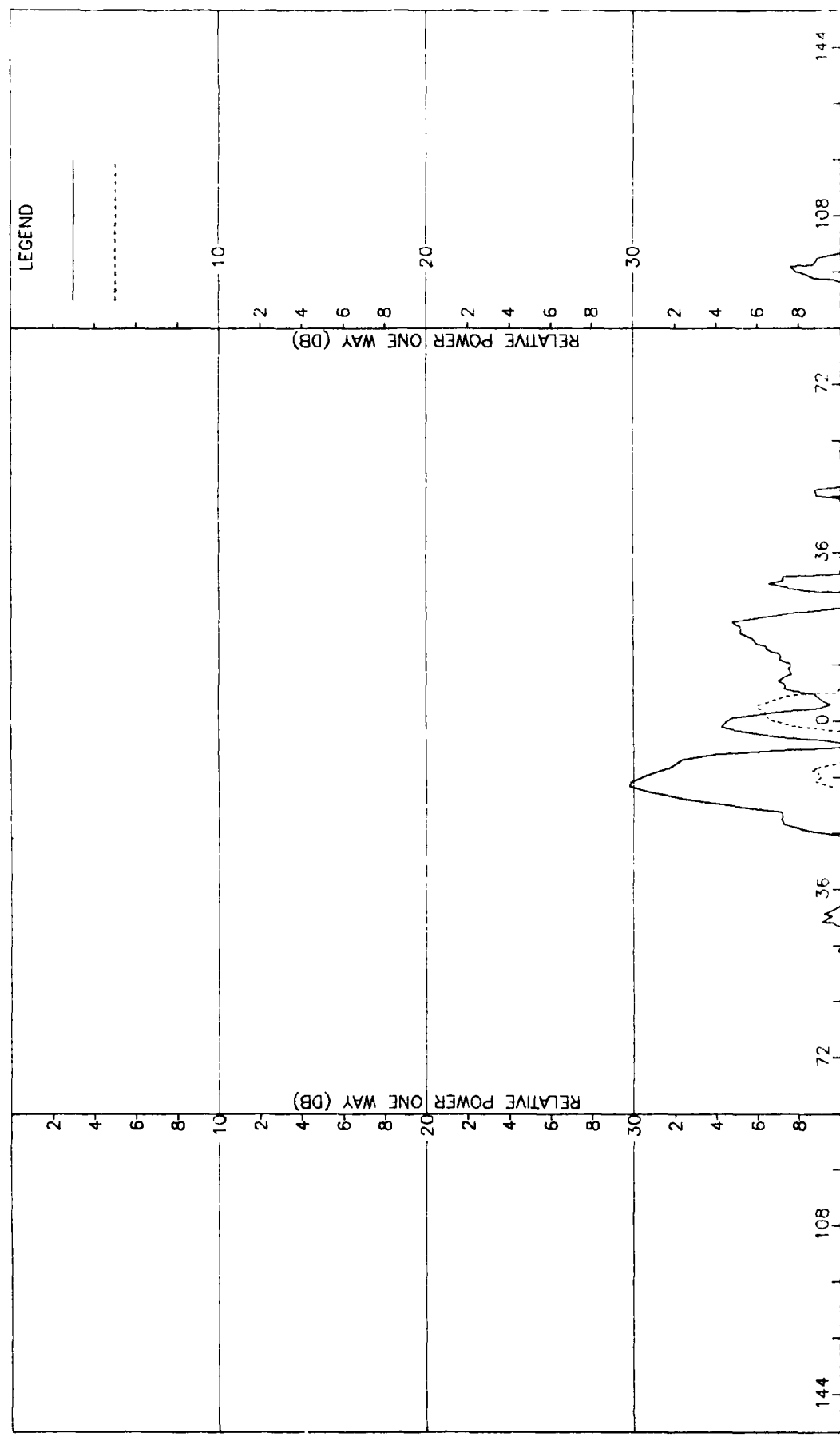


Figure K-4. Pattern of Large Array: F-Plane, Sum, 4-Component, Large Range

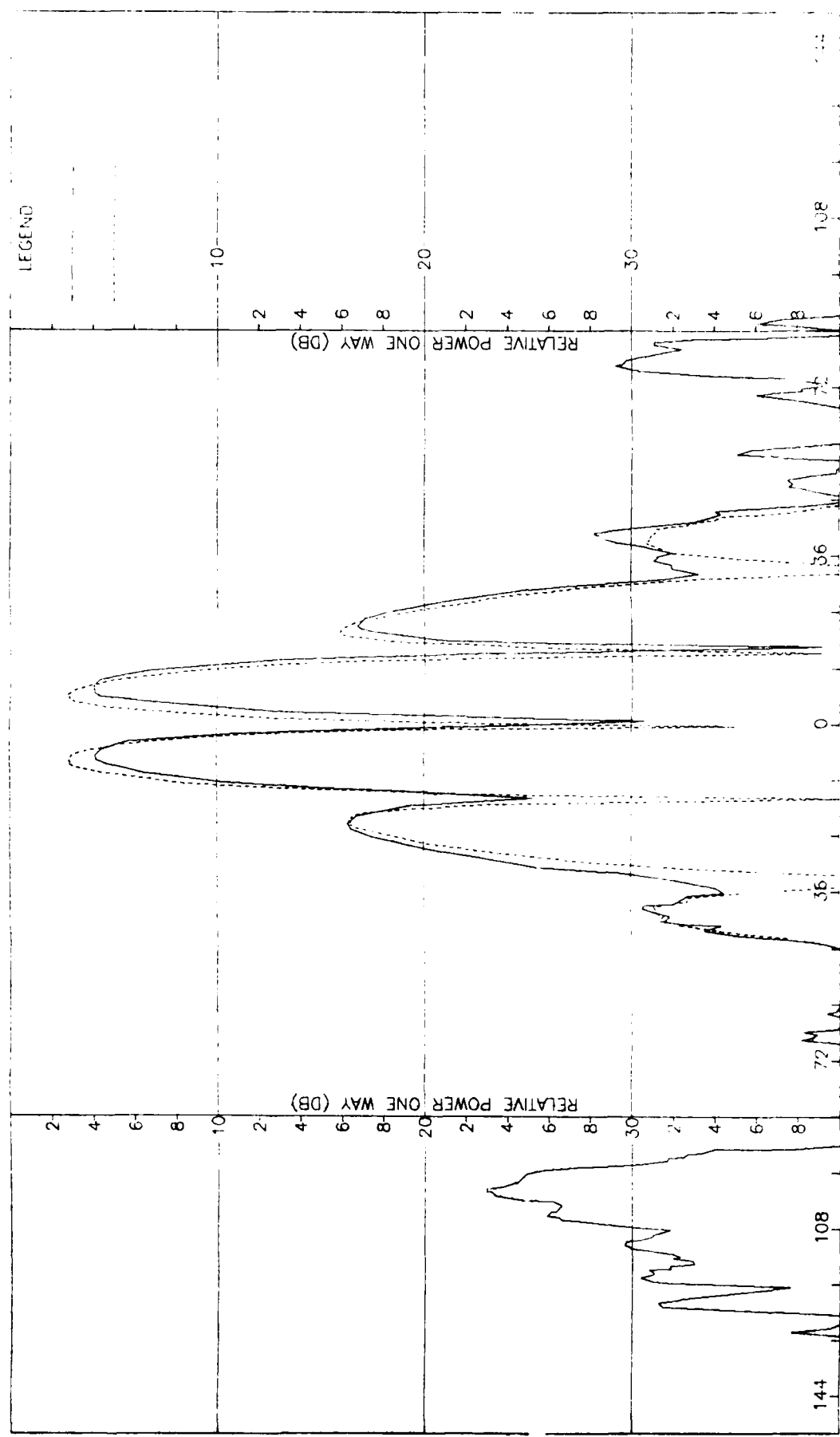


Figure K-5. Pattern of Large Array: H-Plane, Azimuth Diff. deg.; -Component, Large Radome

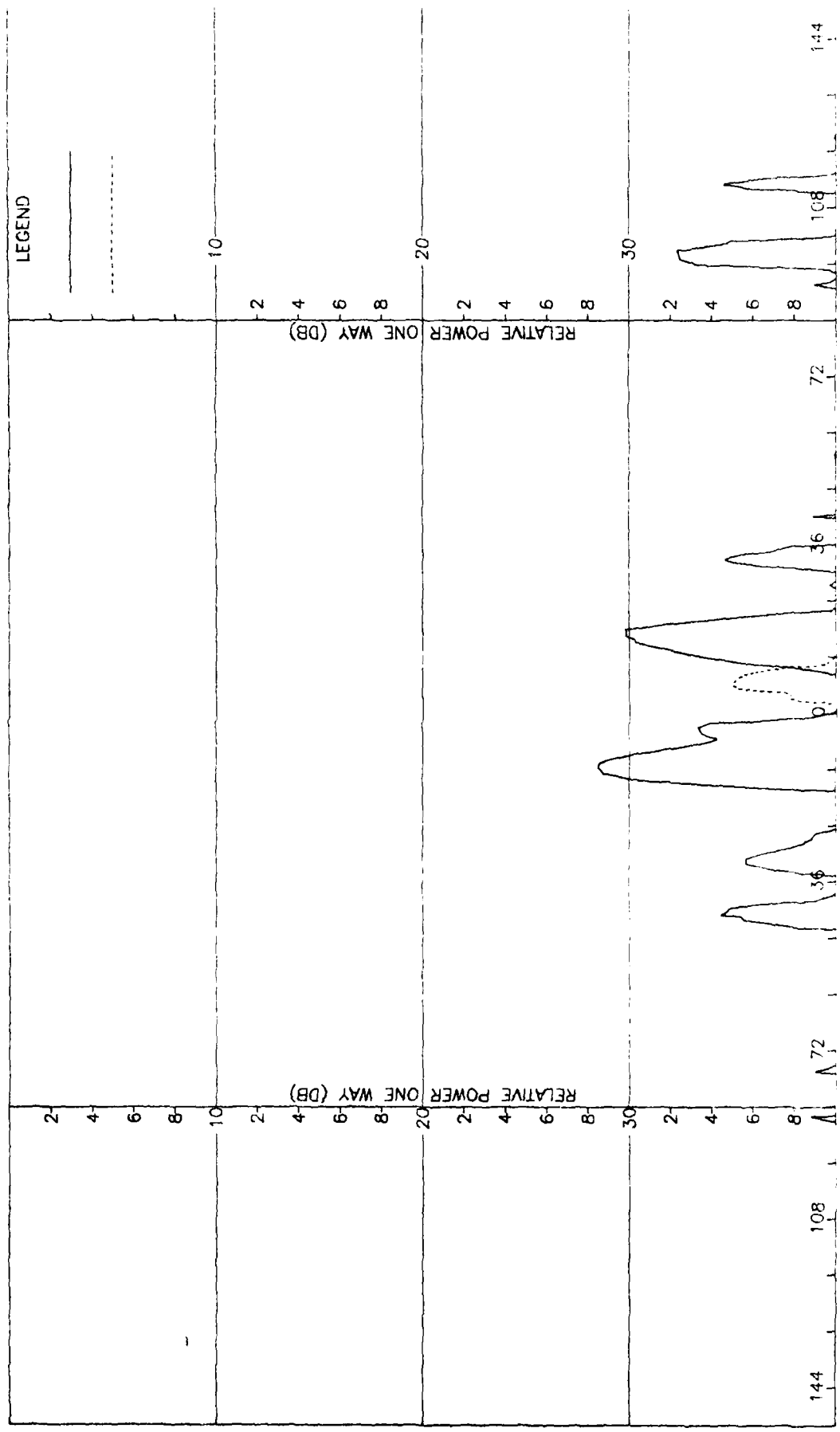


Figure K-6. Pattern of Large Array: H-plane, Azimuth Diff., -Component, Large Radome

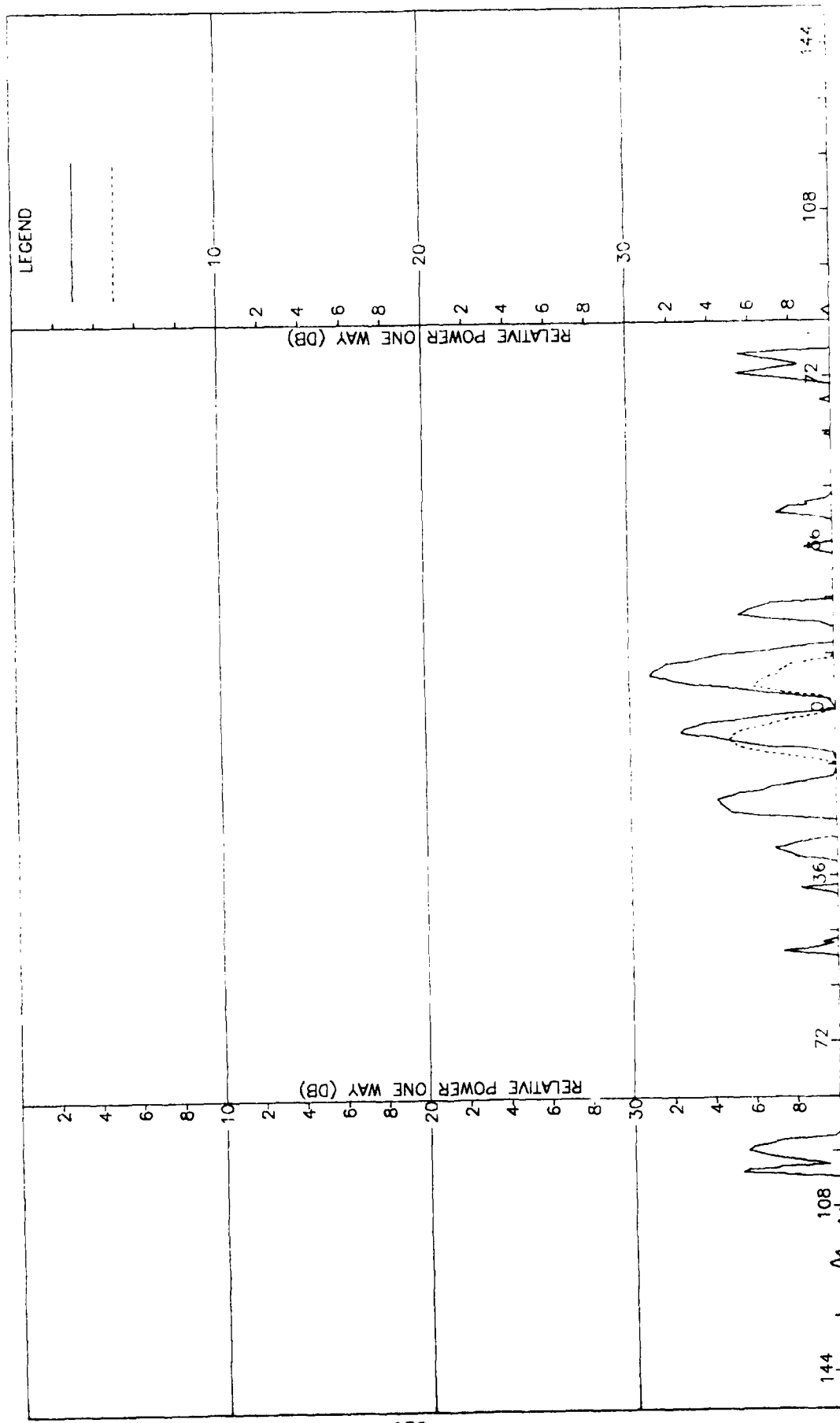


Figure K-7. Pattern of Large Array: E-Plane, Azimuth Diff.,  $a$ -Component, Large Radome

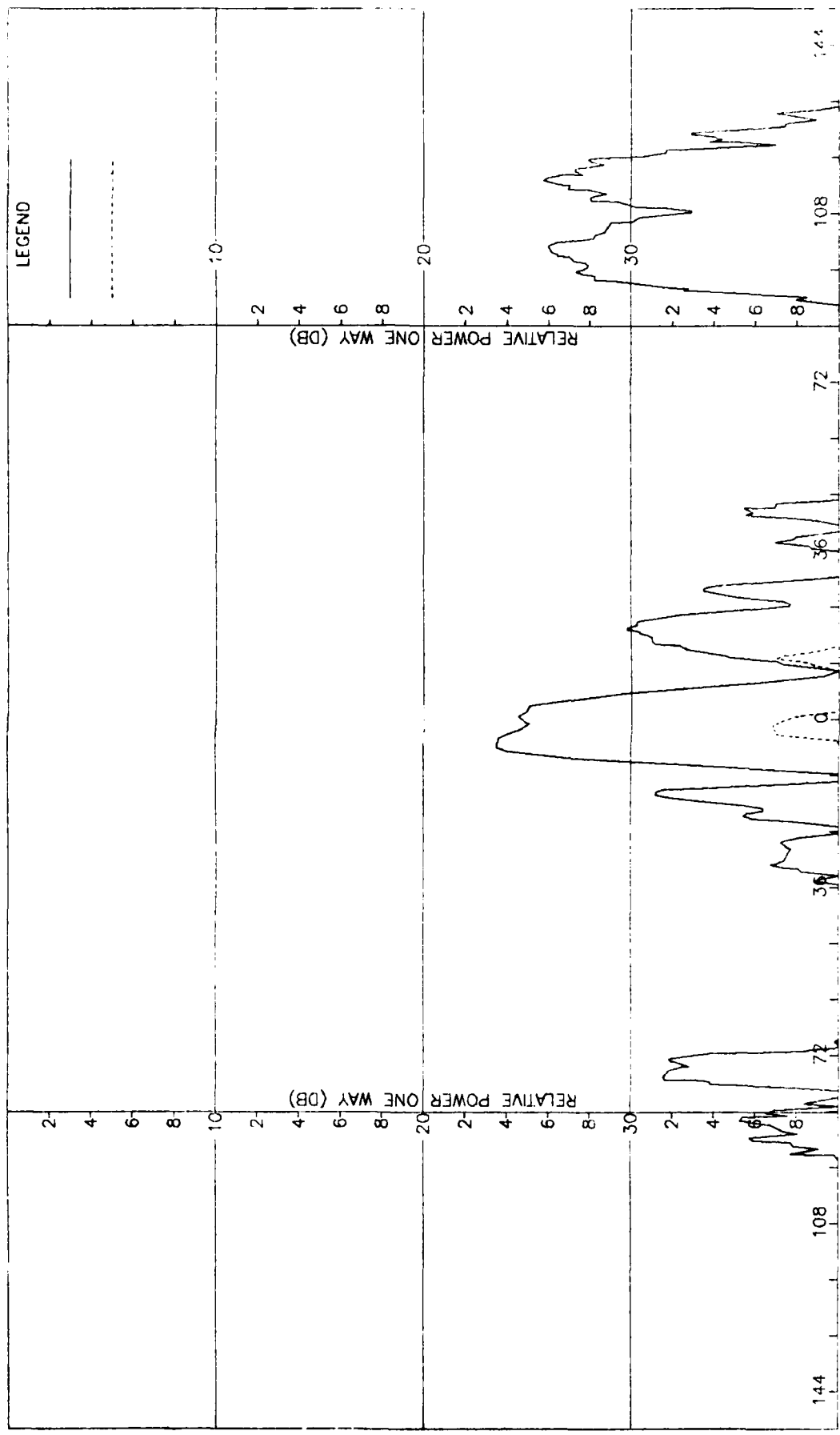


Figure K-8. Pattern of Large Array: E-P Plane, Azimuth Diff.,  $z$ -Component, Large Radome

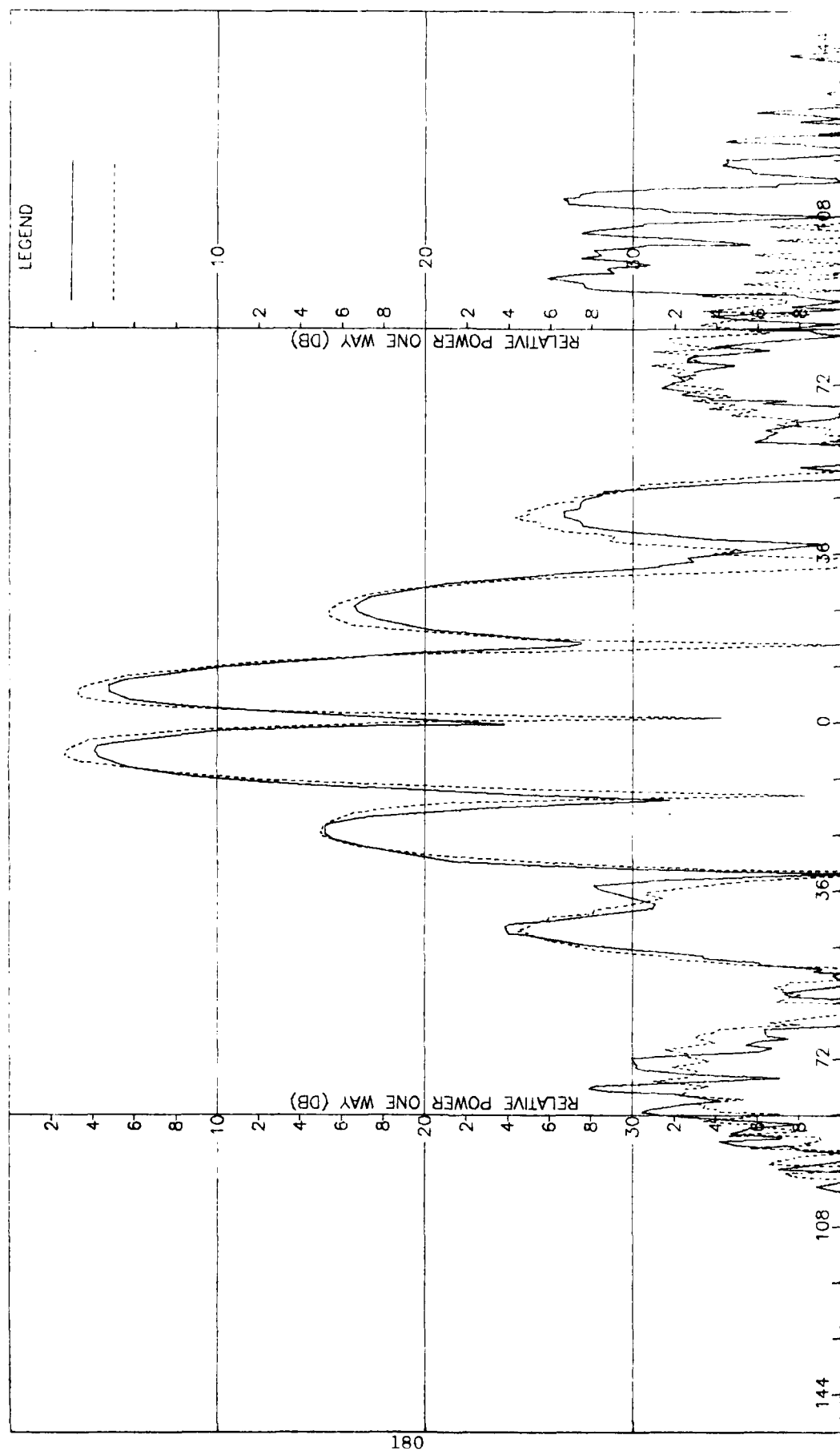


Figure K-9. Pattern of Large Array: E-Plane, Elevation Diff., -Component, Large Radome

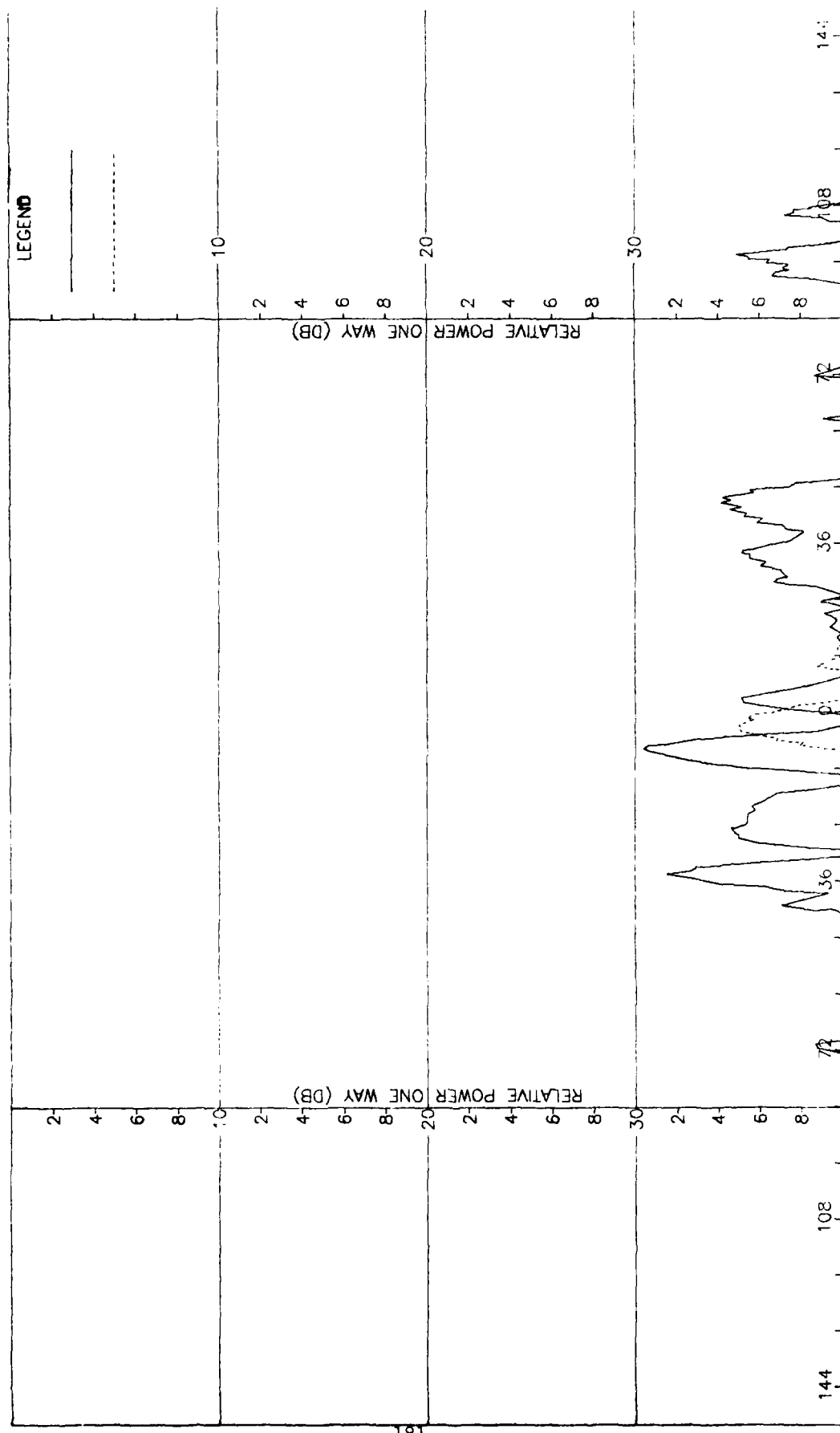


Figure K-10. Pattern of Large Array: E-plane, Elevation Diff.,  $\phi$ -Component, Large Radome

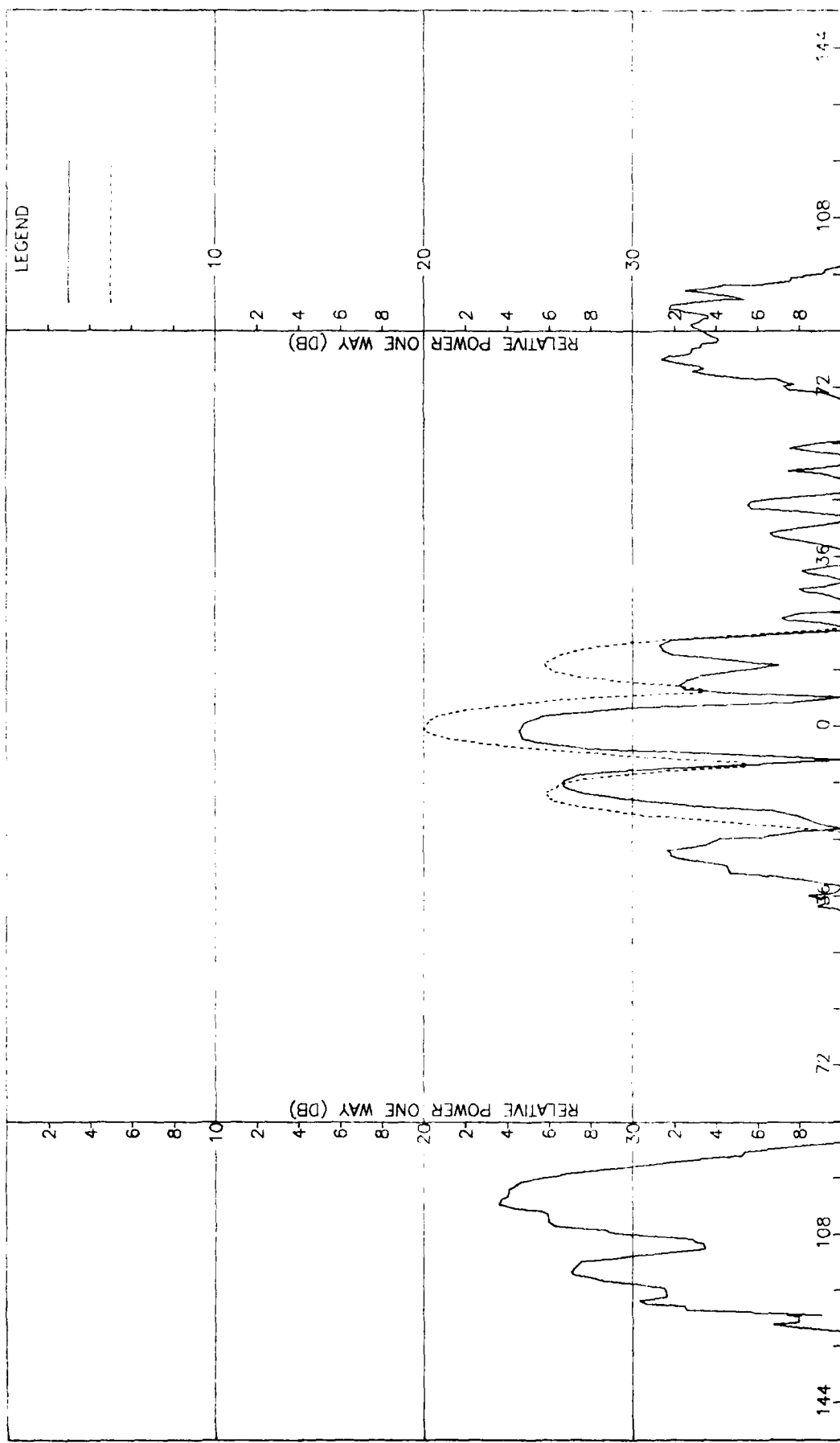


Figure K-11. Pattern of Large Array: H-Plane, Elevation diff., :-Component, Large Radome

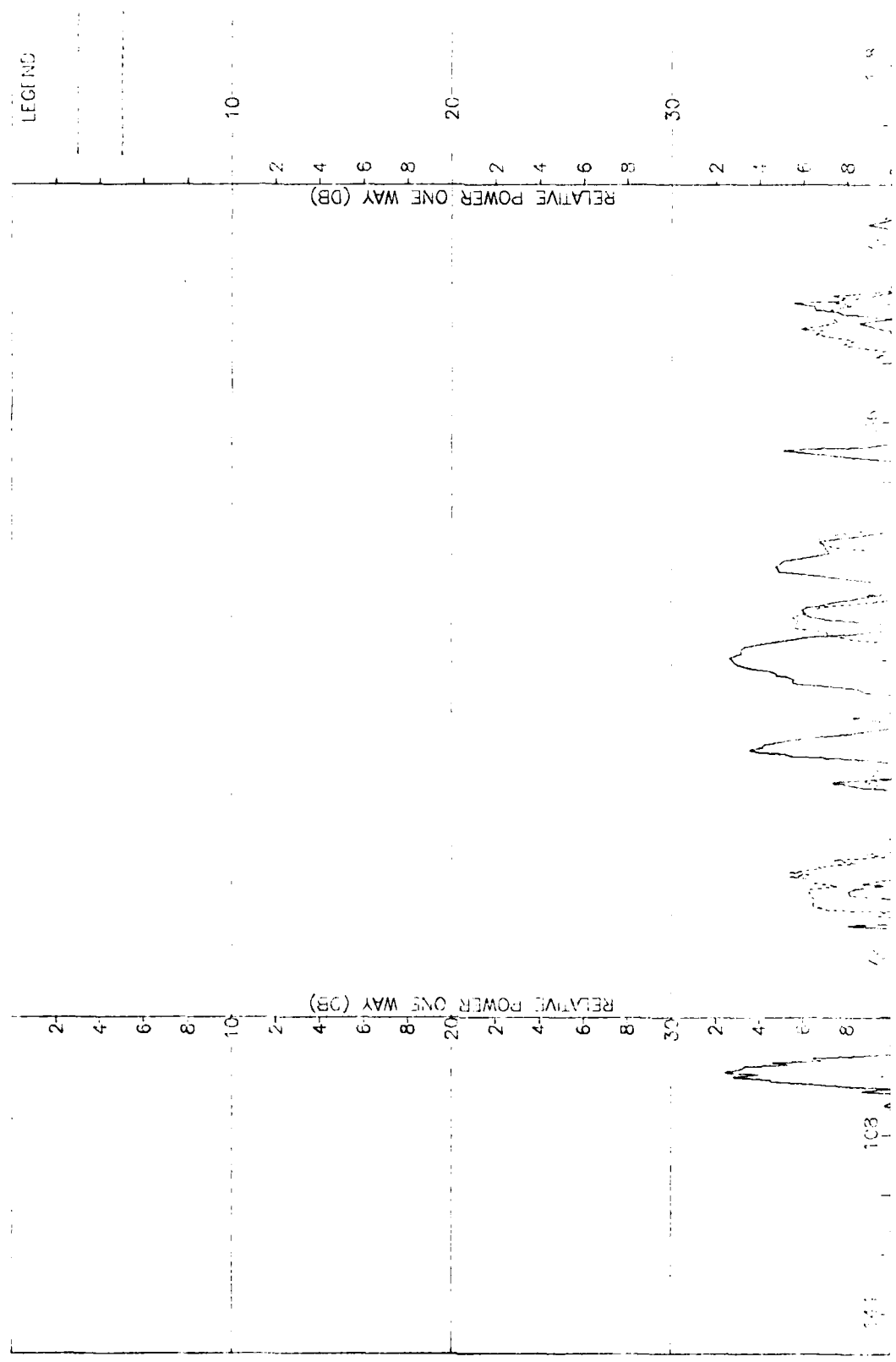


Figure K-12. Pattern of Large Array: Horizontal, Elevation Patterns. - Component, - Large Radome

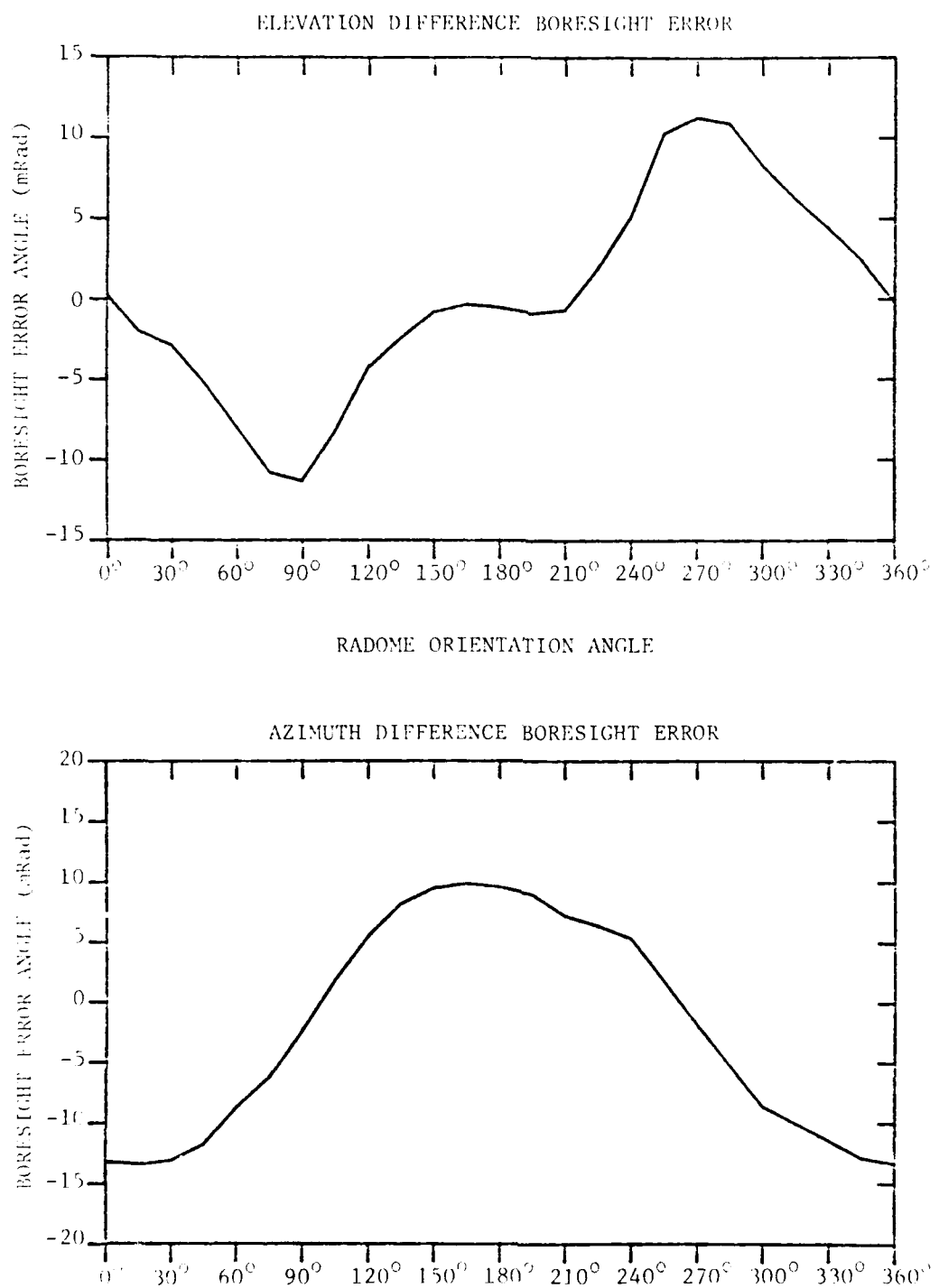


FIGURE K-13. BORESIGHT ERRORS OF LARGE ARRAY AND LARGE ( $F=1$ ) RADOME.

DATE  
FILMED

7 8